

UNIVERSITY OF BELGRADE
FACULTY OF CIVIL ENGINEERING

Emilija V. Jočić

**PROGRESSIVE FAILURE ANALYSIS OF
LAMINAR COMPOSITES UNDER
THREE-DIMENSIONAL STRESS STATE
USING LAYERED FINITE ELEMENTS**

Doctoral Dissertation

Belgrade, 2023



UNIVERZITET U BEOGRADU

GRAĐEVINSKI FAKULTET

Emilija V. Jočić

**ANALIZA PROGRESIVNOG LOMA
KOMPOZITNIH LAMINATA U USLOVIMA
PROSTORNOG STANJA NAPONA
PRIMENOM SLOJEVITIH KONAČNIH
ELEMENATA**

doktorska disertacija

Beograd, 2023.

Advisor:

Assist. Prof. Dr. Miroslav Marjanović
University of Belgrade, Faculty of Civil Engineering

Committee:

Assist. Prof. Dr. Miroslav Marjanović
University of Belgrade, Faculty of Civil Engineering

Assoc. Prof. Dr. Marija Nefovska - Danilović
University of Belgrade, Faculty of Civil Engineering

Assoc. Prof. Dr. Ivan Glišović
University of Belgrade, Faculty of Civil Engineering

Visiting Prof. Dr. Aleksandar Borković
University of Banja Luka, Faculty of Architecture, Civil Engineering and Geodesy
Researcher, TU Graz, Institut für Baumechanik

Prof. Dr.techn. Günther Meschke
Ruhr Universität Bochum, Institute for Structural Mechanics

Defense date: _____

Acknowledgments

First and foremost, I would like to express my deepest gratitude to my supervisor Dr. Miroslav Marjanović for his invaluable assistance and unwavering support throughout the completion of my doctoral dissertation. His guidance and expertise have played a crucial role in shaping the direction of my research and enhancing the quality of my work. His constructive feedback and insightful suggestions have greatly contributed to the development of my ideas and have helped me navigate through various challenges. I am truly fortunate to have had the opportunity to benefit from his mentorship, and I am grateful for his constant availability and willingness to assist me. Moreover, I am particularly thankful for his enduring faith in my capabilities, as he never ceased to believe in me, even during moments of doubt or difficulty. His unwavering belief in my potential has not only fuelled my academic growth but has also inspired me to strive for excellence and become a better researcher in the future.

I would like to express my sincerest gratitude to Dr. Mira Petronijević for not only encouraging me to delve into the fascinating field of Theory of Structures but also for providing unwavering support throughout my academic journey. Her guidance and encouragement have been instrumental in igniting my passion for this discipline. Her expertise and unwavering support have helped shape my understanding and have motivated me to excel in my studies. I am truly grateful for her mentorship and the impact she has had on my academic and personal growth.

I would like to extend my heartfelt gratitude to Dr. Marija Nefovska-Danilović for her invaluable support and for providing me with the opportunity to use the experimental data obtained within the framework of the Substrate4CLT Project. This experiment has been of immense significance to my research, as it has allowed me to gather crucial data and insights that have greatly contributed to the advancement of my work. Additionally, I am deeply grateful to Dr. Nefovska-Danilović for her careful review of this thesis, which has provided valuable feedback and helped refine the quality of my thesis.

I would like to express my deep appreciation to Dr. Günther Meschke from the Ruhr University Bochum for his enthusiastic guidance and valuable discussions, which have been instrumental in shaping the direction of my research. His expertise and insightful advice have not only provided me with a clear sense of direction but have also inspired me to explore new avenues and push the boundaries of my investigation. I am truly grateful for his unwavering support and his willingness to share his knowledge and expertise. Additionally, I am thankful for the opportunity to have been welcomed in Bochum during a three-month scholarship. The research stays at the Institute for Structural Mechanics have been an invaluable experience in my career.

I would also like to extend a special thank you to my good friend Marija Milojević for her exceptional support in helping me overcome numerous programming challenges in LaTeX. I am deeply grateful for her unwavering friendship and her willingness to listen and provide valuable

feedback throughout the writing process of my dissertation. Her keen eye for detail and her ability to help me refine my sentences have greatly contributed to the overall quality of my work. I am truly fortunate to have had her as a friend and colleague, and I am grateful for her continuous support and encouragement.

I would like to express my sincere gratitude to my friends and colleagues from the Department of Engineering Mechanics and Theory of Structures, particularly Miloš Jočković, Marko Radišić, Marko Marinković, Matija Bošković, Jelena Nikolić, and Nevenka Kolarević. Their inspiring discussions, unwavering support, and enjoyable moments have greatly enriched my research journey. I am deeply grateful for their exceptional contributions in covering my duties during my research stay in Germany and the final stages of writing my dissertation. Their dedication and collaboration have made our joint work truly enjoyable.

I am immensely grateful to my husband Vladimir for his unwavering love, patience, and support throughout my PhD studies, especially during my extended periods away from home. His understanding and ability to deal with my occasionally stubborn nature are truly commendable. Without his constant encouragement during moments when everything seemed out of reach, I would not have been able to accomplish this feat. Thank you for always standing by my side and being my rock throughout this journey.

Finally, I would like to express my heartfelt gratitude to my sister Marija, who not only holds a special place in my heart as a beloved sister but also as my closest friend. Her unwavering protectiveness, care, selflessness, and genuine love have been constants in my life, providing me with strength and comfort in every step of my journey. I am forever grateful for her unwavering support and the profound impact she has had on my life. Last but certainly not least, I am deeply grateful to my beloved parents for showing me the true values of life. Their unwavering belief in me, endless support, and dedication to fulfilling my dreams have played a pivotal role in shaping the person I am today. I am deeply grateful for their unwavering belief in my potential, their tireless support, and their persistent commitment to helping me achieve my aspirations. I cannot express enough gratitude for the profound impact they have had on my life and professional growth.

Financial support

The work on this thesis was supported by the Government of the Republic of Serbia Ministry of Education, Science and Technological Development, under the Project **TR-36046** (project leader Prof. Dr. Mira Petronijević).

This thesis was also supported by the Science Fund of the Republic of Serbia, GRANT No.**7677448: Towards Sustainable Buildings: Novel Strategies for the Design of Vibration Resistant Cross-Laminated Timber Floors - Substrate4CLT** (project leader Assoc. Prof. Dr. Marija Nefovska - Danilović).

The author was granted a **ERASMUS +KA103** scholarship that gave her the opportunity to spend three-month (01/03/2021 – 31/05/2021) stay on Ruhr University Bochum, Institute for Structural Mechanics, under management of Prof. Dr.techn. Günther Meschke.

Progressive failure analysis of laminar composites under three-dimensional stress state using layered finite elements

Abstract:

Laminar composites are extensively used in civil engineering due to their exceptional strength, stiffness, corrosion resistance, and cost-effectiveness. They are ideal for high-reliability applications. The 21st century's focus on environmental protection has led to increased use of natural-based materials like cross-laminated timber (CLT) in building construction. CLT panels have a high stiffness-to-weight ratio, making them well-suited as load-bearing elements, such as walls and floors. The optimal design of laminar composites is often hindered by uncertainties in failure prediction and the computational costs associated with progressive failure analysis (PFA), particularly for larger structures.

This study introduces a novel prediction model that combines the smeared crack band (SCB) damage model with the full layerwise theory (FLWT). The aim is to enhance the computational efficiency of PFA in laminar composites while maintaining the accuracy of 3D finite element models. The SCB model accurately captures the response of damaged lamina in both fiber and matrix directions using distinct strain-softening curves, ensuring a precise representation of post-failure behaviour. The damage law is derived based on the assumption that the total energy required to cause failure in an element (released strain energy) is equivalent to the energy necessary to create a crack passing through it. To alleviate mesh dependency, the fracture energy is scaled by a characteristic element length. Failure initiation and modes are determined using the Hashin failure criterion. Furthermore, the model is extended to consider different failure behaviour of timber in tension and compression. This extension enhances the computational framework's applicability to the field of computational mechanics for bio-based composites, such as CLT. The validity of the model is then confirmed through an extensive experimental program carried out at the Faculty of Civil Engineering, University of Belgrade.

Application of layered finite elements for continuum damage modelling in laminar composites remains largely unexplored in literature, particularly when combined with the SCB damage model. The FLWT-based model accurately captures the 3D stress state within each lamina, including continuous transverse stresses between adjacent layers, crucial for accurate prediction of failure initiation. Furthermore, the FLWT demonstrates a weak correlation between the size of the considered domain and the mesh, presenting a notable difference from standard finite element models. The developed FLWT-SCB prediction model is integrated into an original FLWTFEM framework, offering a user-friendly graphical environment for easy visualization of input and output data. The proposed model's efficiency has been verified using numerous benchmark examples during progressive failure analyses of laminar composites and CLT panels with arbitrary geometries, loading and boundary conditions and stacking sequences. The model has demonstrated its accuracy in predicting the response of both intact and damaged laminar composites, and valuable recommendations for future research in this field are included.

Keywords: progressive failure analysis, laminar composites, cross-laminated timber, full layerwise theory, smeared crack-band damage model, 3D stress field

Scientific field: Civil Engineering

Scientific subfield: Engineering Mechanics and Theory of Structures

UDC: 624.04(043.3)

Analiza progresivnog loma kompozitnih laminata u uslovima prostornog stanja napona primenom slojevitih konačnih elemenata

Rezime:

Zbog svojih izuzetnih materijalnih karakteristika u pogledu čvrstoće i krutosti, male sopstvene težine, otpornosti na koroziju i niskih troškova održavanja, kompozitni laminati imaju potencijal za upotrebu u građevinarstvu. Sa porastom svesti o zaštiti životne sredine u 21. veku, sve je češća upotreba prirodnih materijala. U skladu sa tim, u građevinarstvu sve veću popularnost stiče kompozitni laminat na bazi drveta - unakrsno-lamelirano drvo (CLT). Zbog visokog odnosa krutosti i sopstvene težine CLT-a, moguće je projektovati elemente male težine i velikog raspona. Nepouzdanost u predviđanju ponašanja oštećenih kompozitnih laminata, kao i kompleksnost proračuna progresivnog loma znatno otežavaju njihovo projektovanje.

U okviru ove disertacije je razvijen numerički model za analizu progresivnog loma kompozitnih laminata, koristeći model razmazane pukotine (eng. "smeared crack band" - SCB) i slojevitu teoriju ploča. Model poseduje kapacitet trodimenzionalnih numeričkih modela uz smanjeno trajanje proračuna, čime se povećava efikasnost numeričke analize. Kod SCB modela, ponašanje oštećene lamine je opisano različitim krivama loma u naponsko-deformacijskom prostoru, kako bi se u makroskopskom pogledu opisala propagacija oštećenja koje nastaje usled kidanja vlakana i matrice, respektivno. Zakon omekšavanja materijala je određen na osnovu pretpostavke da je oslobođena energija deformacije jednaka energiji potrebnoj da dođe do loma vlakana, odnosno kidanja matrice. Inicijacija i oblici loma su određeni primenom Hashin-ovog kriterijuma loma. Nakon toga, izvršena je modifikacija modela kako bi se opisalo različito ponašanje drveta pri zatezanju i pritisku. Na taj način, mogućnosti razvijenog numeričkog modela su proširene i na analizu progresivnog loma prirodnih kompozitnih laminata, kao što je CLT. Validnost predloženog modela je potvrđena kroz detaljna eksperimentalna ispitivanja na Građevinskom fakultetu Univerziteta u Beogradu.

Upotreba slojevitih konačnih elemenata u analizi progresivnog loma je u velikoj meri neistražena u literaturi, posebno u kombinaciji sa SCB degradacijskim modelima, gde slojeviti model ploče treba objediniti sa fenomenima mehanike loma. Numerički model, zasnovan na slojevitoj teoriji ploča, omogućava precizno određivanje prostornog stanja napona, zadovoljavajući uslove ravnoteže međulaminarnih napona, što je veoma bitno prilikom predviđanja inicijacije loma. Takođe, pri modeliranju većih konstrukcija, primenom slojevite teorije ploča omogućava se znatno smanjenje broja konačnih elemenata u poređenju sa postojećim numeričkim modelima. Razvijeni numerički model je implementiran u FLWTFEM kod, čime je obezbeđeno puno grafičko okruženje, pogodno za vizualizaciju ulaznih podataka i rezultata proračuna. Efikasnost predloženog modela je verifikovana korišćenjem brojnih referentnih numeričkih primera, prilikom analize progresivnog loma kompozitnih laminata i CLT panela sa proizvoljnom geometrijom, opterećenjem, graničnim uslovima i orijentacijom slojeva. Potvrđena je tačnost predloženog modela u predviđanju odgovora kako neoštećenih tako i oštećenih kompozitnih laminata, a date su i važne preporuke za buduća istraživanja u ovoj oblasti.

Ključne reči: analiza progresivnog loma, kompozitni laminati, unakrsno-lamelirano drvo slojevita teorija ploča, model razmazane pukotine, prostorno stanje napona

Naučna oblast: Građevinsko inženjerstvo

Uža naučna oblast: Tehnička mehanika i teorija konstrukcija

UDK: 624.04(043.3)



Contents

Acknowledgments	i
Financial support	iii
1 Introduction	1
2 Review of previous research	5
3 FLWT for 3D analysis of laminar composites	11
3.1 Introduction	11
3.2 Theory formulation	12
3.3 Displacement and strain fields	13
3.4 3D constitutive equations of lamina	14
3.5 Governing equations of motion	15
3.6 Laminate constitutive equations	17
4 Layered FLWT-based FE	21
4.1 Introduction	21
4.2 Development of the layered element stiffness matrix	21
4.3 FLWT vs 3D FE model	24
4.4 Assignment of loads and boundary conditions	25
4.5 Post-Computation of interlaminar stresses	26
5 Failure criteria and modes	31

5.1	Introduction	31
5.2	Non-interactive failure criteria	32
5.2.1	Maximum stress failure criterion	33
5.2.2	Maximum strain failure criterion	33
5.3	Interactive failure criteria	33
5.3.1	Tsai-Hill failure criterion	34
5.3.2	Hoffman failure criterion	36
5.3.3	Tsai-Wu failure criterion	37
5.3.4	Hashin failure criterion	39
5.4	Procedure for the first-ply failure of laminate	41
6	SCB damage model	43
6.1	Introduction	43
6.2	Formulation of SCB damage model	45
6.2.1	Constitutive model	47
6.2.2	Damage evolution	49
6.3	Constitutive model for compressive fiber failure	51
6.4	Procedure for progressive failure analysis	52
7	PFA of CLT panels	55
7.1	Introduction	55
7.2	Timber cracks and material properties	56
7.3	CLT post-failure behaviour	57
8	Software (FLWTFEM) framework	59
8.1	Introduction	59
8.2	Upgrade of the FLWTFEM software	60
8.2.1	FLWTFEM problemtype	60
8.2.2	FLWTFEM classes	61

9	Numerical examples	65
9.1	3D stress analysis of CLT panels	65
9.2	PFA of OHT laminar composites	82
9.2.1	Model validation and mesh dependency study	84
9.2.2	The orthotropy impact on the tension strength of laminar composite . . .	87
9.2.3	Effect of specimen size	90
9.3	PFA of CNT laminar composites	91
9.4	PFA of OHC laminar composites	95
9.4.1	Single element analysis	96
9.4.2	Open-hole compression analysis	98
9.5	PFA of CLT panels in bending	104
9.5.1	Material properties	104
9.5.2	Experimental test set-up for CLT specimens	106
9.5.3	Model applicability verification, results and discussion	108
10	Conclusions and recommendations for future work	113
	Appendix	119
	Biography	147
	Contributions	149

List of Figures

1.1	Cross laminated timber (CLT) panel (left) and typical rolling shear failure mode of CLT panel (right)	2
1.2	Graphical representation of a thesis concept [13]	3
3.1	Laminated composite plate made of n material layers and with N numerical interfaces [13]	12
3.2	Linear lagrangian functions $\Phi^I(z)$ and corresponding displacements distribution through laminate thickness	13
3.3	Global (laminate) coordinate system (xyz) and material (lamina) coordinate system (123)	14
4.1	Quadratic serendipity Q8 layered finite element with corresponding Gauss quadrature points and nodal degrees of freedom	25
4.2	Distribution of interlaminar stresses through the laminate thickness : red color: from constitutive relations (Eqs. (4.18-4.21)); blue color: re-computed from (Eq. 4.22)[112]	28
5.1	Typical intralaminar failure modes in laminar composites	31
5.2	Failure surface for max stress failure criterion (left) and max strain failure criterion (right)	32
5.3	Failure surface for quadratic polynomial failure criteria	34
5.4	Uniaxial tests imposed along the material directions 1, 2 and 3 of the single lamina	35
5.5	Pure shear tests in the three orthogonal symmetry planes 12 , 13 and 23	35
5.6	Typical failure surface of unidirectional lamina for: (a) fiber failure mode; (b) matrix failure mode	39
5.7	Flow chart of procedure for First-ply failure load determination of laminate . . .	41

6.1	Post-failure softening behaviour in laminar composites. σ^0 denotes the material strength, ε^0 is the strain in the moment of damage initiation, while ε^f is the maximum strain	44
6.2	Stress-strain relationship with linear softening law applied for laminate stiffness degradation in global (x, y, z) directions. C is the material stiffness in the undamaged state, while C_D is the material stiffness in the damaged state.	45
6.3	Stress-strain relationship with linear softening law applied for lamina stiffness degradation in material $(1, 2, 3)$ directions	46
6.4	Stress-strain relationship with: (a) linear and (b) linear-brittle softening law; applied in modelling of compressive fiber failure	51
6.5	Flow chart of procedure for Progressive Failure Analysis of laminar composites	52
7.1	Principal material directions (left); Crack propagation directions for timber (right)	56
7.2	Typical failure surface for: fiber tension (FT) failure mode (left); rolling shear (RS) failure mode (right)	57
7.3	Stress-strain relationship with simplified softening law to model post-failure timber behaviour in fiber tension and compression	58
8.1	Typical algorithm used in the GiD-based finite element program [111]	60
8.2	FLWTFEM GiD user interface for pre-processing	61
8.3	FLWTFEM class structure [15]	62
8.4	FLWTFEM GiD user interface for post-processing (fiber tension failure patterns at the time point when the first element reaches $d_{ft}=1$, for an open-hole laminar composite with a central hole	63
9.1	Simply supported CLT panels under uniformly distributed loads at the top surface: a) 3-layer configuration of [26/40/26]mm; b) 5-layer configuration of [26/40/26/40/26]mm [112]	66
9.2	In-plane displacement (u) distribution at $(0, b/2)$ across the thickness of a 3-ply CLT panel using different computational models, element types, and mesh densities [112]	67
9.3	Normal stresses σ_x and σ_y distribution at $(a/2, b/2)$ across the thickness of a 3-ply CLT panel using different computational models, element types, and mesh densities [112]	68
9.4	Transverse shear stresses τ_{xz} at $(0, b/2)$ and τ_{yz} at $(a/2, 0)$ distribution across the thickness of a 3-ply CLT panel using different computational models, element types, and mesh densities [112]	68

9.5	Transverse shear strains γ_{xz} at $(0, b/2)$ and γ_{yz} at $(a/2, 0)$ distribution across the thickness of a 3-ply CLT panel using different computational models, element types, and mesh densities [112]	69
9.6	In-plane displacement u distribution at $(0, b/2)$ across the thickness of a 5-ply CLT panel using different computational models, element types, and mesh densities [112]	70
9.7	Normal stresses σ_x and σ_y distribution at $(a/2, b/2)$ across the thickness of a 5-ply CLT panel using different computational models, element types, and mesh densities [112]	70
9.8	Transverse shear stresses τ_{xz} at $(0, b/2)$ and τ_{yz} at $(a/2, 0)$ distribution across the thickness of a 5-ply CLT panel using different computational models, element types, and mesh densities [112]	71
9.9	Transverse shear strains γ_{xz} at $(0, b/2)$ and γ_{yz} at $(a/2, 0)$ distribution across the thickness of a 5-ply CLT panel using different computational models, element types, and mesh densities [112]	72
9.10	Transverse shear stresses τ_{xz} at $(0, b/2)$ and τ_{yz} at $(a/2, 0)$ distribution across the thickness of a 3-ply CLT panel using different computational models (exact solution and 10×10 mesh of Q8 elements), and different refinements in z -direction [112]	72
9.11	Transverse shear stresses τ_{xz} at $(0, b/2)$ and τ_{yz} at $(a/2, 0)$ distribution across the thickness of a 5-ply CLT panel using different computational models (exact solution and 10×10 mesh of Q8 elements), and different refinements in z -direction [112]	73
9.12	The simply supported [10/50/10]mm CLT panel loaded with $Q = 30$ kN at the plate center (loading scheme Q, green) and at four quarter points (loading scheme 4Q, red) over 150×150 mm surfaces [112]	74
9.13	Comparison of maximum bottom-side deflections of CLT panels predicted by various finite element models, analytical (Navier) solution based on FSDT [96], and experimental results [158]	75
9.14	Comparison of maximum bottom-side normal stress σ_x of CLT panels predicted by various finite element models, analytical (Navier) solution based on FSDT [96], and experimental results [158]	75
9.15	Visualization of σ_x stress distribution [in MPa] in Panel 1 subjected to 4Q loading using different mesh densities and element types (GiD Post-Processing module): Blue color denotes top interface stresses, while red color denotes bottom interface stresses [112]	76
9.16	Stresses σ_x ($L/2, B/2$) and τ_{xz} ($0, B/2$) in slender panel ($L/h=33.3$) subjected to a uniformly distributed load of 5 kN/m ² , for varying L/B ratios and design methods [112]	77

9.17	Stresses $\sigma_x (L/2, B/2)$ and $\tau_{xz} (0, B/2)$ in slender panel ($L/h=16.7$) subjected to a uniformly distributed load of 5 kN/m^2 , for varying L/B ratios and design methods [112]	78
9.18	Configuration of the analyzed CLT slab with applied loads [112]	79
9.19	Comparison of final deflection w_{fin} [in mm] spatial distribution in 7-layers CLT slab using different computational models and mesh densities [112]	81
9.20	Comparison of spatial distributions of stresses S11, S22 and S23 (design stress values - E_d) obtained using: a) Abaqus; b) proposed FLWT-based mode, for a 0.1m mesh [112]	82
9.21	Geometry and boundary conditions for an open-hole composite laminate $203.2 \times 25.4 \text{ mm}$ [13]	83
9.22	Four meshes generated around the circular hole of an open-hole composite laminate $203.2 \times 25.4 \text{ mm}$ (hole diameter 6.35 mm): Mesh 1: 16 elements; Mesh 2: 24 elements; Mesh 3: 36 elements; Mesh 4: 64 elements [13]	84
9.23	Tensile load - displacement curves considering different mesh densities and damage models of an open-hole laminar composite with $[0^\circ/45^\circ/-45^\circ/90^\circ]_s$ stacking sequence [13]	85
9.24	Tensile load - displacement curves of an open-hole composite laminate with $[0^\circ/45^\circ/0^\circ/-45^\circ]_s$ stacking sequence, considering different numerical models and the experimental data [13]	86
9.25	Longitudinal strain distribution of an open-hole laminar composite, at the final failure, obtained from: a) FLWT-SCB prediction model; b) PFA damage model [72]; c) DIC analysis [72]	87
9.26	bottom: Matrix (first row) and fiber tension failure patterns (second row) plotted using FLWTFEM at the time point when the first element reaches $d_{mt}=1$, for an open-hole laminar composite $203.2 \times 25.4 \text{ mm}$ with a central hole; top: considered time point when $d_{mt}=1$ [13]	88
9.27	middle: Matrix (first row) and fiber tension failure patterns (second row) plotted using FLWTFEM at the time point when the first element reaches $d_{ft}=1$, for an open-hole laminar composite $203.2 \times 25.4 \text{ mm}$ with a central hole; bottom: through the thickness distributions of d_{mt} and d_{ft} around the circular hole; top: considered time point when $d_{ft}=1$ [13]	89
9.28	Load-displacement curves of an open-hole laminar composite (Mesh 2), calculated using FLWT-SCB prediction model, for 7 considered specimens with different stacking sequences [13]	90
9.29	Load-displacement curves of an open-hole laminar composite (Mesh 2), calculated using FLWT-SCB prediction model, for 2 specimens with the same orthotropy ratio, but different stacking sequences [13]	91

9.30	Load-displacements curves of quasi-isotropic open-hole laminar composite (L1), predicted by FLWT-SCB prediction model and considering different hole diameters (d [mm]) [13]	91
9.31	Geometry and boundary conditions of centre-notched tensile laminar composite	92
9.32	Generated mesh with 138 Q8 layered quadrilateral elements of a centre-notched tensile specimen	93
9.33	Tensile stress – strain curves of a centre-notched specimen (Scale-8) with $[45^\circ/90^\circ/-45^\circ/0^\circ]_{4s}$ stacking sequence	94
9.34	Comparison of maximum stress values for all CNT specimens from Table2 using FLWT-SCB framework, Nagaraj’s model [73], and experimental data [163] . . .	95
9.35	Compressive stress-strain behaviour of a 1 x 1 mm single element lamina loaded in: (a) Longitudinal (fiber) direction; (b) Transverse (matrix dominated) direction	97
9.36	Compressive stress-strain behaviour of a 1 x 1 mm single element laminate with $[90^\circ/45^\circ/0^\circ/-45^\circ]_{2s}$ stacking sequence considered various methods	98
9.37	Geometry and boundary conditions of open-hole sublaminar scaled laminates loaded in compression	98
9.38	Generated meshes of an open-hole specimen (Scale-1): (a) Mesh 1 (48 elements) and Mesh 2 (407 elements) used in FLWT-SCB model; (b) Mesh used in reference numerical model [68]	99
9.39	Compressive stress - strain responses of an open-hole laminar composite with $[045^\circ/90^\circ/-45^\circ/0^\circ]_{4s}$ stacking sequence, considering various fiber softening laws and damage models	100
9.40	Compressive stress - strain responses of an open-hole laminar composite with $[045^\circ/90^\circ/-45^\circ/0^\circ]_{4s}$ stacking sequence, predicted by PC-30 FLWT-SCB model considering different generated meshes from Figure 9.38	101
9.41	Failure pattern in top 45° ply (top) and damage distribution through the laminate thickness (bottom) of an open-hole $[45^\circ/90^\circ/-45^\circ/0^\circ]_{4s}$ laminate in compression obtained by: (a) Experiment [6]; (b) FLWT-SCB PC-30	102
9.42	Failure pattern in 0° ply of an open-hole $[45^\circ/90^\circ/-45^\circ/0^\circ]_{4s}$ laminate in compression obtained by: (a) Experiment [6]; (b) FLWT-SCB PC-30	102
9.43	Predicted in-plane size effect of an open-hole $[45^\circ/90^\circ/-45^\circ/0^\circ]_{4s}$ laminates from Table 9.16 loaded in compression	103
9.44	Panel testing layout	107
9.45	Test set-up for CLT specimens [source Substrate4CLT project [166]]	107
9.46	Load-deflection curve predicted by the FLWT-SCB prediction model along with the load-deflection curves for all tested CLT panels	109

9.47	Magnified load-displacement curve predicted using FLWT-SCB	109
9.48	Typical failure mode of Series A panels (specimen A1)	110
9.49	Fiber tension (FT) failure patterns of CLT panel, plotted using the FLWTFEM at the failure load ($d_{ft} = 1$). The bottom figure illustrates only the bottom lamination	110
9.50	Rolling shear (RS) failure pattern of CLT panel plotted using the FLWTFEM after the load reaches the maximum value and starts dropping	110
9.51	Longitudinal strain distribution through the thickness, at the mid-span of CLT panel obtained from: left) experimental tests (specimen A2); right) FLWT-SCB prediction model	112

List of Tables

9.1	Material properties of CLT panels (C24 timber class)	66
9.2	Material properties for two considered CLT panels (C24 timber class)	73
9.3	Dimensions L/B [m] of analysed CLT panels ($h = 5 \times 3 = 15$ cm)	76
9.4	Computational (finite element) models properties	79
9.5	Applied permanent distributed loads (kN/m^2)	79
9.6	Strength values of C24 CLT panels (MPa) for both characteristic and design values	80
9.7	Comparison of final deflections w_{fin} (according to Eurocode 5) of a 5-layer CLT slab using different computational models and mesh densities (negative values correspond to uplift)	80
9.8	Comparison of final deflections w_{fin} (according to Eurocode 5) of a 7-layer CLT slab using different computational models and mesh densities (negative values correspond to uplift)	81
9.9	Material properties for T700/epoxy composite material	84
9.10	Laminate stacking sequences and orthotropy ratios	88
9.11	Material properties for IM7/8552 carbon fibre reinforced polymer	92
9.12	List of employed scales and their dimensions	93
9.13	Comparison of maximum stress values for all CNT specimens from Table 9.12 using FLWT-SCB framework, Nagaraj's model [73], and experimental data [163]	94
9.14	Material properties for IM7/8552 carbon fibre reinforced polymer loaded in compression	96
9.15	Maximum compressive stress of $[90^\circ/45^\circ/0^\circ/-45^\circ]_{2s}$ quasi-isotropic laminate obtained by FLWT-SCB with various linear-brittle fiber softening laws	97
9.16	List of employed scales for the open-hole tick laminate with a stacking sequence of $[45^\circ/90^\circ/-45^\circ/0^\circ]_{4s}$ loaded in compression along with their dimensions	99

9.17 Comparison of maximum stress values for all OHC $[45^\circ/90^\circ/-45^\circ/0^\circ]_{4s}$ laminates from Table 9.16 using FLWT-SCB PC-30 framework, Nagaraj’s model [74], and experimental data	103
9.18 Computational efficiency comparison of FLWT-SCB PC-30 and Nagaraj [74] models	104
9.19 Timber strength properties	105
9.20 Timber elastic properties	106
9.21 Material properties of a continuous CLT lamina used in numerical simulations .	106
9.22 Experimental test and numerical results of CLT panels	111

1 Introduction

Composite materials are those produced from two or more constituent materials on a macroscopic scale to achieve better engineering properties in comparison with conventional building materials, such as concrete or masonry. Specialized types of high performance laminar composites are fiber-reinforced polymers (FRP), consisting of high strength fibers embedded in a matrix material. The matrix keeps the fibers in the desired orientation, simultaneously acting as a load transfer medium between fibers. For structural application, FRP are generally made in the form of thin layers (*laminae*) as a fundamental building block. Since unidirectional FRP laminae exhibit very low strength and modulus in the direction transverse to the fibers, they must be stacked together to achieve the desired stiffness and thickness [1]. A collection of laminae with different fiber orientation is called *laminated*. Due to their outstanding strength and stiffness, corrosion resistance and low maintenance costs, FRP have been widely used in the construction of aerospace, mechanical, marine and automotive structures which generally require high reliability levels.

With the growing awareness of environmental protection in the 21st century, the use of natural-based materials, like cross-laminated timber (CLT) (Figure 1.1, left), in building construction is becoming more common [2]. CLT is a laminar composite made of odd number of timber laminae stacked and glued together in a crosswise manner. The advantages of CLT for the building sector are related to the ease of prefabrication, short erection time on site, high stiffness-to-weight ratio and fire resistance. For these reasons, CLT panels are very suitable to act as load-carrying elements in structural system such as walls and floors [3]. Also, small self-weight of CLT reduces the required size of foundations and provides the possibility of using CLT panels in seismically active areas.

However, optimal design with laminar composites is often not achieved due to uncertainties in failure prediction. Failure of a structural element occurs when it cannot perform its intended function. Due to their complex kinematics, laminar composites may fail through various scenarios, such as fiber breakage and pull out, matrix yielding, cracking and delamination [4]. In FRP, the damage progression often starts with matrix cracking transverse to the fibers, followed by fiber breakage and delamination between plies. On the other hand, rolling shear brittle failure (Figure 1.1, right) [5] due to the rotation of wood's fibers is assumed to be the first occurring failure mode in CLT panels, as a consequence of transverse shear strength of cross timber layers. In real structural elements, holes and notches are often present, which further complicates prediction of damage progression and the ultimate strength due to presence of stress concentration zones. Furthermore, the ultimate strength and failure mechanisms depend on geometrical factors and material properties such as specimen width, hole diameter, stacking sequence or ply thickness [6]. Therefore, the understanding of inelastic material behaviour due to damage propagation is crucial step towards the reliable and safe design of laminar composites.



Figure 1.1: Cross laminated timber (CLT) panel (left) and typical rolling shear failure mode of CLT panel (right)

Initiation of damage occurs when stresses in the weakest lamina exceed the allowable fiber or matrix strength. A suitable failure criterion is required to capture the damage initiation of laminar composites in one or more specific failure modes. As damage progresses, progressive failure analysis (PFA) is performed to describe the post-failure behaviour in composite materials. Failure mechanisms often interact with each other, leading to complex crack pathways when modelling damage propagation. For the implementation of failure initiation and propagation algorithms within some computational (i.e. finite element) model, mathematical, so-called damage models are required [7] such as: discrete damage models (DDM) and continuum damage models (CDM). DDM involve explicit geometrical representation of cracks within the structure, typically using cohesive interface elements to handle discontinuities within the finite element (FE) mesh. On the other hand, in CDM approaches, intralaminar cracks are smeared out within the finite element domain and the failure mechanism is then represented through material stiffness degradation, controlled by specific damage variables.

The earliest CDM approach is instantaneous softening method (ISM), in which the damaged material is assumed to lose its entire stiffness and strength in the dominant, stresses directions [8]. It is generally observed that the ISM underestimates laminate strength due neglecting the fact that damage is indeed localized and a failed lamina still has some residual load-carrying capability. Fiber-reinforced composite materials generally exhibit quasi-brittle post-failure behaviour, resulting in a high fracture energy dissipated and therefore a more gradual propagation of damage. An alternative approach to ISM is gradual softening method (GSM), where the material property associated with the failure mode is degraded gradually (i.e. linearly or exponentially) until it reaches zero [9]. Due gradually unloading of the damaged material, the stresses can be redistributed to the remaining undamaged material. GSM are very popular due to their simple implementation in commercial engineering software's based on the finite element method (FEM) and relatively low computational cost. However, the approaches outlined above suffer from a mesh dependency problem related to strain localisation during the PFA. This problem can be reduced by scaling the fracture energy using a characteristic element length, as described by the crack-band theory.

In order to capture the effect of distinct failure modes on the macro-scale, the originally fracture-mechanics augmented smeared crack band (SCB) model was developed by Williams et al. [10]. However, the damage pattern and damage growth trajectory in orthotropic laminar composites cannot be realistically predicted, because the above damage model does not account for any preferred material orientation. Using the above model, the mesh orientation issue in SCB models was improved by devolving the sub-laminate strain-softening response into equivalent stress-strain responses in the principal lamina directions [11]. This damage law is determined based on the assumption that the total energy needed to fail an element (released strain energy) is equal to the energy needed to create a crack that passes through it.

Finally, SCB damage models lead to a good compromise between computational cost and solution accuracy, and they are thus used in most of the studies dealing with composite failure modelling in conjunction with different plate theories. However, the computational costs associated with PFA of laminar composites can be prohibitive, even considering the relative efficiency of SCB models, especially for larger structures. This is usually due to the requirement of refined, often 3D meshes, to obtain an accurate stress field.

This thesis aims to increase the computational efficiency of the PFA of laminar composites and preserve the accuracy of the 3D finite element models, by using a layered finite element model based on the full layerwise theory (FLWT) [12] in conjunction with SCB.

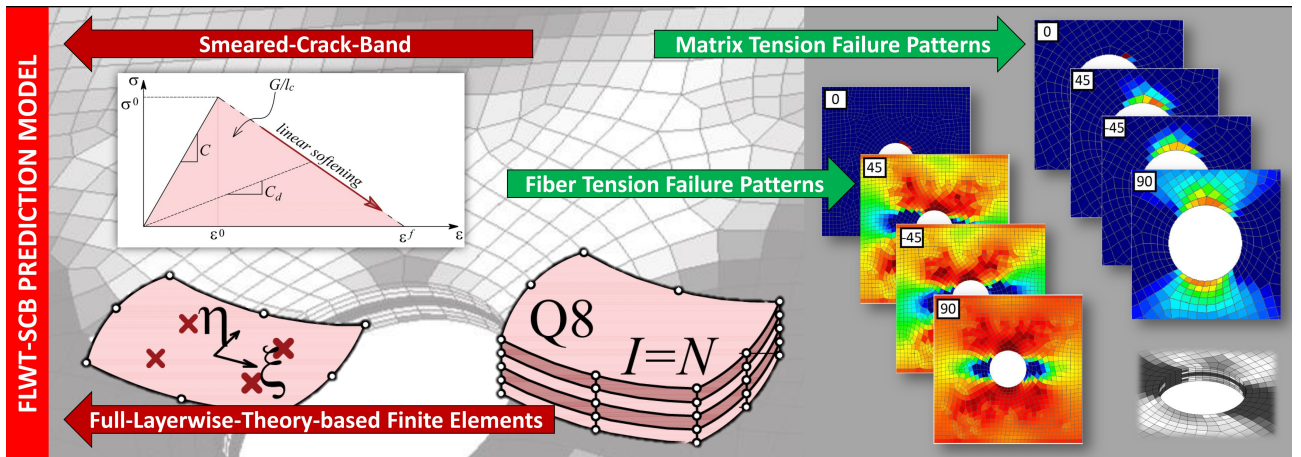


Figure 1.2: Graphical representation of a thesis concept [13]

The use of FLWT is also justified due to the capability to account for continuous transverse (interlaminar) stresses between the adjacent layers in the laminate. Further incorporation of the transverse normal stress, as proposed, is important in modelling the localized effects such as holes, cut-outs or stress-deformation state around point supports. The layerwise expansion of all three displacement components results in the 3D stress state in laminar composites, which provides a very good basis for further prediction of potential damage initiation.

Within this thesis, damage progression and post-failure behaviour are modelled following the SCB damage model with strain-softening, where the damage is smeared out within the FE domain, and is taken into account by reducing the values of material stiffness matrix. The material stiffness matrix degradation is controlled by damage variables, which evolution are governed by an equivalent displacement appropriately defined for each failure mode. The mesh dependency problem is minimized by scaling the fracture energy using a characteristic element length. The response of damaged lamina, in both fiber and matrix direction, is described by distinct strain-softening curves where the peak stress coincides with the fibre and matrix

strength, respectively. The proposed strain-softening curves are then modified to account for the different post-failure behaviour of the timber in tension and compression during the PFA of CLT panels. It is worth highlighting that this thesis presents a significant advancement in the field by introducing the application of the sub-laminate-based SCB damage model for the first time in analysing the progressive failure of CLT panels. Finally, since layered finite elements require only C^0 continuity of generalized displacements along element boundaries, they can be applied for the PFA of laminar composites of arbitrary shape, loading, boundary conditions and stacking sequence.

Both finite element and damage model are implemented into an object-oriented FLWTFEM framework, making the original conjunction between SCB damage model and FLWT, the so-called FLWT-SCB prediction model (Figure 1.2). The FLWTFEM solver is written in Matlab, while the graphical user interface for both pre- and post-processing is developed using GiD [14]. This framework was originally developed by authors in [15] and upgraded in this thesis to be used for all numerical simulations.

The thesis is organized as follows: after the introduction, the literature overview and the previous research in this field is elaborated in Chapter 2. Governing equations of the full-layerwise (FLWT) theory are presented in Chapter 3. This served as a base for the derivation of a layered FLWT-based finite element model, which is elaborated in Chapter 4. In Chapter 5, several macroscopic failure criteria that describe the initiation of the damage of laminar composites, as well as the typical failure modes occurring in both FRP and CLT plates are presented. After that, the mathematical formulation of the considered smeared crack-band (SCB) damage model is described in Chapter 6. Next, the algorithm of damage evolution is presented in order to describe the response of damaged lamina. Structure, design and capabilities of the original object-oriented FLWTFEM framework, used for all numerical simulations within this thesis, are explained in detail in Chapter 7. Chapter 8 consists of various validation and benchmark examples, used to prove the applicability and benefits of the proposed model, for both structural and progressive failure analysis of laminar composites. Finally, the conclusions and future research recommendations in this field are provided in Chapter 9.

2 Review of previous research

Progressive failure analysis (PFA) of laminar composites requires application of appropriate damage model, in order to predict damage progression and post-failure behaviour in composite materials. The first effort to model the failure behaviour of laminar composites using PFA was made by Petit and Waddoups [16] in 1969. They used the instantaneous softening method (ISM) for damage modelling of symmetric plane anisotropic laminates subjected to biaxial membrane loads. In their analyses, the failure of the lamina occurs when any of the strain components relative to the material axes exceeds the limiting strain. A failed lamina was modelled by using negative tangent modulus. They assumed that the tangent modulus relative to one material axis is not influenced by the presence of stresses in other directions. Ultimate failure of a laminate is assumed to occur when stiffness matrix of the laminate becomes singular, or when a negative sign appears on the diagonal of laminate stiffness matrix. Following a similar approach, Sandhu et al. [17] developed a nonlinear total strain energy criterion for failure prediction of unidirectional and angle-ply laminates. The piecewise cubic spline interpolation functions were used to represent experimentally obtained stress-strain curves of lamina. Abu-Farsakh and Abdel-Jawad [18] introduced a similar failure criterion based on an energy concept, but instead of a whole area, the triangular area under the stress-strain curve was used as the total strain energy density. However, the failure modes could not be identified for any criterion which poses difficulties for material degradation modelling and failure propagation.

Engelstad et al. [19] studied progressive failure behaviour of graphite-epoxy panels in axial compression, using both the Tsai–Wu [20] and the maximum stress criteria for failure predictions. They formulated the damage model based on the dominant stress appearing in the criterion. Starting from [19], Singh and Kumar [21] performed the PFA of symmetric thin laminates under uniaxial compression and uniaxial compression combined with in-plane shear loads. The modified Tsai–Hill criterion [22] was used for failure prediction, while the maximum stress criterion was used to predict delamination. Ochoa and Engblom [23] presented a PFA for laminar composites in uniaxial tension using Hashin failure criterion [24].

A 3D finite element model was first used for the PFA by Lee [25] in 1982. He applied the original failure criterion to predict failure modes of a biaxial loaded composite laminate with a central hole. Subsequently, Hwang and Sun [26] followed a similar 3D model and used a modified form of Hashin criterion to predict fiber breakage and matrix cracking, in conjunction with both the criteria of Lee and Chang and Springer [27] for delamination prediction. In [25, 26], the same ISM damage model was used for stiffness reduction. However, Lee [25] defined fiber failure as a complete failure of an element, while Hwang and Sun [26] defined a combined fiber and matrix failure as complete failure of an element. In either case, the stiffness matrix of the failed element was reduced to zero.

The previous studies showed that an instantaneous degradation of particular material properties to zero can lead to some computational problems such as lack of convergence. That can be avoided by using a constant small value for degradation factors instead of zero. Tolson and Zabaras [28] developed a seven degree of freedom plate element based on the HSDT to study progression of failure in graphite/epoxy composite laminates. They used five failure criteria, namely the maximum stress, the Lee, the Hoffman [29], the Tsai–Wu, and the Hashin criteria, respectively, to predict failure mode. The so-called stiffness reduction factor (R) was used for material degradation, and its value showed to depend on the number of failed Gaussian integration points. If failure occurs in only one point then $R=0.75$, and if all the four points have failed then $R=0.0$.

Tan et al. [30–32] proposed a 2D progressive damage model for laminates containing central holes subjected to in-plane tensile or compressive loading, using Tsai-Wu criterion. They used a parametric study to evaluate the appropriate values of the stiffness degradation factors, assumed to be different for failure modes in tension and compression. This is justified by the fact that crack surfaces under tensile loading are traction free, whereas under compressive loadings they can still carry some load. The proposed damage model agreed with experimental results, but the predicted ultimate strength values were very sensitive to the selected values of degradation factors. A very similar approach with degradation factors assigned to different failure modes was developed by Camanho and Matthews [33] and implemented in 3D FE framework in ABAQUS [34]. They used Hashin failure criterion to predict damage progression. A comparison of ISM-based models against the experimental results confirmed that the predicted failure occurs at a substantially lower load than the experimentally determined one, underestimating the laminate strength and neglecting the fact that the damage is indeed localized and a failed lamina still has a residual capability.

An alternative approach to ISM is gradual softening method (GSM). Most early works on GSM [35–38] used the Weibull distribution, based on fiber bundle failure theory [39] to model fiber failure of open-hole laminar composites under uniaxial and biaxial tension. Reddy et al. [40] developed a 3D GSM to study the failure of laminar composites under tensile or bending load. They proposed a gradual stiffness reduction scheme which resulted in the partial unloading of elements and allowed accumulation of damage in the element. The proposed damage model agreed with experimental results, but the predicted ultimate strength values were very sensitive to the selected values of stiffness reduction coefficient (SRC).

Barbero et al. [41] proposed a CDM based on irreversible thermodynamics considerations. Damage propagation was modelled via second-order damage tensor, whose eigenvalues represent the density of distributed microcracks. The degradation factors were calibrated from experiments in order to determine the material softening laws. McGregor et al. [42] developed a GSM model of nonlinear constitutive behaviour to model the compressive failure of notched composites. In order to represent the complete force-displacement response of a representative volume element of the material, an analog model composing of spring, gap, fuse and slider elements was constructed. However, this model is given as a predefined nonlinear force–displacement relationship which is difficult to determine. Hallett and Wisnom [43] and Abisset et al. [44] included delamination in their models by introducing cohesive elements inserted between plies. In [43] a global criterion based on Weibull’s statistical model was used to determine fibre failure of the entire structure, while Abisset et al. [44] used an ISM for fibre breaking and a GSM model for matrix cracking. Their models gave good predictions on the interaction between matrix cracks and delamination which shows that cohesive elements are adaptable for delamination modelling. However, their studies were limited to mainly quasi-isotropic laminates.

The approaches outlined above suffer from a mesh dependency problem related to the strain localization during the PFA, which can be reduced by scaling the fracture energy using a characteristic element length, as described by the crack-band theory [45]. Camanho et al. [46] investigated the size effects in notched composites via an energy-regularized CDM model, whereby the stiffness matrix of the damage material was degraded gradually based on an energy criterion. Some other works based on the CDM approach include the impact analysis of composite plates [47], and PFA of composite pressure vessels [48].

Crack propagation can be more rigorously predicted through discrete damage models (DDM), typically using cohesive interface elements to handle discontinuities within the finite element (FE) mesh [49–51]. Other discrete approaches have also been proposed for the progressive failure modelling of laminar composites, such as: eXtended Finite Element Method (XFEM) [52–54], Phantom Node Method (PNM) [55–57], Augmented Finite Element Method (AFEM) [58, 59] or Floating Node Method (FNM) [60–63]. Generally, discrete techniques lead to models that can accurately predict crack propagation with high fidelity, but at the cost of excessively high computational effort.

A popular approach for damage modelling in laminar composites is a combination of CDM model to describe intralaminar damage within the ply and DDM based approach to model delamination [64, 65]. Accordingly, Chen et al. [66] employed the CDM for in-plane failure progression and cohesive elements for delamination modelling, to study the size effects of open-hole composite laminates under tensile loading (OHT). Ridha et al. [67] followed the same approach in order to predict the OHT strengths and failure progression for notched composite laminates. The proposed damage model was incorporated into ABAQUS user subroutine UMAT for 2D conventional shell elements. The most important feature of this model is the novel material softening approximation using a zig-zag curve. On the other hand, Su et al. [68] developed a computational CDM for the progressive damage modelling of open-hole laminar composites under compressive loading (OHC). The proposed model was based on the OHT-associated model by Ridha et al. [67], with some modifications related to compressive deformation. Ladevèze et al. [69] developed a plane-stress CDM damage model that describes stiffness degradation by matrix micro-cracking, fiber/matrix debonding and brittle fiber failure of unidirectional laminar composites.

In order to capture the effect of matrix cracking and fibre breakage on the macro-scale, the originally sub-laminate based smeared crack-band (SCB) model was developed in [10] and applied to the simulation of braided composite tubes under axial crushing [42]. Since the above damage model do not account for any preferred material orientation, it cannot realistically predict damage pattern and damage growth trajectory in orthotropic laminar composites. The mesh orientation issue in SCB models was improved by devolving the sub-laminate strain-softening response into equivalent stress-strain responses in the principal ply directions [11]. Reiner et al. [70] investigated the progressive intra-laminar damage in notched IM7/8552 CFRP laminar composites under tension via SCB and Ladevèze damage models [69], to assess their predictive capabilities and limitations. The Ladevèze's damage model was enhanced by defining a fracture-mechanics-based post-peak softening law for the fiber direction. Both models are able to predict size-effects in a large number of center-notched quasi-isotropic laminar composites with reasonable accuracy, but Ladevèze damage model showed some path-dependency problem with respect to the transverse and shear response. Forghani et al. [71] proposed a non-local averaging scheme that is specially designed to capture the preferred path of damage in laminar composites, consisting of strongly orthotropic layers, via SCB damage model. Yoon et al. [72] used SCB damage model to study failure behaviour of notched composite laminates under tension and compression, while strain distribution was recorded via a digital image correlation

(DIC) system. Finally, smeared crack-band (SCB) models lead to a good compromise between computational cost and solution accuracy, and they are thus used in most of the studies dealing with composite failure modelling in conjunction with different plate theories. The computational costs associated with PFA of laminar composites can be prohibitive, even considering the relative efficiency of smeared crack-band models, especially for larger structures. This is usually due to the requirement of refined, often 3D meshes, to obtain an accurate stress field. Therefore, Nagaraj et al. integrated the SCB damage model with higher-order theories based on Carrera unified formulation (CUF) to develop a numerical framework for the PFA of unidirectional fiber-reinforced composites loaded in tension [73] and compression [74].

In recent years, the phase-field model (PFM) has emerged as a promising technique to ensure the computational efficiency of the PFA for laminar composites [75–82]. The ability to capture damage initiation and evolution direction without any additional ad-hoc criteria and crack tracking strategies has made the PFM to be one of the most popular and effective approaches in modelling fracture problems with unknown crack paths. A detailed critical review on the developments and recent applications of regularized phase field models for failure problems in laminar composites was outlined by Bui and Hu [83].

Most damage models available in the literature generally focus on the PFA of fiber-reinforced laminar composites, and the application of these models for the PFA of CLT panels is relatively rare due their unpredictable and unconventional failure mechanisms. Nie [84] pointed out that the variation of annual ring pattern in the orthogonal layers is directly linked to the propagation of failure. The main structural issue relating to the failure behaviour of CLT is the low transverse shear strength of cross layers. This leads to the rotation of wood's fibers and so-called *rolling shear brittle failure* [85]. This phenomenon becomes more expressive with decreasing the slenderness ratio and initiates failure in the longitudinally oriented fibers, which in turn causes fiber tension failure. Mestek et al. investigated a small-scaled CLT elements reinforced against shear failures at their support [86]. Zhou et al. [87] pointed out that CLT beams or panels with low span-to-depth ratios suffer from rolling shear failure. For all investigations, the estimation of failure behaviour is limited to surface information of the specimens, and the main focus was on the structural behaviour up to the elastic limit. A detailed evaluation of plate-bending tests on CLT elements was performed by Hochreiner et al. [5] in order to accurately determine failure modes within the CLT panels. The global load-displacement behaviour as well as the observed failure modes within the plates were experimentally obtained and discussed. Recently, Franzoni et al. investigated the bending behaviour of CLT panels [88] by means of the linear elastic exact solution from Pagano [89] and van der Put failure criterion [90]. Nairn included the effect of environmental stresses in failure prediction of notched CLT plate [91], while Navaratnam et al. used the digital image correlation for identifying failure characteristics of CLT under transverse loading [92]. Also, failure behaviour of CLT panels loaded with combined out-of-plane bending and compression [93], as well as a deep CLT lintels subjected to concentric and eccentric loading [94], was analysed.

Material stiffness degradation due to the post-failure behaviour in cross layers can be modelled by treating the cross layers as mechanical joints that connect the longitudinal layers [95]. However, the material stiffness depends on the joint efficiency of the cross layers which are theoretically determined by the cross layer shear properties and the bonding degree, which cannot be quantitatively evaluated due to the complexity of the shear damage mode [94]. In order to overcome this problem, current design codes employ effective bending stiffness to account for the stiffness degradation [96]. This method was originally developed in [97] for calculating the bending stiffness of composite I-shape or T-shape beam.

Analysing the post-failure behaviour of CLT structures in conventional ways requires extensive experimental testing. Consequently, there is a need to employ numerical methods for the analysis of CLT structures in order to address the most commonly occurring scenarios in practical applications, particularly regarding PFA. However, the application of numerical methods for the damage modelling of CLT structures is relatively scarce. Qui et al. developed XFEM based models to simulate the crack propagation behaviour of wood [98]. Lavrenčič and Boštjan used the nonlinear finite element method for structural modelling and SCB damage model for stimulation of failure propagation of CLT plate with ribs [99]. Ma et al. [100] investigated the feasibility of CLT panels fabricated from salvaged dead standing trees after the beetle outbreak, by evaluating the flexural and shear properties through mechanical tests and computational analysis.

From the plate theory point of view, the global behaviour of laminar composites (including CLT as a natural-based multilayer plate) may be accurately predicted using Equivalent Single Layer (ESL) theories [101–103], especially for very thin laminates. However, if a highly accurate assessment of the 3D stress field is needed (e.g., for consideration of local damage effects or in the 3D stress state), refined theories are recommended [104–106]. In addition, the prediction of damage initiation and further progression begins with the accurate determination of the 3D stress fields at the lamina level. The Generalized Laminated Plate Theory (GLPT), originally designed to capture the laminate-specific mechanical characteristics, became the basis for the development of layered finite elements, capable to deliver accurate results for thick laminar composites even under concentrated loadings [107]. The application of partial layerwise theories served as the basis in the development of numerical solution for global response prediction of intact laminar composites and sandwich plates [108]. Marjanović and Vuksanović [109] used this model to account for delamination kinematics and further applied it for calculation of fundamental dynamic characteristics [110], as well as for the geometrically nonlinear transient analysis of delaminated laminar composites and sandwich plates [111].

However, the partial layerwise theories neglect the interlaminar normal stress (due to the assumption that deflection is constant through the thickness), which is important in modelling the localized effects such as holes, as well as for the prediction of damage initiation. In order to overcome these limitations, a family of layered quadrilateral finite elements based on the FLWT has been developed in author's previous work [112] and applied for structural analysis of CLT panels. While many researchers focused their attention on the analysis of laminar composites using layered finite elements, there is still a lack of investigations regarding their application for the PFA of laminar composites, especially in conjunction with SCB damage model and applications for real-size elements in civil engineering. Consequently, Jočić and Marjanović presented the original incorporation of the (SCB) damage model within the FLWT framework for PFA of open-hole laminar composites [13], which served as a strong foundation of this dissertation.

3 Full layerwise theory for 3D analysis of laminar composites

3.1 Introduction

Unlike homogenous isotropic plates, the heterogeneous anisotropic constitution of laminar composites often results in the appearance of many unique phenomena that can occur on different geometric scales. Global deformation of laminar composites is characterized by the coupling between bending, extension, and shear, while at the lamina level, laminar composites exhibit transverse stress concentrations near material and geometric discontinuities, resulting in different forms of damage, i.e. *fiber breakage* or *matrix cracking*. Also, the strength and stiffness of laminar composites are increased without a corresponding increase in weight [113], resulting in a rapid change of displacement field slopes at the interface of adjacent layers.

In contrary to prediction of global laminate response, previously mentioned ESL theories are often inadequate for determining the 3D stress field at the lamina level, since they assume that the displacements are continuous functions of thickness coordinate. As a result of such assumption, the interlaminar stresses ($\tau_{xz}, \tau_{yz}, \sigma_z$) are discontinuous across interfaces between different materials, which does not satisfy the continuity conditions between the stress fields of the adjacent layers. This deficiency is especially evident in thick laminates, or in localized regions where the damage initiation is likely to occur. In order to obtain the three-dimensional (3D) stress state and kinematically correct representation of cross-section warping, refined theories are recommended, such as: layerwise theories (LWT) or a 3D elasticity theory.

In contrast to the ESL theories, the layerwise theories assume a unique displacement field, that exhibits only C^0 continuity through the laminate thickness. This results in continuous displacement components at the interfaces between the adjacent layers, allowing for the possibility of discontinuous derivatives of displacement components with respect to the thickness coordinate. The LWT are generally of two types: the partial layerwise theories (PLWT) and the full layerwise theories (FLWT). While PLWT assume the piece-wise expansion only for the in-plane displacement components within each material layer; the FLWT go one step further by using the piece-wise expansion for all displacement components through the thickness. Thus, the continuity conditions of stresses at the interfaces between adjacent layers are satisfied: the in-plane stresses are discontinuous, while the transverse (interlaminar) stresses are continuous through the thickness. Also, it is noticed that FLWT can provide such accurate 3D stress fields as a conventional 3D models, with reduced computational costs.

3.2 Theory formulation

A laminated composite plate made of n perfectly bonded orthotropic layers is considered in this study (Figure 3.1). The total plate thickness is denoted as h , while the thickness of the k^{th} lamina is denoted as h_k .

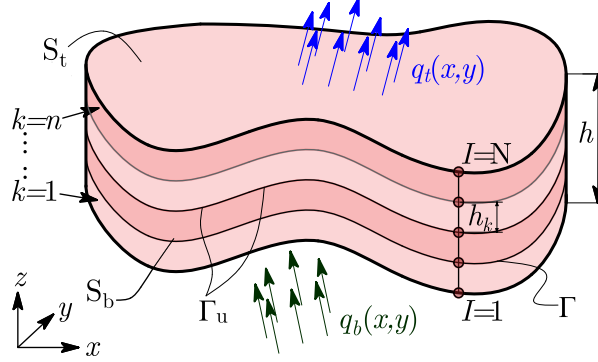


Figure 3.1: Laminated composite plate made of n material layers and with N numerical interfaces [13]

The plate is supported along the portion Γ_u of the boundary Γ and loaded with arbitrary loadings $q_t(x, y)$ and $q_b(x, y)$ acting to either top S_t ($z = h/2$) or the bottom surface S_b ($z = -h/2$) of the plate.

In the formulation of Full Layerwise Theory (FLWT), the following assumptions are used:

1. Each layer of which the laminate composite plate is made is homogeneous and orthotropic. Orthotropy originates from high-strength fibers that are oriented in the appropriate direction and equally distributed in a homogeneous base material (matrix).
2. All material layers are perfectly bonded together.
3. The relation between strain and displacement is linear, i.e. the assumption of geometric linearity holds.
4. Deflection is a variable function across the laminate thickness, i.e. the assumption of transverse normal extensibility with respect to the mid-plane of the plate holds.
5. Material of each layer is linearly elastic until the initiation of damage in the weakest lamina occur; after that the composite material exhibits strain-softening behaviour, i.e. the relationship between stress and strain becomes non-linear.
6. Material non-linearity is taken into account by gradual degradation of the stiffness of the damaged lamina, i.e. quasi-brittle material behaviour is assumed after the initiation of failure.
7. The damage can only propagate within the plane of the laminate, in either the fiber or matrix direction, i.e. there is no damage at the interface between adjacent layers of the laminate (delamination).

3.3 Displacement and strain fields

Piece-wise linear variation of all three displacement components through the laminate thickness is imposed, leading to the 3D stress description of all material layers. The displacement field (u, v, w) of an arbitrary point (x, y, z) of the laminate is represented as product of functions of in-plane coordinates and functions of thickness coordinates:

$$\begin{aligned} u(x, y, z) &= \sum_{i=1}^N U^I(x, y) \Phi^I(z) \\ v(x, y, z) &= \sum_{i=1}^N V^I(x, y) \Phi^I(z) \\ w(x, y, z) &= \sum_{i=1}^N W^I(x, y) \Phi^I(z) \end{aligned} \quad (3.1)$$

In Eq. (3.1), $U_I(x, y)$, $V_I(x, y)$ and $W_I(x, y)$ are the displacement components in the I^{th} numerical layer of the plate in directions x , y and z , respectively, while N ($N = n + 1$) is the number of interfaces between the layers including S_b and S_t . $\Phi^I(z)$ are selected to be one-dimensional linear Lagrangian functions of the z -coordinate, defined over the considered layer (Figure 3.2):

$$\begin{aligned} \Phi^1(z) &= 1 - \frac{\bar{z}}{h_1}, \quad 0 \leq \bar{z} \leq h_1, \\ \Phi^I(z) &= \begin{cases} \frac{\bar{z}}{h_{I-1}}, & 0 \leq \bar{z} \leq h_{I-1} \\ 1 - \frac{\bar{z}}{h_I}, & 0 \leq \bar{z} \leq h_I \end{cases}, \quad I = 2, 3, \dots, N-1, \\ \Phi^N(z) &= \frac{\bar{z}}{h_N}, \quad 0 \leq \bar{z} \leq h_N \end{aligned} \quad (3.2)$$

In Eq. (3.2), \bar{z} is the local coordinate in thickness direction defined through the considered layer, while h_I denotes the thickness of I^{th} layer.

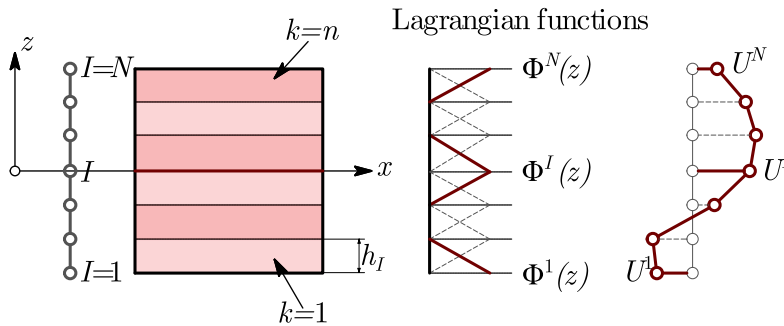


Figure 3.2: Linear lagrangian functions $\Phi^I(z)$ and corresponding displacements distribution through laminate thickness

As the consequence of the assumed displacement field, all displacement components are piecewise continuous through the laminate thickness. Also, the independent in-plane and through the thickness discretization of the laminate is achieved.

The linear strain field associated with the previously shown displacement field from Eq. (3.1) can be written as follows:

$$\begin{aligned}
\varepsilon_x(x, y, z) &= \sum_{i=1}^N \frac{\partial U^I(x, y)}{\partial x} \Phi^I(z), \\
\varepsilon_y(x, y, z) &= \sum_{i=1}^N \frac{\partial V^I(x, y)}{\partial y} \Phi^I(z), \\
\varepsilon_z(x, y, z) &= \sum_{i=1}^N W^I(x, y) \frac{d\Phi^I(z)}{dz}, \\
\gamma_{yz}(x, y, z) &= \sum_{i=1}^N V^I(x, y) \frac{d\Phi^I(z)}{dz} + \frac{\partial W^I(x, y)}{\partial y} \Phi^I(z), \\
\gamma_{xz}(x, y, z) &= \sum_{i=1}^N U^I(x, y) \frac{d\Phi^I(z)}{dz} + \frac{\partial W^I(x, y)}{\partial x} \Phi^I(z), \\
\gamma_{xy}(x, y, z) &= \sum_{i=1}^N \left(\frac{\partial U^I(x, y)}{\partial y} + \frac{\partial V^I(x, y)}{\partial x} \right) \Phi^I(z)
\end{aligned} \tag{3.3}$$

3.4 3D constitutive equations of lamina

In order to establish a 3D constitutive model of lamina, two reference coordinate systems (Figure 3.3) must be defined: global coordinate system (xyz), which is unique for the whole laminate, and material coordinate system (123) which is set for each lamina.

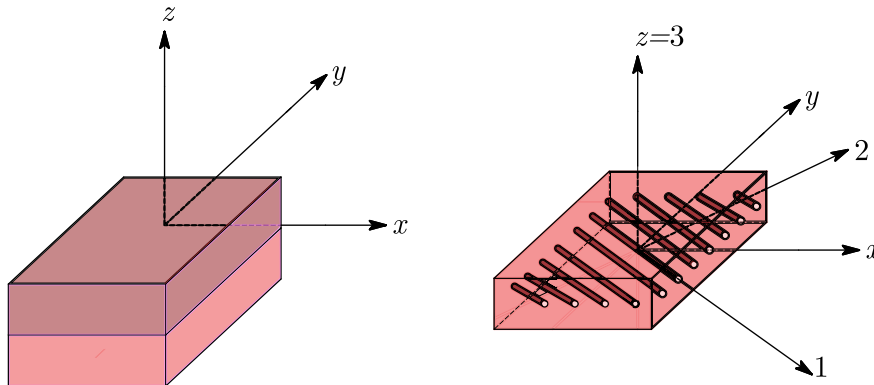


Figure 3.3: Global (laminate) coordinate system (xyz) and material (lamina) coordinate system (123)

As can be seen from the Figure 3.3, directions 1, 2 and 3 represent: fiber direction, direction transverse to the fiber but in the plane of the laminate, and direction transverse to both the

fiber and to the laminate, respectively. Cartesian orthogonal coordinate system xyz is adopted as a global coordinate system of laminate.

The stresses for the k^{th} orthotropic layer, in material coordinate system (123) , can be computed from the 3D constitutive equations for each lamina:

$$\begin{Bmatrix} \sigma_1 \\ \sigma_2 \\ \sigma_3 \\ \tau_{23} \\ \tau_{13} \\ \tau_{12} \end{Bmatrix}^{(k)} = \begin{bmatrix} C_{11} & C_{12} & C_{13} & 0 & 0 & 0 \\ C_{21} & C_{22} & C_{23} & 0 & 0 & 0 \\ C_{31} & C_{23} & C_{33} & 0 & 0 & 0 \\ 0 & 0 & 0 & C_{44} & 0 & 0 \\ 0 & 0 & 0 & 0 & C_{55} & 0 \\ 0 & 0 & 0 & 0 & 0 & C_{66} \end{bmatrix}^{(k)} \begin{Bmatrix} \varepsilon_1 \\ \varepsilon_2 \\ \varepsilon_3 \\ \gamma_{23} \\ \gamma_{13} \\ \gamma_{12} \end{Bmatrix}^{(k)} \quad (3.4)$$

where C_{ij} are the stiffness matrix coefficients in the material $(1, 2, 3)$ coordinates. Since the laminate is generally made of several orthotropic laminae, with their material axes oriented arbitrarily with respect to the global coordinates, the constitutive relations for each lamina must be transformed from the material (123) to the global (xyz) coordinate system [12]. The stiffness matrix for the k^{th} layer in global coordinate system will be of the form:

$$\bar{\mathbf{C}}^{(k)} = \mathbf{T}^{(k)-1} \mathbf{C}^{(k)} \mathbf{T}^{(k)} \quad (3.5)$$

where $\mathbf{T}^{(k)}$ is the transformation matrix of the k^{th} layer:

$$\mathbf{T}^{(k)} = \begin{bmatrix} \cos^2 \theta & \sin^2 \theta & 0 & 0 & 0 & 2 \sin \theta \cos \theta \\ \sin^2 \theta & \cos^2 \theta & 0 & 0 & 0 & -2 \sin \theta \cos \theta \\ 0 & 0 & 1 & 0 & 0 & 0 \\ 0 & 0 & 0 & \cos \theta & -\sin \theta & 0 \\ 0 & 0 & 0 & -\sin \theta & \cos \theta & 0 \\ -\sin \theta \cos \theta & \sin \theta \cos \theta & 0 & 0 & 0 & \cos^2 \theta - \sin^2 \theta \end{bmatrix}^{(k)} \quad (3.6)$$

Therefore, 3D constitutive relations for the k^{th} orthotropic layer, in global coordinate system (xyz) , can now be written as:

$$\begin{Bmatrix} \sigma_x \\ \sigma_y \\ \sigma_z \\ \tau_{yz} \\ \tau_{xz} \\ \tau_{xy} \end{Bmatrix}^{(k)} = \begin{bmatrix} \bar{C}_{11} & \bar{C}_{12} & \bar{C}_{13} & 0 & 0 & \bar{C}_{16} \\ \bar{C}_{21} & \bar{C}_{22} & \bar{C}_{23} & 0 & 0 & \bar{C}_{26} \\ \bar{C}_{31} & \bar{C}_{32} & \bar{C}_{33} & 0 & 0 & \bar{C}_{36} \\ 0 & 0 & 0 & \bar{C}_{44} & \bar{C}_{45} & 0 \\ 0 & 0 & 0 & \bar{C}_{54} & \bar{C}_{55} & 0 \\ \bar{C}_{61} & \bar{C}_{62} & \bar{C}_{63} & 0 & 0 & \bar{C}_{66} \end{bmatrix}^{(k)} \begin{Bmatrix} \varepsilon_x \\ \varepsilon_y \\ \varepsilon_z \\ \gamma_{yz} \\ \gamma_{xz} \\ \gamma_{xy} \end{Bmatrix}^{(k)} \quad (3.7)$$

3.5 Governing equations of motion

The governing equations of motion for the FLWT are derived by using the principle of virtual displacements (note that virtual kinetic energy δK is equal to zero for the static problems):

$$\delta U + \delta V = 0 \quad (3.8)$$

The virtual strain energy (virtual work of internal forces) is given as:

$$\delta U = \int_{\Omega} \left[\int_{-h/2}^{h/2} (\sigma_x \delta \varepsilon_x + \sigma_y \delta \varepsilon_y + \sigma_z \delta \varepsilon_z + \tau_{yz} \delta \gamma_{yz} + \tau_{xz} \delta \gamma_{xz} + \tau_{xy} \delta \gamma_{xy}) dz \right] dxdy \quad (3.9)$$

where $\delta \varepsilon_x$, $\delta \varepsilon_y$, $\delta \varepsilon_z$, $\delta \gamma_{yz}$, $\delta \gamma_{xz}$ and $\delta \gamma_{xy}$ are corresponding virtual strains obtained from the previously derived strain field (Eq. (3.3)) and given in [12].

In order to reduce the 3D model to a 2D one, the z -coordinate is eliminated by the explicit integration of stress components multiplied with the corresponding functions $\Phi^I(z)$, introducing the stress resultants in the I^{th} layer as:

$$\begin{pmatrix} N_x^I \\ N_y^I \\ N_{xy}^I \\ Q_y^I \\ Q_x^I \end{pmatrix} = \sum_{k=1}^n \int_{z_b^k}^{z_t^k} \begin{pmatrix} \sigma_x \\ \sigma_y \\ \tau_{xy} \\ \tau_{yz} \\ \tau_{xz} \end{pmatrix} \Phi^I dz, \quad \begin{pmatrix} \bar{Q}_y^I \\ \bar{Q}_x^I \\ \bar{Q}_z^I \end{pmatrix} = \sum_{k=1}^n \int_{z_b^k}^{z_t^k} \begin{pmatrix} \tau_{yz} \\ \tau_{xz} \\ \sigma_z \end{pmatrix} \frac{d\Phi^I}{dz} dz \quad (3.10)$$

where z_b^k and z_t^k are coordinates of the bottom and top of the k^{th} layer.

After the incorporation of virtual strains and stress resultants (Eq. (3.10)), the virtual strain energy is obtained in the following form [12]:

$$\delta U = \int_{\Omega} \sum_{I=1}^N \left\{ \begin{aligned} &N_x^I \frac{\partial \delta U^I}{\partial x} + N_y^I \frac{\partial \delta V^I}{\partial y} + N_{xy}^I \left(\frac{\partial \delta U^I}{\partial y} \frac{\partial \delta V^I}{\partial x} \right) + \\ &+ Q_x^I \frac{\partial \delta W^I}{\partial x} + Q_y^I \frac{\partial \delta W^I}{\partial y} + \bar{Q}_x^I \delta U^I + \bar{Q}_y^I \delta V^I + \bar{Q}_z^I \delta W^I \end{aligned} \right\} dxdy \quad (3.11)$$

After the integration by parts for the surface integral, done to eliminate the derivations of virtual displacements, all members corresponding to the specific virtual displacement are grouped. Consequently, the following form of the virtual strain energy is obtained:

$$\delta U = \int_{\Omega} \sum_{I=1}^N \left\{ \begin{aligned} &\delta U^I \left(\frac{\partial N_x^I}{\partial x} + \frac{\partial N_{xy}^I}{\partial y} - \bar{Q}_x^I \right) + \\ &+ \delta V^I \left(\frac{\partial N_y^I}{\partial y} + \frac{\partial N_{xy}^I}{\partial x} - \bar{Q}_y^I \right) + \\ &+ \delta W^I \left(\frac{\partial Q_x^I}{\partial x} + \frac{\partial Q_y^I}{\partial y} - \bar{Q}_z^I \right) \end{aligned} \right\} dxdy \quad (3.12)$$

The virtual work of external forces is given as:

$$\delta V = \int_{\Omega} (q_b \delta W^1 + q_t \delta W^N) dxdy \quad (3.13)$$

In Eq. (3.13), δW_1 and δW_N are virtual displacements at the S_b and S_t , respectively (see Figure 3.1).

Finally, the system of 3N Euler-Lagrange governing equations of motion for the FLWT are derived using the principle of virtual displacements (Eq. (3.8)), by satisfying the equilibrium of the virtual strain energy δU (Eq. (3.12)) and the work done by the applied forces δV (Eq. (3.13)):

$$\begin{aligned} \frac{\partial N_x^I}{\partial x} + \frac{\partial N_{xy}^I}{\partial y} - \bar{Q}_x^I &= 0 \\ \frac{\partial N_y^I}{\partial y} + \frac{\partial N_{xy}^I}{\partial x} - \bar{Q}_y^I &= 0 \\ \frac{\partial Q_x^I}{\partial x} + \frac{\partial Q_y^I}{\partial y} - \bar{Q}_z^I + q_b + q_t &= 0 \end{aligned} \quad (3.14)$$

3.6 Laminate constitutive equations

The laminate constitutive equations in the FLWT are derived by substituting the constitutive equations of the single lamina (Eq. (3.7)) into expressions for stress resultants (Eq. (3.10)):

$$\begin{aligned} \begin{Bmatrix} N_x^I \\ N_y^I \\ N_{xy}^I \end{Bmatrix} &= \sum_{k=1}^n \int_{z_b^k}^{z_t^k} \begin{bmatrix} \bar{C}_{11} & \bar{C}_{12} & \bar{C}_{13} & \bar{C}_{16} \\ \bar{C}_{21} & \bar{C}_{22} & \bar{C}_{23} & \bar{C}_{26} \\ \bar{C}_{61} & \bar{C}_{62} & \bar{C}_{63} & \bar{C}_{66} \end{bmatrix}^{(k)} \begin{Bmatrix} \varepsilon_x \\ \varepsilon_y \\ \varepsilon_z \\ \gamma_{xy} \end{Bmatrix}^{(k)} \Phi^I dz = \\ &= \sum_{J=1}^N \begin{bmatrix} A_{11}^{IJ} & A_{12}^{IJ} & \tilde{A}_{13}^{IJ} & A_{16}^{IJ} \\ A_{21}^{IJ} & A_{22}^{IJ} & \tilde{A}_{23}^{IJ} & A_{26}^{IJ} \\ A_{61}^{IJ} & A_{62}^{IJ} & \tilde{A}_{63}^{IJ} & A_{66}^{IJ} \end{bmatrix} \begin{Bmatrix} \frac{\partial U^J}{\partial x} \\ \frac{\partial J^I}{\partial y} \\ W^J \\ \frac{\partial U^J}{\partial y} + \frac{\partial V^J}{\partial x} \end{Bmatrix} \end{aligned} \quad (3.15)$$

$$\begin{aligned} \begin{Bmatrix} Q_y^I \\ Q_x^I \end{Bmatrix} &= \sum_{k=1}^n \int_{z_b^k}^{z_t^k} \begin{bmatrix} \bar{C}_{44} & \bar{C}_{45} \\ \bar{C}_{54} & \bar{C}_{55} \end{bmatrix}^{(k)} \begin{Bmatrix} \gamma_{yz} \\ \gamma_{xz} \end{Bmatrix}^{(k)} \Phi^I dz = \\ &= \sum_{J=1}^N \begin{bmatrix} \tilde{A}_{44}^{IJ} & \tilde{A}_{45}^{IJ} \\ \tilde{A}_{54}^{IJ} & \tilde{A}_{55}^{IJ} \end{bmatrix} \begin{Bmatrix} V^J \\ U^J \end{Bmatrix} + \sum_{J=1}^N \begin{bmatrix} A_{44}^{IJ} & A_{45}^{IJ} \\ A_{54}^{IJ} & A_{55}^{IJ} \end{bmatrix} \begin{Bmatrix} \frac{\partial W^J}{\partial y} \\ \frac{\partial W^J}{\partial x} \end{Bmatrix} \end{aligned} \quad (3.16)$$

$$\begin{aligned}
\begin{Bmatrix} \bar{Q}_y^I \\ \bar{Q}_x^I \end{Bmatrix} &= \sum_{k=1}^n \int_{z_b^k}^{z_t^k} \begin{bmatrix} \bar{C}_{44} & \bar{C}_{45} \\ \bar{C}_{54} & \bar{C}_{55} \end{bmatrix}^{(k)} \begin{Bmatrix} \gamma_{yz} \\ \gamma_{xz} \end{Bmatrix}^{(k)} \frac{d\Phi^I}{dz} dz = \\
&= \sum_{J=1}^N \begin{bmatrix} \bar{A}_{44}^{IJ} & \bar{A}_{45}^{IJ} \\ \bar{A}_{54}^{IJ} & \bar{A}_{55}^{IJ} \end{bmatrix} \begin{Bmatrix} V^J \\ U^J \end{Bmatrix} + \sum_{J=1}^N \begin{bmatrix} \bar{\bar{A}}_{44}^{IJ} & \bar{\bar{A}}_{45}^{IJ} \\ \bar{\bar{A}}_{54}^{IJ} & \bar{\bar{A}}_{55}^{IJ} \end{bmatrix} \begin{Bmatrix} \frac{\partial W^J}{\partial y} \\ \frac{\partial W^J}{\partial x} \end{Bmatrix}
\end{aligned} \tag{3.17}$$

$$\begin{aligned}
\{\bar{Q}_z^I\} &= \sum_{k=1}^n \int_{z_b^k}^{z_t^k} \begin{bmatrix} \bar{C}_{31} & \bar{C}_{32} & \bar{C}_{33} & \bar{C}_{36} \end{bmatrix}^{(k)} \begin{Bmatrix} \varepsilon_x \\ \varepsilon_y \\ \varepsilon_z \\ \gamma_{xy} \end{Bmatrix}^{(k)} \frac{d\Phi^I}{dz} dz = \\
&= \sum_{J=1}^N \begin{bmatrix} \bar{\bar{A}}_{31}^{IJ} & \bar{\bar{A}}_{32}^{IJ} & \bar{\bar{A}}_{33}^{IJ} & \bar{\bar{A}}_{36}^{IJ} \end{bmatrix} \begin{Bmatrix} \frac{\partial U^J}{\partial y} \\ \frac{\partial U^J}{\partial x} \\ W^J \\ \frac{\partial U^J}{\partial y} + \frac{\partial V^J}{\partial x} \end{Bmatrix}
\end{aligned} \tag{3.18}$$

The laminate stiffness components in (Eq. (3.15)- Eq. (3.18)) are defined as [12]:

$$\begin{aligned}
A_{ij}^{IJ} &= \sum_{k=1}^n \int_{z_b^k}^{z_t^k} \bar{C}_{ij}^{(k)} \Phi^I \Phi^J dz, & \bar{A}_{ij}^{IJ} &= \sum_{k=1}^n \int_{z_b^k}^{z_t^k} \bar{C}_{ij}^{(k)} \frac{d\Phi^I}{dz} \frac{d\Phi^J}{dz} dz \\
\tilde{A}_{ij}^{IJ} &= \sum_{k=1}^n \int_{z_b^k}^{z_t^k} \bar{C}_{ij}^{(k)} \Phi^I \frac{d\Phi^J}{dz} dz, & \bar{\bar{A}}_{ij}^{IJ} &= \sum_{k=1}^n \int_{z_b^k}^{z_t^k} \bar{C}_{ij}^{(k)} \frac{d\Phi^I}{dz} \Phi^J dz
\end{aligned} \tag{3.19}$$

For the linear interpolation function Φ^I through the laminate thickness, the elements of laminate stiffness matrices are:

$$\begin{aligned}
A_{ij}^{1,1} &= \bar{C}_{ij}^{(1)} \frac{h_1}{3}, & A_{ij}^{1,2} &= \bar{C}_{ij}^{(1)} \frac{h_1}{6}, & A_{ij}^{N-1,N} &= \bar{C}_{ij}^{(N-1)} \frac{h_{N-1}}{6}, & A_{ij}^{N,N} &= \bar{C}_{ij}^{(N-1)} \frac{h_{N-1}}{3} \\
A_{ij}^{I-1,I} &= \bar{C}_{ij}^{(I-1)} \frac{h_{I-1}}{6}, & A_{ij}^{I,I} &= \frac{\bar{C}_{ij}^{(I-1)} h_{I-1} + \bar{C}_{ij}^{(I)} h_I}{3}, & A_{ij}^{I,I+1} &= \bar{C}_{ij}^{(I)} \frac{h_I}{6}
\end{aligned} \tag{3.20}$$

$$\begin{aligned}
\bar{A}_{ij}^{1,1} &= \frac{\bar{C}_{ij}^{(1)}}{h_1}, & \bar{A}_{ij}^{1,2} &= -\frac{\bar{C}_{ij}^{(1)}}{h_1}, & \bar{A}_{ij}^{N-1,N} &= -\frac{\bar{C}_{ij}^{(N-1)}}{h_{N-1}}, & \bar{A}_{ij}^{N,N} &= \frac{\bar{C}_{ij}^{(N-1)}}{h_{N-1}} \\
\bar{A}_{ij}^{I-1,I} &= -\frac{\bar{C}_{ij}^{(I-1)}}{h_{I-1}}, & \bar{A}_{ij}^{I,I} &= \frac{\bar{C}_{ij}^{(I-1)}}{h_{I-1}} + \frac{\bar{C}_{ij}^{(I)}}{h_I}, & \bar{A}_{ij}^{I,I+1} &= -\frac{\bar{C}_{ij}^{(I)}}{h_I},
\end{aligned} \tag{3.21}$$

$$\begin{aligned}
\tilde{A}_{ij}^{1,1} &= -\frac{\bar{C}_{ij}^{(1)}}{2}, & \tilde{A}_{ij}^{1,2} &= \frac{\bar{C}_{ij}^{(1)}}{2}, & \tilde{A}_{ij}^{N-1,N} &= -\frac{\bar{C}_{ij}^{(N-1)}}{2}, & \tilde{A}_{ij}^{N,N} &= \frac{\bar{C}_{ij}^{(N-1)}}{2} \\
\tilde{A}_{ij}^{I-1,I} &= -\frac{\bar{C}_{ij}^{(I-1)}}{2}, & \tilde{A}_{ij}^{I,I} &= \frac{\bar{C}_{ij}^{(I-1)} + \bar{C}_{ij}^{(I)}}{2}, & \tilde{A}_{ij}^{I,I+1} &= \frac{\bar{C}_{ij}^{(I)}}{2},
\end{aligned} \tag{3.22}$$

$$\begin{aligned}
\bar{A}_{ij}^{1,1} &= -\frac{\bar{C}_{ij}^{(1)}}{2}, & \bar{A}_{ij}^{1,2} &= -\frac{\bar{C}_{ij}^{(1)}}{2}, & \bar{A}_{ij}^{N-1,N} &= \frac{\bar{C}_{ij}^{(N-1)}}{2}, & \bar{A}_{ij}^{N,N} &= \frac{\bar{C}_{ij}^{(N-1)}}{2} \\
\bar{A}_{ij}^{I-1,I} &= \frac{\bar{C}_{ij}^{(I-1)}}{2}, & \bar{A}_{ij}^{I,I} &= \frac{\bar{C}_{ij}^{(I-1)} + \bar{C}_{ij}^{(I)}}{2}, & \bar{A}_{ij}^{I,I+1} &= -\frac{\bar{C}_{ij}^{(I)}}{2}, \\
\bar{A}_{ij}^{1,1} &= -\frac{\bar{C}_{ij}^{(1)}}{2}, & \bar{A}_{ij}^{1,2} &= -\frac{\bar{C}_{ij}^{(1)}}{2}, & \bar{A}_{ij}^{N-1,N} &= \frac{\bar{C}_{ij}^{(N-1)}}{2}, & \bar{A}_{ij}^{N,N} &= \frac{\bar{C}_{ij}^{(N-1)}}{2}
\end{aligned} \tag{3.23}$$

$$\bar{A}_{ij}^{I-1,I} = \frac{\bar{C}_{ij}^{(I-1)}}{2}, \quad \bar{A}_{ij}^{I,I} = \frac{\bar{C}_{ij}^{(I-1)} + \bar{C}_{ij}^{(I)}}{2}, \quad \bar{A}_{ij}^{I,I+1} = -\frac{\bar{C}_{ij}^{(I)}}{2},$$

For the sake of simplicity, the following deformations vectors are introduced:

$$\{\varepsilon^I\} = \begin{Bmatrix} \frac{\partial U^J}{\partial x} \\ \frac{\partial V^I}{\partial y} \\ W^J \\ \frac{\partial U^J}{\partial y} + \frac{\partial V^J}{\partial x} \end{Bmatrix}, \quad \{\bar{\varepsilon}^I\} = \begin{Bmatrix} V^I \\ U^I \\ \frac{\partial W^J}{\partial y} \\ \frac{\partial W^J}{\partial x} \end{Bmatrix} \tag{3.24}$$

Constitutive relations of the laminate now can be re-written in the matrix form:

$$\begin{Bmatrix} N_x^I \\ N_y^I \\ \bar{Q}_z^I \\ N_{xy}^I \end{Bmatrix} = \begin{bmatrix} A_{11}^{IJ} & A_{12}^{IJ} & \tilde{A}_{13}^{IJ} & A_{16}^{IJ} \\ A_{21}^{IJ} & A_{22}^{IJ} & \tilde{A}_{23}^{IJ} & A_{26}^{IJ} \\ \bar{A}_{31}^{IJ} & \bar{A}_{32}^{IJ} & \bar{A}_{33}^{IJ} & \bar{A}_{36}^{IJ} \\ A_{61}^{IJ} & A_{62}^{IJ} & \tilde{A}_{63}^{IJ} & A_{66}^{IJ} \end{bmatrix} \begin{Bmatrix} \frac{\partial U^J}{\partial x} \\ \frac{\partial V^I}{\partial y} \\ W^J \\ \frac{\partial U^J}{\partial y} + \frac{\partial V^J}{\partial x} \end{Bmatrix} \tag{3.25}$$

$$\begin{Bmatrix} Q_y^I \\ Q_x^I \\ \bar{Q}_y^I \\ \bar{Q}_x^I \end{Bmatrix} = \begin{bmatrix} \tilde{A}_{44}^{IJ} & \tilde{A}_{45}^{IJ} & A_{44}^{IJ} & A_{45}^{IJ} \\ \tilde{A}_{54}^{IJ} & \tilde{A}_{55}^{IJ} & A_{54}^{IJ} & A_{55}^{IJ} \\ \bar{A}_{44}^{IJ} & \bar{A}_{45}^{IJ} & \bar{A}_{44}^{IJ} & \bar{A}_{45}^{IJ} \\ \bar{A}_{54}^{IJ} & \bar{A}_{55}^{IJ} & \bar{A}_{54}^{IJ} & \bar{A}_{55}^{IJ} \end{bmatrix} \begin{Bmatrix} V^J \\ U^J \\ \frac{\partial W^J}{\partial y} \\ \frac{\partial W^J}{\partial x} \end{Bmatrix} \tag{3.26}$$

i.e. in abbreviated form:

$$\{N^I\} = \sum_{J=1}^N [A_1^{IJ}] \{\varepsilon^J\}, \quad \{Q^I\} = \sum_{J=1}^N [A_2^{IJ}] \{\bar{\varepsilon}^J\} \tag{3.27}$$

In Eq. (3.27), $\{N^I\}$ and $\{Q^I\}$ are stress resultants vectors, while $[A_1^{IJ}]$ and $[A_2^{IJ}]$ are corresponding stiffness matrices.

4 Layered FLWT-based finite element

4.1 Introduction

Analytical solution of the FLWT exists only for the relatively simple plate geometries, boundary and loading conditions. However, for the structural analysis of laminar composites of arbitrary shape, loading, boundary conditions or stacking sequence, numerical models are required.

The finite element method (FEM) is a powerful computational technique for solving problems which are described by partial differential equations [114]. A domain of interest is approximated as an assemblage of simple geometric shapes, i.e., finite elements (FE). The approximation functions, also called the interpolation functions [12], are determined in terms of nodal values of a requested physical field. In that manner, a continuous physical problem is transformed into a discretized finite element problem with unknown nodal values. By utilizing FEs to approximate physical fields in a piece-wise manner, it is possible to obtain a high level of accuracy even with basic approximating functions. Additionally, precision can be further enhanced by increasing the number of elements. Also, the localization of the approximation results in equation systems that are sparse for a discretized problem. This sparsity is beneficial when solving problems that involve a large number of nodal unknowns.

It should be noted that this Chapter is based on work published by the author [15].

4.2 Development of the layered element stiffness matrix

The system of 3N Euler-Lagrange governing equations of motion, derived in previous chapter, serve as a basis for the development of a numerical solution based on FEM. Applying the procedure presented in [12], the "weak" formulation of the Euler-Lagrange governing equations of layered finite element can be written in the following form:

$$\begin{aligned} \int_{\Omega^e} \left[\frac{\partial \delta U^I}{\partial x} N_x^I + \frac{\partial \delta U^I}{\partial y} N_{xy}^I - \bar{Q}_x^I \delta U^I \right] d\Omega^e &= 0 \\ \int_{\Omega^e} \left[\frac{\partial \delta V^I}{\partial y} N_y^I + \frac{\partial \delta V^I}{\partial x} N_{xy}^I - \bar{Q}_y^I \delta V^I \right] d\Omega^e &= 0 \\ \int_{\Omega^e} \left[\frac{\partial \delta W^I}{\partial x} Q_x^I + \frac{\partial \delta W^I}{\partial x} Q_y^I - \bar{Q}_z^I \delta W^I - q_b \delta W^1 - q_t \delta W^N \right] d\Omega^e &= 0 \end{aligned} \tag{4.1}$$

where Ω^e is layered finite element domain.

The Eqs. (4.1) can be re-written in matrix form, by grouping all stress resultants corresponding to the same virtual deformations vectors:

$$\int_{\Omega^e} \left[\sum_{I=1}^N \{\delta\varepsilon^I\}^T \{N^I\} + \sum_{I=1}^N \{\delta\bar{\varepsilon}^I\}^T \{Q^I\} - q_b \delta W^1 - q_t \delta W^N \right] d\Omega^e = 0 \quad (4.2)$$

The solution of the weak formulation is sought in layered finite element domain, defined by the interpolation functions. Accordingly, the displacement field can be assumed in the following form:

$$\begin{aligned} U^I(x, y) &= \sum_{j=1}^m U_j^I \psi_j(x, y), \\ V^I(x, y) &= \sum_{j=1}^m V_j^I \psi_j(x, y), \\ W^I(x, y) &= \sum_{j=1}^m W_j^I \psi_j(x, y) \end{aligned} \quad (4.3)$$

In Eq. (4.3), m is the number of nodes per 2D element, U_j^I , V_j^I , W_j^I are the nodal values of displacements U^I , V^I and W^I , respectively, in the j^{th} node and I^{th} numerical interface of the layered finite element. Finally, $\psi_j(x, y)$ are the 2D Lagrange interpolation polynomials (shape functions for quadrilateral domains) associated with the j^{th} element node. For the sake of simplicity, the Eq. (4.3) is re-written in matrix form:

$$\begin{Bmatrix} U^I(x, y) \\ V^I(x, y) \\ W^I(x, y) \end{Bmatrix} = \begin{Bmatrix} \sum_{j=1}^m U_j^I \psi_j(x, y) \\ \sum_{j=1}^m V_j^I \psi_j(x, y) \\ \sum_{j=1}^m W_j^I \psi_j(x, y) \end{Bmatrix} = [\psi] \{\Delta^I\} \quad (4.4)$$

where $\{\Delta^I\}$ is displacement vector in I^{th} numerical interface:

$$\{\Delta^I\} = \begin{Bmatrix} U_1^I \\ V_1^I \\ W_1^I \\ \vdots \end{Bmatrix}_{3m \times 1} \quad (4.5)$$

while, $[\psi]$ is the matrix of Lagrangian interpolation functions:

$$[\psi] = \begin{bmatrix} \psi_1 & 0 & 0 & \dots \\ 0 & \psi_1 & 0 & \dots \\ 0 & 0 & \psi_1 & \dots \end{bmatrix}_{3 \times 3m} \quad (4.6)$$

The strain field is interpolated in the usual manner, by incorporating Eq. (4.4) in the kinematic relations of the FLWT from Eqs. (3.24), and is given in matrix form as:

$$\begin{aligned} \{\varepsilon^I\}_{4 \times 1} &= [B]_{4 \times 3m} \{\Delta^I\}_{3m \times 1} \\ \{\bar{\varepsilon}^I\}_{4 \times 1} &= [\bar{B}]_{4 \times 3m} \{\Delta^I\}_{3m \times 1} \end{aligned} \quad (4.7)$$

In Eqs. (4.7), $[B]$ and $[\bar{B}]$ represent kinematic matrices:

$$[B]_{4 \times 3m} = \begin{bmatrix} \frac{\partial \psi_1}{\partial x} & 0 & 0 & & \\ 0 & \frac{\partial \psi_1}{\partial y} & 0 & \dots & \\ \frac{\partial \psi_1}{\partial y} & \frac{\partial \psi_1}{\partial x} & 0 & & \\ 0 & 0 & \psi_1 & & \end{bmatrix}_{4 \times 3m}, \quad [\bar{B}]_{4 \times 3m} = \begin{bmatrix} \psi_1 & 0 & 0 & & \\ 0 & \psi_1 & 0 & \dots & \\ 0 & 0 & \frac{\partial \psi_1}{\partial x} & & \\ 0 & 0 & \frac{\partial \psi_1}{\partial y} & & \end{bmatrix}_{4 \times 3m} \quad (4.8)$$

Based on Eqs. (4.7), the corresponding virtual strain matrices are:

$$\begin{aligned} \{\delta \varepsilon^I\}_{4 \times 1} &= [B]_{4 \times 3m} \{\delta \Delta^I\}_{3m \times 1} \\ \{\delta \bar{\varepsilon}^I\}_{4 \times 1} &= [\bar{B}]_{4 \times 3m} \{\delta \Delta^I\}_{3m \times 1} \end{aligned} \quad (4.9)$$

The distributed forces $q_t(x, y)$ and $q_b(x, y)$ are interpolated using the same degree of interpolation as in displacement field components (Eqs. 4.3):

$$\begin{aligned} \{q_t\} &= \left\{ \sum_{j=1}^m q_{t,j} \psi_j(x, y) \right\} = \{\bar{\psi}\} \{Q^N\} \\ \{q_b\} &= \left\{ \sum_{j=1}^m q_{b,j} \psi_j(x, y) \right\} = \{\bar{\psi}\} \{Q^1\} \end{aligned} \quad (4.10)$$

where $\{Q_t\}$ and $\{Q_b\}$ are the vectors of external nodal loading at S_t and S_b , respectively, while $\{\bar{\psi}\}$ is the vector of Lagrangian interpolation functions:

$$\{Q^N\} = \begin{Bmatrix} Q_{x,1}^N \\ Q_{y,1}^N \\ Q_{z,1}^N \\ \vdots \end{Bmatrix}_{3m \times 1}, \quad \{Q^1\} = \begin{Bmatrix} Q_{x,1}^1 \\ Q_{y,1}^1 \\ Q_{z,1}^1 \\ \vdots \end{Bmatrix}_{3m \times 1}, \quad \{\bar{\psi}\} = \{\psi_1 \quad \psi_1 \quad \psi_1 \quad \dots\}_{1 \times 3m} \quad (4.11)$$

Finally, the discretized weak formulation is obtained by substituting the matrix form of the laminate constitutive equations from Eqs. (3.27), together with Eqs. (4.9) and Eqs. (4.10) into Eqs. (4.2):

$$\int_{\Omega^e} \left\{ \begin{aligned} &\sum_{I,J=1}^N \{\delta \Delta^I\}^T [B]^T [A_1^{IJ}] [B] \{\Delta^J\} + \\ &+ \sum_{I,J=1}^N \{\delta \Delta^I\}^T [\bar{B}]^T [A_2^{IJ}] [\bar{B}] \{\Delta^J\} - \\ &- \{\delta \Delta^1\}^T \{\bar{\psi}\}^T \{\bar{\psi}\} \{Q_b\} - \{\delta \Delta^N\}^T \{\bar{\psi}\}^T \{\bar{\psi}\} \{Q_t\} \end{aligned} \right\} d\Omega^e = 0 \quad (4.12)$$

Collecting the coefficients of each layer displacement vectors $\{\Delta^I\}$ from the previous equations, the matrix form of the finite element model is obtained:

$$\begin{bmatrix} [K^{11}] & [K^{12}] & \dots & [K^{1N}] \\ [K^{21}] & [K^{22}] & \dots & [K^{2N}] \\ \vdots & \vdots & \ddots & \\ [K^{2N}] & [K^{N2}] & \dots & [K^{NN}] \end{bmatrix}^e \begin{Bmatrix} \{\Delta^1\} \\ \{\Delta^2\} \\ \vdots \\ \{\Delta^N\} \end{Bmatrix}^e = \begin{Bmatrix} \{F^1\} \\ 0 \\ \vdots \\ \{F^N\} \end{Bmatrix}^e \quad (4.13)$$

or in abbreviated form:

$$[K]_{3mN \times 3mN}^e \{d\}_{3mN \times 1}^e = \{f\}_{3mN \times 1}^e \quad (4.14)$$

In Eq. (4.14), $[K]^e$ is layered element stiffness matrix, $\{d\}^e$ is the vector of generalized displacements and $\{f\}^e$ is the layered element force vector. In this study, linear (Q4) and quadratic serendipity (Q8) layered quadrilateral finite elements have been considered. To prevent shear locking, reduced integration is employed (2×2 points for Q8 and 1×1 point for Q4 element).

The element stiffness submatrices $[K^{IJ}]$ ($I, J = 1, \dots, N$) are derived as:

$$[K^{IJ}] = \int_{\Omega^e} \left([B]^T [A_1^{IJ}] [B] + [\bar{B}]^T [A_2^{IJ}] [\bar{B}] \right) d\Omega^e \quad (4.15)$$

while, the element force subvectors $\{F^1\}$ and $\{F^N\}$ are obtained as:

$$\begin{aligned} \{F^1\} &= \int_{\Omega^e} \left(\{\delta\Delta^1\}^T \{\bar{\psi}\}^T \{\bar{\psi}\} \{Q^1\} \right) d\Omega^e, \\ \{F^N\} &= \int_{\Omega^e} \left(\{\delta\Delta^1\}^T \{\bar{\psi}\}^T \{\bar{\psi}\} \{Q^N\} \right) d\Omega^e \end{aligned} \quad (4.16)$$

Once the characteristic element matrices have been derived, the assembly procedure is performed using the optimized algorithm explained in [115, 116]. The mathematical model at the structural level is ultimately derived as:

$$\mathbf{Kd} = \mathbf{f} \quad (4.17)$$

4.3 Relationship between FLWT-based finite element model and 3D finite element model

As the present FLWT-based FE model aims to offer the same modelling capability as a conventional 3D FE model of laminar composites, it is worth examining the resemblances and contrasts between these two models [117]. Firstly, let's compare the principles used to formulate each model. The conventional 3D FE model utilizes the elasticity theory, and Navier's equations represent the related governing equations of motion. On the other hand, the FLWT-based FE model is established by a set of $3N$ partial differential equations, which can be seen as a semi-discretized version of Navier's equations. Although the governing equations of motion of the current FLWT-based FE model are an approximation to the exact 3D equations of motion, the approximation can be made more accurate by enhancing the number of subdivisions throughout

the laminate thickness or elevating the order of interpolation throughout the thickness. While the governing equations of motion for these two theories differ, both FE models are fully discretized versions of their respective theories. As a result, the modelling capabilities of the two FE models are essentially equivalent.

Same as 3D finite elements, the layered finite elements (Figure 4.1) require only C^0 continuity of generalized displacements along element boundaries, because only translational displacement components in three orthogonal directions are adopted as the nodal degrees of freedom (DOFs). As can be seen from Figure 4.1, the number of DOFs is layer dependent and is equal to $3mN$, where m is the number of nodes per 2D element. Although the FLWT-based FE model is similar

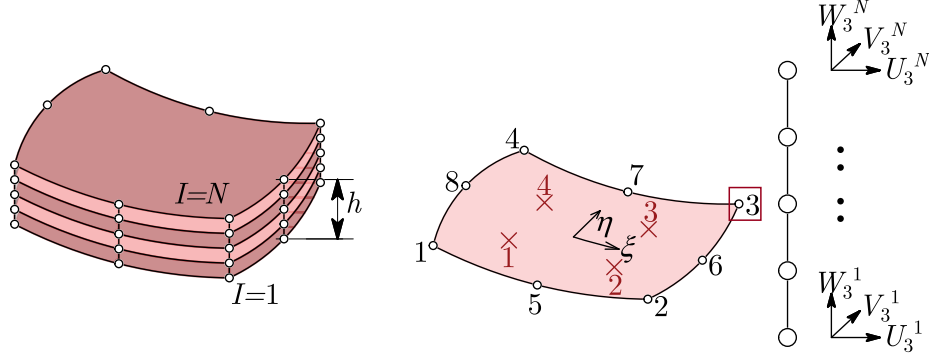


Figure 4.1: Quadratic serendipity Q8 layered finite element with corresponding Gauss quadrature points and nodal degrees of freedom

to a conventional 3D FE model in terms of interpolation capability and problem size, the FLWT formulation allows for the 2D data structure similar to the FE models of the ESL theories, due to independent in-plane and through the thickness discretization of the laminate. Thus, a numerous benefits can be obtained over conventional 3D models. These benefits include: (i) reduced volume of input data, (ii) the out-of-plane interpolation can be refined independently of the in-plane one, and (iii) increased computational savings during the construction of the element stiffness matrix, which increase with the number of elements and interfaces through the plate thickness.

4.4 Assignment of loads and boundary conditions

Considering the introduced translational DOFs, it is possible to specify the following sets of boundary conditions along the edges of the laminate:

1. Simply-supported edge parallel to X -axis: $U^I = W^I = 0$
2. Simply-supported edge parallel to Y -axis: $V^I = W^I = 0$
3. Clamped edge: $U^I = V^I = W^I = 0$

In addition, the displacements U^1, V^1, W^1, U^N, V^N or W^N could be constrained, simulating the supports along either the bottom (1) or top surface (N) of the laminate.

Due to symmetry in geometry, stacking sequence, loading and boundary conditions, only a half, quarter or eighth of laminate could be modelled to reduce the number of DOFs. Accordingly, the removed parts must be replaced with appropriate symmetry constraints:

1. Symmetry plane parallel to the XZ -plane: $V^I = 0$
2. Symmetry plane parallel to the YZ -plane: $U^I = 0$
3. Symmetry plane parallel to the XY -plane: $W^I = 0$

Considering the possible loading assignments, point forces $F_x^1, F_y^1, F_z^1, F_x^N, F_y^N$ or F_z^N or distributed loadings $q_x^1, q_y^1, q_z^1, q_x^N, q_y^N$ or q_z^N can be assigned on either the bottom (1) or top surface (N).

4.5 Post-Computation of interlaminar stresses

The assumed piece-wise linear interpolation of displacement field through the laminate thickness results in discontinuous stresses across the interface between adjacent layers. After obtaining the nodal displacements from Eq. (4.17), the stresses in each layer can be computed from 3D constitutive relations (Eq. (3.7)):

$$\begin{aligned}
 \begin{Bmatrix} \sigma_x \\ \sigma_y \\ \sigma_z \\ \tau_{xy} \end{Bmatrix}_b^k &= \begin{bmatrix} \bar{C}_{11} & \bar{C}_{12} & \bar{C}_{16} \\ \bar{C}_{21} & \bar{C}_{22} & \bar{C}_{26} \\ \bar{C}_{31} & \bar{C}_{32} & \bar{C}_{36} \\ \bar{C}_{61} & \bar{C}_{62} & \bar{C}_{66} \end{bmatrix}^{(k)} \sum_{j=1}^m \begin{bmatrix} \frac{\partial \psi_j}{\partial x} & 0 \\ 0 & \frac{\partial \psi_j}{\partial y} \\ \frac{\partial \psi_j}{\partial y} & \frac{\partial \psi_j}{\partial x} \end{bmatrix} \begin{Bmatrix} U_j^I \\ V_j^I \end{Bmatrix} + \\
 &+ \begin{Bmatrix} \bar{C}_{13} \\ \bar{C}_{23} \\ \bar{C}_{33} \\ \bar{C}_{36} \end{Bmatrix}^k \sum_{j=1}^m \psi_j (W_j^{I+1} - W_j^I) \frac{1}{h_k}
 \end{aligned} \tag{4.18}$$

$$\begin{aligned}
\begin{Bmatrix} \sigma_x \\ \sigma_y \\ \sigma_z \\ \tau_{xy} \end{Bmatrix}_t^k &= \begin{bmatrix} \bar{C}_{11} & \bar{C}_{12} & \bar{C}_{16} \\ \bar{C}_{21} & \bar{C}_{22} & \bar{C}_{26} \\ \bar{C}_{31} & \bar{C}_{32} & \bar{C}_{36} \\ \bar{C}_{61} & \bar{C}_{62} & \bar{C}_{66} \end{bmatrix}^{(k)} \sum_{j=1}^m \begin{bmatrix} \frac{\partial \psi_j}{\partial x} & 0 \\ 0 & \frac{\partial \psi_j}{\partial y} \\ \frac{\partial \psi_j}{\partial y} & \frac{\partial \psi_j}{\partial x} \end{bmatrix} \begin{Bmatrix} U_j^{I+1} \\ V_j^{I+1} \end{Bmatrix} + \\
&+ \begin{Bmatrix} \bar{C}_{13} \\ \bar{C}_{23} \\ \bar{C}_{33} \\ \bar{C}_{36} \end{Bmatrix}^k \sum_{j=1}^m \psi_j (W_j^{I+1} - W_j^I) \frac{1}{h_k}
\end{aligned} \tag{4.19}$$

$$\begin{aligned}
\begin{Bmatrix} \tau_{yz} \\ \tau_{xz} \end{Bmatrix}_b^k &= \begin{bmatrix} \bar{C}_{44} & \bar{C}_{45} \\ \bar{C}_{54} & \bar{C}_{55} \end{bmatrix}^{(k)} \sum_{j=1}^m \begin{Bmatrix} \frac{\partial \psi_j}{\partial x} \\ \frac{\partial \psi_j}{\partial y} \end{Bmatrix} W_j^I + \\
&+ \begin{bmatrix} \bar{C}_{44} & \bar{C}_{45} \\ \bar{C}_{54} & \bar{C}_{55} \end{bmatrix}^{(k)} \sum_{j=1}^m \begin{bmatrix} \psi_j & 0 \\ 0 & \psi_j \end{bmatrix} \left(\begin{Bmatrix} U_j^{I+1} \\ V_j^{I+1} \end{Bmatrix} - \begin{Bmatrix} U_j^I \\ V_j^I \end{Bmatrix} \right) \frac{1}{h_k}
\end{aligned} \tag{4.20}$$

$$\begin{aligned}
\begin{Bmatrix} \tau_{yz} \\ \tau_{xz} \end{Bmatrix}_t^k &= \begin{bmatrix} \bar{C}_{44} & \bar{C}_{45} \\ \bar{C}_{54} & \bar{C}_{55} \end{bmatrix}^{(k)} \sum_{j=1}^m \begin{Bmatrix} \frac{\partial \psi_j}{\partial x} \\ \frac{\partial \psi_j}{\partial y} \end{Bmatrix} W_j^{I+1} + \\
&+ \begin{bmatrix} \bar{C}_{44} & \bar{C}_{45} \\ \bar{C}_{54} & \bar{C}_{55} \end{bmatrix}^{(k)} \sum_{j=1}^m \begin{bmatrix} \psi_j & 0 \\ 0 & \psi_j \end{bmatrix} \left(\begin{Bmatrix} U_j^{I+1} \\ V_j^{I+1} \end{Bmatrix} - \begin{Bmatrix} U_j^I \\ V_j^I \end{Bmatrix} \right) \frac{1}{h_k}
\end{aligned} \tag{4.21}$$

As the interlaminar stresses (red color in Figure 4.2) computed in this way do not fulfill a continuous distribution throughout the thickness of the laminate, they are re-calculated (blue color in Figure 4.2) by assuming a quadratic distribution within each layer for each stress component ($s = xz, yz$ or z):

$$\left\{ \bar{\tau}^k \right\} = \begin{Bmatrix} \bar{\tau}_{xz}^k \\ \bar{\tau}_{yz}^k \\ \bar{\sigma}_z^k \end{Bmatrix} = a_s^k \bar{z}^2 + b_s^k \bar{z} + c_s^k, \quad k = 1, \dots, N, \quad 0 \leq \bar{z} \leq h_k \tag{4.22}$$

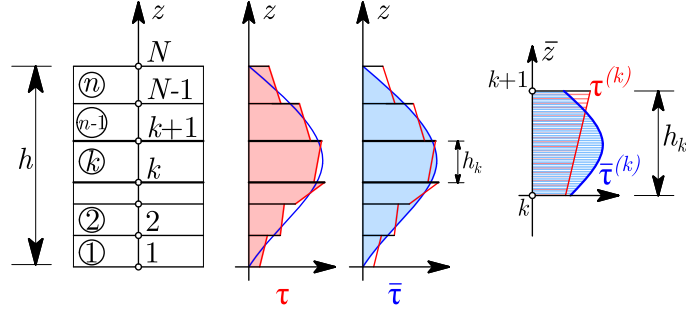


Figure 4.2: Distribution of interlaminar stresses through the laminate thickness : red color: from constitutive relations (Eqs. (4.18-4.21)); blue color: re-computed from (Eq. 4.22)[112]

For each of the interlaminar stresses, a total of $3N$ equations are needed, where N represents the number of interfaces, including S_b and S_t . The following conditions can be used to obtain these equations:

1. Satisfying the traction boundary conditions at S_b and S_t (2 equations)

$$\bar{\tau}^1(\bar{z} = 0) = q_b, \quad \bar{\tau}^N(\bar{z} = h_N) = q_t \quad (4.23)$$

2. Providing the continuity of interlaminar stresses along interfaces ($n - 1$ equations)

$$\bar{\tau}^{k-1}(\bar{z} = h_{k-1}) = \bar{\tau}^k(\bar{z} = 0) \quad (4.24)$$

3. Assuming the interlaminar stresses from the constitutive equations to be average interlaminar stresses within a considered layer (n equations)

$$\int_0^{h_k} \bar{\tau}^k(z) dz = \frac{\bar{\tau}_b^k + \bar{\tau}_t^k}{2} h_k \quad (4.25)$$

4. Computing the jump gap in interlaminar stresses at each interface utilizing the 3D equations of equilibrium in terms of stresses ($n - 1$ equations)

$$\frac{\partial \bar{\tau}^{k-1}(\bar{z} = h_{k-1})}{\partial \bar{z}} - \frac{\partial \bar{\tau}^k(\bar{z} = 0)}{\partial \bar{z}} = \frac{\partial \bar{\tau}_{3D}^{k-1}}{\partial z} - \frac{\partial \bar{\tau}_{3D}^k}{\partial z} \quad (4.26)$$

where

$$\{\tau_{3D}\} = \{\tau_{xz}^{3D} \quad \tau_{yz}^{3D} \quad \sigma_z^{3D}\}^T \quad (4.27)$$

is the vector of interlaminar stresses obtained from 3D equilibrium equations:

$$\begin{aligned} \frac{\partial \tau_{xz}^{3D}}{\partial z} &= - \left(\frac{\partial \sigma_x}{\partial x} + \frac{\partial \tau_{xy}}{\partial y} \right), \\ \frac{\partial \tau_{yz}^{3D}}{\partial z} &= - \left(\frac{\partial \tau_{xy}}{\partial x} + \frac{\partial \sigma_y}{\partial y} \right), \\ \frac{\partial \sigma_z^{3D}}{\partial z} &= - \left(\frac{\partial \tau_{xz}}{\partial x} + \frac{\partial \tau_{yz}}{\partial y} \right) \end{aligned} \quad (4.28)$$

The derivates of interlaminar stresses $\frac{\partial \tau_{xz}^{3D}}{\partial x}$, $\frac{\partial \tau_{yz}^{3D}}{\partial y}$ and $\frac{\partial \sigma_z^{3D}}{\partial z}$ are calculated as:

$$\begin{aligned} \left\{ \begin{array}{c} \frac{\partial \tau_{xz}^{3D}}{\partial z} \\ \frac{\partial \tau_{yz}^{3D}}{\partial z} \end{array} \right\}_b^k &= - \left[\begin{array}{ccc} \bar{C}_{11} & \bar{C}_{12} & \bar{C}_{16} \\ \bar{C}_{61} & \bar{C}_{62} & \bar{C}_{66} \end{array} \right]^{(k)} \sum_{j=1}^m \left[\begin{array}{cc} \frac{\partial^2 \psi_j}{\partial x^2} & 0 \\ 0 & \frac{\partial^2 \psi_j}{\partial x \partial y} \\ \frac{\partial^2 \psi_j}{\partial x \partial y} & \frac{\partial^2 \psi_j}{\partial x^2} \end{array} \right] \left\{ \begin{array}{c} U_j^I \\ V_j^I \end{array} \right\} - \\ &- \left\{ \begin{array}{c} \bar{C}_{13} \\ \bar{C}_{63} \end{array} \right\}^{(k)} \sum_{j=1}^m \frac{\partial \psi_j}{\partial x} (W_j^{I+1} - W_j^I) \frac{1}{h_k} - \left[\begin{array}{ccc} \bar{C}_{61} & \bar{C}_{62} & \bar{C}_{66} \\ \bar{C}_{21} & \bar{C}_{22} & \bar{C}_{26} \end{array} \right]^{(k)} \end{aligned} \quad (4.29)$$

$$\sum_{j=1}^m \left[\begin{array}{cc} \frac{\partial^2 \psi_j}{\partial x \partial y} & 0 \\ 0 & \frac{\partial^2 \psi_j}{\partial y^2} \\ \frac{\partial^2 \psi_j}{\partial y^2} & \frac{\partial^2 \psi_j}{\partial x \partial y} \end{array} \right] \left\{ \begin{array}{c} U_j^I \\ V_j^I \end{array} \right\} - \left\{ \begin{array}{c} \bar{C}_{63} \\ \bar{C}_{23} \end{array} \right\}^{(k)} \sum_{j=1}^m \frac{\partial \psi_j}{\partial y} (W_j^{I+1} - W_j^I) \frac{1}{h_k}$$

$$\begin{aligned} \left\{ \begin{array}{c} \frac{\partial \tau_{xz}^{3D}}{\partial z} \\ \frac{\partial \tau_{yz}^{3D}}{\partial z} \end{array} \right\}_b^t &= - \left[\begin{array}{ccc} \bar{C}_{11} & \bar{C}_{12} & \bar{C}_{16} \\ \bar{C}_{61} & \bar{C}_{62} & \bar{C}_{66} \end{array} \right]^{(k)} \sum_{j=1}^m \left[\begin{array}{cc} \frac{\partial^2 \psi_j}{\partial x^2} & 0 \\ 0 & \frac{\partial^2 \psi_j}{\partial x \partial y} \\ \frac{\partial^2 \psi_j}{\partial x \partial y} & \frac{\partial^2 \psi_j}{\partial x^2} \end{array} \right] \left\{ \begin{array}{c} U_j^{I+1} \\ V_j^{I+1} \end{array} \right\} - \\ &- \left\{ \begin{array}{c} \bar{C}_{13} \\ \bar{C}_{63} \end{array} \right\}^{(k)} \sum_{j=1}^m \frac{\partial \psi_j}{\partial x} (W_j^{I+1} - W_j^I) \frac{1}{h_k} - \end{aligned} \quad (4.30)$$

$$\begin{aligned} &- \left[\begin{array}{ccc} \bar{C}_{61} & \bar{C}_{62} & \bar{C}_{66} \\ \bar{C}_{21} & \bar{C}_{22} & \bar{C}_{26} \end{array} \right]^{(k)} \sum_{j=1}^m \left[\begin{array}{cc} \frac{\partial^2 \psi_j}{\partial x \partial y} & 0 \\ 0 & \frac{\partial^2 \psi_j}{\partial y^2} \\ \frac{\partial^2 \psi_j}{\partial y^2} & \frac{\partial^2 \psi_j}{\partial x \partial y} \end{array} \right] \left\{ \begin{array}{c} U_j^{I+1} \\ V_j^{I+1} \end{array} \right\} - \\ &- \left\{ \begin{array}{c} \bar{C}_{63} \\ \bar{C}_{23} \end{array} \right\}^{(k)} \sum_{j=1}^m \frac{\partial \psi_j}{\partial y} (W_j^{I+1} - W_j^I) \frac{1}{h_k} \end{aligned}$$

$$\begin{aligned}
\left\{ \frac{\partial \sigma_z^{3D}}{\partial z} \right\}_b^k &= - \left\{ \bar{C}_{55} \quad \bar{C}_{54} \quad \bar{C}_{44} \right\}^{(k)} \sum_{j=1}^m \begin{Bmatrix} \frac{\partial^2 \psi_j}{\partial x^2} \\ 2 \frac{\partial^2 \psi_j}{\partial x \partial y} \\ \frac{\partial^2 \psi_j}{\partial y^2} \end{Bmatrix} \left\{ W_j^I \right\} - \\
&- \left\{ \bar{C}_{55} \quad \bar{C}_{54} \quad \bar{C}_{44} \right\}^{(k)} \sum_{j=1}^m \begin{Bmatrix} \frac{\partial \psi_j}{\partial x} & 0 \\ \frac{\partial \psi_j}{\partial y} & \frac{\partial \psi_j}{\partial x} \\ 0 & \frac{\partial \psi_j}{\partial y} \end{Bmatrix} \left(\begin{Bmatrix} U_j^{I+1} \\ V_j^{I+1} \end{Bmatrix} - \begin{Bmatrix} U_j^I \\ V_j^I \end{Bmatrix} \right) \frac{1}{h_k}
\end{aligned} \tag{4.31}$$

$$\begin{aligned}
\left\{ \frac{\partial \sigma_z^{3D}}{\partial z} \right\}_t^k &= - \left\{ \bar{C}_{55} \quad \bar{C}_{54} \quad \bar{C}_{44} \right\}^{(k)} \sum_{j=1}^m \begin{Bmatrix} \frac{\partial^2 \psi_j}{\partial x^2} \\ 2 \frac{\partial^2 \psi_j}{\partial x \partial y} \\ \frac{\partial^2 \psi_j}{\partial y^2} \end{Bmatrix} \left\{ W_j^{I+1} \right\} - \\
&- \left\{ \bar{C}_{55} \quad \bar{C}_{54} \quad \bar{C}_{44} \right\}^{(k)} \sum_{j=1}^m \begin{Bmatrix} \frac{\partial \psi_j}{\partial x} & 0 \\ \frac{\partial \psi_j}{\partial y} & \frac{\partial \psi_j}{\partial x} \\ 0 & \frac{\partial \psi_j}{\partial y} \end{Bmatrix} \left(\begin{Bmatrix} U_j^{I+1} \\ V_j^{I+1} \end{Bmatrix} - \begin{Bmatrix} U_j^I \\ V_j^I \end{Bmatrix} \right) \frac{1}{h_k}
\end{aligned} \tag{4.32}$$

where $\frac{\partial^2 \psi_j}{\partial x^2}$, $\frac{\partial^2 \psi_j}{\partial y^2}$ and $\frac{\partial^2 \psi_j}{\partial x \partial y}$ denotes the second derivative of ψ_j with respect to x , y and xy , respectively.

5 Failure criteria and failure modes in laminar composites

5.1 Introduction

Although the global-level static elastic response of an undamaged laminate can be predicted directly, from laminate constitutive equations, comprehending the inelastic material behaviour resulting from damage is crucial for the secure and efficient use of laminar composites in the construction sector. Under service conditions, laminar composites can develop various failure intralaminar mechanisms [4], such as fiber breakage and pull-out, matrix yielding and cracking, and fiber-matrix debonding (Figure 5.1). These mechanisms cause a permanent loss of integrity within the laminate, and ultimately results in reduced stiffness and strength of the composite material. Consequently, the load-carrying capacity and service life of the structure are reduced. To ascertain the load carrying capacity and service life of a laminar composites, it is essential to predict the initiation and progression of failure.

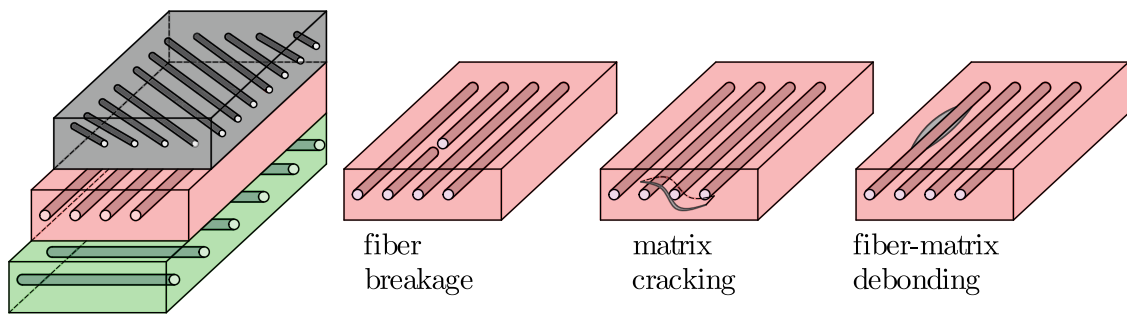


Figure 5.1: Typical intralaminar failure modes in laminar composites

The main challenge in mathematical modelling of damage arises from the presence of different geometric scales during failure initiation and progression. At a microscopic level, the failure of laminar composites is attributed to molecular-level damage. According to [118], damage refers to a group of permanent microstructural alterations that result from a set of irreversible physical or chemical processes caused by thermo-mechanical loads. The behaviour of laminar composites at the macro-level can be inferred by examining their behaviour at the micro-level, as stated in [119]. However, in practical scenarios, the macroscopic behaviour is often determined solely by analysing load-displacement data from test specimens, without getting insight the microscopic level details.

Initially, a failure typically begins at a micro-level and gradually progresses into a macro defect or failure mode. Nonetheless, when the aim is to predict the failure behaviour of a laminate, it becomes excessively challenging to concentrate on the occurrences happening at the micro-level. As a result, in analysing the failure of laminar composites, the focus is directed towards failures at the lamina-level.

Failure initiation occurs when stresses in the weakest lamina overstep the allowable fiber or matrix strength. To effectively identify the onset of damage in laminar composites within particular failure modes, it is necessary to establish an appropriate failure criterion. Lamina failure criteria consist of equations with parameters that are tailored to match experimental data on the failure of single-lamina composites [1]. These criteria are then utilized in design situations where experimental data is not available, including the design of laminar composites. The use of lamina failure criteria in PFA of laminar composites is restricted to prediction of First-Ply Failure (FPF). After the initiation of damage, these criteria become inadequate in providing useful information for predicting the evolution of damage, redistribution of stress to other laminae, and the ultimate failure load. The lamina failure criteria for composite materials rely on the tensile, compressive, and shear strengths of unidirectional lamina, and they are typically grouped into two categories: *non-interactive* and *interactive*.

5.2 Non-interactive failure criteria

Non-interactive failure criteria, such as maximum Stress and maximum Strain failure criteria, do not take into account interactions between stress or strain components. Instead, they compare these components separately to their respective material strength values. These criteria have rectangular failure surfaces in both stress and strain spaces (Figure 5.2), and they are suitable for uniaxial stress state.

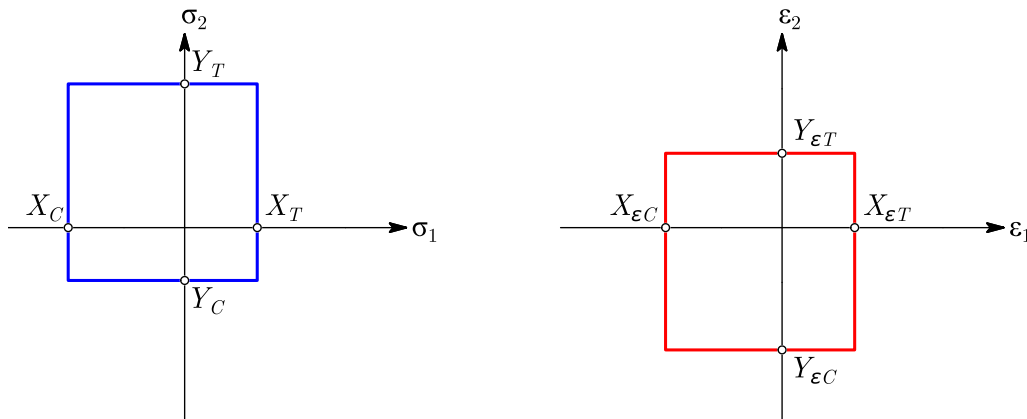


Figure 5.2: Failure surface for max stress failure criterion (left) and max strain failure criterion (right)

5.2.1 Maximum stress failure criterion

In this criterion, failure of a lamina is assumed to occur when at least one of the stresses in material (1, 2, 3) coordinates exceeds the corresponding strength value:

$$\begin{aligned} \sigma_1 > X_T, \quad \sigma_2 > Y_T, \quad \sigma_3 > Z_T, \\ |\tau_{23}| > R, \quad |\tau_{13}| > S, \quad |\tau_{12}| > T \end{aligned} \quad (5.1)$$

In Eq. (5.1), X_T , Y_T and Z_T are the normal tensile strengths of the lamina in the 1, 2 and 3 directions, respectively, while R , S and T represent shear strengths in the 23 , 13 and 12 material planes, respectively. When normal stresses ($\sigma_1, \sigma_2, \sigma_3$) are of compressive nature, then their absolute value should be compared with the normal compressive strengths of the lamina, X_C , Y_C , and Z_C , respectively.

The maximum Stress Criterion has the benefit of providing insight into the failure mode. However, it tends to overpredict the strength of the structure, when dealing with stress states that aren't primarily influenced by a single stress component [120].

5.2.2 Maximum strain failure criterion

The maximum strain criterion predicts initiation of failure when the maximum strain in a material coordinates reaches a critical value. This criterion assumes that failure initiation occurs when any of the following conditions are satisfied:

$$\begin{aligned} \varepsilon_1 > X_{\varepsilon T}, \quad \varepsilon_2 > Y_{\varepsilon T}, \quad \varepsilon_3 > Z_{\varepsilon T}, \\ |\gamma_{23}| > R_{\varepsilon}, \quad |\gamma_{13}| > S_{\varepsilon}, \quad |\gamma_{12}| > T_{\varepsilon} \end{aligned} \quad (5.2)$$

where $X_{\varepsilon T}$, $Y_{\varepsilon T}$ and $Z_{\varepsilon T}$ are the normal tensile strain strengths of the lamina in the 1, 2 and 3 directions, respectively, while R_{ε} , S_{ε} and T_{ε} represent shear strain strengths in the 23 , 13 and 12 planes, respectively. In case of negative normal strains ($\varepsilon_1, \varepsilon_2, \varepsilon_3$), their absolute value should be compared with the normal compressive strain strengths of the lamina, $X_{\varepsilon C}$, $Y_{\varepsilon C}$, and $Z_{\varepsilon C}$, respectively.

The maximum strain criterion is commonly used in the design of ductile materials, such as metals, which typically fail due to excessive plastic deformation. However, this criterion may not be suitable for quasi-brittle materials, such as laminar composites, which tend to fail due to the formation and propagation of cracks [1].

5.3 Interactive failure criteria

The failure criteria in Section 5.2 consider each mode of failure independently from the others. This means that a multiaxial state of stress is viewed as a set of independent, uniaxial states of stress. If any of these uniaxial states of stress surpass their corresponding strength values, the material is considered to have failed, regardless of the fact that the material is being subjected to combined stresses. This approach may result in designs that overestimate or even underestimate

the failure like in case when multiple modes of failure interact to cause failure at a stress state that is lower, or higher, than what would be predicted by each failure mode acting independently.

Interactive failure criteria, in contrast to non-interactive failure criteria, take into account the interactions between stress and strain components. The Tsai-Hill, Hoffman, and Tsai-Wu criteria, which are quadratic polynomial criteria, belong to this category. These criteria utilize a polynomial function based on the material strengths to describe an ellipsoidal-shaped failure surface (Figure 5.3).

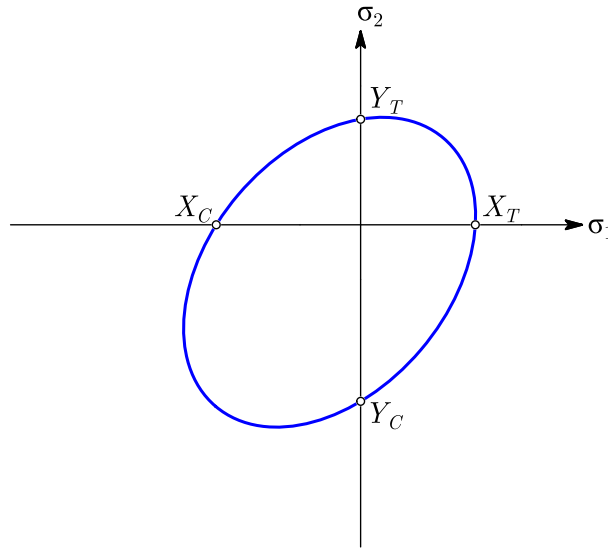


Figure 5.3: Failure surface for quadratic polynomial failure criteria

5.3.1 Tsai-Hill failure criterion

Tsai et al.'s research in 1966 was a pioneering effort to develop failure criteria for composite materials [121]. They based their approach on Hill's theory from 1948 [22], which was originally formulated to describe the yielding and plastic deformation of anisotropic metals. Hill observed that when metals undergo processes such as rolling, drawing, and extrusion, they develop a preferred orientation due to the alignment of crystalline planes. To generalize Hill's theory for orthotropic materials, a mathematical extension of the Von Mises yield criterion, originally developed for isotropic metals, was proposed. This extension was based on two assumptions: first, the absence of the Bauschinger effect, implying that the yield stress remains constant in both tension and compression, and second, the independence of the plastic potential from the superposition of hydrostatic pressure. Therefore, the following form of Tsai-Hill criterion was obtained:

$$\phi = F(\sigma_2 - \sigma_3)^2 + G(\sigma_3 - \sigma_1)^2 + H(\sigma_1 - \sigma_2)^2 + 2(L\tau_{23}^2 + M\tau_{31}^2 + N\tau_{12}^2) = 1 \quad (5.3)$$

where ϕ is maximum failure index, F , G and H are material constants obtained through uniaxial tests imposed along the material directions 1, 2 and 3 of the single lamina (Figure 5.4):

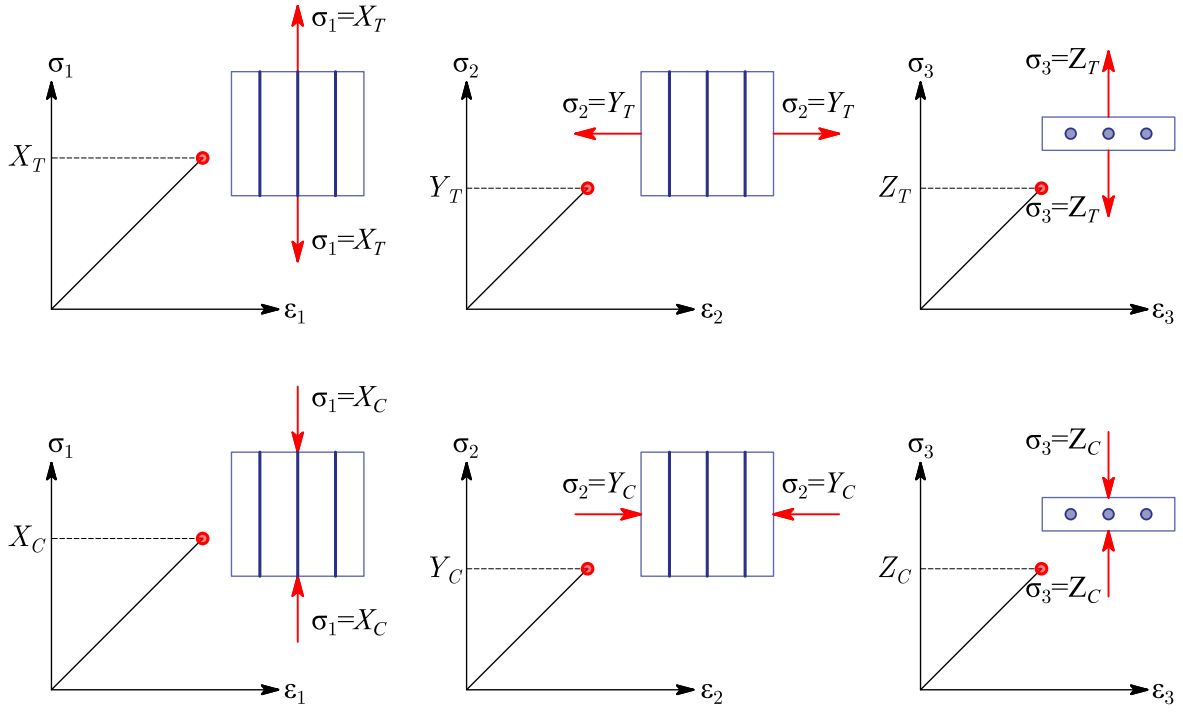
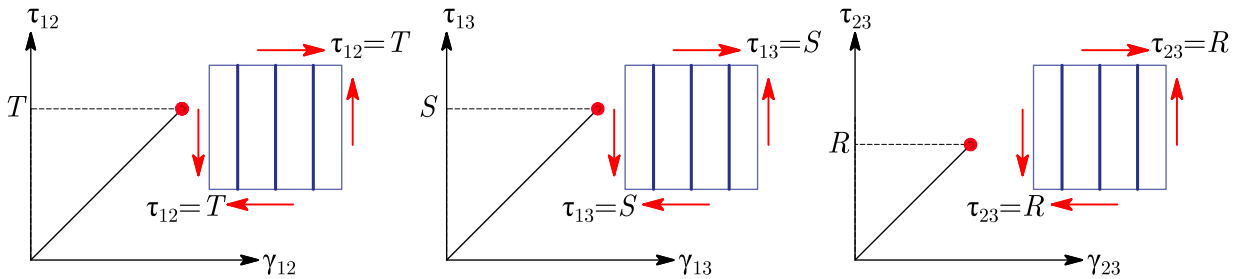


Figure 5.4: Uniaxial tests imposed along the material directions 1, 2 and 3 of the single lamina

$$\begin{aligned}
 F &= \frac{1}{2} \left(\frac{1}{Y^2} + \frac{1}{Z^2} - \frac{1}{X^2} \right), \\
 G &= \frac{1}{2} \left(\frac{1}{Z^2} + \frac{1}{X^2} - \frac{1}{Y^2} \right), \\
 H &= \frac{1}{2} \left(\frac{1}{X^2} + \frac{1}{Y^2} - \frac{1}{Z^2} \right)
 \end{aligned} \tag{5.4}$$

The material constants L , M and N from Eq. (5.3) are obtained from pure shear tests in the three orthogonal symmetry planes 23 , 13 and 12 respectively (see Figure 5.5):

Figure 5.5: Pure shear tests in the three orthogonal symmetry planes 12 , 13 and 23

$$L = \frac{1}{2} \frac{1}{R^2}, \quad M = \frac{1}{2} \frac{1}{S^2}, \quad N = \frac{1}{2} \frac{1}{T^2} \tag{5.5}$$

Replacing the material constants from Eq. (5.4) and Eq. (5.5) into the Eq. (5.3), the final form of Tsai-Hill failure criterion is obtained as:

$$\begin{aligned} \phi = & \left(\frac{\sigma_1}{X}\right)^2 + \left(\frac{\sigma_2}{Y}\right)^2 + \left(\frac{\sigma_3}{Z}\right)^2 + \left(\frac{\tau_{23}}{R}\right)^2 + \left(\frac{\tau_{13}}{S}\right)^2 + \left(\frac{\tau_{12}}{T}\right)^2 - \\ & - \left(\frac{1}{X^2} + \frac{1}{Y^2} - \frac{1}{Z^2}\right)\sigma_1\sigma_2 - \left(\frac{1}{X^2} + \frac{1}{Z^2} - \frac{1}{Y^2}\right)\sigma_1\sigma_3 - \left(\frac{1}{Y^2} + \frac{1}{Z^2} - \frac{1}{X^2}\right)\sigma_2\sigma_3 = 1 \end{aligned} \quad (5.6)$$

Note that the values of X , Y , Z in Tsai-Hill criterion Eq. (5.6) are taken as either X_T , Y_T , Z_T , or as X_C , Y_C , Z_C , depending upon the sign of σ_1 , σ_2 and σ_3 , respectively. The condition for failure, as defined by Eq. (5.6), is such that failure will occur when the linear elastic response in any combination of stress components reaches the limit condition specified by that equation.

Due to its derivation from the von Mises criterion, the Tsai-Hill criterion assumes fixed interactions between stresses in Eq. (5.6). As a result, this criterion is applicable to orthotropic metal sheets with rotational symmetry about one of the symmetry axes. Attempting to extend its use to predict failure behaviour in unidirectional composite, such as lamina, raises significant concerns about the validity of the model, as different failure mechanisms can occur under various stress states [122].

5.3.2 Hoffman failure criterion

The Hoffman failure criterion for unidirectional composites was introduced in 1967 [29]. It assumed that all failure modes in composites were brittle fracture, although no physical evidence supported this. This assumption meant that the linear elastic response for each stress component ended abruptly at a limiting value (failure strength) for that component. The fracture strength in combined stresses was represented by a "yield condition," despite the assumption of brittle fracture. Tsai et al. [121] did not explicitly state these assumptions, but they essentially implied them by renaming yield stresses in Hill's [22] criterion as composite strength values. The Hoffman and Tsai-Hill criteria are both used to assess the strength of composite materials, but they differ in their approach to assigning strengths for tension and compression in different directions. The Tsai-Hill criterion assumes that the material has isotropic properties, and assigns the same strength in tension and compression in all directions. On the other hand, the Hoffman criterion assigns different strengths for tension and compression along and normal to the fibers, respectively, in each principal composite direction. This inclusion of the Bauschinger effect, which Hill ignored, led Hoffman to add three linear terms to Eq. (5.3), increasing the number of material constants from six to nine in Hill's version:

$$\begin{aligned} \phi = & A\sigma_1 + B\sigma_2 + D\sigma_3 + F(\sigma_2 - \sigma_3)^2 + G(\sigma_3 - \sigma_1)^2 + H(\sigma_1 - \sigma_2)^2 + \\ & + 2(L\tau_{23}^2 + M\tau_{31}^2 + N\tau_{12}^2) = 1 \end{aligned} \quad (5.7)$$

The material constants L , M and N are the same as in Tsai-Hill criterion (Eq. (5.5)), while the remaining material constants are defined as:

$$\begin{aligned} A &= \frac{1}{X_T} - \frac{1}{X_C}, \quad B = \frac{1}{Y_T} - \frac{1}{Y_C}, \quad D = \frac{1}{Z_T} - \frac{1}{Z_C}, \\ F &= \frac{1}{2} \left(\frac{1}{Y_T Y_C} + \frac{1}{Z_T Z_C} - \frac{1}{X_T X_C} \right), \quad G = \frac{1}{2} \left(\frac{1}{Z_T Z_C} + \frac{1}{X_T X_C} - \frac{1}{Y_T Y_C} \right), \\ H &= \frac{1}{2} \left(\frac{1}{X_T X_C} + \frac{1}{Y_T Y_C} - \frac{1}{Z_T Z_C} \right) \end{aligned} \quad (5.8)$$

Finally, the Hoffman failure criterion is given as:

$$\begin{aligned} \phi &= \left(\frac{1}{X_T} - \frac{1}{X_C} \right) \sigma_1 + \left(\frac{1}{Y_T} - \frac{1}{Y_C} \right) \sigma_2 + \left(\frac{1}{Z_T} - \frac{1}{Z_C} \right) \sigma_3 + \frac{\sigma_1^2}{X_T X_C} + \frac{\sigma_2^2}{Y_T Y_C} + \frac{\sigma_3^2}{Z_T Z_C} - \\ &- \left(\frac{1}{X_T X_C} + \frac{1}{Y_T Y_C} - \frac{1}{Z_T Z_C} \right) \sigma_1 \sigma_2 - \left(\frac{1}{X_T X_C} + \frac{1}{Z_T Z_C} - \frac{1}{Y_T Y_C} \right) \sigma_1 \sigma_3 - \\ &- \left(\frac{1}{Y_T Y_C} + \frac{1}{Z_T Z_C} - \frac{1}{X_T X_C} \right) \sigma_2 \sigma_3 + \left(\frac{\tau_{23}}{R} \right)^2 + \left(\frac{\tau_{13}}{S} \right)^2 + \left(\frac{\tau_{12}}{T} \right)^2 = 1 \end{aligned} \quad (5.9)$$

This criterion resulted in an ellipsoid graphical representation of failure surface, where the center is offset from the origin of material axes 1, 2, and 3.

5.3.3 Tsai-Wu failure criterion

Several future efforts focused on the ellipsoidal representation of the failure surface, with notable work being done by Tsai and Wu [20] in 1971. They assumed that the maximum failure index, $f(\phi)$, was associated with the failure surface and was dependent on the strength tensor components:

$$\phi = F_i \sigma_i + F_{ij} \sigma_i \sigma_j = 1 \quad (5.10)$$

where F_i and F_{ij} are second order and fourth order strength tensors, respectively. The established patterns of anisotropic materials' diffusion and elastic properties are reflected in the symmetry properties of the strength tensors [123]. Previous equation can be expressed in expanded form as:

$$\begin{aligned} \phi &= F_1 \sigma_1 + F_2 \sigma_2 + F_3 \sigma_3 + F_4 \tau_{23} + F_5 \tau_{13} + F_6 \tau_{12} + \\ &+ F_{11} \sigma_1^2 + 2F_{12} \sigma_1 \sigma_2 + 2F_{13} \sigma_1 \sigma_3 + 2F_{14} \sigma_1 \tau_{23} + 2F_{15} \sigma_1 \tau_{13} + 2F_{16} \sigma_1 \tau_{12} + \\ &+ F_{22} \sigma_2^2 + 2F_{23} \sigma_2 \sigma_3 + 2F_{24} \sigma_2 \tau_{23} + 2F_{25} \sigma_2 \tau_{13} + 2F_{26} \sigma_2 \tau_{12} + \\ &+ F_{33} \sigma_3^2 + 2F_{34} \sigma_3 \tau_{23} + 2F_{35} \sigma_3 \tau_{13} + 2F_{36} \sigma_3 \tau_{12} + \\ &+ F_{44} \tau_{23}^2 + 2F_{45} \tau_{23} \tau_{13} + 2F_{46} \tau_{23} \tau_{12} + \\ &+ F_{55} \tau_{13}^2 + 2F_{56} \tau_{13} \tau_{12} + \\ &+ F_{66} \tau_{12}^2 = 1 \end{aligned} \quad (5.11)$$

The values of strength tensor components F_4 , F_5 , and F_6 , which are linked to τ_{23} , τ_{13} , and τ_{12} , are assumed to be zero because the shear strengths remain unchanged under both positive and negative shear stress. Additionally, it is assumed that there is no interaction between normal and shear stresses, leading to the values of F_{14} , F_{26}, \dots, F_{36} equal to zero. Using a similar approach, it is presumed that all shear stresses are uncoupled [20], meaning that F_{45} , F_{46} , and F_{56} are all equal to zero. However, the coupling between normal stresses is anticipated to persist. By assuming these symmetry relations, the number of independent components is reduced to 3 and 9, respectively. Therefore, Eq. (5.11) can be rewritten as:

$$\begin{aligned} \phi = & F_1\sigma_1 + F_2\sigma_2 + F_3\sigma_3 + F_{11}\sigma_1^2 + F_{22}\sigma_2^2 + F_{33}\sigma_3^2 + \\ & + 2F_{12}\sigma_1\sigma_2 + 2F_{13}\sigma_1\sigma_3 + 2F_{23}\sigma_2\sigma_3 + F_{44}\tau_{23}^2 + F_{55}\tau_{13}^2 + F_{66}\tau_{12}^2 = 1 \end{aligned} \quad (5.12)$$

According to Tsai and Wu [20], the values of nine out of the twelve constants in Eq. (3.12) are derived from uniaxial and pure shear tests, and can be described in relation to the material strengths through the following relationships:

$$\begin{aligned} F_1 &= \frac{1}{X_T} - \frac{1}{X_C}, & F_2 &= \frac{1}{Y_T} - \frac{1}{Y_C}, & F_3 &= \frac{1}{Z_T} - \frac{1}{Z_C}, \\ F_{11} &= \frac{1}{X_T X_C}, & F_{22} &= \frac{1}{Y_T Y_C}, & F_{33} &= \frac{1}{Z_T Z_C}, \\ F_{44} &= \frac{1}{R^2}, & F_{55} &= \frac{1}{S^2}, & F_{66} &= \frac{1}{T^2} \end{aligned} \quad (5.13)$$

The strength tensor constants F_{12} , F_{13} and F_{23} cannot be uniquely determined. For the Eq. (5.12) to represent an ellipsoid in the stress space, the magnitude of these constants must satisfy a certain inequalities:

$$\begin{aligned} F_{11}F_{22} - F_{12} &> 0 \\ F_{11}F_{33} - F_{13} &> 0 \\ F_{22}F_{33} - F_{23} &> 0 \end{aligned} \quad (5.14)$$

Finally, Tsai and Wu [20] proposed that the constants F_{12} , F_{13} , and F_{23} , related to the interaction of two stress components, can be obtained by corresponding biaxial tests:

$$\begin{aligned} F_{12} &= -\frac{1}{2} \frac{1}{\sqrt{X_T X_C Y_T Y_C}}, \\ F_{13} &= -\frac{1}{2} \frac{1}{\sqrt{X_T X_C Z_T Z_C}}, \\ F_{23} &= -\frac{1}{2} \frac{1}{\sqrt{Y_T Y_C Z_T Z_C}} \end{aligned} \quad (5.15)$$

Eq. (5.12) is observed to be unchanged under coordinate transformation and has the ability to model varying strengths in tension and compression, making it a more adaptable tool for curve fitting in the unidirectional composite strength field than Tsai-Hill's failure criterion (Eq. (5.6)), as well as Hoffman's modification, which includes the Bauschinger effect (Eq. (5.9)). However, it is important to note that the ellipsoidal depiction of unidirectional composite strength in the stress components is purely speculative and lacks any physical basis in terms of failure mechanisms.

5.3.4 Hashin failure criterion

In 1980, Hashin [24] analysed the ability of the Tsai-Wu criterion [20] to accurately predict failure in unidirectional composites. He discovered that the criterion's representation of failure in stress space using a single ellipsoidal surface, as shown in Eq. (5.12), was not always appropriate due to certain limitations. One of the main challenges he identified was the off-diagonal strength tensor constants F_{12} , F_{13} and F_{23} in Eq. (5.12), which can produce unacceptable values when determined through biaxial tests. Specifically, these values derived from biaxial tension tests depend on compressive strengths in the fiber and transverse directions, which is not a physically reasonable assumption. In fact, the values assigned to constants F_{12} , F_{13} and F_{23} through Eq. (5.15) are solely determined by the requirement for the ellipsoidal surface to be closed. These values are not based on any observed or anticipated physical properties of unidirectional composites in stress space.

Instead of requiring a single continuous smooth surface to represent the strength of unidirectional composite, Hashin [24] proposed the use of piecewise smooth surfaces, with each branch representing a distinct failure mode. This approach ensures that stress components only interact with relevant failure modes, avoiding the issues associated with off-diagonal constants in the Tsai-Wu criterion. Hashin further suggested separating the fiber failure modes from the matrix failure modes. For each failure mode, he argued that the governing stress interactions should be expressed using quadratic polynomials, as linear terms would typically be insufficient and more than quadratic terms would make the resulting failure criteria impractical. He formulated the quadratic failure criteria using stress invariants for transversely isotropic symmetry and argued that unidirectional composites typically have randomly distributed fibers in the cross-section.

Hashin [24] contended that if a failure surface can be pinpointed, then the failure is caused by the normal and shear stresses acting upon that surface. In the case of fiber tension (f_t) failure mode, the failure surface proceeds in a direction perpendicular to the fiber, as illustrated in Figure 5.6a.

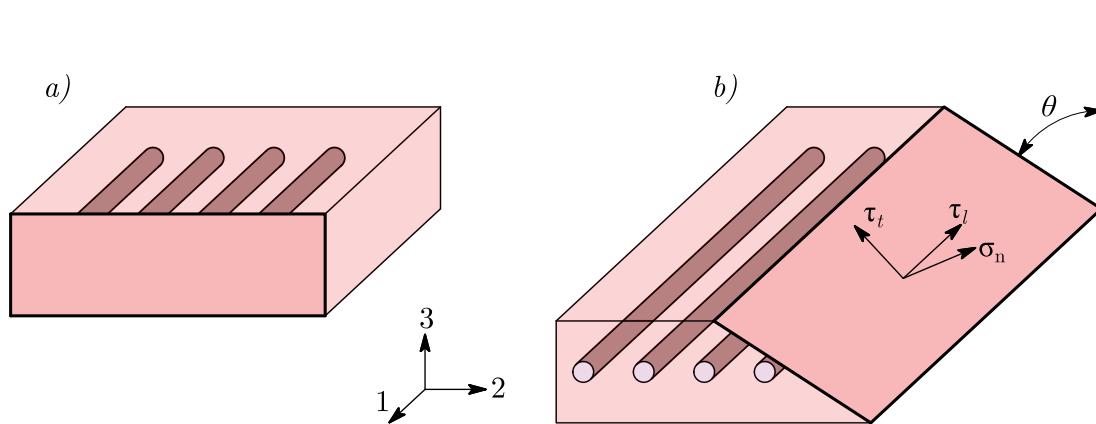


Figure 5.6: Typical failure surface of unidirectional lamina for: (a) fiber failure mode; (b) matrix failure mode

As a result, the stresses responsible for this mode of failure are σ_1 , τ_{12} and τ_{13} , and the Hashin criterion for (f_t) failure mode takes the following quadratic form:

Fiber tension failure:

$$f_{f_t} = \left(\frac{\sigma_1}{X_T} \right)^2 + \left(\frac{\tau_{12}}{T} \right)^2 + \left(\frac{\tau_{13}}{S} \right)^2 = 1, \quad \sigma_1 > 0 \quad (5.16)$$

The criterion for fiber compression (f_c) failure mode is expressed in a basic maximum stress form, due to insufficient knowledge of the impact of shear stress on this mode of failure [124].

Fiber compression failure:

$$f_{f_c} = \left(-\frac{\sigma_1}{X_C} \right)^2 = 1, \quad \sigma_1 < 0 \quad (5.17)$$

For matrix failure modes, Hashin proposed the existence of a failure surface between fibers that goes through the matrix (Figure 5.6b), where the inclination angle (θ) of the surface with the thickness material (3) direction is determined by the critical normal (σ_n) and shear (τ_t , τ_l) traction components, acting on it [122]. The normal σ_n and shear τ_t component are expressed in terms of the stresses σ_2 , σ_3 and τ_{23} , while the shear τ_l component is expressed in terms of σ_{12} and σ_{13} . These expressions are given in detail in [24]. The concept of failure on a surface is not new, as it was proposed for soil failure by Mohr in 1905 [125] and earlier by Coulomb in 1776 [122].

As mention before, failure modes of the matrix differ between matrix tension and matrix compression. In cases of matrix tension, the failure is caused by a combination of in-plane shear and matrix opening, resulting in a failure surface that is typically perpendicular to the direction of transverse tension. Conversely, matrix compression specimens usually fail due to out-of-plane shear, with the failure surface parallel to the fiber direction at an inclination angle of $\theta = 45^\circ$, indicating failure occurring in the plane of maximum shear stress [24]. However, experimental evidence shows that for most technical composite materials, the angle is generally $\theta = 53 \pm 2^\circ$ [64]. This can be attributed to the presence of a compressive stress acting on the potential failure surfaces, along with an associated friction stress [68]. Finally, the Hashin failure criterion for the matrix tension (m_t) and compression (m_c) failure mode is given in the following form:

Matrix tension failure:

$$f_{m_t} = \left(\frac{\sigma_2 + \sigma_3}{Y_T} \right)^2 + \left(\frac{\tau_{23}^2 + \sigma_2\sigma_3}{Y_T} \right) + \left(\frac{\tau_{12}}{T} \right)^2 + \left(\frac{\tau_{13}}{S} \right)^2 = 1, \quad \sigma_2 + \sigma_3 > 0 \quad (5.18)$$

Matrix compression failure:

$$\begin{aligned} f_{m_c} = & \frac{1}{Y_C} \left(\frac{Y_C}{2R} - 1 \right) (\sigma_2 + \sigma_3) + \frac{1}{4R^2} (\sigma_2 + \sigma_3)^2 + \\ & + \frac{1}{R^2} (\tau_{23}^2 - \sigma_2\sigma_3) + \left(\frac{\tau_{12}}{T} \right)^2 + \left(\frac{\tau_{13}}{S} \right)^2 = 1, \quad \sigma_2 + \sigma_3 < 0 \end{aligned} \quad (5.19)$$

Finally, the maximum failure index, ϕ , is obtained as the maximum value of each failure mode index: f_{f_t} , f_{f_c} , f_{m_t} and f_{m_c} .

5.4 Procedure for the first-ply failure of laminate

The load at which the failure criterion is met within the weakest lamina of a laminate is known as the First-ply failure (FPF) load. In FRP laminar composites, the transverse and shear strengths are typically lower than the longitudinal strength, so FPF is often caused by matrix failure modes, such as matrix cracking.

To calculate the FPF load, the stress problem is solved for an initial load. The stress distribution is piece-wise linear through the thickness of the laminate, as shown in Figure 4.2, and the maximum value of stress component is found on the top or bottom of each layer. The lamina stresses in the material coordinate system (123) are then used in a chosen failure criterion to calculate the maximum failure index ϕ . To determine whether the laminate has failed, the absolute value of $(\phi - 1)$ is compared against δ , a predetermined value of maximum tolerable error (1% in most studies [126]). If the absolute value is less than δ , the first ply within the laminate has failed. If not, the initial load is increased or decreased by a predetermined percentage and the procedure is repeated until failure occurs. A flow chart of described procedure is illustrated in Figure 5.7.

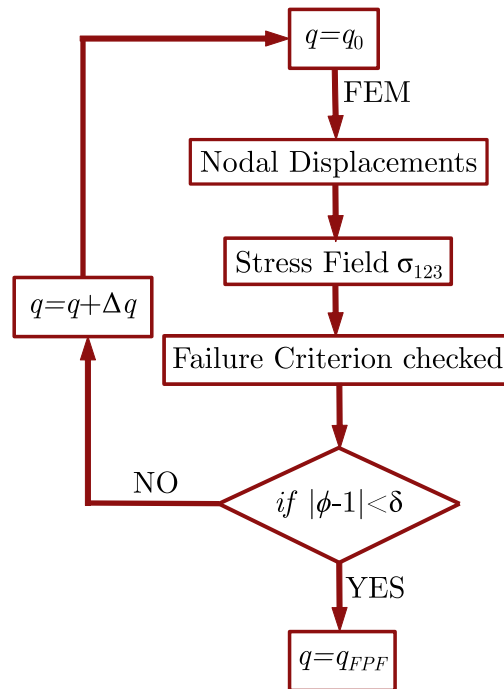


Figure 5.7: Flow chart of procedure for First-ply failure load determination of laminate

In layerwise theory, stress state is determined at all layer interfaces, in Gauss points associated with the selected finite element. Then, to find the maximum failure index ϕ , each element's failure index is calculated at every Gauss point at the top and bottom interfaces of each layer, and the maximum value is recorded along with the element number, Gaussian point number, layer number, and interface location. This process is repeated until all layered finite elements have been searched for the maximum failure index.

In contrast to the unidirectional lamina, the laminae in a laminate are bound by neighbouring laminae, preventing cracks from easily spreading and inhibiting the development of multiple cracks that could result in significant loss of stiffness and strength. This constraining effect

slows the propagation of inherent micro-defects and delays the appearance of a fully developed initial crack.

Hence, the stress level at which an unconstrained unidirectional lamina fails is lower compared to the same lamina embedded in a laminate. Furthermore, while failure initiation coincides with the ultimate failure of a unidirectional lamina, this is not the case for a laminate made up of multiple layers. Consequently, the next chapter will focus on discussing the progressive failure analysis (PFA) of a laminate.

6 Smearred crack-band damage model

6.1 Introduction

After the failure has been detected in the weakest lamina of the laminar composite, the properties of that lamina must be reduced and its stress redistributed to the remaining laminae. Progressive failure analysis (PFA) is performed to describe the post-failure behaviour in composite materials, through the material stiffness degradation. To estimate the strength of a laminate, it is necessary to monitor the degradation of most, if not all, laminae until the laminate can no longer sustain the applied load. However, the lamina failure criteria explained in the previous chapter do not account for the gradual process of damage accumulation, stiffness reduction, and stress redistribution. Therefore, it is essential to incorporate damage models to accurately predict these phenomena. Generally, such models can be categorized into two groups [7]: discrete damage models (DDM) and continuum damage models (CDM).

The explicit representation of cracks within the structure in DDM results in physically realistic description of damage mechanisms and their interactions. Nonetheless, this approach comes with the drawback of considerably increased computational expenses and numerical complexity. In contrary, in CDM approaches, intralaminar cracks are smeared out across the finite element domain and failure mechanisms are represented through material stiffness degradation using methods such as: instantaneous softening method (ISM) or gradual softening method (GSM) [8]. In ISM, the material property associated with the failure mode degrades immediately to zero (or a small value) of the undamaged material properties (blue color in Figure 6.1). It is commonly observed that the strength of laminates is often underestimated by the ISM because it fails to consider that damage is localized and a failed lamina still has some capacity to carry loads [127]. Instead of the instantaneous softening, fiber-reinforced composite materials typically exhibit a quasi-brittle post-failure behaviour, resulting in a dissipation of high fracture energy and a gradual progression of damage [66]. Therefore the gradual softening method (GSM) is recommended, in which the material property associated with the failure mode degrades gradually (i.e., linearly or exponentially) until it reaches zero (red color in Figure 6.1). As the damaged material is unloaded gradually, the stresses may be redistributed to the intact material in the vicinity of the damaged area.

GSM models are commonly used in PFA of laminar composites to simulate the evolution of material damage due to the convenience of their implementation in general purpose FE-based software. These models can be formulated at different length scales, ranging from the microscopic to the macroscopic one, depending on the level of detail required to accurately capture the failure behaviour of the material being analysed [128].

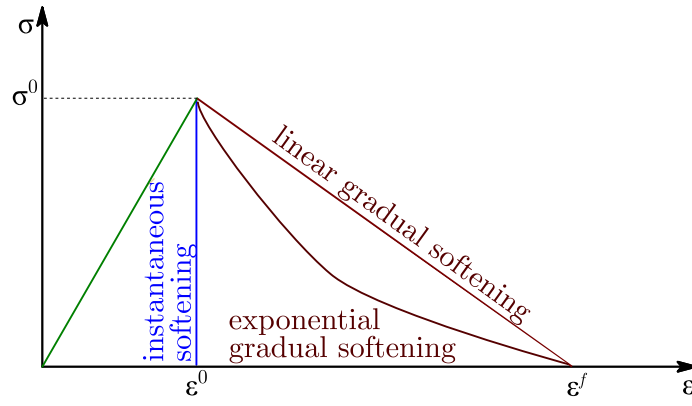


Figure 6.1: Post-failure softening behaviour in laminar composites. σ^0 denotes the material strength, ε^0 is the strain in the moment of damage initiation, while ε^f is the maximum strain

The micro-scale GSM models investigate the intricate interactions between the fibers and the matrix. Although these models have proven successful in predicting the properties of undamaged materials and the onset of damage, they are inadequate in forecasting damage evolution [129, 130]. This is because the representative volume assumed in a micro-scale model for predicting the behaviour of the intact material cannot be used as a representative volume for extensively damaged materials. In essence, smearing cannot be performed at the same scale in damaged and undamaged materials.

At the next scale, ply-based GSM models focus on the behaviour of the composite laminate at the lamina-level. The damage behaviour of each lamina is determined through tests performed on unidirectional (UD) laminates, and it is modelled independently of its adjacent laminae [131, 132]. Although ply-based models provide a detailed representation of the post-failure behaviour in each damaged lamina, the parameters used to describe the initiation and growth of damage may not accurately reflect the behaviour of damaged lamina in multi-directional laminate. In the multi-directional laminates, neighbouring layers provide structural support to the damaged layers and introduce alternative load paths within the laminate, which can significantly affect the behaviour of damaged lamina. Furthermore, considering that the simulation of every layer in the laminate is necessary, ply-based models become unfeasible for simulating structures of actual size due to the excessive computational expenses and time required. Large-scale structures can be more easily simulated using macro-scale GSM models [10]. Such models are designed to predict the general failure behaviour of the laminate and the resulting load-carrying capacity of the structure. However, they do not take into account the impact of damage events in individual layers on the overall nonlinear response of the laminate.

Selecting the suitable material length scale is crucial for precisely predicting failure progression. In quasi-brittle materials such as composites, damage is fundamentally a non-local phenomenon, and its advancement is influenced by both material and structural behaviour. Therefore, the validity of utilizing an averaging scheme to bridge different scales (micro-scale, meso-scale, and macro-scale) becomes questionable since the characteristic material length, which is associated with the constitutive model at the macro-scale, cannot be constructed hierarchically from lower scales [133, 134].

A major shortcoming of many of the existing CDM models is that assumed strain softening post-failure behaviour leads to localization of damage over a surface of zero thickness, which means no energy can be dissipated [135]. This issue is not affected by the shape of the softening portion of the stress-strain curve and causes a spurious dependence on the mesh size in finite

element solutions. As a result, the damage pattern becomes more localized with smaller mesh sizes, eventually becoming confined to a zero-volume zone, preventing numerical predictions from converging to a unique solution [136]. Therefore, the overall system response becomes dependent on the spatial discretization.

In order to alleviate the mesh-dependency issue and capture multi-scale nature of failure in laminar composites, the originally fracture-mechanics augmented smeared crack band (SCB) model was developed in [10] and applied successfully in this study.

6.2 Formulation of SCB damage model

The SCB damage model was initially proposed by Williams et al. [10], to capture the effect of matrix cracking and fibre breakage on the overall behaviour of the considered material. In SCB approaches, the response of damage material is smeared out within the finite representative volume element of the laminate and the failure mechanism is then represented through material stiffness degradation. This results in the inclusion of a length parameter relative to the element dimensions in the damage law [45]. The damage law is derived on the assumption that the total energy required to cause an element to fail (released strain energy) is equal to the energy needed to create a crack that propagates through it [65]. The released strain energy of a failed element is determined by multiplying the area under the stress-strain curve, as defined in Figure 6.2, by a characteristic element length l_c . In this study, l_c is defined as the square root of an area of a layered finite element. This energy is then equated to the fracture toughness (G), which represents the dissipated fracture energy of the composite material:

$$\varepsilon^f = \frac{2G}{\sigma_0 l_c} \quad (6.1)$$

In the Eq. (6.1), ε^f is maximum strain, while σ_0 is the material strength. The incorporation of the characteristic element length in the material damage law results in a consistent dissipated fracture energy, irrespective of the size of the elements.

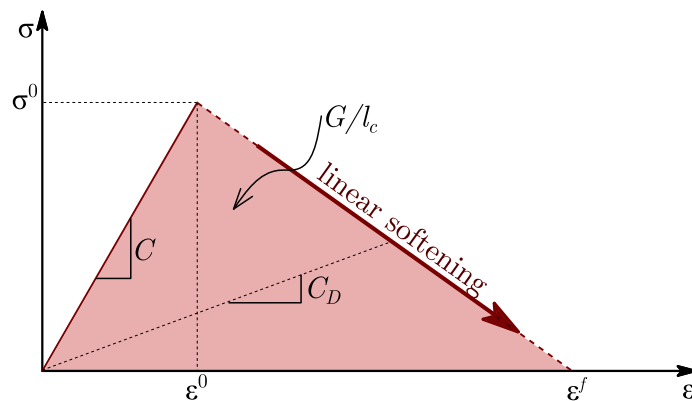


Figure 6.2: Stress-strain relationship with linear softening law applied for laminate stiffness degradation in global (x, y, z) directions. C is the material stiffness in the undamaged state, while C_D is the material stiffness in the damaged state.

The laminate stiffness degradation was controlled by damage variables, whose evolution is governed by strain components in the global laminate (xyz) coordinate system. This would be

a valid approach for unidirectional laminates, where the coordinate system coincides with the material directions (1, 2, 3) that dictate the crack paths. However, damage growth in multi-layer laminates can be manifested in different orientations within the material. These orientations may not be related to any particular coordinate system used to describe the material. For example, if a global coordinate system (xyz) is chosen to describe a laminate material, damage may occur at an angle that is not aligned with any of these axes. Attempting to describe and analyze the damage using this coordinate system can lead to limitations in accurately representing the orientation and growth of the damage [11]. This is because the damage is being forced to conform to a specific coordinate system, which may not accurately reflect its true nature. In other words, describing damage in terms of a fixed coordinate system may introduce inaccuracies in the progressive analysis of the failure, particularly when the damage occurs at orientations that are not aligned with the coordinate system. To ensure an accurate analysis of the failure in multi-layer laminates, it is important to consider the complex orientations of the damage and avoid relying solely on global coordinate systems to describe it.

Using the above model, the mesh orientation issue in SCB models was overcome by expressing the sub-laminate material response in terms of equivalent strain components in the principal lamina directions [70, 71]. Distinct bi-linear strain-softening curves (see Figure 6.3a) were used to describe the response of the damaged lamina in both the fiber and transverse to the fiber direction. These curves were designed such that the peak stress coincides with the fiber and matrix strength, respectively. When these stress-strain responses are integrated for each layer in a quasi-isotropic laminate, such as $[0^\circ/45^\circ/-45^\circ/90^\circ]_s$, the overall stress-strain behaviour of the laminate becomes non-linear, as shown in Figure 6.3b. The key points along the stress-strain curve are denoted ($a-e$) to describe the sequence of damage events. For instance, matrix damage initiation in the 90° layer corresponds to point (a), while point (b) marks the beginning of fiber damage in the 0° layer. As the 0° layer carries a significant portion of the load, the onset of its fiber damage coincides with the strain-softening behaviour of the laminate. At point (c), the fibers in the $\pm 45^\circ$ layers begin to degrade, and at point (d), fiber damage in the 0° layer saturates. When damage is completely saturated (or fully developed) at point (e), the laminate loses its load carrying capacity.

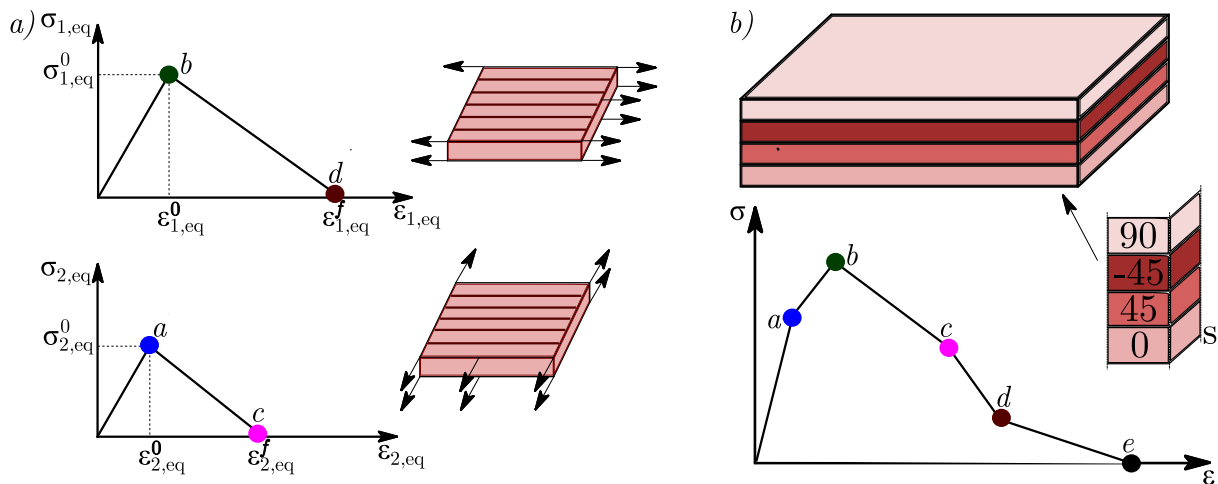


Figure 6.3: Stress-strain relationship with linear softening law applied for lamina stiffness degradation in material (1, 2, 3) directions

6.2.1 Constitutive model

The initial challenge when establishing a damage model for laminar composites is determining the material stiffness matrix in a damaged state. For the uniaxial case, only the undamaged portion of the cross-sectional area (referred to as the net-area) is expected to bear the load. Consequently, when the damaged material experiences a strain (ε) and is under nominal stress (σ), it must be represented as an undamaged material that is subjected to the same strain but under an effective stress state ($\hat{\sigma}$) [137]. This implies that the failure criteria, described in the previous chapter, are considered to be valid based on the effective stresses, ($\hat{\sigma}$), instead of the nominal stresses (σ). The relation between the effective stress and the nominal stress is given by:

$$\begin{Bmatrix} \hat{\sigma}_1 \\ \hat{\sigma}_2 \\ \hat{\sigma}_3 \\ \hat{\tau}_{23} \\ \hat{\tau}_{13} \\ \hat{\tau}_{12} \end{Bmatrix}^{(k)} = \mathbf{M}^{(k)} \begin{Bmatrix} \sigma_1 \\ \sigma_2 \\ \sigma_3 \\ \tau_{23} \\ \tau_{13} \\ \tau_{12} \end{Bmatrix}^{(k)} \quad (6.2)$$

where $\mathbf{M}^{(k)}$ represents the damage operator for the k^{th} layer, which has the following diagonal form:

$$\mathbf{M}^{(k)} = \begin{bmatrix} \frac{1}{1-d_f} & 0 & 0 & 0 & 0 & 0 \\ 0 & \frac{1}{1-d_m} & 0 & 0 & 0 & 0 \\ 0 & 0 & \frac{1}{1-d_m} & 0 & 0 & 0 \\ 0 & 0 & 0 & 1 & 0 & 0 \\ 0 & 0 & 0 & 0 & 1 & 0 \\ 0 & 0 & 0 & 0 & 0 & \frac{1}{1-d_s} \end{bmatrix}^{(k)} \quad (6.3)$$

In Eq. (6.3) d_f , d_m and d_s represent damage variables for fiber, matrix and shear damage, respectively. The postulate of strain equivalence typically results in an unsymmetrical material stiffness matrix $\mathbf{C}^{(k)}$ for any arbitrary damage operator $\mathbf{M}^{(k)}$. Therefore, this matrix cannot be considered as a valid representation of elastic behaviour.

This hypothesis, in conjunction with physical reasoning, served as a basis for constructing the stiffness matrix in damage state $\mathbf{C}_d^{(k)}$. In order to incorporate the impact of damage into the constitutive law, it is more convenient to use the compliance relationship, which facilitates the connection between material properties and inelastic response of the damage lamina along material directions (1, 2, 3). Specifically, the compliance relationship for orthotropic elasticity

in 3D stress state is recalled and expressed in terms of effective stresses [137]:

$$\begin{Bmatrix} \varepsilon_1 \\ \varepsilon_2 \\ \varepsilon_3 \\ \gamma_{23} \\ \gamma_{13} \\ \gamma_{12} \end{Bmatrix}^{(k)} = \mathbf{H}^{(k)} \begin{Bmatrix} \hat{\sigma}_1 \\ \hat{\sigma}_2 \\ \hat{\sigma}_3 \\ \hat{\tau}_{23} \\ \hat{\tau}_{13} \\ \hat{\tau}_{12} \end{Bmatrix}^{(k)} \quad (6.4)$$

where $\mathbf{H}^{(k)}$ represents the compliance matrix for the k^{th} layer. Substitution of effective stress vector, $(\hat{\sigma})$, from Eq. (6.2) into Eq. (6.4) results in:

$$\begin{Bmatrix} \varepsilon_1 \\ \varepsilon_2 \\ \varepsilon_3 \\ \gamma_{23} \\ \gamma_{13} \\ \gamma_{12} \end{Bmatrix}^{(k)} = \mathbf{H}^{(k)} \mathbf{M}^{(k)} \begin{Bmatrix} \sigma_1 \\ \sigma_2 \\ \sigma_3 \\ \tau_{23} \\ \tau_{13} \\ \tau_{12} \end{Bmatrix}^{(k)} \quad (6.5)$$

The symmetric 3D compliance matrix in damage state $\mathbf{H}_d^{(k)}$ was obtained after applying suitable reduction factors to the Poisson's ratios, as proposed by Matzenmiller et al. [137]:

$$\mathbf{H}_d^{(k)} = \begin{bmatrix} \frac{1}{E_1(1-d_f)} & -\frac{\nu_{21}}{E_2} & -\frac{\nu_{31}}{E_3} & 0 & 0 & 0 \\ -\frac{\nu_{12}}{E_1} & \frac{1}{E_2(1-d_m)} & -\frac{\nu_{32}}{E_3} & 0 & 0 & 0 \\ -\frac{\nu_{13}}{E_1} & -\frac{\nu_{23}}{E_2} & \frac{1}{E_3(1-d_m)} & 0 & 0 & 0 \\ 0 & 0 & 0 & \frac{1}{G_{23}(1-d_s)} & 0 & 0 \\ 0 & 0 & 0 & 0 & \frac{1}{G_{13}(1-d_s)} & 0 \\ 0 & 0 & 0 & 0 & 0 & \frac{1}{G_{12}(1-d_s)} \end{bmatrix}^{(k)} \quad (6.6)$$

Finally, the symmetric 3D stiffness matrix in damage state $\mathbf{C}_d^{(k)}$ was obtained in inverse form:

$$\mathbf{C}_d^{(k)} = \left(\mathbf{H}_d^{(k)} \right)^{-1} = \begin{bmatrix} C_{11}^d & C_{12}^d & C_{13}^d & 0 & 0 & 0 \\ C_{21}^d & C_{22}^d & C_{23}^d & 0 & 0 & 0 \\ C_{31}^d & C_{23}^d & C_{33}^d & 0 & 0 & 0 \\ 0 & 0 & 0 & C_{44}^d & 0 & 0 \\ 0 & 0 & 0 & 0 & C_{55}^d & 0 \\ 0 & 0 & 0 & 0 & 0 & C_{66}^d \end{bmatrix}^{(k)} \quad (6.7)$$

The damage stiffness matrix coefficients C_{ij}^d are written as [72]:

$$\begin{aligned} C_{11}^d &= \frac{E_1(1-d_f) \left(\nu_{23}\nu_{32}(1-d_m)^2 - 1 \right)}{\Delta}, \\ C_{22}^d &= \frac{E_2(1-d_m) \left(\nu_{13}\nu_{31}(1-d_f)(1-d_m) - 1 \right)}{\Delta}, \\ C_{33}^d &= \frac{E_3(1-d_m) \left(\nu_{12}\nu_{21}(1-d_f)(1-d_m) - 1 \right)}{\Delta}, \\ C_{12}^d &= -\frac{E_1(1-d_f)(1-d_m) \left(\nu_{23}\nu_{31}(1-d_m) + \nu_{21} \right)}{\Delta}, \\ C_{13}^d &= -\frac{E_1(1-d_f)(1-d_m) \left(\nu_{21}\nu_{32}(1-d_m) + \nu_{31} \right)}{\Delta}, \\ C_{23}^d &= -\frac{E_2(1-d_m)^2 \left(\nu_{12}\nu_{31}(1-d_f) + \nu_{32} \right)}{\Delta}, \\ C_{44}^d &= G_{23}(1-d_s), \quad C_{55}^d = G_{13}(1-d_s), \quad C_{66}^d = G_{12}(1-d_s) \end{aligned} \quad (6.8)$$

where

$$\begin{aligned} \Delta &= (1-d_m)^2 \left((\nu_{12}\nu_{23}\nu_{31} + \nu_{13}\nu_{21}\nu_{32})(1-d_f) + \nu_{23}\nu_{32} \right) + \\ &+ (\nu_{12}\nu_{21} + \nu_{13}\nu_{31})(1-d_f)(1-d_m) - 1 \end{aligned} \quad (6.9)$$

The damage variables d_f and d_m may exhibit varying values depending on whether the material is under tension (t) or compression (c). These variables, which are associated with failure modes J ($J = ft, fc, mt, mc$), range from zero (indicating no damage) to one (signifying complete damage). Additionally, the shear damage variable d_s is interdependent and can be mathematically expressed in terms of the other variables [72]:

$$d_s = 1 - (1-d_{ft})(1-d_{fc})(1-d_{mt})(1-d_{mc}) \quad (6.10)$$

6.2.2 Damage evolution

Softening laws that govern the condition for evolution of damage variables are typically described in relation to the strain state in the single lamina. Because various damage mechanisms interact

with one another, the evolution of each damage variable is controlled by the equivalent strain $\varepsilon_{J,eq}$. Consequently, each damage mode is depicted as a 1D stress-strain issue (as shown in Figure 6.3a) instead of the actual 3D stress-strain relationship. The equivalent strain and corresponding equivalent stress for each failure mode were defined as follows [72]:

Fiber tension failure:

$$\begin{aligned}\varepsilon_{ft,eq} &= \sqrt{\langle \varepsilon_1 \rangle^2 + \gamma_{12}^2 + \gamma_{13}^2}, \\ \sigma_{ft,eq} &= \frac{\langle \sigma_1 \rangle \langle \varepsilon_1 \rangle + \tau_{12} \gamma_{12} + \tau_{13} \gamma_{13}}{\varepsilon_{ft,eq}}\end{aligned}\quad (6.11)$$

Fiber compression failure:

$$\begin{aligned}\varepsilon_{fc,eq} &= \langle -\varepsilon_1 \rangle, \\ \sigma_{fc,eq} &= \frac{\langle -\sigma_1 \rangle \langle -\varepsilon_1 \rangle}{\varepsilon_{fc,eq}}\end{aligned}\quad (6.12)$$

Matrix tension failure:

$$\begin{aligned}\varepsilon_{mt,eq} &= \sqrt{\langle \varepsilon_2 \rangle^2 + \langle \varepsilon_3 \rangle^2 + \gamma_{12}^2 + \gamma_{13}^2 + \gamma_{23}^2}, \\ \sigma_{mt,eq} &= \frac{\langle \sigma_2 \rangle \langle \varepsilon_2 \rangle + \langle \sigma_3 \rangle \langle \varepsilon_3 \rangle + \tau_{12} \gamma_{12} + \tau_{13} \gamma_{13} + \tau_{23} \gamma_{23}}{\varepsilon_{mt,eq}}\end{aligned}\quad (6.13)$$

Matrix compression failure:

$$\begin{aligned}\varepsilon_{mc,eq} &= \sqrt{\langle -\varepsilon_2 \rangle^2 + \langle -\varepsilon_3 \rangle^2 + \gamma_{12}^2 + \gamma_{13}^2 + \gamma_{23}^2}, \\ \sigma_{mc,eq} &= \frac{\langle -\sigma_2 \rangle \langle -\varepsilon_2 \rangle + \langle -\sigma_3 \rangle \langle -\varepsilon_3 \rangle + \tau_{12} \gamma_{12} + \tau_{13} \gamma_{13} + \tau_{23} \gamma_{23}}{\varepsilon_{mc,eq}}\end{aligned}\quad (6.14)$$

where $\langle \rangle$ denotes the Macaulay bracket. In the SCB approach, it is assumed that the evolution of damage variables (d_J) follows a hyperbolic function (as depicted in Figure 3(a)) in relation to the equivalent strains. This approach, when combined with stiffness reduction factors that change linearly with the damage parameters (as illustrated in Figure 3(b)), leads to a strain-softening response that is linear for each failure mode. Following this relation, damage variables are obtained as:

$$d_J = \frac{\varepsilon_{J,eq}^f (\varepsilon_{J,eq} - \varepsilon_{J,eq}^0)}{\varepsilon_{J,eq} (\varepsilon_{J,eq}^f - \varepsilon_{J,eq}^0)}, \quad \varepsilon_{J,eq}^0 \leq \varepsilon_{J,eq} \leq \varepsilon_{J,eq}^f \quad (6.15)$$

where $\varepsilon_{J,eq}^0$ is the equivalent strain at the initial failure state ($d_J = 0$), while $\varepsilon_{J,eq}^f$ is the equivalent strain at the final failure state ($d_J = 1$). Given that damage evolution is an irreversible process, the damage variable is determined as the maximum value between its current state and the value obtained from Eq. (6.15). Eq. (6.1) can be used to calculate the equivalent strain at the point of final failure, denoted as $\varepsilon_{J,eq}^f$:

$$\varepsilon_{J,eq}^f = \frac{2G_J}{\sigma_{J,eq}^0 l_c} \quad (6.16)$$

In Eq. (6.16) $\sigma_{J,eq}^0$ is the equivalent stress at the state of initial failure. By utilizing the failure criterion parameter, f_J , it is possible to determine the equivalent strain and stress at the beginning of failure for each failure mode, using the following relation:

$$\varepsilon_{J,eq}^0 = \frac{\varepsilon_{J,eq}}{\sqrt{f_J}}, \quad \sigma_{J,eq}^0 = \frac{\sigma_{J,eq}}{\sqrt{f_J}} \quad (6.17)$$

6.3 Constitutive model for compressive fiber failure

Bilinear constitutive models (Figure 6.4a) may not accurately capture the material behaviour during compressive damage initiation and propagation when using a simple linear post-peak fiber softening. This is because fiber failure initiation can lead to instabilities such as fiber micro-buckling and kink-bands, resulting in a sudden drop in load-carrying capability followed by a stress response plateau [138]. To address this issue, additional softening curves are used to improve the predictive capabilities of the material model, requiring a modification of the damage evolution law (Eq. (6.15)). Based on approach proposed in [74], a linear-brittle post-peak softening curve is used in this study, to simulate the sudden drop and stable stress plateau (Figure 6.4b). As shown in Figure 6.4b, the residual plateau stress magnitude is expressed as a percentage (PC) of the peak stress value.

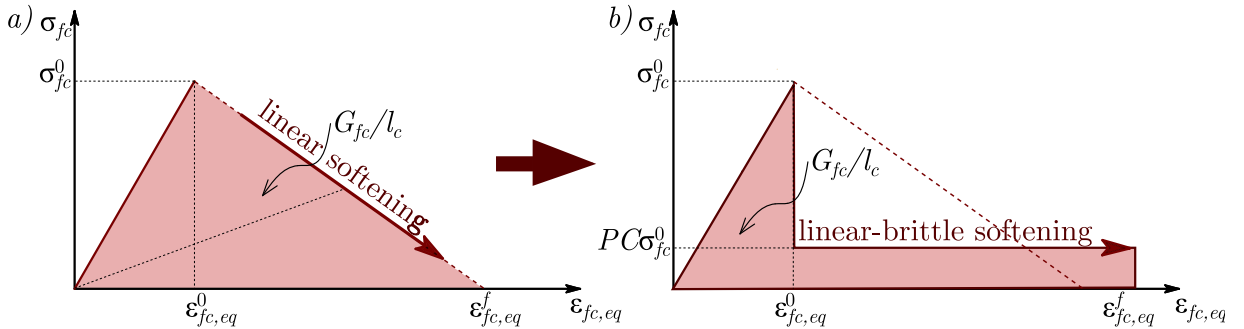


Figure 6.4: Stress-strain relationship with: (a) linear and (b) linear-brittle softening law; applied in modelling of compressive fiber failure

The area under the stress-strain curve, multiplied by the characteristic element length, remains constant and represents the fracture toughness associated with the fiber constituent. Therefore, the equivalent strain at the final failure state, $\varepsilon_{fc,eq}^f$ is calculated from the below Equation, instead of Eq. (6.16)

$$\varepsilon_{fc,eq}^f = \frac{2G_{fc} - \sigma_{fc,eq}^0 \varepsilon_{fc,eq}^0 l_c (1 - 2PC)}{2PC \sigma_{fc,eq}^0 l_c} \quad (6.18)$$

Following the above mention, damage variable for fiber compression failure is obtained as:

$$d_{fc} = 1 - PC \frac{\varepsilon_{fc,eq}^0}{\varepsilon_{fc,eq}}, \quad \varepsilon_{fc,eq}^0 \leq \varepsilon_{fc,eq} < \varepsilon_{fc,eq}^f \quad (6.19)$$

$$d_{fc} = 1, \quad \varepsilon_{fc,eq} = \varepsilon_{fc,eq}^f$$

6.4 Procedure for progressive failure analysis

Progressive failure analysis (PFA) is a method used to model the post-failure behaviour of a material after the failure criterion has been satisfied. The PFA algorithm within FE analysis is illustrated in Figure 6.5, and involves the following steps:

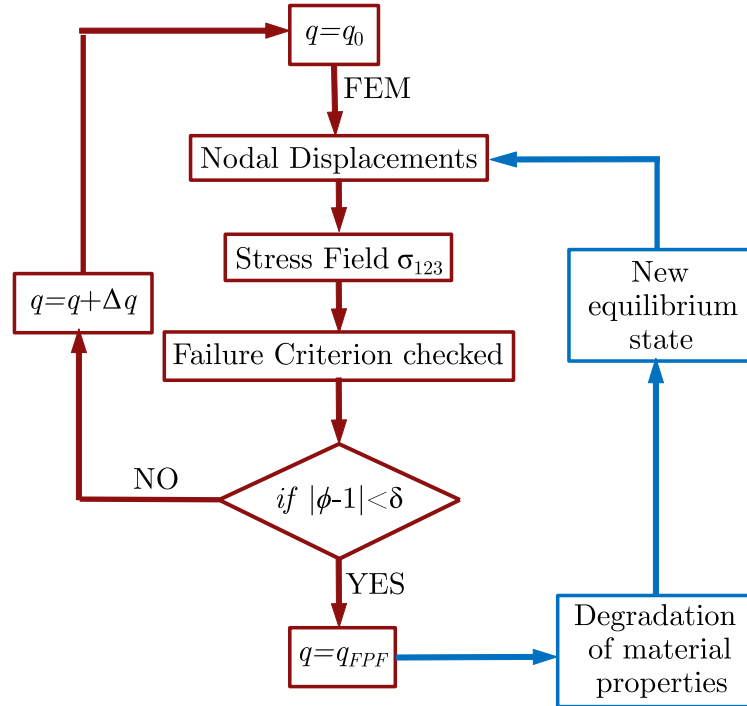


Figure 6.5: Flow chart of procedure for Progressive Failure Analysis of laminar composites

1. Divide the applied load into smaller increments to facilitate the PFA and simulation of laminate's response
2. Determine the displacement field through the laminate thickness for an initial load, based on the current stiffness properties.
3. Compute the stresses at each Gaussian integration point on the top and bottom interfaces of each lamina of each element, and express them in the local material coordinate system.
4. Use the failure criterion to check if any lamina of any element fails at the initial load, based on the calculated stresses.
5. If failure is detected, degrade the corresponding material properties of the damaged lamina according to the SCB damage model.
6. Re-establish equilibrium of the structure using the modified properties for the failed lamina while maintaining the current load level, as the initial solution no longer corresponds to an equilibrium state.
7. Repeat steps 1-5 iteratively to obtain nonlinear equilibrium solutions until no further damage occurs at the same externally applied load.

8. Increment the load step and repeat the entire procedure until the PFA detects complete failure of the structure, which occurs when the structure degrades to a point where it can no longer carry additional load.

The Newton-Raphson iteration method is commonly used to solve nonlinear finite element equations, often in combination with an incremental loading approach. However, due to the inability to acquire a direct stiffness matrix as a result of damage, this study does not utilize the Newton-Raphson method. Instead, a novel technique for PFA is employed, as proposed by Robinson [117], where the equivalent properties are used to describe post-failure behaviour of damage material, rather than using instantaneous properties. Equivalent properties take into account the effects of the damage on the overall response of the material and the damaged material is then modelled as an undamaged material with different properties. By substituting the equivalent material properties into the damage stiffness matrix, the direct stiffness matrix can be obtained, allowing for the application of the nonlinear iteration through the direct stiffness method.

7 Progressive failure analysis of cross laminated timber panels

7.1 Introduction

This chapter focuses on extending the SCB model, which was initially developed for composites, to consider the distinct failure behaviour of timber in tension and compression. By extending its applicability to the field of computational mechanics of bio-based composites, the computational framework has the potential to be further expanded for large cross laminated timber (CLT) floor structures. CLT is a bio-based (i.e. wood) laminar composite made by gluing the cross-wise layers of solid timber boards, resulting in large-scale panels. CLT's thick and orthogonal structure provides significant stiffness while maintaining a low weight, making it suitable for use as full-size walls or floors that can bear loads in-plane and out-of-plane [2]. Compared to solid wood, CLT exhibits improved load-bearing and stiffness properties. This is due to the ability to eliminate wood growth defects during production or distribute them throughout the final product. Moreover, there are other notable benefits such as the flexibility to select various geometric shapes, the capacity to align individual layer quality with expected stress levels, and enhanced dimensional and shape stability when exposed to moisture [139].

The complex failure behaviour of crosswise lay-up highly anisotropic timber layers in CLT panels can result in significant structural damage and collapse, leading to costly economic expenses and even human injuries or fatalities [140]. Therefore, it is crucial to have a safe and reliable structural design, which requires understanding the failure and structural behaviour and its modelling.

In practical timber engineering, linear elastic stress analysis and stress-based failure criterion are commonly used to assess failure in CLT. However, this approach has limitations as it disregards stress redistribution effects and material nonlinear effects, making strength predictions for elements with high stress gradients unreliable. To develop more accurate and reliable design methods, it is necessary to gain insight into the failure propagation within CLT after failure initiation. This study aims to analyse the post-failure behaviour of CLT using the SCB damage model of conventional laminar composites. By doing so, we hope to improve our understanding of the failure behaviour of CLT and develop better design methods for safer and more reliable structures.

7.2 Timber cracks and material properties

From the mechanics point of view, wood is an orthotropic material with three principal material axes (Figure 7.1, left): the first one is aligned with the wood fiber direction (L), while the remaining two axes are in the radial – R and tangential direction - T. Accordingly, six possible principal crack propagation directions may be identified for timber, as shown in Figure 7.1, right, where the first index denotes the normal to the crack surface and the second index denotes the direction of crack propagation[98].

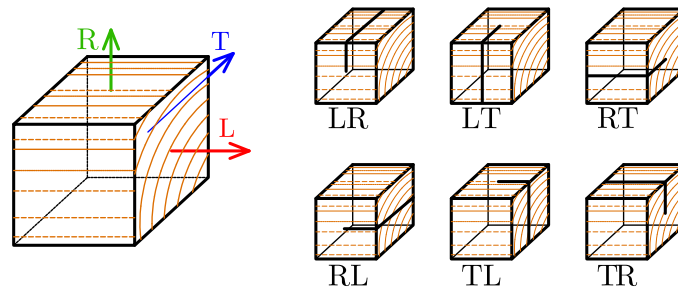


Figure 7.1: Principal material directions (left); Crack propagation directions for timber (right)

When it comes to CLT, each layer consists of timber boards with varying growth ring orientations placed adjacent to each other. This leads to an unknown orientation of the material (local) coordinate system. Additionally, the manufacturing process determines whether the wooden boards are bonded together on their lateral faces or not.

To simplify the modelling process, the lateral edges of the timber boards are glued to create a continuous layer for each CLT lamina [88]. A unique material coordinate system (123) is established for each lamina (see Figure 3.3), where direction 1 aligns with the wood fiber direction (L), while directions 2 and 3 represent the direction perpendicular to the wood fiber within the lamina plane and the direction perpendicular to both the wood fiber and the lamina, respectively. To overcome the irregularity of growth rings, the material behaviour in directions 2 and 3 are assumed to be the same within this study. This involves defining the moduli for directions 2 and 3 as the average values of the corresponding T and R values for solid wood.

The strength parameters, which are used for material description and failure analysis, differ between considering small *clear* wood samples (free from defects) and structural-sized timber in engineering design context [141]. Natural imperfections like knots, growth ring irregularities, and resin pockets that form during its growth process, can greatly affect strength properties. For instance, knots can weaken a structural-sized beam under tension or bending as the wood fiber direction deviates from the beam axis around the knot and introduces the stress perpendicular to the wood fiber. However, knots can act as reinforcement in applications with tensile stress perpendicular to the wood fiber direction, thereby increasing the strength [142].

Timber engineering design typically relies on characteristic (5%) strength values, determined according to a standardized procedure on small clear wood samples with a specified moisture content (usually 12%), as specified in codes and handbooks [143].

However, these obtained values do not directly correspond to the strength characteristics of structural timber with real dimensions. To address this issue, structural timber strengths are

determined by taking into account the strengths obtained from small wood samples and applying correction factors that account for the size of the sample [144].

7.3 CLT post-failure behaviour

The crosswise lay-up of highly anisotropic timber layers can result in complex failure behaviour for CLT panels. Under different types of loading, cross-laminated timber (CLT) panels can develop various failure mechanisms. The four most common modes of failure in CLT are:

1. Fiber tension (FT) is the most critical mode of failure, caused by tensile stress parallel to the wood fiber, resulting in a failure surface that propagates perpendicular to the fiber (Figure 7.2, left).
2. Transverse tension (TT) failure occurs due to the combination of in-plane shear stress and tensile or shear stress perpendicular to the wood fiber. This combination of stresses causes the rolling of the wood's fibers, which is why this failure mode is often called rolling shear failure (RS). The failure surface usually occurs in the interior of the transverse lamina and follows the annual rings as closely as possible. Typical RS failure mode is illustrated in Figure 7.2, right).
3. Fiber compression failure (FC), which leads to the typical fiber kinking band formation, due to the local instabilities of the wood cells. This phenomenon results in a quasi-plastic behaviour on the macro scale.
4. Transverse compression (TC) failure generally results from transverse shear stress and transverse compressive stresses perpendicular to the wood fiber, where the corresponding failure surface is usually parallel to the wood fiber.

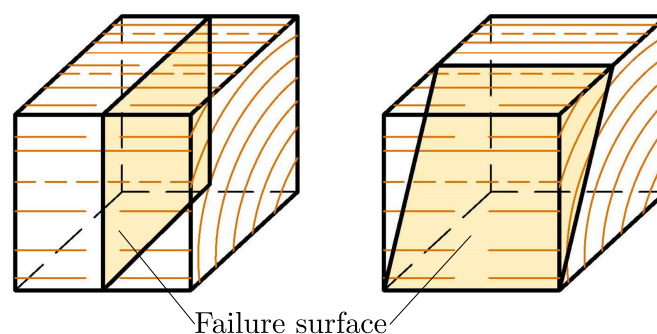


Figure 7.2: Typical failure surface for: fiber tension (FT) failure mode (left); rolling shear (RS) failure mode (right)

Establishing an appropriate failure criterion is essential for identifying the onset of damage in CLT for specific failure modes. By utilizing the failure criteria outlined in Chapter 5, the FT and RS failure modes can be associated with the LT-LR and TL-RL crack propagation scenarios, respectively.

In addition, the response of a damaged CLT lamina also vary depending on the type of loading applied. When subjected to compression parallel or perpendicular to the wood fiber, the response

of the damaged lamina can be described as ideally-plastic. This means that the stiffness remains constant even as strain increases after failure initiation in the weakest lamina. Conversely, in tension, the behaviour is typically more brittle. The loading types that cause the most issues are tension perpendicular to the wood fibers and shear. If the loading in these modes becomes too high, RS failure can occur [145]. This failure usually happens in a brittle way with little warning, similar to how FRP laminar composites behave after failure initiation. Therefore, the transverse tension post-failure behaviour can be modeled using the SCB damage model with linear softening (Figure 6.2), as described in Chapter 6.

On the other hand, when modelling the post-failure behaviour of fiber tension and compression, the proposed damage law can be simplified. Specifically, to capture the brittle post-failure behaviour of a damaged lamina under fiber tension, the fracture toughness parameter (G) is set to zero. Conversely, to describe the plastic post-peak softening response of a damaged lamina under compression, an infinity value of G is utilized. These modifications of the bilinear softening law are illustrated in the accompanying Figure 7.3.

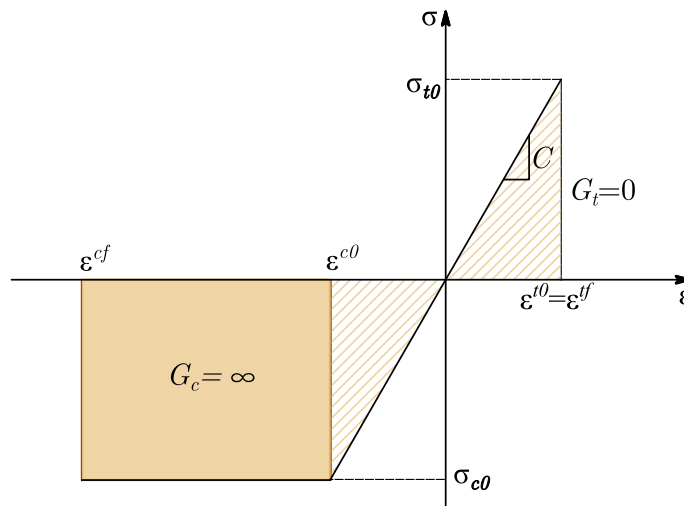


Figure 7.3: Stress-strain relationship with simplified softening law to model post-failure timber behaviour in fiber tension and compression

The proposed algorithm's effectiveness will be demonstrated in the Chapter 9 through a numerical example. Additionally, a comprehensive experimental program was conducted by Dr. Ivan Glišović, Dr. Marija Todorović and Nađa Simović in the Laboratory of Structures at the Faculty of Civil Engineering, University of Belgrade in order to validate the algorithm's performance.

8 Software (FLWTFEM) framework

8.1 Introduction

Extensive research has been conducted in the field of computational mechanics of multilayer structures over the past few decades, which has significantly enhanced the ability to tackle complex problems. Among various numerical methods, the FEM has been the most widely utilized to solve the governing differential equations arising in the mechanics of multilayer structures, as evidenced by numerous studies [114]. Performance and memory efficiency are essential requirements for finite element software development from a programming perspective. As such, the code must be well-structured to enhance flexibility and minimize maintenance expenses. Additionally, it should be adaptable to incorporate new algorithms, formulations, and ideas. The FEM solution process comprises three primary stages: *Pre-processing*, *Simulation* and *Post-processing*. Careful execution of each step is essential, and the user should find them easy to perform.

The initial stage involves defining geometric entities such as points, lines, surfaces, or volumes, as well as assigning attributes and conditions to them, and generating a finite element mesh. Mesh generation is decoupled from analysis by adding interfaces to existing CAD software packages [146]. Once the mesh is generated, new attributes or conditions can be assigned directly to the finite element mesh.

The next phase involves solving the governing equations of the mathematical model using a solver. Two possible programming approaches are procedure-oriented programming (POP) and object-oriented programming (OOP). OOP is widely utilized in engineering software development, including the FEM, because it provides flexibility and clear structuring, making it suitable for education, application, and research. Also, It requires less time and effort to introduce a new feature or improve an existing one in OOP. Furthermore, OOP has brought about a substantial reduction in program size and complexity. OOP is founded on the idea of objects that encapsulate properties and methods. Objects serve as instances of classes and can be linked through various relationships. In the 1990s, the initial object-oriented finite element codes were introduced for structural analysis applications [147–149]. These codes began with linear analysis procedures and were subsequently expanded to accommodate both geometrical and material nonlinearity. Later, the FE codes were enhanced with the addition of new object-oriented algorithms for linear and nonlinear static and dynamic analysis of structures. For example, Archer et al. [150], Cardona et al. [151] made contributions in this area.

Finally, the obtained results are visualized in the *Post-processing* stage.

8.2 Upgrade of the FLWTFEM software

The object-oriented computational framework FLWTFEM [15] was primarily written for the analysis of laminated composite plates, and implied the static and dynamic (free vibration) analysis of multilayered plate-like structures of arbitrary geometry.

For the pre- and post-processing phases in this framework, the GiD Pre/Post Processor software developed by CIMNE in Barcelona is utilized. This software allows for changes to be made to the geometry while maintaining attribute definitions and discretizations on the same geometric domain. Figure 8.1 illustrates the typical algorithm used in the GiD-based finite element program.

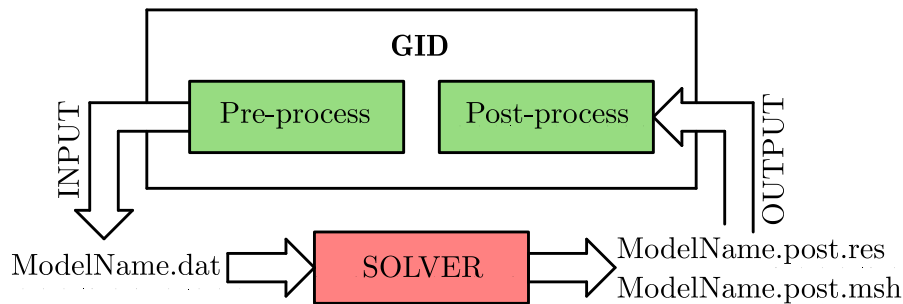


Figure 8.1: Typical algorithm used in the GiD-based finite element program [111]

The FLWTFEM solver is written using an object-oriented Matlab paradigm, which leverages the language’s powerful desktop environment to simplify programming tasks and enable interactive data manipulation. With Matlab, algorithms can be tested immediately without the need for re-compilation. Given Matlab’s extensive documentation and large user community, along with a multitude of application examples, it is a highly suitable choice for educational purposes.

Within this thesis, FLWTFEM framework is extended to incorporate a PFA of multilayer structures using the SCB damage model. The source code will be presented in Appendix.

8.2.1 FLWTFEM problemtype

The main advantage of GiD lies in its capacity to enable users to design and customize their own graphical user interface (GUI). This is accomplished by generating multiple configuration files that determine fresh windows where end-users can input data. The assembly of these files is referred to as **problem type**, and the configuration files are described as follows.

FLWTFEM.cnd is the file that contains information about the conditions that can be applied to different entities, where each geometrical entity can have different field values for the condition. The conditions included in the **FLWTFEM.cnd** file are: *Constraints*, *NodalForces*, *CompositeSection* and *DistributedLoadings*.

FLWTFEM.mat contains the definitions of materials and laminas that are applicable to a numerical model. It enables the user to specify the mechanical properties of the orthotropic material (*Orthotropic*) and define the material, thickness, and fiber orientation of the orthotropic

lamina (*Lamina*). This thesis has upgraded the **FLWTFEM.mat** input file by incorporating the material strengths into the existing mechanical properties of the orthotropic material.

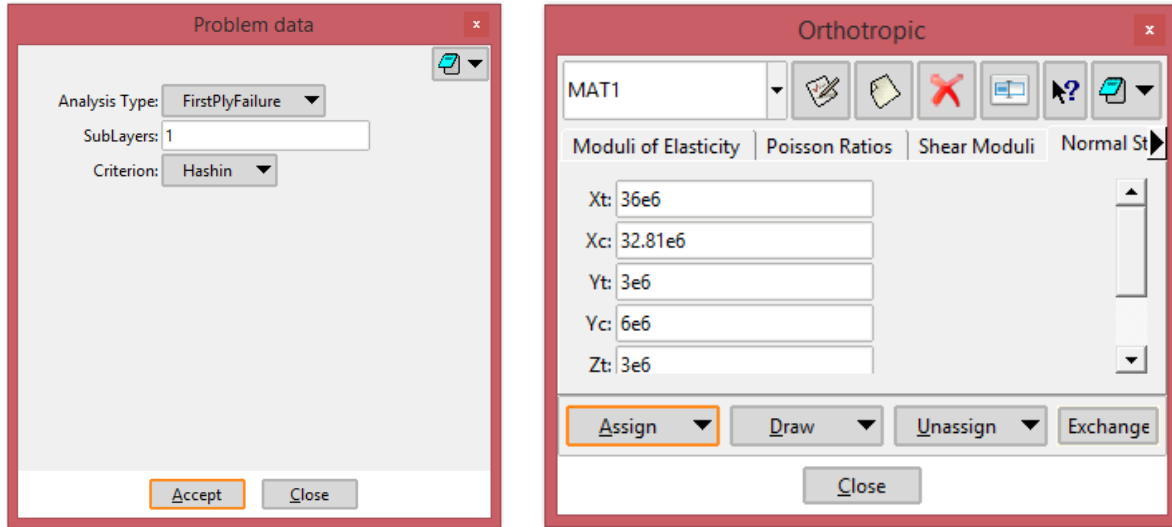


Figure 8.2: FLWTFEM GiD user interface for pre-processing

The **FLWTFEM.prb** file provides fundamental details about the necessary data for conducting an analysis, without focusing on any specific geometric entity. Within this file, one can define the *AnalysisType* and *SubLayers* (the number of material layer divisions for interlaminar stress interpolation) as options for general problem data. By changing the **FLWTFEM.prb** input file in this thesis, the PFA was added in the *AnalysisType* drop-down menu (Figure 14) and the appropriate failure criterion can be selected.

Once the geometry of the model is established and conditions are specified, GiD generates a mesh utilizing its available options (e.g. mesh regularity, quadratic type, element type, element size, and mesh criteria). In order to create the necessary data input file for the solver to process during simulation, GiD employs the **FLWTFEM.bas** file, which outlines the format and structure of the required input data for the Matlab solver. The resulting ***.dat** file is subsequently created and utilized as input. Lastly, the **FLWTFEM.tcl** file is employed to streamline the program's environment for end-users by eliminating extraneous menus.

8.2.2 FLWTFEM classes

The FLWTFEM software has classes grouped into three categories: *material classes*, *finite element model classes*, and *post-processing algorithms and utility functions*. The relationships between these classes are shown in Figure 8.3, and a detailed description of each class can be found in [15].

To upgrade the FLWTFEM solver, the following classes were edited: **FLWTFEM**, **LW_3D**, and **OrthotropicMaterial**. The **OrthotropicMaterial** class is an abstract class that contains information about the material properties used in the analysis. In this upgrade, material strength properties were added to the class. On the other hand, **LW_3D** class is the core of the layered finite element model and provides an interface for calculating the necessary matrices and vectors for assembling the global system of equations. The **LW_3D** class was upgraded by

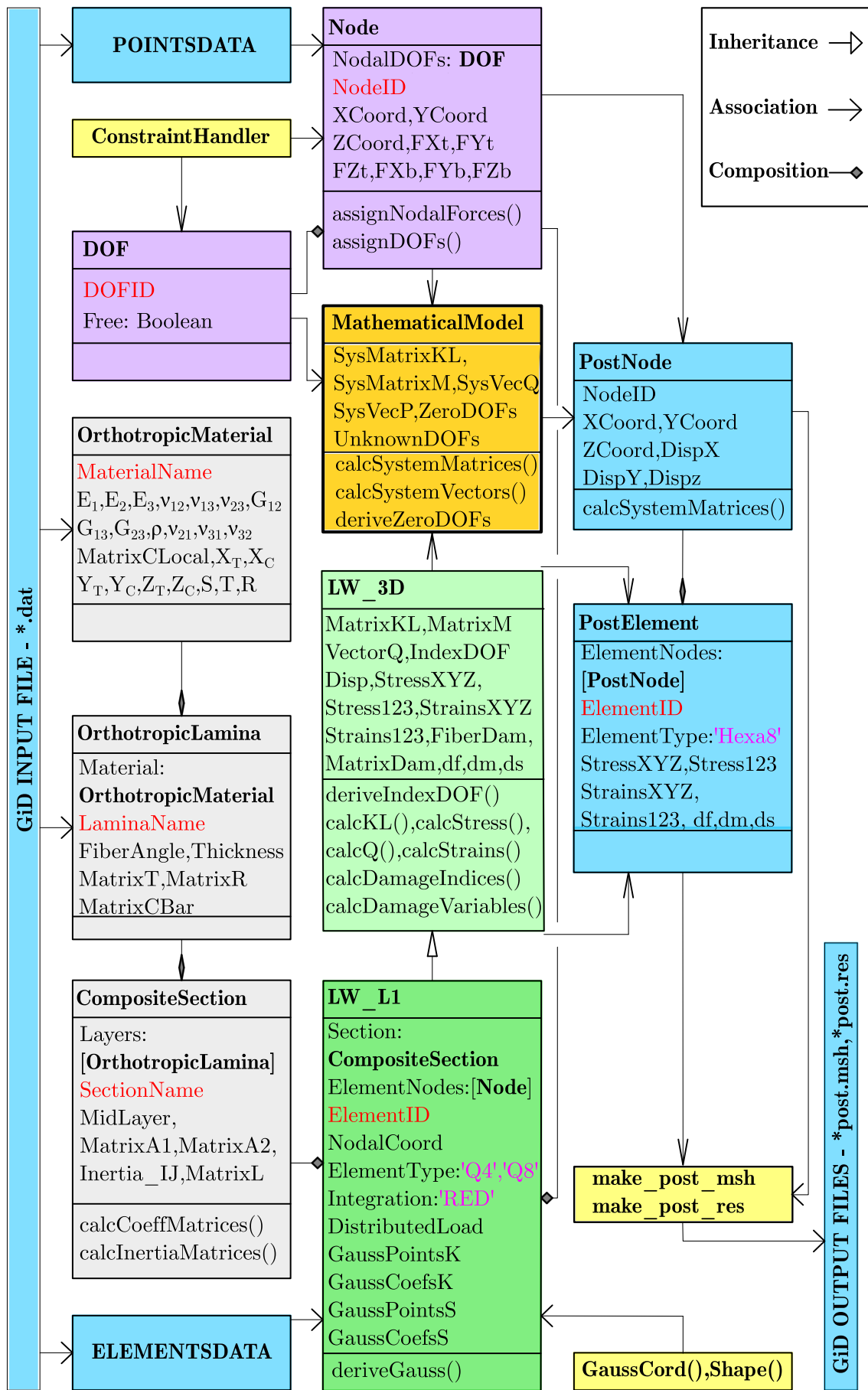


Figure 8.3: FLWTFEM class structure [15]

adding an interface for stress (`calcStresses()`) and strain (`calcStrains()`) calculations, as well as damage indices (`calcDamageIndices()`) and variables (`calcDamageVariables()`).

Additionally, post-processing and damage propagation algorithms were implemented: first to calculate the interlaminar stress distribution accurately through the plate thickness and second to calculate the damage variables for material degradation during PFA.

Once all classes are created, **FLWTFEM** performs the implicit PFA of the considered laminar composite, and then calculates the damage variables in each element of each lamina, in order to describe the response of damage laminae.

The results are visualised in 3D by the GiD Post-Processing module. For visualisation purposes, **FLWTFEM** utilises two classes, **PostNode** and **PostElement**, which store the necessary information for post-processing. Communication between the Matlab solver and GiD is established through two output files, namely `*.post.res` and `*.post.msh`. To generate these files, the `make_post_res()` and `make_post_msh()` functions are modified within the project. The resulting post-process files contain detailed information on stresses, strains and damage variables, captured during PFA of corresponding laminar composites (Figure 8.4).

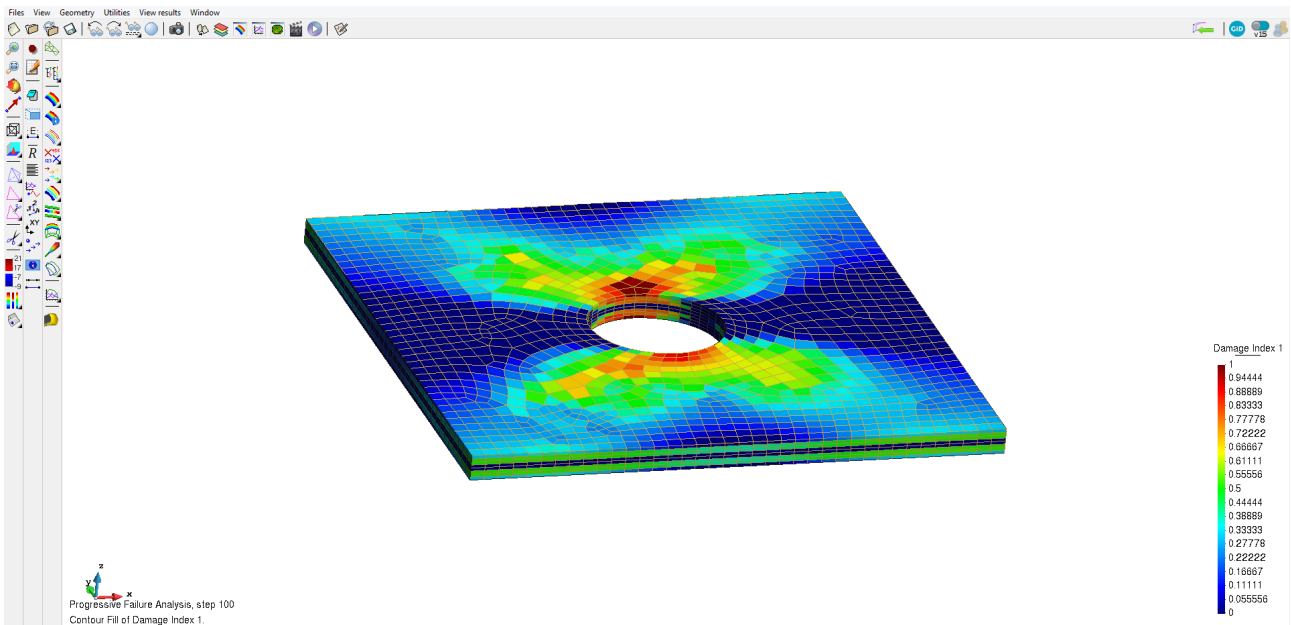


Figure 8.4: FLWTFEM GiD user interface for post-processing (fiber tension failure patterns at the time point when the first element reaches $d_{ft}=1$, for an open-hole laminar composite with a central hole)

9 Numerical examples

This chapter consists of validation and benchmark examples, used to demonstrate the applicability of the FLWT-SCB prediction model to determine the results of the progressive failure analysis (PFA) of laminar composites. The author has used an original object-oriented FLWTFEM framework, developed by the author and co-workers at the Institute of an Numerical Analysis and Design of Structures (INP) of the University of Belgrade to carry out the all calculations. Wherever possible, the obtained results have been cross-checked against existing exact, analytical, numerical, and experimental data from various sources in the literature. Most of the results presented in this chapter have been carefully selected from the author's publications [13, 15, 112], published during the PhD studies. It should be noted that the prediction model presented in this study is not limited to any specific geometry, stacking sequence, boundary conditions or loading type. In all examples dealing with the PFA of laminar composites, the quasi-3D stress analysis was conducted using Q8 layered quadrilateral elements with reduced integration.

The first part of the chapter shows the FLWT-based finite element model's ability to accurately capture the 3D stress field and account for the continuous distribution of interlaminar stresses throughout the laminate thickness. This demonstration establishes a strong foundation for the subsequent analysis of damage progression and post-failure assessment. In the second part of the chapter, the FLWT-SCB prediction model, which combines the SCB model with FLWT, will be applied to further investigate the progressive damage behaviour and post-failure response of the laminate.

9.1 Three-dimensional stress analysis of cross-laminated timber panels

Example 9.1.1

The primary objective of the first example is to validate the proposed model by analysing thick CLT panels through finite element analysis. The main focus is to ensure accurate representation of the 3D stress and strain distributions across the thickness of the CLT panel, demonstrating the need for applying the FLW Theory to achieve this. The inadequacy of ESL-based models for accurate prediction of the 3D stress state in CLT is highlighted by considering thick panels.

The panels are simply supported along all sides for the purpose of comparison with analytical solutions. These analytical solutions are based on classical plate theory (CPT) and first-order shear deformation laminate theory (FSDT), and the exact solution by Pagano [152], which is based on the exponential distribution of displacements across the plate thickness. The

benchmark results are taken from [96], where analytical solutions with 25×25 Fourier terms were considered.

The example involves analysing of two square ($a = b$) CLT panels, as shown in Figure 9.1. The first panel consists of three layers, with a thickness of $h = [h_0/h_{90}/h_0] = [26/40/26] = 92\text{mm}$, and a side length of $a = b = 920\text{mm}$ ($a/h = 10$). The second panel is composed of five layers, with a thickness of $h = [h_0/h_{90}/h_0/h_{90}/h_0] = [26/40/26/40/26] = 158\text{mm}$, and a side length of $a = b = 1580\text{mm}$ ($a/h = 10$).

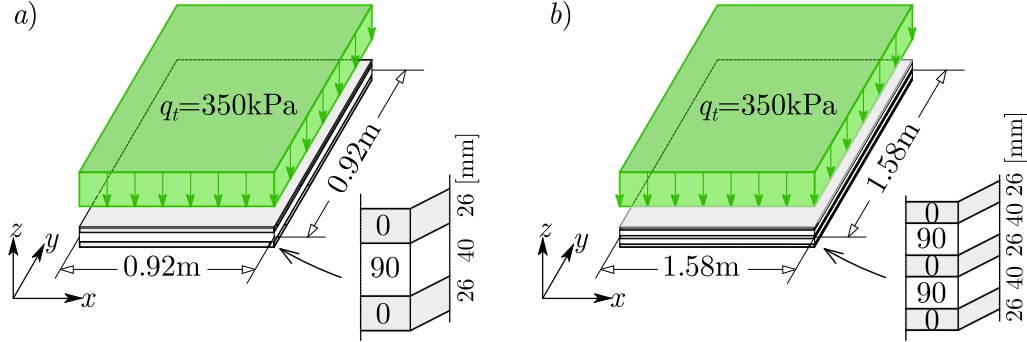


Figure 9.1: Simply supported CLT panels under uniformly distributed loads at the top surface: a) 3-layer configuration of $[26/40/26]\text{mm}$; b) 5-layer configuration of $[26/40/26/40/26]\text{mm}$ [112]

The material properties of each layer in the CLT panels are defined based on the C24 unidirectional lamina, with details provided in Table 9.1. The given mechanical properties of the CLT are adopted based on [153–155]. The rolling shear modulus is defined as $G_{23} = 0.1G_{12} = 0.10G_{13}$, which is based on the shear modulus in the longitudinal-transverse direction. However, based on the current approvals, it is defined as 50MPa [156]. Poisson's ratios are based on experimental measurements available in References [153–155], carried out on different samples at about 12% moisture content for hardwoods and softwoods. It should be noted that the material model is analysed for the timber class and not for a specific type of wood.

Table 9.1: Material properties of CLT panels (C24 timber class)

Property [MPa]	Value
E_1	11000
$E_2 = E_3$	370
$G_{12} = G_{13}$	690
G_{23}	50
ν_{12} (-)	0.49
ν_{13} (-)	0.39
ν_{23} (-)	0.64

The edge nodes are subject to prescribed boundary conditions, with $U^I = W^I = 0$ for the edge parallel to the x -axis and $V^I = W^I = 0$ for the edge parallel to the y -axis. The panels are subjected to high distributed loads of $q_t = 350\text{kPa}$ on the top surface. To avoid shear locking caused by spurious transverse shear and normal stiffnesses, the convergence study is conducted using Q4 and Q8 elements with reduced integration. Both models are tested with two different

mesh sizes: 6 x 6 and 10 x 10 for the first panel, and 10 x 10 and 16 x 16 FEs for the second panel. The laminae are represented as a single numerical layer, featuring a linear distribution of displacements throughout its thickness.

The distributions of in-plane displacement u at $(0, b/2)$ and normal stresses σ_x and σ_y at $(a/2, b/2)$ through the thickness of the first (3-ply) panel are shown in Figures 9.2 and 9.3, respectively.

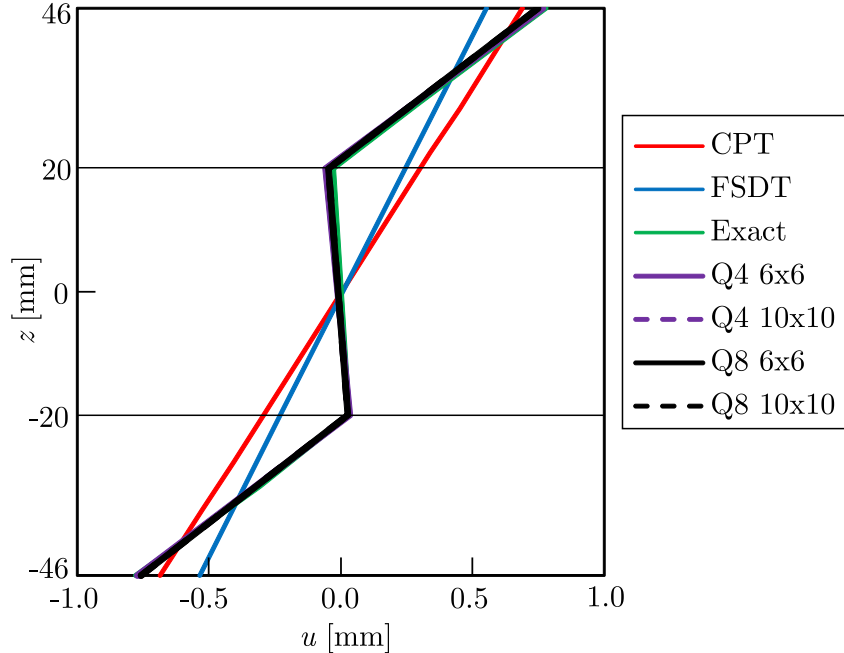


Figure 9.2: In-plane displacement (u) distribution at $(0, b/2)$ across the thickness of a 3-ply CLT panel using different computational models, element types, and mesh densities [112]

FLWT is utilized to obtain the zig-zag displacement u distribution for both element types and mesh densities (purple and black lines in Figure 9.2), which is consistent with the exact solution [152] (green lines in Figure 9.2). However, the ESL plate theories (red and blue lines in Figure 9.2) fail to reproduce the zig-zag shaped displacement distribution and only allow for the constant rotation of the line segment, thus limiting cross-section warping.

Two in-plane stress components, σ_x and σ_y , display the characteristic discontinuous shape with considerably varying slopes in the soft and stiff wood layers, across all considered models. Nevertheless, the CPT and FSDT theories underestimate the maximum normal stresses σ_x and σ_y , which could result in design errors when dealing with thick CLT panels. Specifically, the CPT theory underpredicts σ_y by 53.35% at the interface between longitudinal and transverse layers, and σ_x by 3.31% at the top and bottom interfaces of the plate. The FSDT theory also underpredicts σ_x by 23.05% at the same interfaces. In contrast, the FLWT-based models show excellent agreement with the exact solution even with the coarse mesh and relatively simple element type (Q4). The average relative difference in maximum stresses for all considered FLWT-based models is 1.71% for σ_x and 4.60% for σ_y , demonstrating the superiority of these models over CPT and FSDT theories.

Figure 9.4 displays the distribution of the considered transverse shear stresses, τ_{xz} and τ_{yz} , along the thickness coordinate z at the locations $(0, b/2)$ and $(a/2, 0)$, respectively, for the 3-ply panel. These locations correspond to where the shear stress components reach their maximum values. It's worth noting that determining transverse shear stresses in the CPT and FSDT, requires a

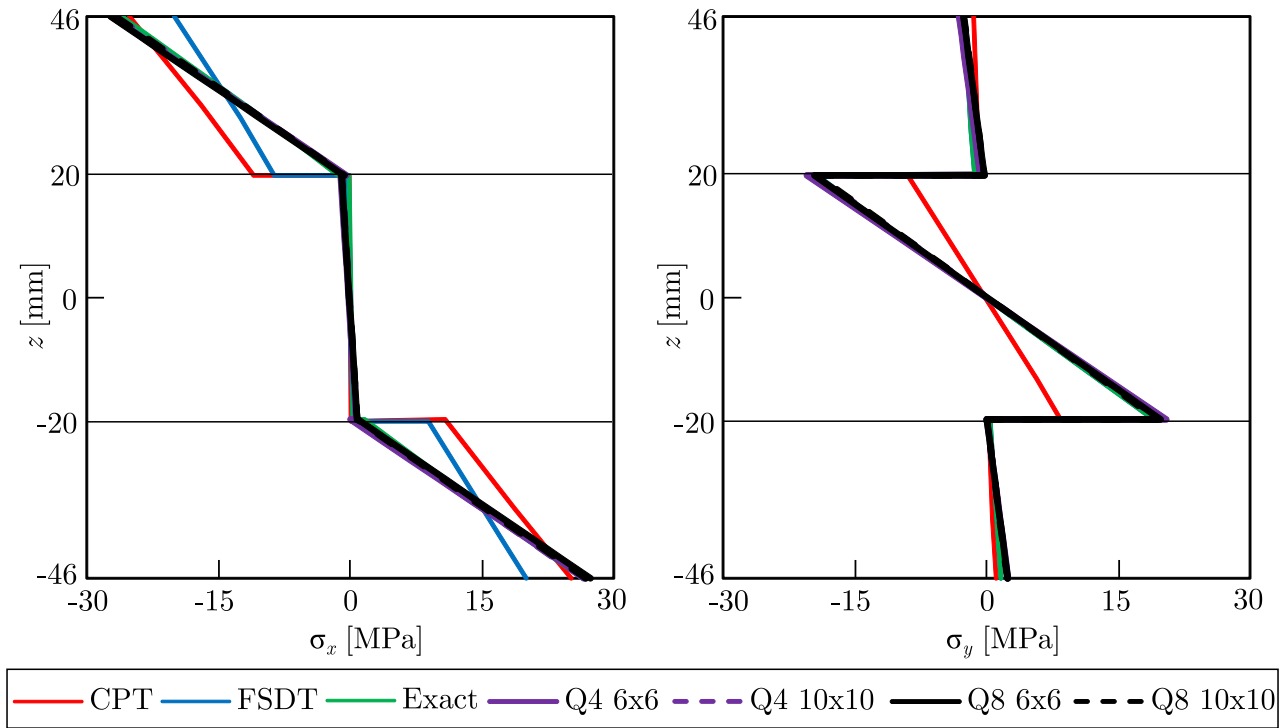


Figure 9.3: Normal stresses σ_x and σ_y distribution at $(a/2, b/2)$ across the thickness of a 3-ply CLT panel using different computational models, element types, and mesh densities [112]

post-processing (integration) procedure, which starts from the previously calculated σ_x , σ_y and τ_{xy} .

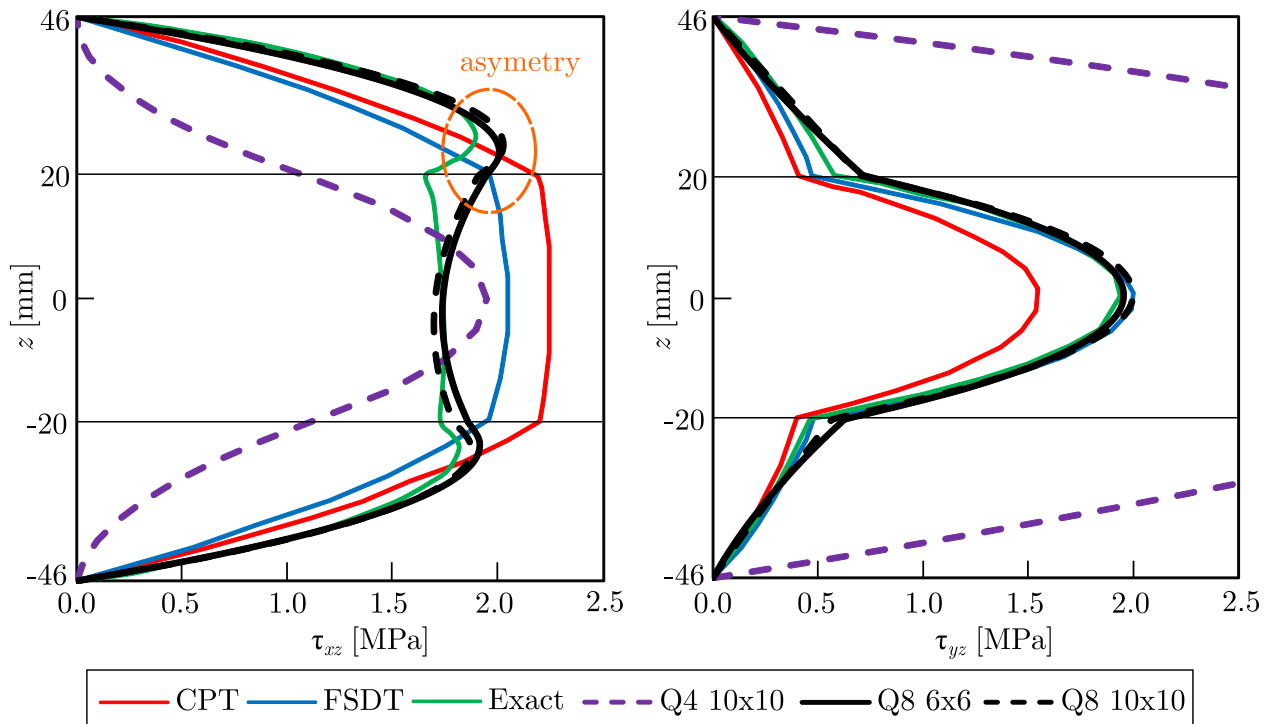


Figure 9.4: Transverse shear stresses τ_{xz} at $(0, b/2)$ and τ_{yz} at $(a/2, 0)$ distribution across the thickness of a 3-ply CLT panel using different computational models, element types, and mesh densities [112]

As expected, the correct distribution of τ_{xz} and τ_{yz} through the plate thickness cannot be represented by ESL theories. However, both the exact solution and Q8 finite element models based on FLWT exhibit the characteristic laminate-specific course of transverse shear stress distributions. The transverse shear stress distributions in the above solutions exhibit a slight asymmetry with respect to the mid-plane, as seen in Figure 9.4. This asymmetry is due to the impact of the transverse normal stress σ_z , which is neglected in the ESL plate. According to Reference [157], using FSDT to determine out-of-plane shear strains γ_{xz} and γ_{yz} can lead to unrealistic results for the corresponding transverse shear stresses τ_{xz} and τ_{yz} , due to the adoption of a relatively simple Hooke's law formula in classical timber structure design standards.

As depicted in Figure 9.4, the use of Q4 (linear) elements based on FLWT results in inaccurate predictions of transverse shear stresses, due to the reduced integration of element stiffness matrices using a relatively low number of integration points. Conversely, Q8 (quadratic) elements are capable of accurately predicting the laminate-specific distribution of transverse shear stresses. However, a slight overprediction of both maximum τ_{xz} and τ_{yz} is observed, amounting to 1.63% for a 10×10 mesh and 2.17% for a 16×16 mesh (τ_{xz}), as well as 3.41% for a 10×10 mesh and 4.55% for a 16×16 mesh (τ_{yz}). Finally, increasing the mesh density leads to a convergence of the results towards the exact solution, as observed in the decreasing trend of the relative differences of maximum transverse shear stresses with mesh refinement.

Figure 9.5 displays the plots of transverse shear strains γ_{xz} and γ_{yz} along the thickness coordinate z for the 3-ply CLT panel at locations $(0, b/2)$ and $(a/2, 0)$, respectively. It is evident that the

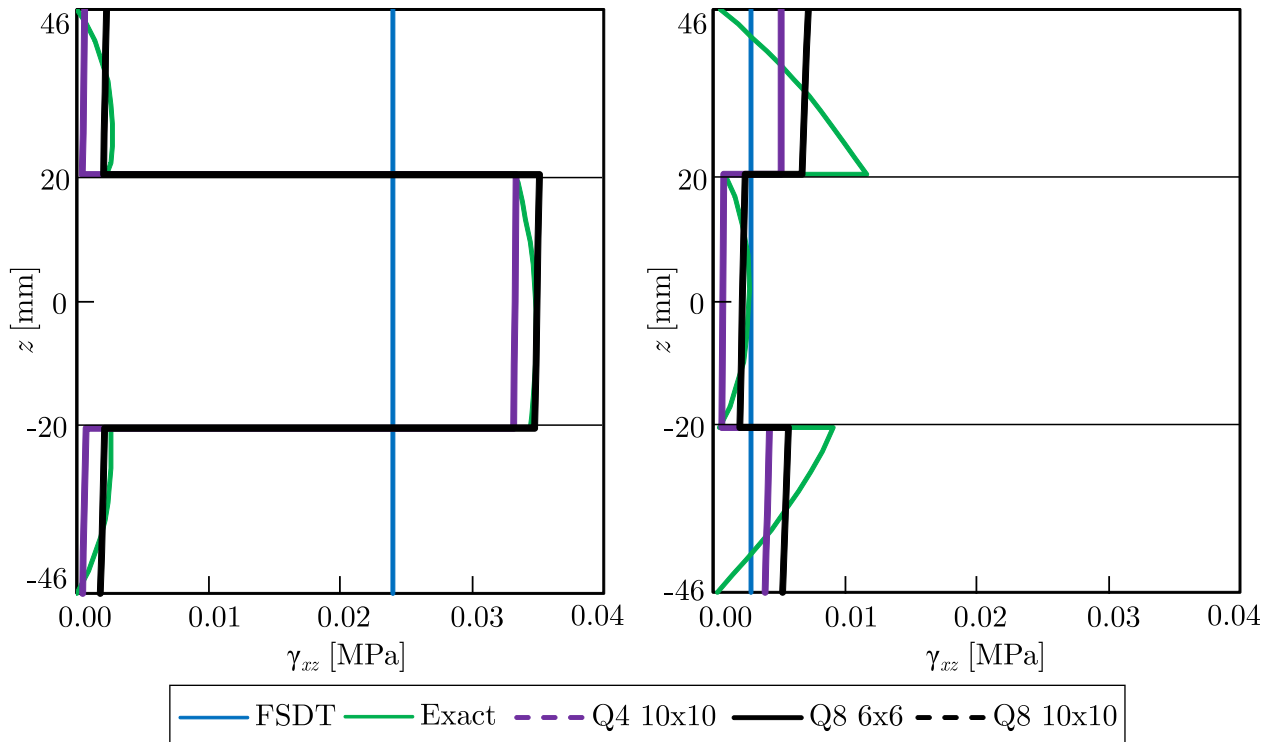


Figure 9.5: Transverse shear strains γ_{xz} at $(0, b/2)$ and γ_{yz} at $(a/2, 0)$ distribution across the thickness of a 3-ply CLT panel using different computational models, element types, and mesh densities [112]

strain field resulting from the use of FLWT is linear layerwise due to the utilization of linear $\Phi^I(z)$ functions for displacement field interpolation throughout the plate thickness. Q8 elements exhibited superior agreement of maximum strain values within a given layer when compared to

Q4 elements. It is worth noting that transverse shear strains are constant through the thickness in FSDT and zero in CPT due to the simplifications related to transverse shear deformation.

The distribution of u at the location $(0, b/2)$ is illustrated in Figure 9.6, whereas Figure 9.7 demonstrates the distribution of σ_x and σ_y at the location $(a/2, b/2)$, along the thickness of the second panel with 5 plies. The zigzag pattern of u distribution is once again obtained using

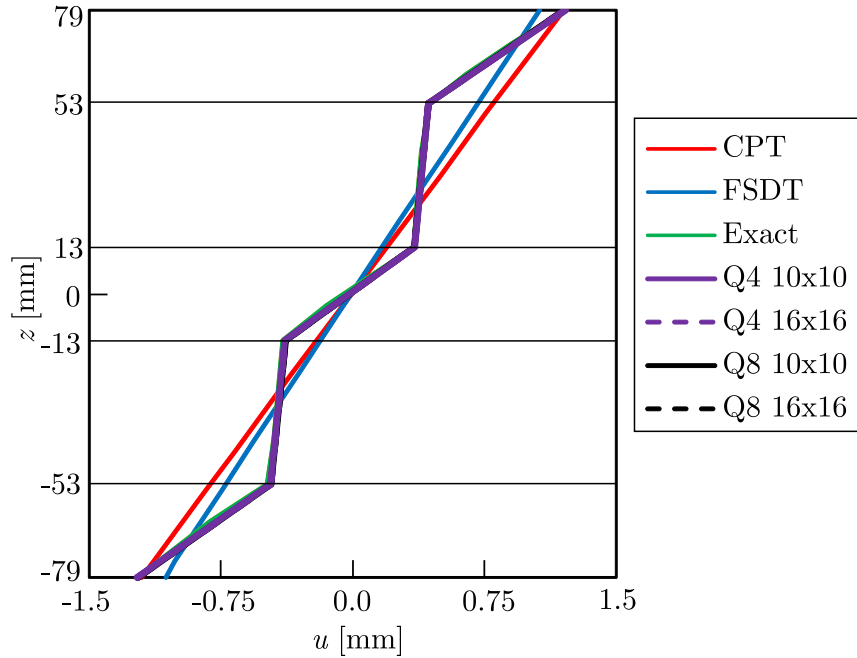


Figure 9.6: In-plane displacement u distribution at $(0, b/2)$ across the thickness of a 5-ply CLT panel using different computational models, element types, and mesh densities [112]

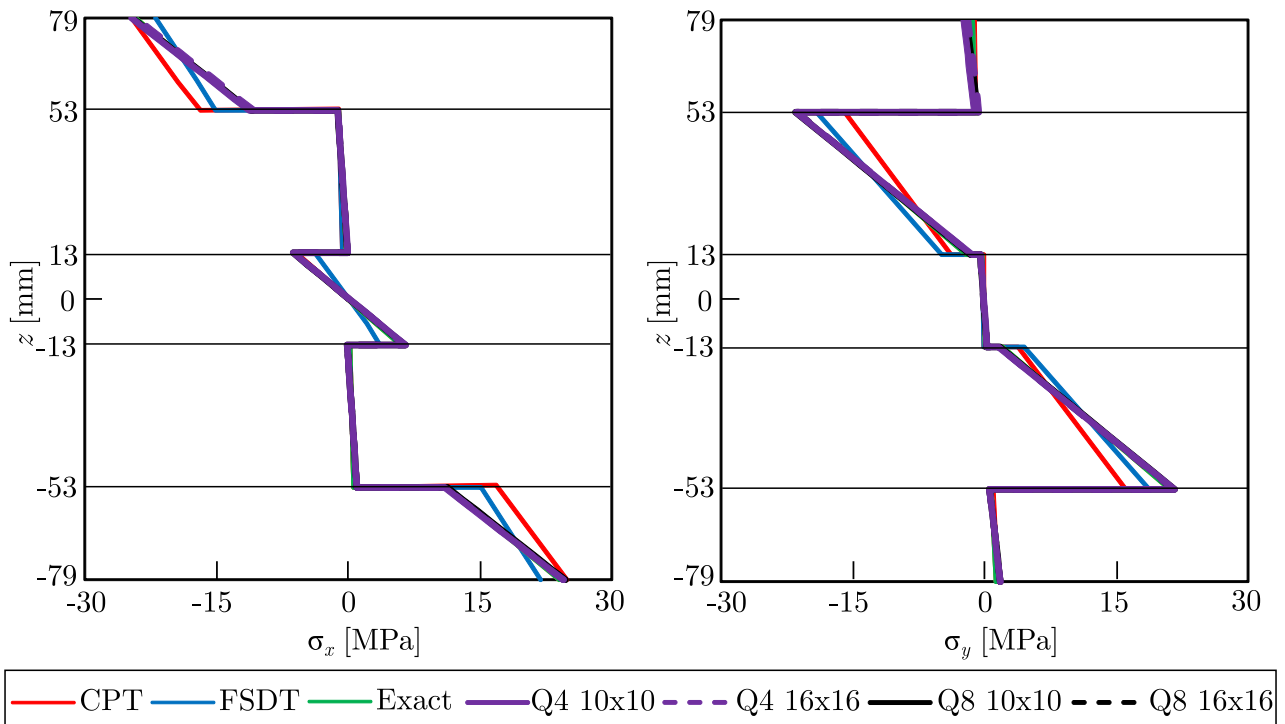


Figure 9.7: Normal stresses σ_x and σ_y distribution at $(a/2, b/2)$ across the thickness of a 5-ply CLT panel using different computational models, element types, and mesh densities [112]

FLWT. In the case of the 5-ply panel, all the models considered provide a precise estimation of the maximum normal stresses σ_x and σ_y . However, the models based on ESL do not entirely match the exact stress distribution, particularly at the interfaces between layers.

Figure 9.8 illustrates the distribution of transverse shear stresses τ_{xz} and τ_{yz} at specific locations, where they attain their maximum values. As can be seen in Figure 9.8, the ESL theories are

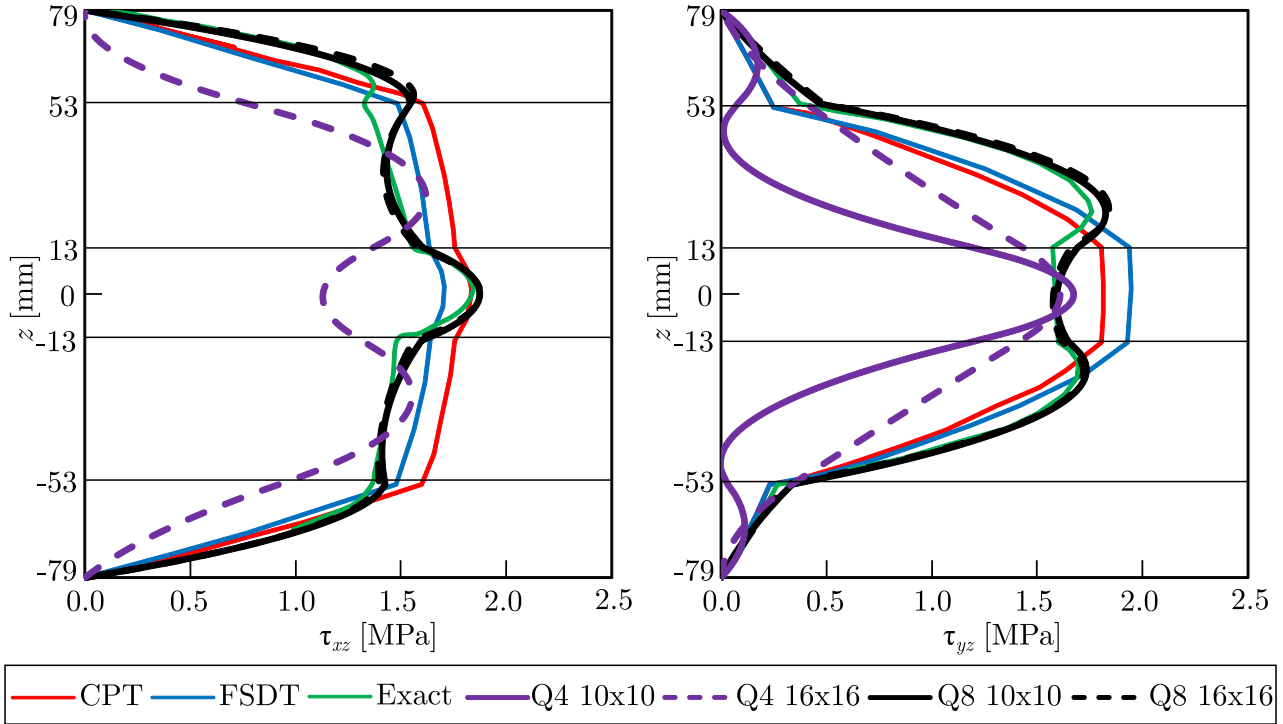


Figure 9.8: Transverse shear stresses τ_{xz} at $(0, b/2)$ and τ_{yz} at $(a/2, 0)$ distribution across the thickness of a 5-ply CLT panel using different computational models, element types, and mesh densities [112]

incapable of accurately representing the distribution of τ_{xz} and τ_{yz} , while the Q8 finite element models based on FLWT produce transverse shear stress distributions that match the exact solution. Linear (Q4) FLWT elements are unable to predict transverse shear stresses, whereas Q8 (quadratic) elements can accurately predict the laminate-specific distribution of τ_{xz} and τ_{yz} , albeit with a slight overprediction.

Figure 9.9 displays the transverse shear strains γ_{xz} and γ_{yz} for the 5-ply CLT panel. Similar to previous observations, the FLWT produces a layerwise linear strain field. Among the considered models, the Q8 elements showed better agreement in the maximum strain values within each layer than the Q4 elements. The transverse shear strains γ_{xz} and γ_{yz} are not zero due to the layerwise expansion of transverse displacement w . Additionally, the asymmetry observed is caused by the effect of transverse normal stress σ_z . Once the convergence of results for τ_{xz} and τ_{yz} due to mesh refinement is achieved, further analysis is conducted to determine the effect of model refinement in the z -direction. In both the 3-ply and 5-ply panels, a mesh consisting of 10×10 Q8 elements is used, as Q4 elements have already been shown to produce inaccurate predictions for τ_{xz} and τ_{yz} (as shown in Figures 9.4 and 9.8).

The z -refinement process involves utilizing the sublaminata concept [12], which divides each physical lamina into multiple numerical layers with identical elastic properties. In order to perform this refinement on the finite element model of the 3-ply panel, three different stacking

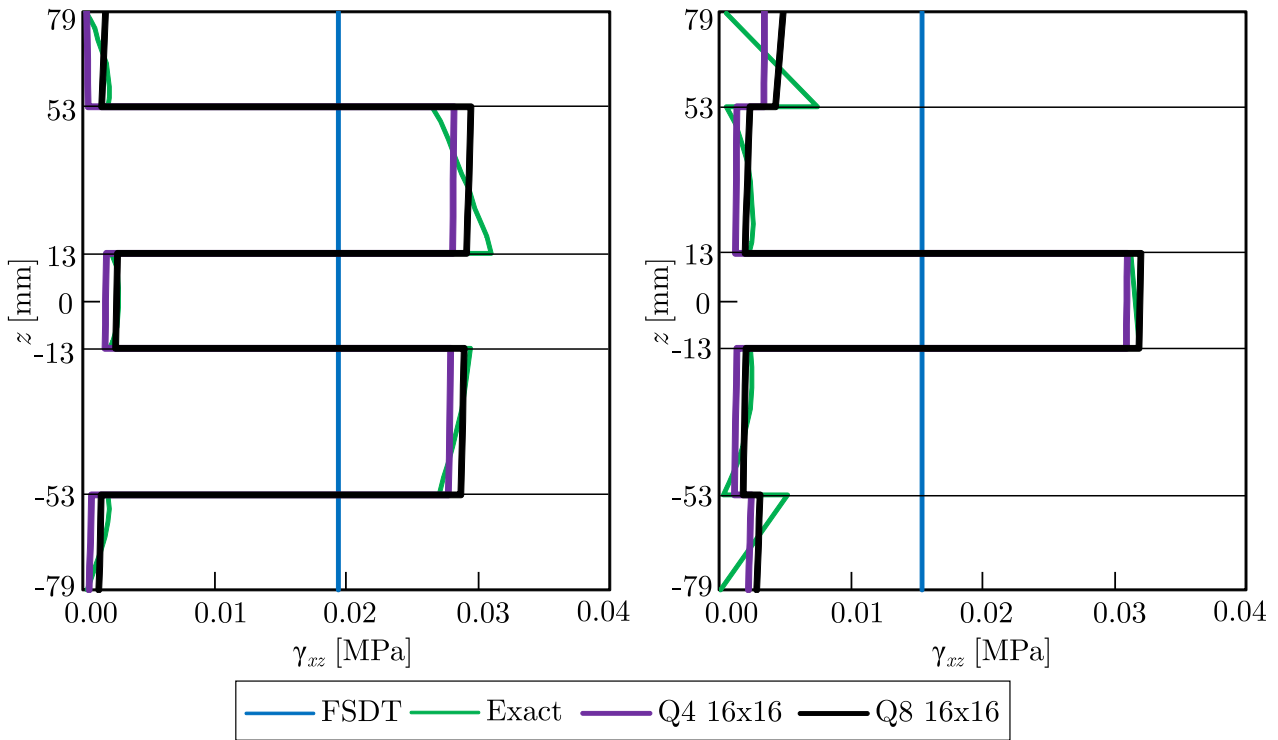


Figure 9.9: Transverse shear strains γ_{xz} at $(0, b/2)$ and γ_{yz} at $(a/2, 0)$ distribution across the thickness of a 5-ply CLT panel using different computational models, element types, and mesh densities [112]

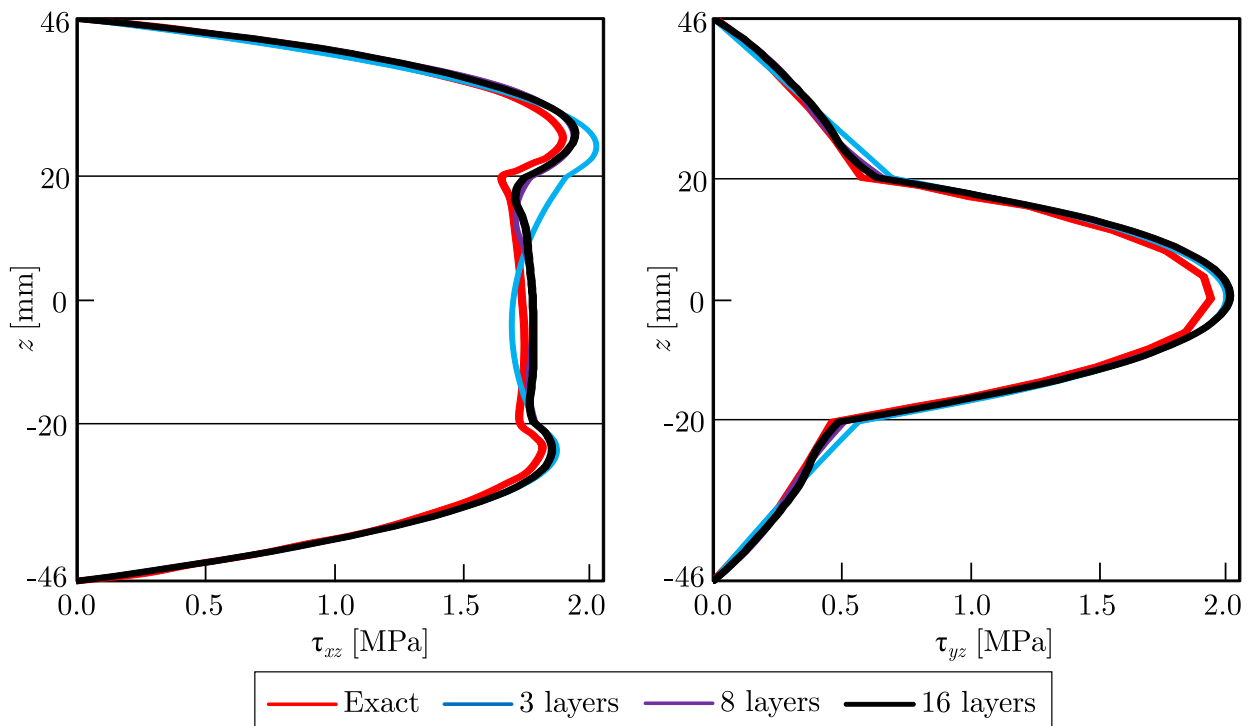


Figure 9.10: Transverse shear stresses τ_{xz} at $(0, b/2)$ and τ_{yz} at $(a/2, 0)$ distribution across the thickness of a 3-ply CLT panel using different computational models (exact solution and 10×10 mesh of Q8 elements), and different refinements in z -direction [112]

sequences [in mm] are employed: $h_3 = [26/40/26]$, $h_8 = [132/104/132]$, and $h_{16} = [6.54/5.08/6.54]$. On the other hand, the FE model of the 5-ply panel is refined using two stacking sequences: $h_5 =$

[26/40/26/40/26] and $h_{14} = [132/104/132/104/132]$. It is worth noting that the subscript used in the previous sentence indicates the number of numerical subdivisions within each physical layer. Figures 9.10 and 9.11 indicate that z -refinement results in convergence, but for practical purposes, using one numerical layer per lamina is sufficient without significant loss of accuracy.

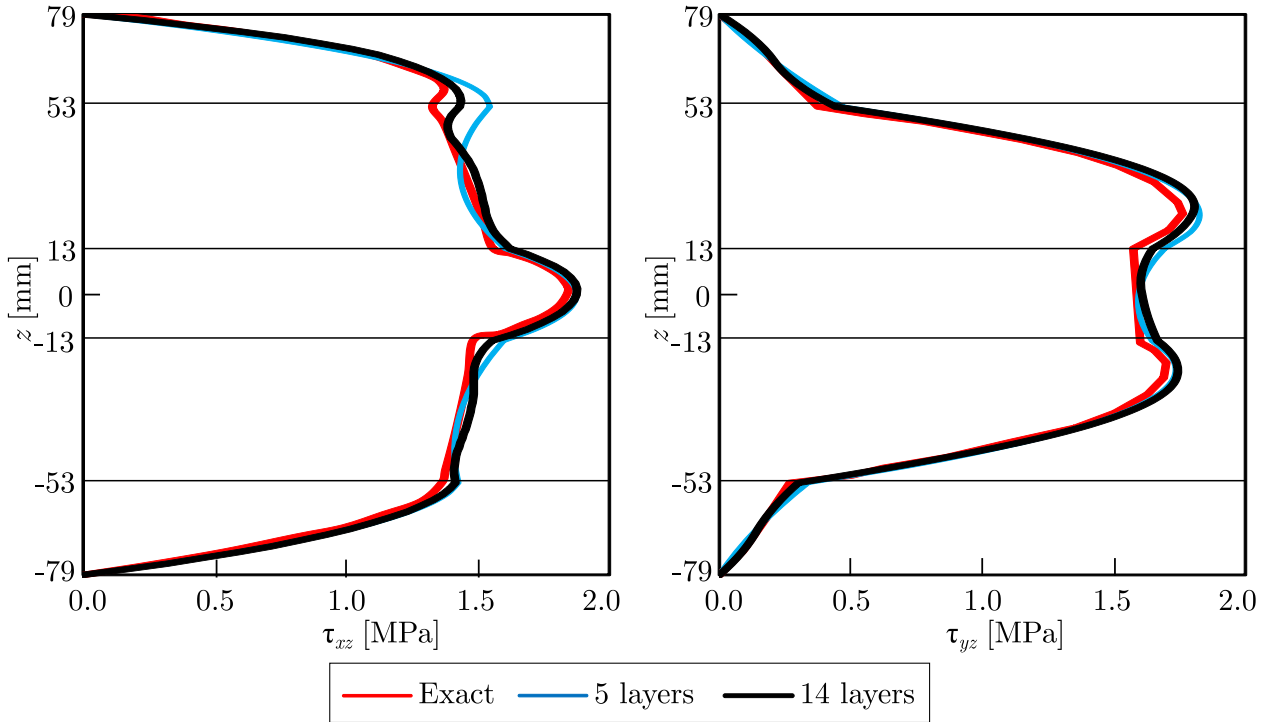


Figure 9.11: Transverse shear stresses τ_{xz} at $(0, b/2)$ and τ_{yz} at $(a/2, 0)$ distribution across the thickness of a 5-ply CLT panel using different computational models (exact solution and 10×10 mesh of Q8 elements), and different refinements in z -direction [112]

Example 9.1.2

The proposed model is further validated using the experimental data from Reference [158]. The aim is to emphasize the importance of advanced plate theories for precise stress prediction in CLT under concentrated loading. The study focuses on simply supported thin, square CLT panels ($a=b=2450$ mm) with a height of $h=[h_0/h_{90}/h_0]=[10/50/10]=70$ mm ($a/h=35$) as shown in Figure 9.12.

Table 9.2: Material properties for two considered CLT panels (C24 timber class)

	Panel 1	Panel 2
Property [MPa]	Value	Value
E_1	11500	12500
$E_2 = E_3$	575	625
$G_{12} = G_{13}$	720	780
G_{23}	70	80
ν_{12} (-)	0.49	0.49
ν_{13} (-)	0.39	0.39
ν_{23} (-)	0.64	0.64

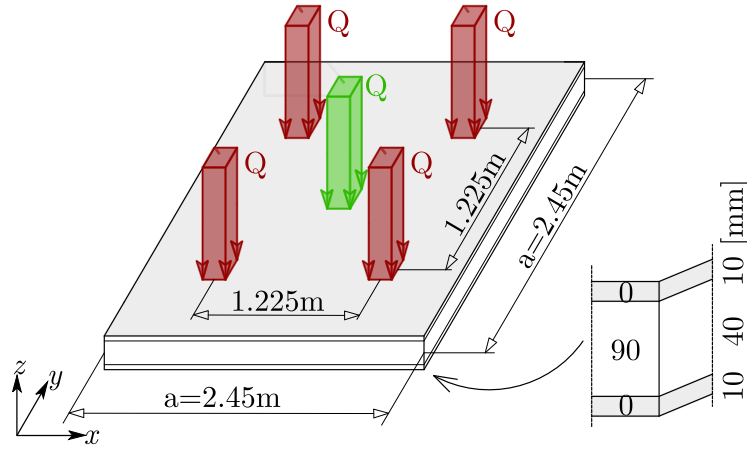


Figure 9.12: The simply supported [10/50/10]mm CLT panel loaded with $Q = 30$ kN at the plate center (loading scheme Q, green) and at four quarter points (loading scheme 4Q, red) over 150×150 mm surfaces [112]

Each layer of the CLT panel is modelled as a unidirectional lamina, using two sets of material properties based on [158] (see Table 2). The panels are subjected to concentrated loads of 30 kN applied on subareas of 150×150 mm². Two load layouts are considered: a single force at the center of the panel (Q), and four equal forces at each quarter point (4Q), as shown in Figure 9.12. The boundary conditions are set such that $U^I = W^I = 0$ for the edge parallel to the x -axis, and $V^I = W^I = 0$ for the edge parallel to the y -axis. The analysis is carried out using both Q4 and Q8 elements with reduced integration, and two different mesh sizes of 17×17 and 32×32 finite elements are considered in both models.

To compare the accuracy of the proposed model with other existing models, Figures 9.13 and 9.14 show the mean experimental data [158] for the deflection w and stress component σ_x , respectively, obtained from measurements on three replicates of each plate set. Additionally, results obtained using the analytical solution based on the FSDT from Reference [157] are also included for comparison.

The proposed model shows a slightly stiffer response of CLT panels compared to the experimental data in terms of the deflection w , as shown in Figure 9.13. The proposed model shows an average relative deviation from the measured data of -6.80%. The agreement is slightly better (-6.50%) for the 4Q loading scheme as compared to the Q loading scheme (-7.10%). The values obtained from the proposed model are expectedly lower than those of the FSDT due to the more accurate consideration of transverse shear deformation. The average deviation of the obtained results from all models, compared to the FSDT results, is -9.10%, which can be seen as the difference between the gray and blue bars in Figure 9.13.

It can be observed from Figure 9.14 that the FSDT-based results for σ_x exhibit a significant under-prediction of about 20% compared to the experimental data for all cases considered. This discrepancy can be attributed to the simplifications associated with the transverse shear deformation, which underestimated the σ_x values even for the slender plates with $a/h = 35$. The precision of the proposed model in predicting σ_x under concentrated loading is dependent on the mesh density and element type chosen. Significant deviations from the experimental data are only observed for Panel 2 under the Q loading scheme (third set of bars in Figure 9.14). Reference [96] documents that the plates in this set showed some variation in the measured elastic moduli at the bottom layers. However, for the other three sets of results, which include Panel 1 with both loading schemes and Panel 2 with loading scheme 4Q, the average relative

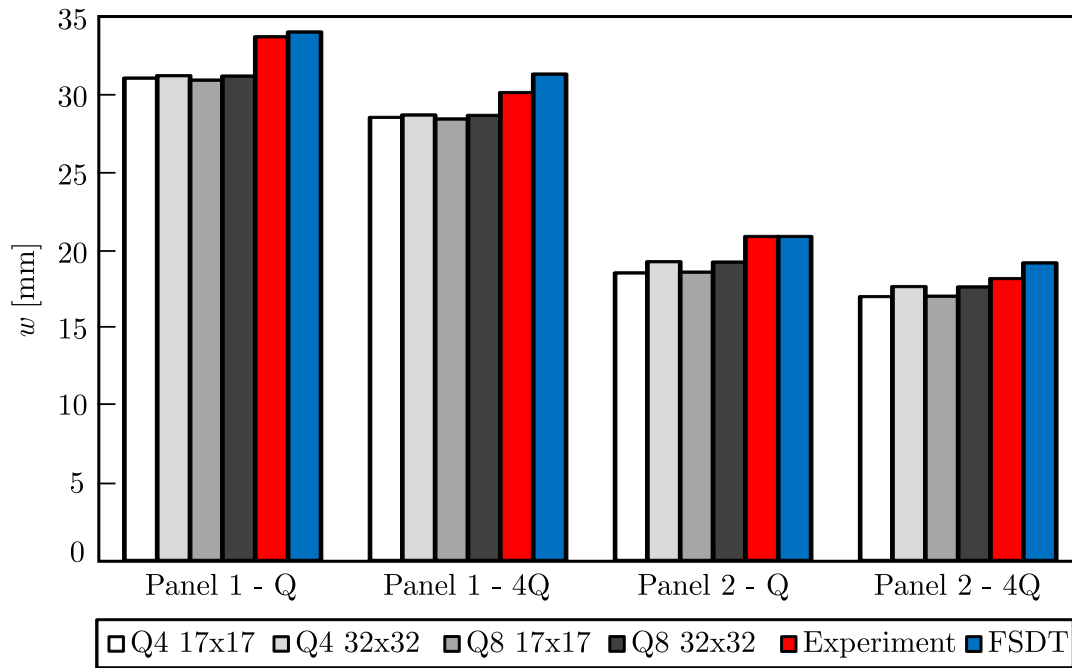


Figure 9.13: Comparison of maximum bottom-side deflections of CLT panels predicted by various finite element models, analytical (Navier) solution based on FSDT [96], and experimental results [158]

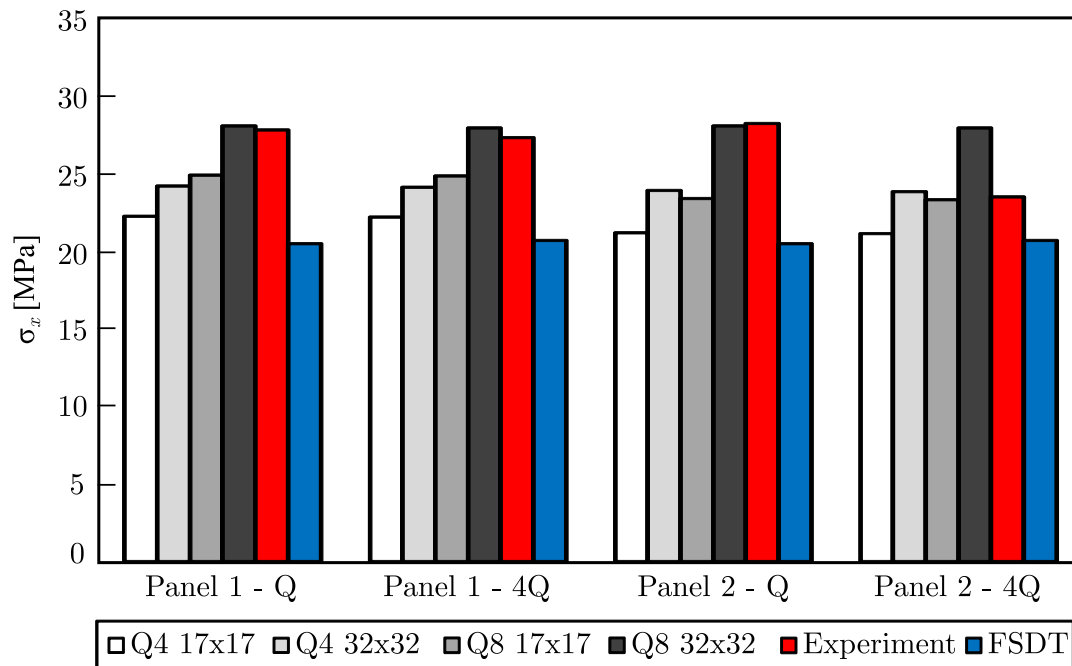


Figure 9.14: Comparison of maximum bottom-side normal stress σ_x of CLT panels predicted by various finite element models, analytical (Navier) solution based on FSDT [96], and experimental results [158]

differences for the normal stress σ_x are smaller, indicating the convergence of results and the reliability of the proposed model. Specifically, the average relative differences for these sets are -22.6% for Q4 17×17, 13.7% for Q4 32×32, 14.1% for Q8 17×17, and only 0.9% for Q8 32×32 elements.

Figure 9.15 presents the spatial distribution of stresses σ_x in Panel 1 under 4Q loading, for various mesh densities and element types generated through GiD Post-Processing module [14]. This figure demonstrates the developed framework's ability to accurately visualize the results. Additionally, the deformed shape can be visualized using GiD Post-Processor, as demonstrated in the last example.

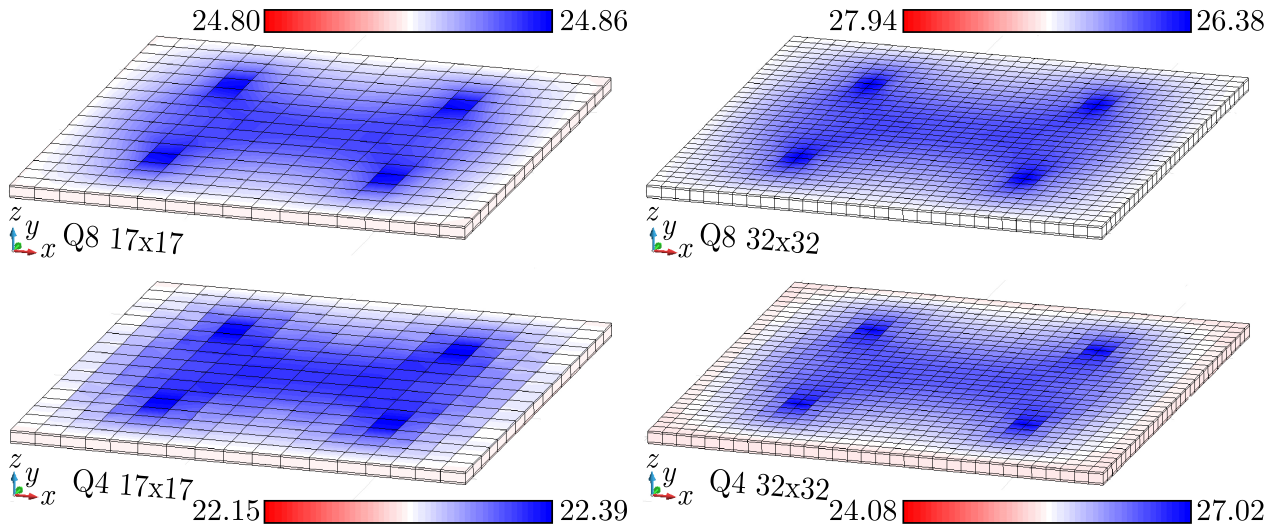


Figure 9.15: Visualization of σ_x stress distribution [in MPa] in Panel 1 subjected to 4Q loading using different mesh densities and element types (GiD Post-Processing module): Blue color denotes top interface stresses, while red color denotes bottom interface stresses [112]

Example 9.1.3

The purpose of this particular example is twofold: to demonstrate the restrictions of the standard design procedures for CLT and to establish the suitability of the proposed approach for practical engineering calculations. To achieve this, the outcomes produced by the FLWT finite elements are contrasted with those from the design procedures for CLT slabs.

The example takes into account slender and thick cross-laminated timber (CLT) panels with varying length-to-width (L/B) and length-to-height (L/h) ratios, as shown in Table 3. The panels are supported only at the y -edges (B) and are free along the x -edges (L). Each panel consists of five laminae, each with a thickness of 3 cm, resulting in L/h ratios of 33.3 for the slender panel and 16.7 for the thick panel. The individual layers are simulated as C24 unidirectional laminae, with material properties specified in Table 9.1. A uniform load of 5 kN/m² is applied to the panels. The y -edges are constrained with prescribed boundary conditions of $V^I=W^I=0$. The analysis is conducted using Q8 elements with reduced integration and an element size of 0.1 m.

Table 9.3: Dimensions L/B [m] of analysed CLT panels ($h = 5 \times 3 = 15$ cm)

Slender panel ($L/h = 33.3$)		Thick panel ($L/h = 16.7$)	
L/B	5.0/1.0	L/B	2.5/1.0
L/B	5.0/2.0	L/B	2.5/1.5
L/B	5.0/3.0	L/B	2.5/2.0
L/B	5.0/4.0	L/B	2.5/2.5
L/B	5.0/5.0	-	-

To comparison, a simplified approach commonly used in conventional codes for the design of timber structures [96, 159] was employed. Using the γ -method [96], transverse deflection w , normal stress σ_x , and transverse shear stress τ_{xz} were calculated. The stiffness properties were defined based on the effective moment of inertia $I_{0,ef}$, which is dependent on the section properties and the connection efficiency factor γ . Notably, the γ -method considers the analysed CLT slabs as equivalent beams that are 1 m wide. Subsequently, the k -method by Blass and Fellmoser [159] was employed for calculation. The composition factors k_i were utilized to account for the strength and stiffness properties of individual layers, while the slabs were once again analysed as equivalent beams that are 1 m wide.

Figures 9.16 and 9.17 depict the distributions of stress components σ_x and τ_{xz} , as well as the corresponding results obtained using the γ -method [96] and k -method by Blass and Fellmoser [159]. As the plates were subjected to cylindrical bending with S-F-S-F boundary conditions, the L/B ratio was found to have no effect on the results. As a result, the results obtained using the proposed model overlap with each other (as seen in Figures 16 and 17).

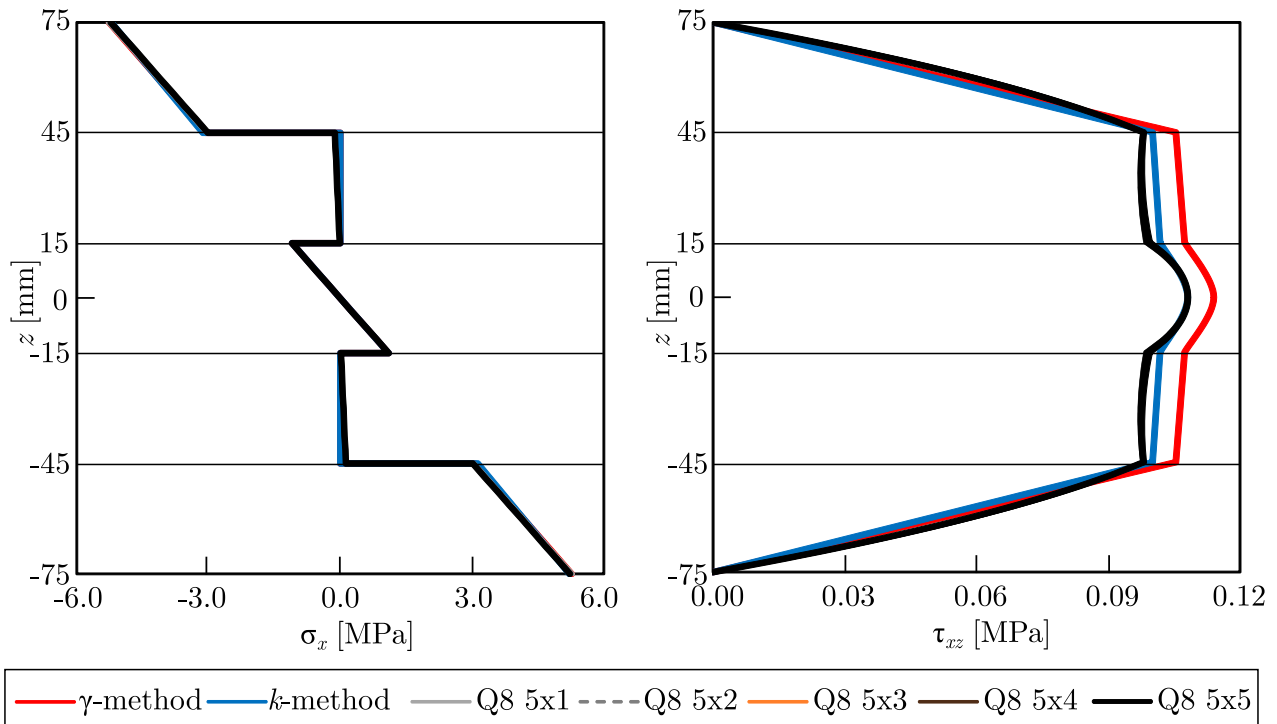


Figure 9.16: Stresses σ_x ($L/2, B/2$) and τ_{xz} ($0, B/2$) in slender panel ($L/h=33.3$) subjected to a uniformly distributed load of 5 kN/m^2 , for varying L/B ratios and design methods [112]

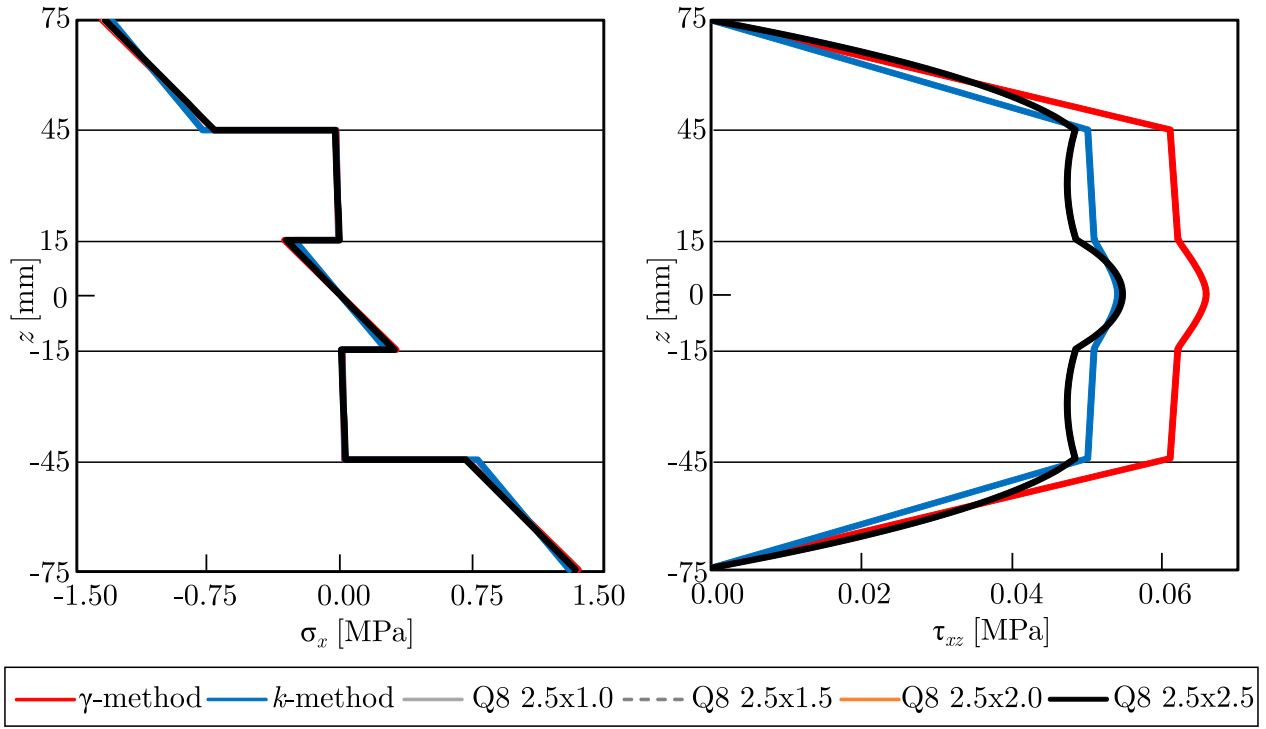


Figure 9.17: Stresses σ_x ($L/2, B/2$) and τ_{xz} ($0, B/2$) in slender panel ($L/h=16.7$) subjected to a uniformly distributed load of 5 kN/m^2 , for varying L/B ratios and design methods [112]

The normal stress σ_x exhibited excellent agreement for both slender and thick panels, across all considered L/B ratios. The maximum relative difference in σ_x for all FLWT-based models was -0.34% (compared to the γ -method) and 0.62% (compared to the k -method). The obtained solution is consistent with the one derived using the k -method, while the γ -method slightly overpredicted the transverse shear stress (by 5.56% for the slender panel). This effect was especially prominent in the case of thick plates (as seen in Figure 9.17), where the overprediction amounted to 19.64% .

Example 9.1.4

The last example demonstrates the application of the FLWT-based numerical model for solving a practical engineering problem. This will demonstrate that the proposed model has the potential to serve as an alternative to commercial software typically utilized to compute the stress-deformation state in plate-like structures with orthotropic material properties.

To demonstrate the capabilities of the FLWT-based numerical model, a complex-shaped CLT slab, consisting of 5 and 7 layers and with the geometry depicted in Figure 9.18, has been selected as a representative example. These slabs are widely used as standard floor structures in residential and commercial buildings. The CLT slabs are simply supported by the edges highlighted in red (Figure 9.18) while being free on the stairs opening and balcony edges. They are subjected to both uniformly distributed loading across the indoor and balcony sections, and a line load (from the stairs) along the free edge (shown as the blue line in Figure 9.18). The installation opening located in the upper left corner is utilized to analyse stress concentration.

The CLT slabs consist of layers of timber class C24 in accordance with EN 338 [155], resulting in a total thickness of 15 cm (5 layers) and 21 cm (7 layers), respectively, with each layer having a thickness of 3 cm . Table 9.1 provides the material properties of C24. The prescribed boundary conditions are as follows: for two edges parallel to the x -axis, $U^I=W^I=0$ is specified, while for

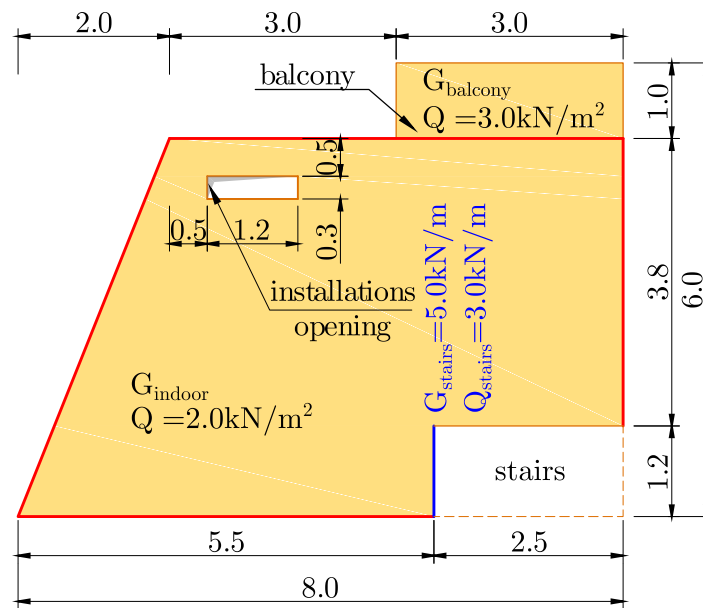


Figure 9.18: Configuration of the analyzed CLT slab with applied loads [112]

an edge parallel to the y -axis, $V^I=W^I=0$ is specified. W^I is prescribed along the skew edge on the left. The analysis utilizes Q8 elements with reduced integration and two different mesh sizes: 0.20 m and 0.10 m.

To compare, Abaqus CAE commercial software was used to generate computational models of the analyzed CLT slabs using C3D20R finite elements, which are general purpose quadratic brick elements with reduced integration and $2 \times 2 \times 2$ integration points. One brick element was generated per layer in Abaqus CAE. Table 9.4 presents the properties of the models, including the number of elements (NELEM), the number of nodes (NNODE), and the total number of degrees-of-freedom (DOF). It is worth noting that the FLWT-based model required approximately 30% fewer DOFs for the same mesh size.

Table 9.4: Computational (finite element) models properties

Model/Mesh size	5 layers			7 layers		
	N_{ELEM}	N_{NODE}	DOF	N_{ELEM}	N_{NODE}	DOF
Abaqus/0.1m	21190	100494	301482	29001	132519	397557
FLWT/0.1m	3625	11169	201042	3625	11169	268056
Abaqus/0.2m	5200	25444	76332	7420	34922	104766
FLWT/0.2m	826	2624	47232	826	2624	62976

The CLT slabs were subjected to a combination of permanent and variable loads. The permanent distributed loads were attributed to the self-weight of the CLT slab, floor layers, and walls above it, and were assigned according to Table 9.5. Additionally, a permanent line load of $G_{stair} = 5.0$ kN/m was included as a reaction force from the staircase structure. Variable distributed loads were assigned based on EN 1991-1-1 [160], with $Q_{indoor} = 2.0$ kN/m² and $Q_{balcony} = 3.0$ kN/m². A variable line load of $Q_{stair} = 3.0$ kN/m was included to account for activities on the staircases.

Table 9.5: Applied permanent distributed loads (kN/m²)

5 layers		7 layers	
Indoor	Balcony	Indoor	Balcony
2.5	2.1	2.75	2.35

The stress state is determined for the combination of design limit states 1.35G + 1.5Q. The calculation of serviceability limit state (slab deflection) is done for the exploitation load scheme 1.0G+1.0Q. As per Eurocode 5 [96], the final deflection w_{fin} is the sum of the instantaneous deflection w_{inst} and creep deflection w_{creep} :

$$\begin{aligned}
 w_{inst} &= w_G + \psi_2 w_Q = w_G + 0.3w_Q, \\
 w_{creep} &= k_{def} w_{inst} = 0.8w_{inst}, \\
 w_{fin} &= w_{inst} + w_{creep} = 1.8(w_G + 0.3w_Q) \leq \frac{L}{250} = 1.25\text{cm}
 \end{aligned} \tag{9.1}$$

where w_G represents the deflection from permanent load, w_Q represents the deflection from variable load, ψ_2 is the factor for quasi-permanent value of a variable action, and L is the span (shortest) of the CLT slab. In this example, the values of $k_{def} = 0.8$, $\psi_2 = 0.3$ and $L = 3.8$ m are adopted.

The design values of timber strength, R_d , are determined using the following equation [96]:

$$R_d = k_{mod} \frac{R_k}{\gamma_M} = 0.8 \frac{R_k}{1.25} = 0.64R_k \tag{9.2}$$

In Equation 9.2, R_k denotes the strength characteristic value, γ_M denotes the partial safety factor for material property, and k_{mod} is the modification factor considering the effect of load duration and service class. The present study adopts $k_{mod} = 0.8$ and $\gamma_M = 1.25$. Table 9.6 [161] provides the characteristic (R_k) and design strength values (R_d) of timber class C24, which is used in this example.

Table 9.6: Strength values of C24 CLT panels (MPa) for both characteristic and design values

Bending	Compression	Tension ⊥	Compression ⊥	Rolling shear
$f_{m,k} = 24.00$	$f_{c,0,k} = 21.00$	$f_{t,90,k} = 0.40$	$f_{c,90,k} = 2.5$	$f_{V,R,k} = 1.10$
$f_{m,d} = 15.36$	$f_{c,0,d} = 13.44$	$f_{t,90,d} = 0.256$	$f_{c,90,d} = 1.60$	$f_{V,R,d} = 0.704$

Initially, the computational model of a 5-layer CLT slab was used for preliminary calculations. However, the results revealed that the slab did not meet the serviceability limit state criteria due to overestimated final deflection w_{fin} . The obtained findings are presented in Table 9.7, which indicates the model's high potential in predicting the CLT slab response. Moreover, the average relative difference compared to the solid model in Abaqus was merely -0.31% for both models considered.

Table 9.7: Comparison of final deflections w_{fin} (according to Eurocode 5) of a 5-layer CLT slab using different computational models and mesh densities (negative values correspond to uplift)

Model/Mesh size	$w_{fin,max}$ (balcony) [mm]	$w_{fin,min}$ (indoor) [mm]	w_{max} [mm]
Abaqus/0.1m	-10.91	23.29	15.20
FLWT/0.1m	-10.88	23.22	
Abaqus/0.2m	-10.91	23.27	
FLWT/0.2m	-10.87	23.18	

The next step involved conducting a computational analysis on a 7-layer CLT slab, which resulted in satisfactory deflection values as shown in Table 9.8. The comparison with the solid model in Abaqus revealed an average relative difference of only -0.16% for both models.

Table 9.8: Comparison of final deflections w_{fin} (according to Eurocode 5) of a 7-layer CLT slab using different computational models and mesh densities (negative values correspond to uplift)

Model/Mesh size	$w_{fin,max}$ (balcony) [mm]	$w_{fin,min}$ (indoor) [mm]	w_{max} [mm]
Abaqus/0.1m	-4.35	10.10	15.20
FLWT/0.1m	-4.34	10.07	
Abaqus/0.2m	-4.34	10.09	
FLWT/0.2m	-4.34	10.08	

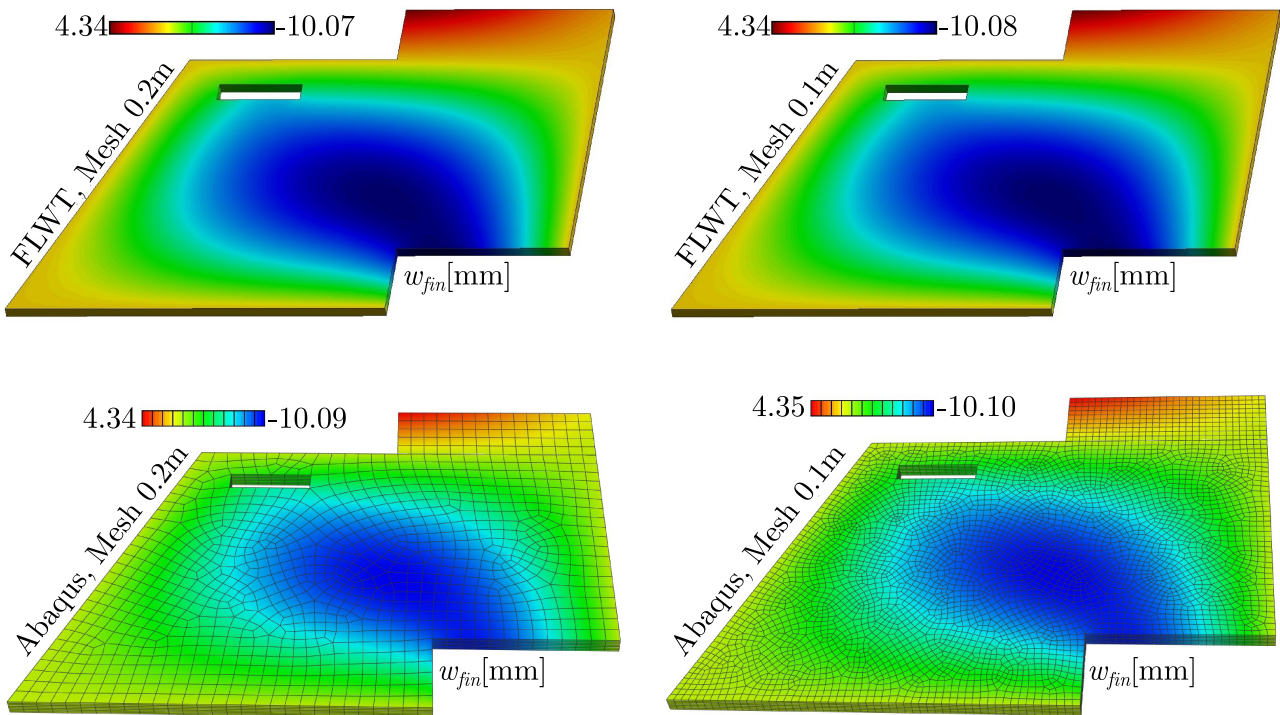


Figure 9.19: Comparison of final deflection w_{fin} [in mm] spatial distribution in 7-layers CLT slab using different computational models and mesh densities [112]

To demonstrate the ability of the object-oriented software framework to display the spatial distribution of deflections in a CLT slab, the final deflection w_{fin} (computed using Q8 elements) is visualized using GiD and compared to the results obtained from Abaqus CAE in Figure 9.19. Figure 9.19 shows that there is an excellent agreement between the two methods, with an average relative difference of only 0.198% for the maximum w_{fin} . It is worth noting that the corner of the balcony is rising.

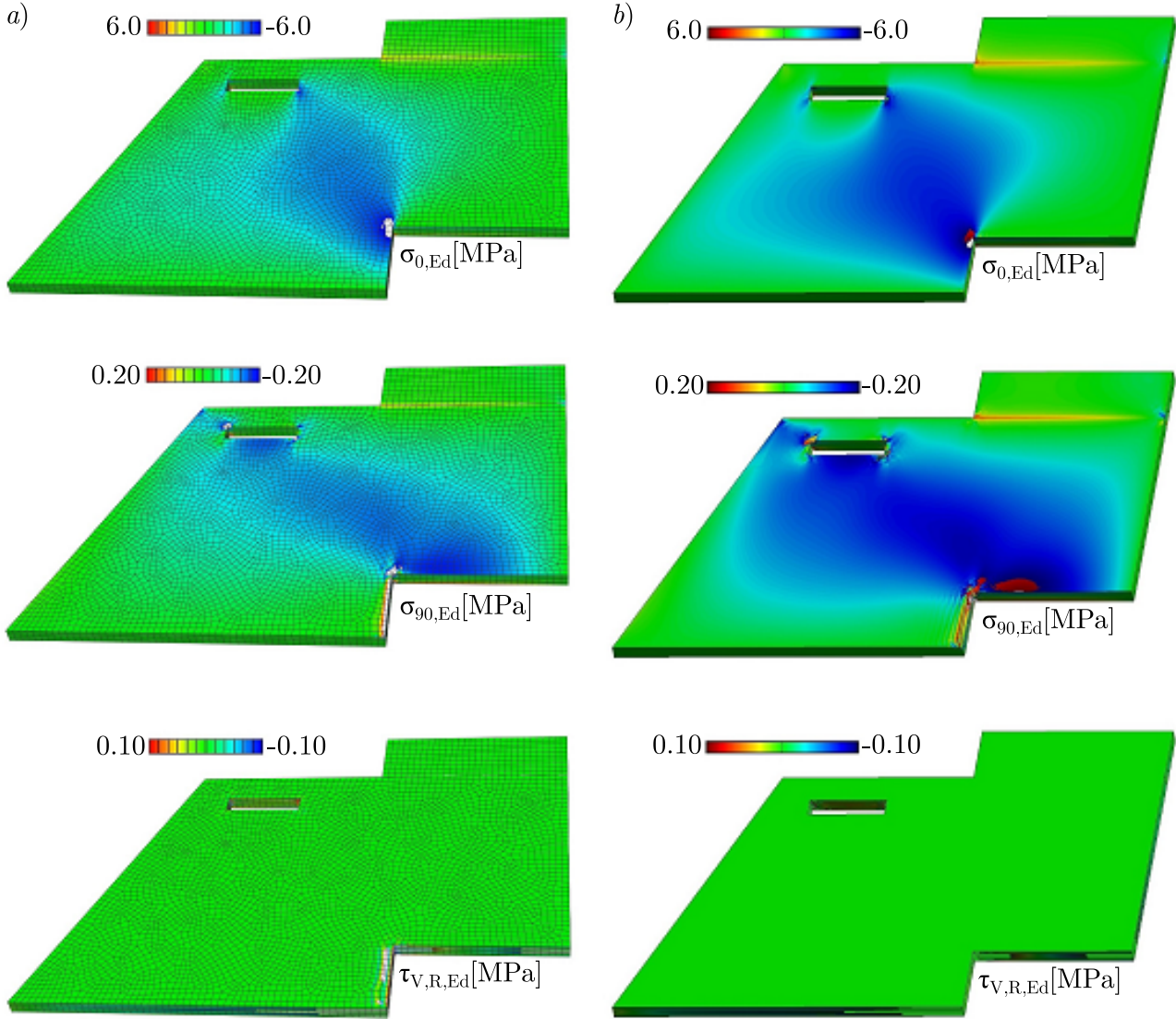


Figure 9.20: Comparison of spatial distributions of stresses S11, S22 and S23 (design stress values - E_d) obtained using: a) Abaqus; b) proposed FLWT-based mode, for a 0.1m mesh [112]

After verifying the serviceability limit state, the ultimate limit state was checked. This was done by comparing the design values of tension and compression stresses parallel to the grain ($\sigma_{0,Ed}$), tension and compression stresses perpendicular to the grain ($\sigma_{90,Ed}$), and rolling shear stress ($\tau_{V,R,Ed}$) against their corresponding design strength values $f_{m,d}$, $f_{90,d}$, and $f_{V,R,d}$ listed in Table 9.5. The analysis demonstrated that the 7-layers slab being studied passed the stress checks and can be utilized as the floor structure.

Figures 9.20 show the spatial distributions of stresses σ_1 (which is equal to σ_0), σ_2 (equal to σ_0) and τ_{23} (equal to $\tau_{V,R}$ – rolling shear) (design values - E_d) in the local (123) coordinate system obtained using both Abaqus and the proposed FLWT-based model. To simplify the

presentation, stress concentrations near geometrical discontinuities are excluded from the Figure 9.20. Moreover, the distributions of σ_3 , τ_{12} , and τ_{13} are not included as they are relatively small and not relevant to the design of the CLT slab under consideration. The results demonstrate excellent agreement between the FLWT-based model and Abaqus, as evident from the Figure 9.20.

9.2 Progressive failure analysis of open-hole laminar composites in tension

In this section, the FLWT-SCB prediction model is utilized to predict damage progression and tensile strength of an open-hole laminar composite measuring 203.2×25.4 mm, with a 6.35 mm diameter hole in the middle. The first laminate, denoted as L1, comprises 8 layers arranged in a $[0^\circ/45^\circ/-45^\circ/90^\circ]_s$ stacking sequence. Each layer has a thickness of $h_i = 0.15$ mm and is simulated as a T700/epoxy unidirectional lamina using mechanical properties from Yoon et al. [72] (see Table 9.9). For the tensile test, one side of the laminate was clamped, and the opposite side was loaded using a 2 mm displacement (see Figure 9.21).

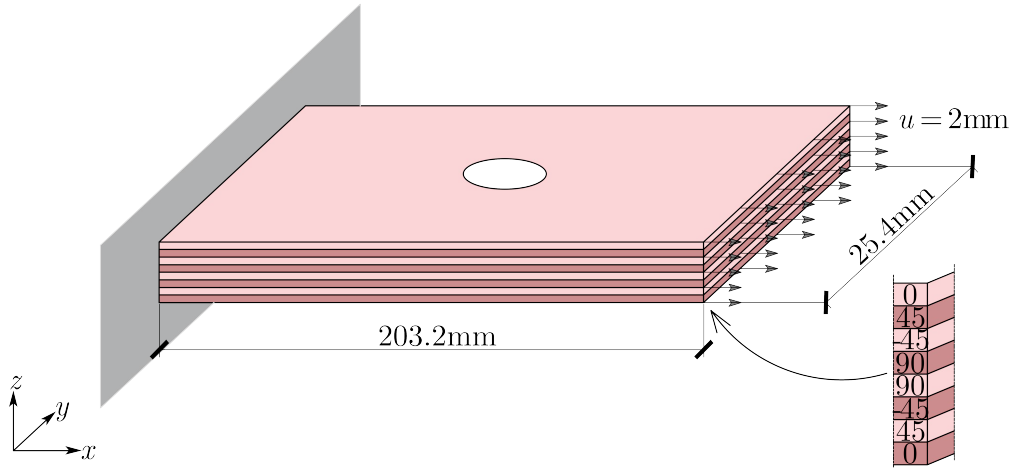


Figure 9.21: Geometry and boundary conditions for an open-hole composite laminate 203.2×25.4 mm [13]

To decrease the number of elements, only half of the laminate thickness was modelled since the stacking sequence is symmetrical. At the clamped end, all degrees of freedom (DOFs) were constrained, while displacements in the thickness direction were set to zero in the symmetry plane. The laminae are represented as a single numerical layer, utilizing a linear distribution of displacements along the lamina thickness. To validate the FLWT-SCB prediction model, the results were compared against the experimental load-displacement curves and strain diagram obtained by Yoon et al. [72]. In addition, an extra numerical study was presented to examine the impact of laminate orthotropy and specimen size on the tensile strength of open-hole laminar composites.

Table 9.9: Material properties for T700/epoxy composite material

Property	Value
E_1 (GPa)	147.7
$E_2 = E_3$ (GPa)	8.52
$G_{12} = G_{13}$ (GPa)	4.59
G_{23} (GPa)	3.91
$\nu_{12} = \nu_{13}$	0.3
ν_{23}	0.38
X_t (MPa)	2737
X_c (MPa)	1600
$Y_t = Z_t$ (MPa)	51.32
$Y_c = Z_c$ (MPa)	201.08
$S = T$ (MPa)	81
R (MPa)	65
G_{ft} (KJ/m ²)	180
G_{fc} (KJ/m ²)	100
G_{mt} (KJ/m ²)	0.3
G_{mc} (KJ/m ²)	1.71

9.2.1 Model validation and mesh dependency study

In the first subsection, the influence of mesh size on the finite element solution is analysed, to confirm the effectiveness of the proposed strategy compared to the GSM suggested by Reddy et al. [40]. Consequently, the FLWTFEM framework incorporates the GSM model, and a fixed value of SRC is selected as 0.5. As stress concentrations caused by holes can result in localized damage at the hole edges, only a narrow area surrounding the circular hole is refined with smaller elements, resulting in a significant reduction in the number of DOFs for the examined problem. To quantify the mesh dependency, four distinct meshes are considered around the circular hole (see Figure 9.22).

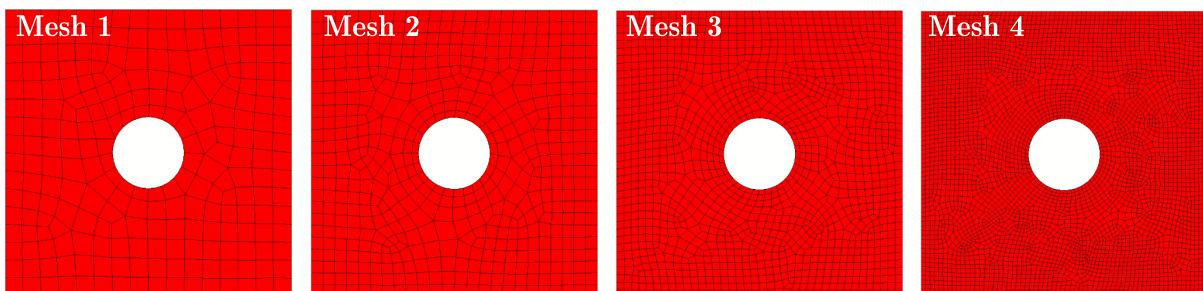


Figure 9.22: Four meshes generated around the circular hole of an open-hole composite laminate 203.2 x 25.4 mm (hole diameter 6.35 mm): Mesh 1: 16 elements; Mesh 2: 24 elements; Mesh 3: 36 elements; Mesh 4: 64 elements [13]

Figure 9.23 illustrates the load-displacement curves predicted using four different methods, including the developed FLWT-SCB framework, Reddy's GSM damage model, experimental data, and Yoon's PFA damage model. Various mesh densities shown in Figure 9.22 have been considered.

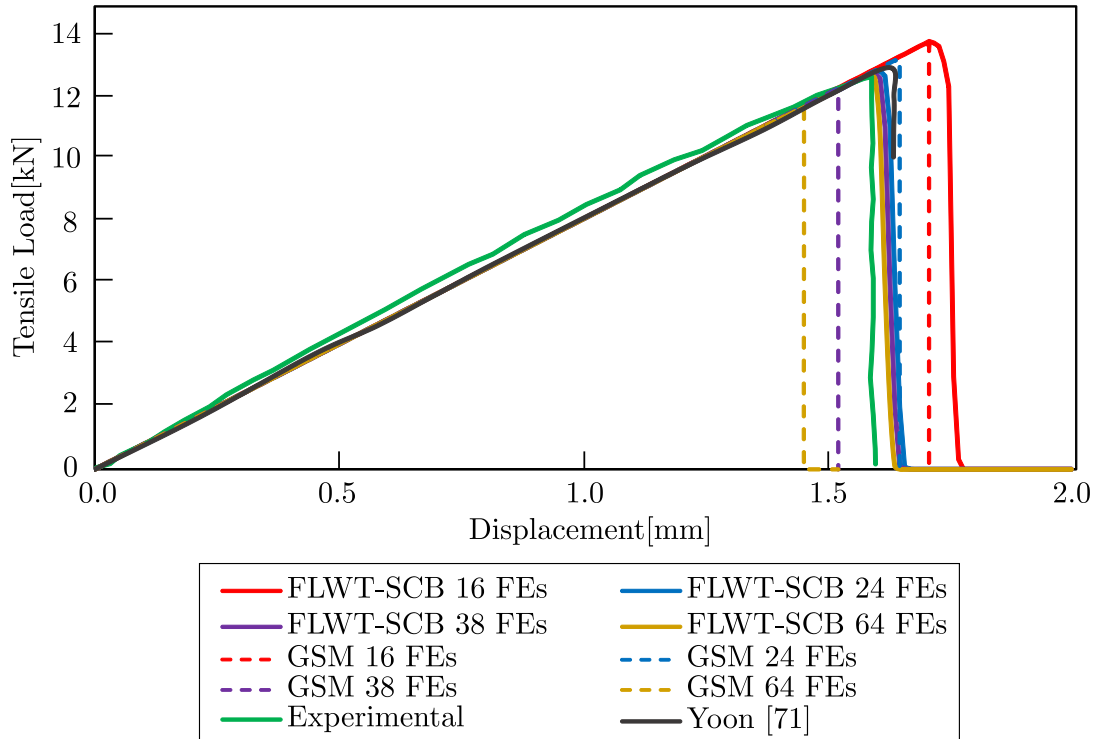


Figure 9.23: Tensile load - displacement curves considering different mesh densities and damage models of an open-hole laminar composite with $[0^\circ/45^\circ/-45^\circ/90^\circ]_s$ stacking sequence [13]

The load-displacement curves in Figure 9.23 demonstrate the brittle behaviour of the tensile specimen, characterized by a linear elastic increase in load up to the peak value, after which there is an abrupt loss of stiffness leading to failure. Reddy's GSM solutions were found to be strongly dependent on mesh density (dashed lines in Figure 9.23), resulting in a reduction in external work for failure as element size decreased. The reason for this is that the energy dissipation is directly related to the volume of the failed element instead of the fractured surface area. As a result, as the mesh becomes more refined, the energy dissipation tends to decrease towards zero.

The load-displacement curves obtained by the FLWT-SCB framework exhibit a notable difference from Reddy's GSM. Specifically, the responses observed from Mesh 2 onwards (represented by the blue, purple, and gold solid lines in Figure 9.23) are not influenced by mesh refinement. This is because the FLWT-SCB framework adjusts the equivalent strain at the final failure state $\varepsilon_{J,eq}^f$ (Eq. 6.1) in a manner that maintains the fracture energy for every failure mode, instead of keeping it constant. As a result, each element fails based on the constant fracture toughness, G_J , irrespective of its size. The obtained results show a better level of agreement with experimental data [72] (green line in Figure 9.23), compared to Yoon's PFA damage model (black line in Figure 9.23) [72]. When comparing the maximum load of FLWT-SCB to the experimental data, the average relative differences are: 9.01% for Mesh 1, 1.5% for Mesh 2, 0.86% for Mesh 3, and 0.49% for Mesh 4. On the other hand, Yoon's PFA damage model has an average relative difference of 2.35% when compared to the experiment's maximum load. Also, the FLWT-SCB prediction model offers a solution that converges for a coarser mesh with

24 elements around the circular hole, compared to Yoon's PFA damage model which used 32 elements. This results in enhanced computational efficiency without sacrificing accuracy. The reason for this improvement is attributed to the utilization of Q8 layered quadrilateral elements with linear extension in the FLWT-SCB damage model, whereas Yoon et al. [72] employed linear solid elements in ABAQUS. The results obtained from Mesh 1, which is a very coarse mesh, exhibit some over-prediction because the equivalent displacement at the final failure state ($\varepsilon_{J,eq}^f$) is lower than that at the initial failure state ($\varepsilon_{J,eq}^0$). This is caused by the fact that the elements in Mesh 1 may possess more elastic energy during failure initiation than the energy required to generate a crack passing through them. As a result, the PFA proceeds by maintaining $\varepsilon_{J,eq}^f$ equal to ($\varepsilon_{J,eq}^0$) for the affected element. Alternatively, the issue could be due to the ply element's excessive size in Mesh 1, which prevents it from capturing the stress concentration around the hole, resulting in an underestimation of the stress around the hole, which delays failure initiation. Furthermore, Figure 9.24 illustrates the load-displacement behaviour of a $[0^\circ/45^\circ/0^\circ/-45^\circ]_s$

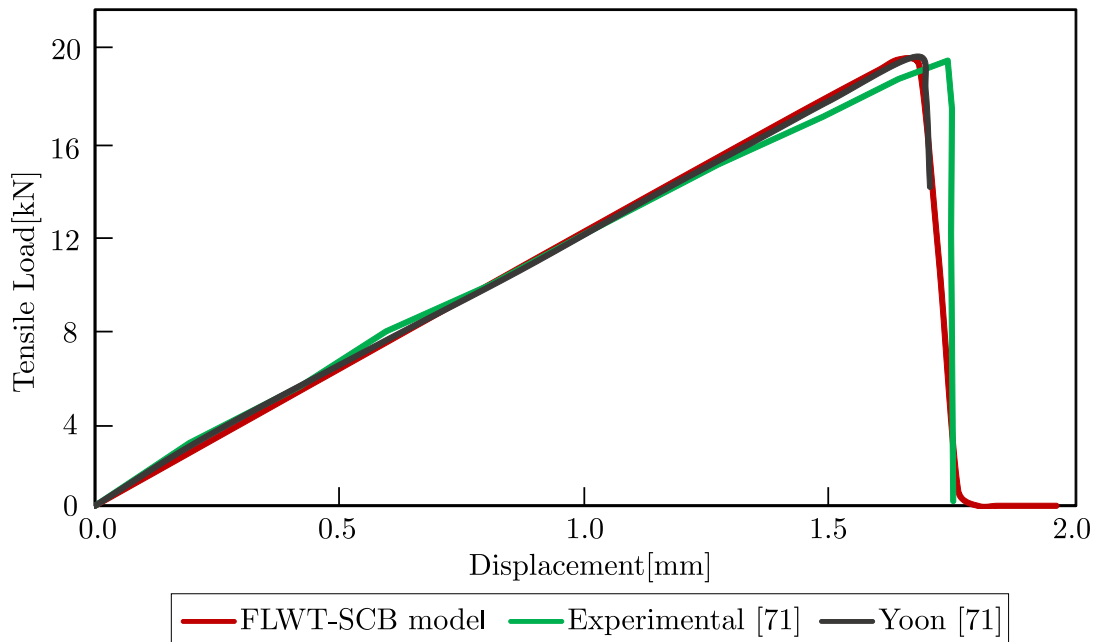


Figure 9.24: Tensile load - displacement curves of an open-hole composite laminate with $[0^\circ/45^\circ/0^\circ/-45^\circ]_s$ stacking sequence, considering different numerical models and the experimental data [13]

laminates, using Mesh 2, to confirm the accuracy of the model for an extra stacking sequence. The outcome indicates exceptional consistency with both experimental results [72] and Yoon's PFA model [72].

In order to assess the predicted strain distribution of the developed SCB damage model, a spatial plot of longitudinal strain ε_1 at the final failure, considering Mesh 2, is presented in Figure 9.25. The purpose was to compare the results with experimental data obtained from digital image correlation (DIC) [72] and those from the PFA damage model [72]. The capability of the developed framework to visualize the results accurately is also demonstrated in Figure. Due to the geometric discontinuity, causing stress concentration, the strain values are mainly concentrated near the open hole. It can be observed that the overall longitudinal strain distribution is similar among all three models. The FLWT-SCB model exhibits a maximum strain value of 0.01879, which shows excellent agreement with the experimental value (with an average relative difference of 4.16%).

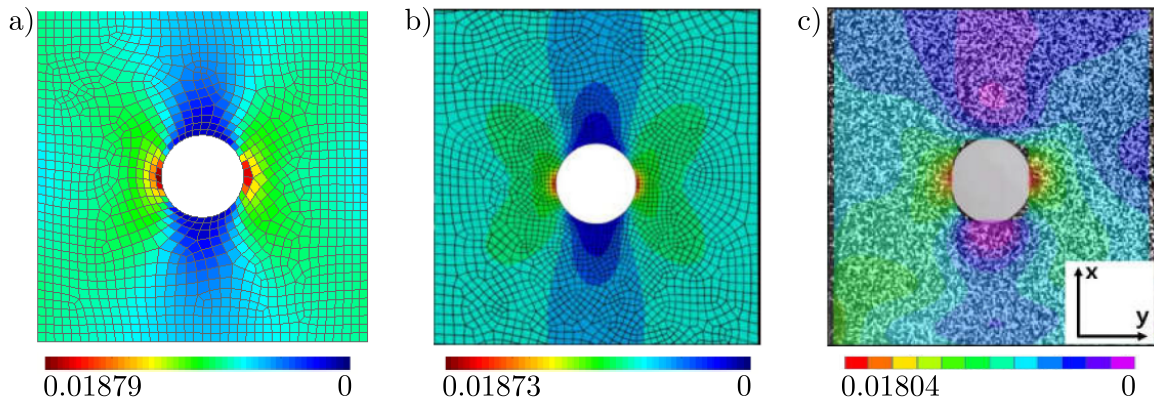


Figure 9.25: Longitudinal strain distribution of an open-hole laminar composite, at the final failure, obtained from: a) FLWT-SCB prediction model; b) PFA damage model [72]; c) DIC analysis [72]

Figure 9.26 displays contour plots of both the matrix (d_{mt}) and fiber tension damage variable (d_{ft}) in all plies (for Mesh 2) at the time when (d_{mt}) reaches 1 for the first time. This occurs in the element located along the open-hole edge in a 0° ply when the specimen's extension reaches 1.4 mm. At that point, the 90° ply displays a distinct matrix crack pattern in the shape of an "X". This is due to its bonding with the -45° plies, causing stress concentrations from the -45° plies to transfer onto the 90° ply and form the "X" shaped region.

Figure 9.27 shows contour plots of the matrix (d_{mt}) and fiber tension damage variable (d_{ft}) for all plies at the time point when (d_{ft}) first reaches 1, which occurs after the load reaches its maximum value and starts decreasing. Fiber failure causes several elements concentrated in the hole zone across the width of the 0° ply to completely fracture, and the fiber failure propagates from the circular hole towards the "X" shaped area in the 0° ply. Upon initiation of fiber failure in the 0° ply, the resulting stresses are transferred to the undamaged material in the 45° ply above, causing a similar fiber failure pattern in that ply. At that moment, there is extensive matrix cracking observed in both the $\pm 45^\circ$ plies and the 90° ply (refer to the first row of Figure 9.27, middle). As anticipated, the 0° ply has minimal matrix cracking, whereas the 90° ply shows severe matrix cracking (first row of Figure 9.27, middle) and hardly any fiber breakage (second row of Figure 9.27, middle).

9.2.2 The orthotropy impact on the tension strength of laminar composite

In this subsection, following the model validation, numerical investigations were conducted to examine the impact of orthotropy on the open-hole tension strength of composite laminates. This was accomplished by varying the ply orientation near the mid plane (90° ply) of the quasi-isotropic laminate L1. The degree of orthotropy was defined by the laminate orthotropy ratio, E_x/E_y , with the x -axis representing the direction of the applied load. Seven laminates with varying stacking sequences were analysed, and Table 9.10 provides additional information on each of these laminates.

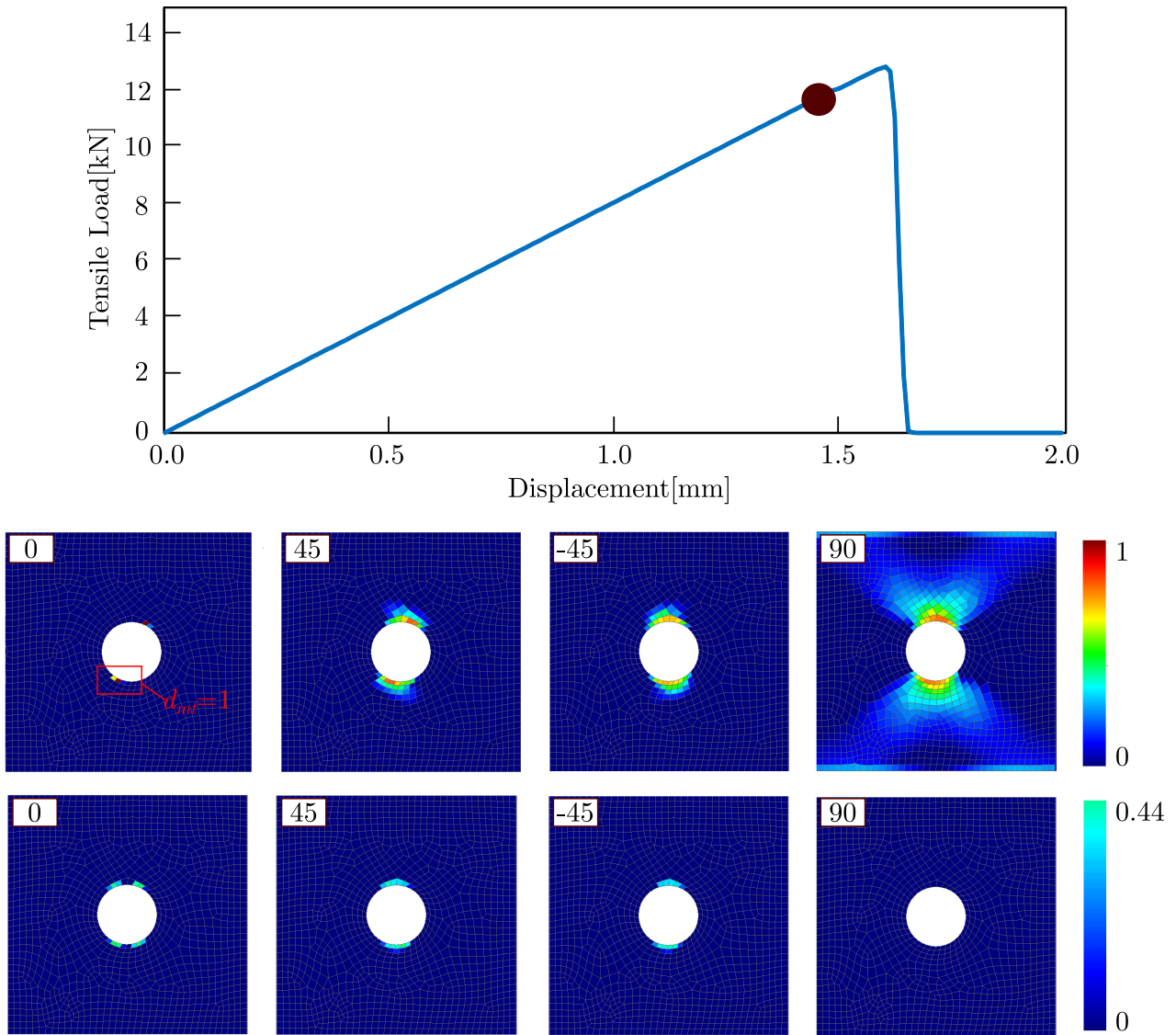


Figure 9.26: bottom: Matrix (first row) and fiber tension failure patterns (second row) plotted using FLWTFEM at the time point when the first element reaches $d_{mt}=1$, for an open-hole laminar composite 203.2 x 25.4 mm with a central hole; top: considered time point when $d_{mt}=1$ [13]

Table 9.10: Laminate stacking sequences and orthotropy ratios

Label	Stacking sequences	E_x/E_y
L1	$[0^\circ/45^\circ/-45^\circ/90^\circ]_s$	1.00
L2	$[0^\circ/45^\circ/-45^\circ/75^\circ]_s$	1.08
L3	$[0^\circ/45^\circ/-45^\circ/60^\circ]_s$	1.37
L4	$[0^\circ/45^\circ/-45^\circ/45^\circ]_s$	1.97
L5	$[0^\circ/45^\circ/-45^\circ/30^\circ]_s$	2.79
L6	$[0^\circ/45^\circ/-45^\circ/15^\circ]_s$	3.41
L7	$[0^\circ/45^\circ/-45^\circ/0^\circ]_s$	3.60

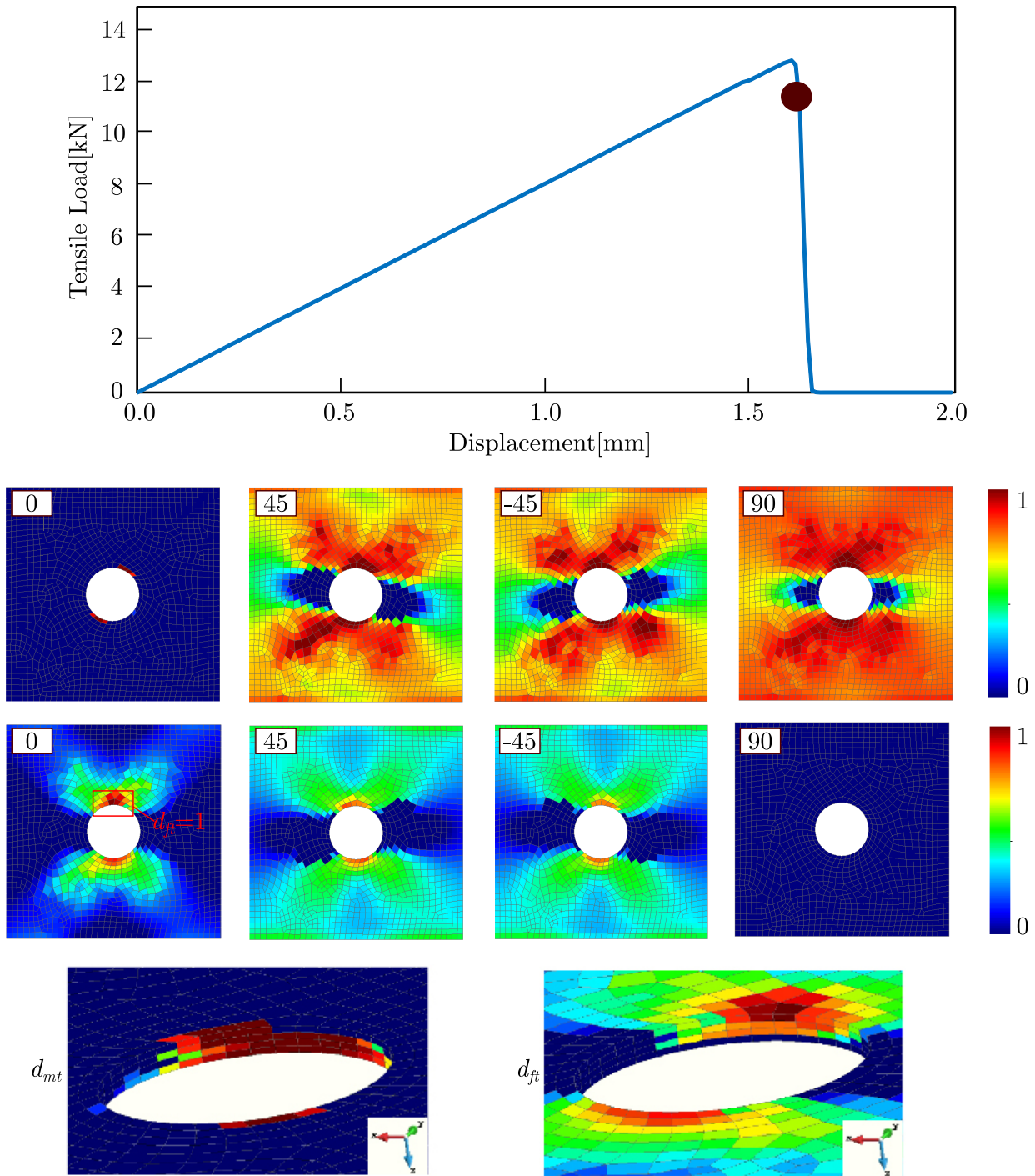


Figure 9.27: middle: Matrix (first row) and fiber tension failure patterns (second row) plotted using FLWTFEM at the time point when the first element reaches $d_{ft}=1$, for an open-hole laminar composite 203.2 x 25.4 mm with a central hole; bottom: through the thickness distributions of d_{mt} and d_{ft} around the circular hole; top: considered time point when $d_{ft}=1$ [13]

Figure 9.28 summarizes the load-displacement curves for all 7 specimens, as predicted by the FLWT-SCB prediction model (Mesh 2). As the orthotropy ratio increases, the laminates become more anisotropic, and the fibers' orientation becomes more aligned with the direction of the applied load. This alignment of fibers results in a higher stiffness in the direction of the load and increased tensile strength of the laminate in that direction. Thus, the laminates' tensile strength exhibits an upward trend as the orthotropy ratio increases from L1 to L7, as can be seen from Figure 9.28.

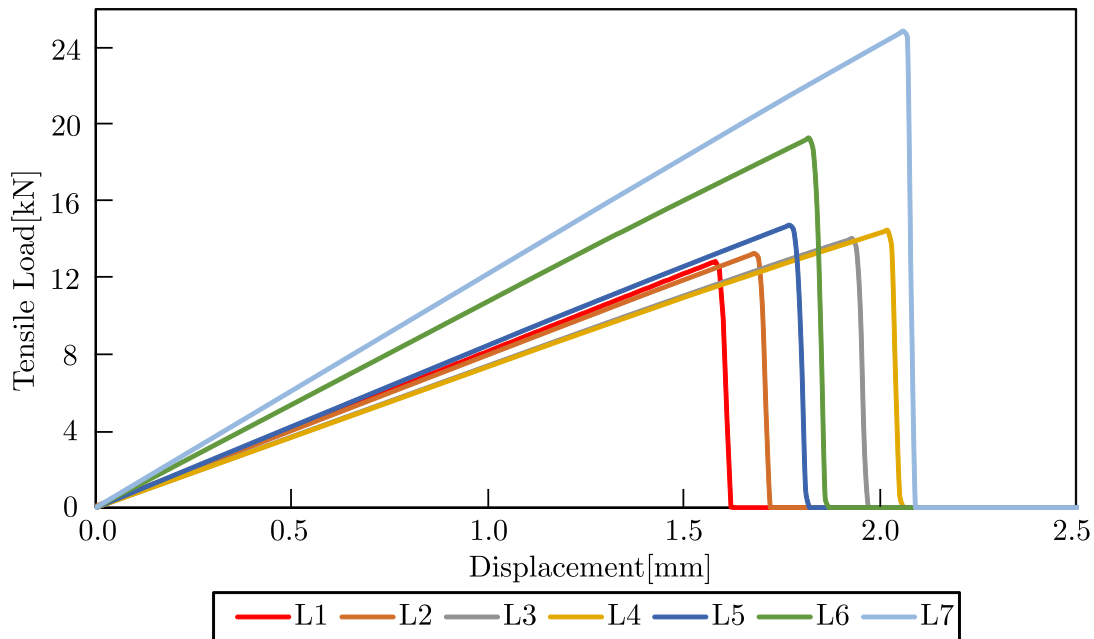


Figure 9.28: Load-displacement curves of an open-hole laminar composite (Mesh 2), calculated using FLWT-SCB prediction model, for 7 considered specimens with different stacking sequences [13]

Moreover, even when the laminates have the same ratio of orthotropy, it has been discovered that the open-hole tension strength is significantly affected by the stacking sequence. As depicted in Figure 9.29, the strength of laminate L7, which consists of 0° plies near the mid-plane of the laminate and on the surface with the stacking sequence $[0^\circ/45^\circ/-45^\circ/0^\circ]_s$, is higher than other stacking sequences like $[0^\circ/45^\circ/0^\circ/-45^\circ]_s$. This is due to the fact that the plies in laminate L7 are arranged in a stacking sequence that optimizes the distribution of stresses throughout the structure, resulting in a higher overall strength compared to other stacking sequences. Additionally, the alternating 45° and -45° plies may provide added reinforcement and improve the overall mechanical properties of the laminate. Hallet's computational simulation [43] also confirmed this observation.

9.2.3 Effect of specimen size

The final subsection focused on examining how the size of the specimens affected the open hole tension (OHT) strength of laminar composites.

The hole diameters considered for the quasi-isotropic laminate (L1) were 3.175, 6.350, 9.525, 12.700 and 15.875 mm. To maintain a constant width-to-diameter (w/d) ratio of 4, the length and width were adjusted according to the chosen diameters, while the length-to-width (l/w) ratio was kept at 2. Figure 9.30 illustrates the load-displacement curves predicted by the FLWT-SCB prediction model for all 5 specimens. Although all 5 specimens were composed of the same quasi-isotropic laminate L1 and had the same stiffness, the OHT strength of the laminate varied considerably depending on specimen size; as specimen size increased, the predicted OHT strength decreased.

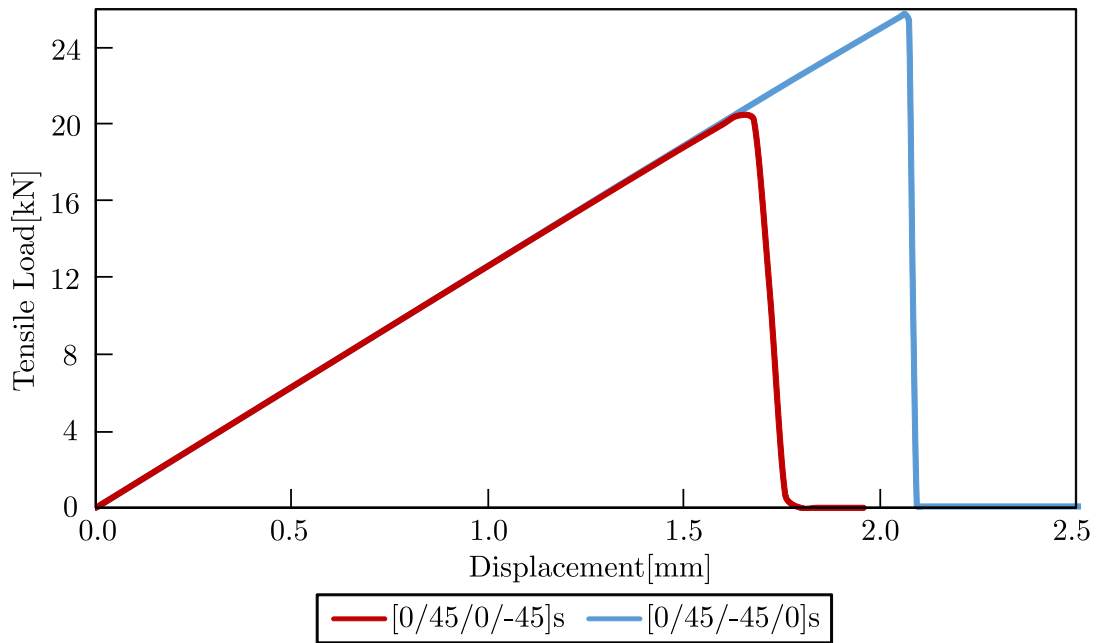


Figure 9.29: Load-displacement curves of an open-hole laminar composite (Mesh 2), calculated using FLWT-SCB prediction model, for 2 specimens with the same orthotropy ratio, but different stacking sequences [13]

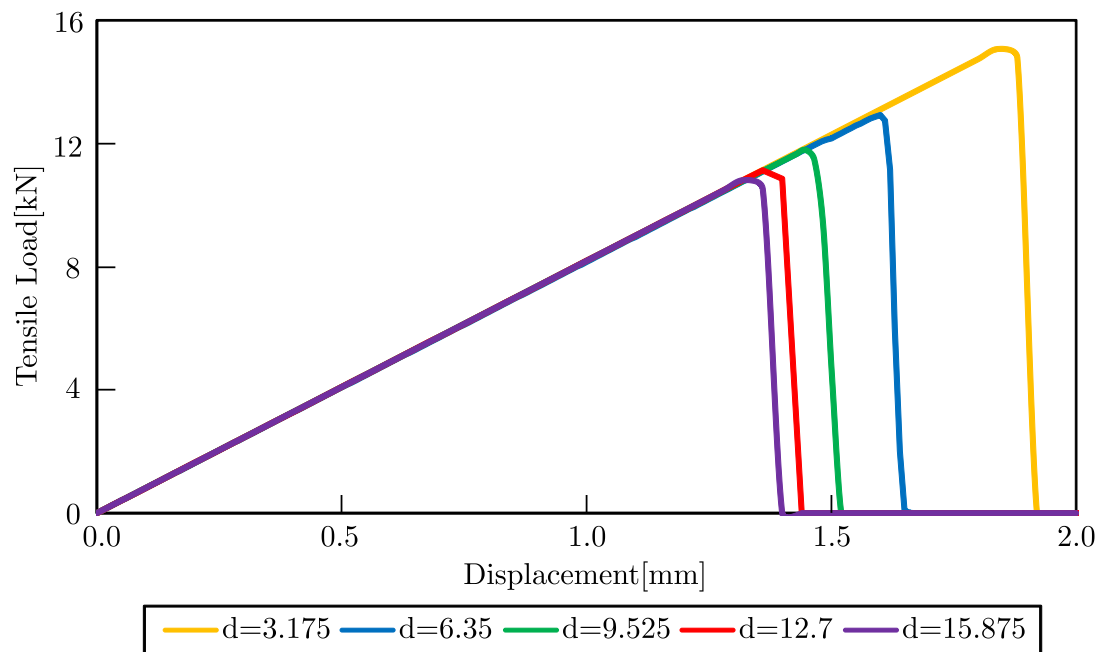


Figure 9.30: Load-displacements curves of quasi-isotropic open-hole laminar composite (L1), predicted by FLWT-SCB prediction model and considering different hole diameters (d [mm]) [13]

9.3 Progressive failure analysis of centre-notched laminar composites in tension

The next example pertains to the PFA of a centre-notched tensile (CNT) laminar composite. The configuration of the laminate is illustrated in Figure 9.31, and consists of 32 layers of thickness $h_k = 0.125$ mm, assembled in $[45^\circ/90^\circ/-45^\circ/0^\circ]_{4s}$ stacking sequence. One end of the coupon is constrained while a displacement u is imposed on the opposite end. The material used in this example is IM7/8552 carbon fibre reinforced polymer (CFRP) with material properties provided in Table 9.11.

Table 9.11: Material properties for IM7/8552 carbon fibre reinforced polymer

Property	Value
E_1 (GPa)	165
$E_2 = E_3$ (GPa)	9
$G_{12} = G_{13}$ (GPa)	5.6
G_{23} (GPa)	2.8
$\nu_{12} = \nu_{13}$	0.34
ν_{23}	0.5
X_t (MPa)	2560
X_c (MPa)	1690
$Y_t = Z_t$ (MPa)	73
$Y_c = Z_c$ (MPa)	250
$S = T$ (MPa)	90
R (MPa)	70
G_{ft} (KJ/m ²)	120
G_{fc} (KJ/m ²)	80
G_{mt} (KJ/m ²)	2.6
G_{mc} (KJ/m ²)	4.2

To showcase the capability of the FLWT-SCB framework in forecasting size effects in laminar composites, multiple sizes of the specimen have been numerically analysed.

Table 9.12 comprises a list of employed scales and their dimensions. The present example has been verified using the research of Nagaraj et al. [73], which use SCB for damage modelling and higher-order theories based on Carrera Unified Formulation (CUF) for structural modelling [162]. Additionally, the maximum strengths estimated in the current example have been also experimentally validated [163].

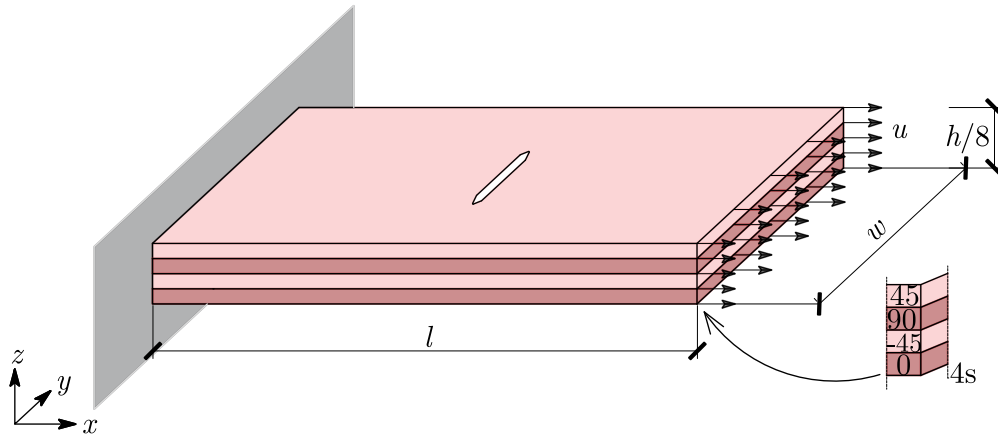


Figure 9.31: Geometry and boundary conditions of centre-notched tensile laminar composite

Table 9.12: List of employed scales and their dimensions

Scale	Notch length c [mm]	Specimen Width w [mm]	Specimen Length l [mm]
1	3.2	15.9	63.5
2	6.4	31.8	127
4	12.7	63.5	254
8	25.4	127	508
16	50.8	254	508

The numerical analysis was performed using 138 Q8 layered quadrilateral elements, with only a small area surrounding the notch being refined with smaller elements (see Figure 9.32). The fracture process zone has a mesh size of roughly 0.5×0.5 mm for the scale-8 mesh. Due to symmetry in stacking sequence, only a half of the laminate was modelled to reduce the number of finite elements. At the clamped edge, all DOFs were restricted, while in the symmetry plane, displacements in the thickness direction were set to zero. The laminae were treated as a single numerical layer, with a linear distribution of displacements across the thickness of the lamina. The element distribution remained constant for all CNT specimens, with the element edge size scaling according to the specimen's dimensions.

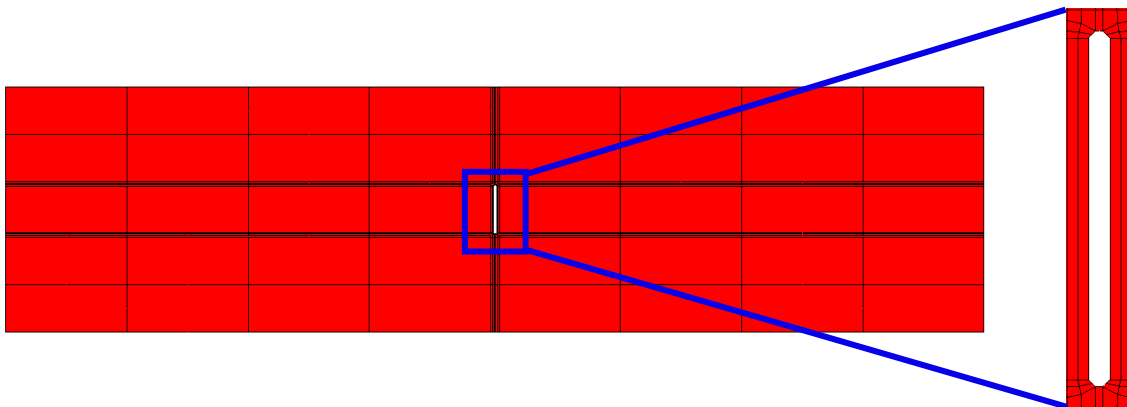


Figure 9.32: Generated mesh with 138 Q8 layered quadrilateral elements of a centre-notched tensile specimen

Figure 9.33 displays a typical stress-strain curve for a scale-8 CNT sample, as predicted by both the FLWT-SCB framework and Nagaraj’s model [73]. The minimum and maximum strength values obtained from experiments are indicated by green horizontal lines. Figure 9.33 shows that the specimen exhibits a brittle behaviour, characterized by a linear elastic rise in stress up to the maximum value, followed by an abrupt decrease in stiffness leading to failure. The results obtained from the current approach are consistent with both numerical and experimental reference results. According to Nagaraj’s model (blue line), the CNT sample’s tensile strength is expected to be 323.9 MPa, which is approximately 5.9% lower than the experimental results. In contrast, when simulated using the FLWT-SCB framework (red line), the sample’s tensile strength is 338.3 MPa, which is in better agreement with experimental data (with an average relative difference of 1.7%).

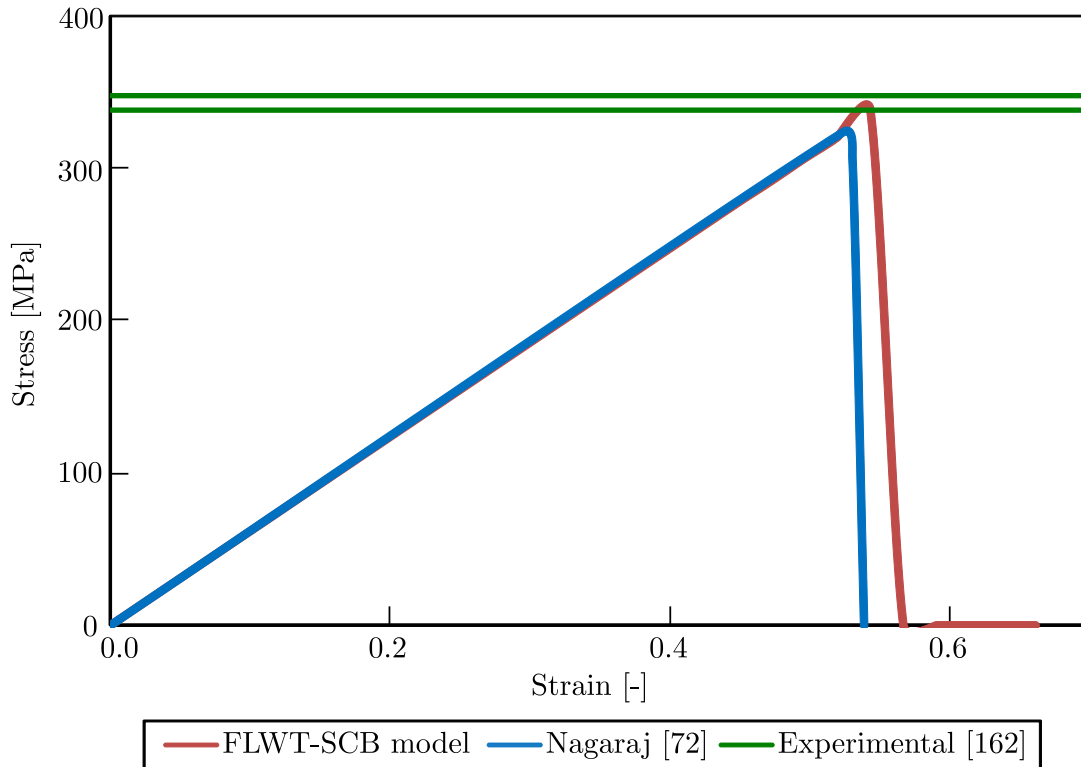


Figure 9.33: Tensile stress – strain curves of a centre-notched specimen (Scale-8) with $[45^\circ/90^\circ/-45^\circ/0^\circ]_{4s}$ stacking sequence

Table 9.13: Comparison of maximum stress values for all CNT specimens from Table 9.12 using FLWT-SCB framework, Nagaraj’s model [73], and experimental data [163]

Scale	FLWT-SCB	Nagaraj [73]	Experimental [163]	Δ^a [%]	Δ^b [%]
1	572.3	593.2	581.4	1.6	2.0
2	505.3	498.3	519.1	2.6	4.1
4	442.3	425.6	455.3	2.9	6.5
8	338.3	323.9	344.1	1.7	5.9
16	250.3	268.4	258.1	3.0	4.0

^a Percentage relative difference of proposed model compared to experimental data

^b Percentage relative difference of reference numerical model [73] compared to experimental data

The stress-strain curves for the remaining CNT scaled specimens are not included here because they are similar to the data presented in the Figure 9.33. Instead, the maximum stress obtained by FLWT-SCB along with the experimental and reference numerical results, for all scales, have been presented in Table 9.13 and plotted in Figure 9.34.

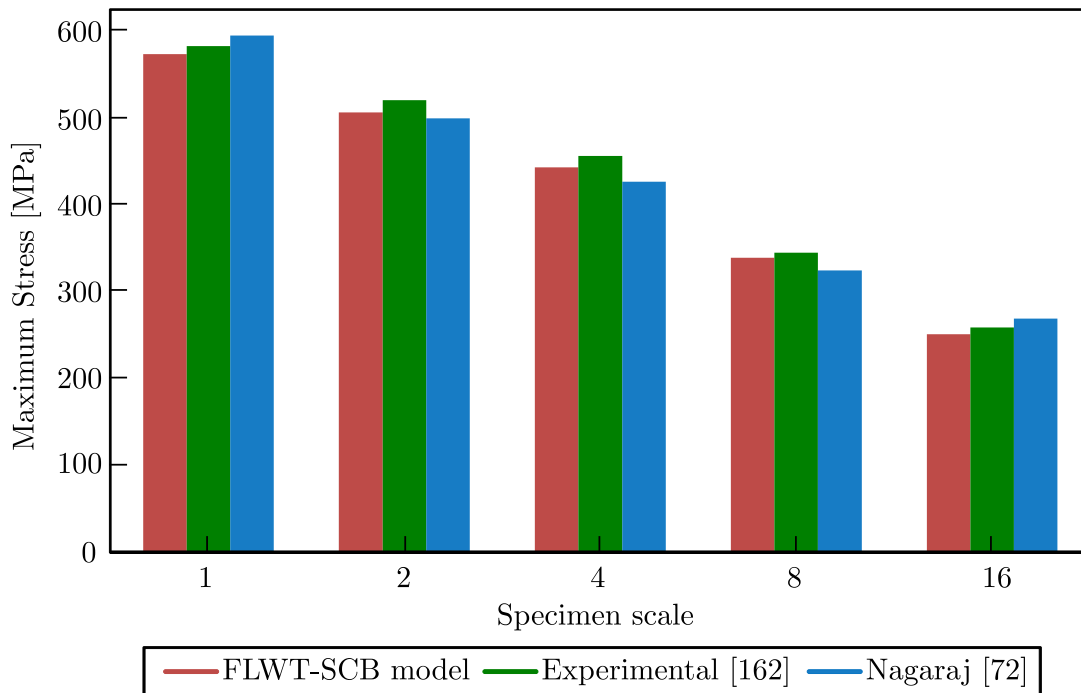


Figure 9.34: Comparison of maximum stress values for all CNT specimens from Table 2 using FLWT-SCB framework, Nagaraj's model [73], and experimental data [163]

Based on Table 9.13 and Figure 9.34, it becomes evident that FLWT-SCB consistently forecasts tensile strengths that are more similar to the experimental data compared to Nagaraj's [73] results.

9.4 Progressive failure analysis of laminar composites in compression

In this section, the proposed FLWT-SCB model's capability for predicting damage progression and the laminate strength in compression is demonstrated. Unlike the outlined SCB model with linear softening (Figure 6.4a), used for PFA of laminar composites in tension, the lamina response in fiber direction under compression is described by trilinear softening with stress plateau to account for fiber kinking (see Figure 6.4b). To validate the PFA of laminar composites under compression, a series of numerical assessments were conducted, which involved analysing the impact of fiber post-peak softening curves and specimen size on the accuracy of predicted results by the FLWT-SCB model.

The section focuses on dispersed quasi-isotropic laminates since they typically undergo progressive failure based on experimental observations [164, 165]. One advantage of using this stacking sequence under in-plane loading is that delamination can be neglected in the numerical modelling as it is minimized. The material used in each case is IM7/8552 carbon fibre reinforced polymer

(CFRP) with material properties provided in Table 9.14. Each lamina of thickness $h_k=0.125$ mm is represented as a single numerical layer, where displacements are linearly distributed through its thickness.

Table 9.14: Material properties for IM7/8552 carbon fibre reinforced polymer loaded in compression

Property	Value
E_1 (GPa)	150
$E_2 = E_3$ (GPa)	11
$G_{12} = G_{13}$ (GPa)	5.8
G_{23} (GPa)	2.9
$\nu_{12} = \nu_{13}$	0.34
ν_{23}	0.48
X_t (MPa)	2560
X_c (MPa)	1690
$Y_t = Z_t$ (MPa)	73
$Y_c = Z_c$ (MPa)	250
$S = T$ (MPa)	90
R (MPa)	70
G_{ft} (KJ/m ²)	120
G_{fc} (KJ/m ²)	80
G_{mt} (KJ/m ²)	2.6
G_{mc} (KJ/m ²)	4.2

9.4.1 Single element analysis

The initial set of numerical assessments involve conducting uniaxial compression tests on individual elements with dimensions of 1 x 1 mm. These simulations offer a convenient way to validate the applicability of the FLWT-SCB prediction model for damage initiation and progression, as each failure mode can be assessed separately. To conduct the simulations, one end of the specimen was clamped (all DOFs are constrained), and a 2mm displacement was applied on the other end.

The initial simulation involves a sample composed of a single unidirectional layer positioned longitudinally (0°) and subjected to compression along the fiber direction (0°), resulting in fiber failure. The stress-strain curve for this scenario is depicted in Figure 9.35a. Following this, the same sample, consisting of a single unidirectional layer (0°), was exposed to transverse compression (perpendicular to the fiber), leading to matrix failure. The stress-strain diagram for this scenario is presented in Figure 9.35b.

Form Figure 9.35, the response of a sample composed of a single unidirectional layer (0°) subjected to compression along and perpendicular to the fiber, follows the bilinear trajectory described by the FLWT-SCB model. It is noteworthy that the maximum stress in both directions

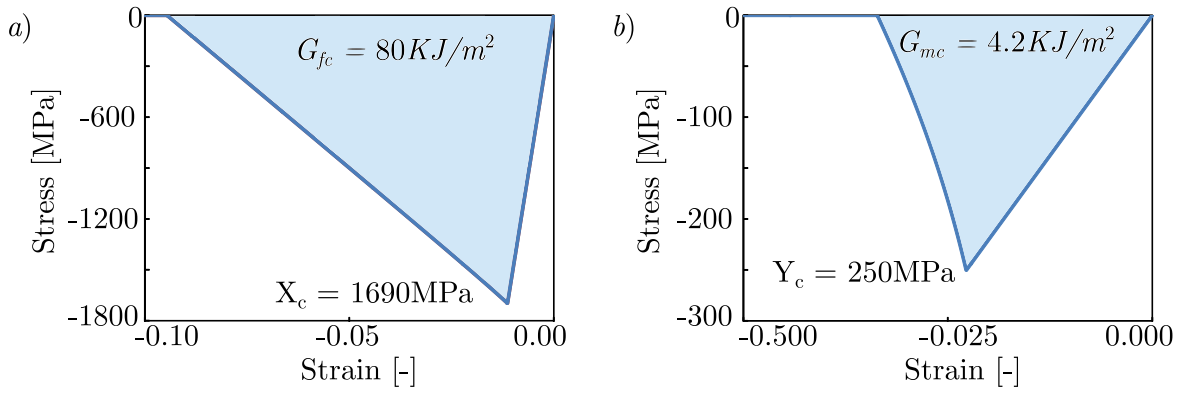


Figure 9.35: Compressive stress-strain behaviour of a 1 x 1 mm single element lamina loaded in: (a) Longitudinal (fiber) direction; (b) Transverse (matrix dominated) direction

matches the strengths of the fiber (1690 MPa) and matrix (250 MPa) materials. Additionally, the area beneath the stress-strain curve equals the fracture energy in the longitudinal (80 KJ/m²) and transverse (4.2 KJ/m²) directions.

Lastly, a quasi-isotropic laminate composed of 16 layers assembled in a $[90^\circ/45^\circ/0^\circ/-45^\circ]_{2s}$ stacking sequence was subjected to compressive loading for the final evaluation. To reduce the number of DOFs, only half of the laminate through the thickness was modelled because of the symmetrical stacking sequence. Displacements in the thickness direction were set to zero in the symmetry plane. To study the impact of fiber softening on the initiation and progression of failure, both linear and linear-brittle fiber softening laws were employed.

Table 9.15 illustrates the highest stresses obtained using various linear-brittle fiber softening options in the FLWT-SCB framework. The PC-30 FLWT-SCB model, which is a linear-brittle FLWT-SCB model with 30% residual stress, predicts a peak stress with the lowest error (0.9%) when compared to the peak stress of 755.8 MPa, observed in experiments. The stress-strain response predicted by both the FLWT-SCB and PC-30 FLWT-SCB models, as well as the reference numerical [74] and experimental results [138], are shown in Figure 9.36.

Table 9.15: Maximus compressive stress of $[90^\circ/45^\circ/0^\circ/-45^\circ]_{2s}$ quasi-isotropic laminate obtained by FLWT-SCB with various linear-brittle fiber softening laws

FLWT-SCB	Maximum Stress	Δ^a [%]
PC-20	743.9	1.6
PC-30	748.7	0.9
PC-40	769.8	1.9
PC-60	775.3	2.6
PC-80	781.4	3.4

^a Percentage relative difference

As can be seen in Figure 9.36, the stress-strain response of the single element $[90^\circ/45^\circ/0^\circ/-45^\circ]_{2s}$ laminate obtained by FLWT-SCB prediction model (blue line in Figure 9.36) is in good agreement with reference numerical results (red line in Figure 9.36) [74]. Nevertheless, when compared to experimentally measured stress-strain response (purple line in Figure 9.36), the outcomes are dissimilar in nature, indicating the limited ability of bilinear damage models to explain laminate

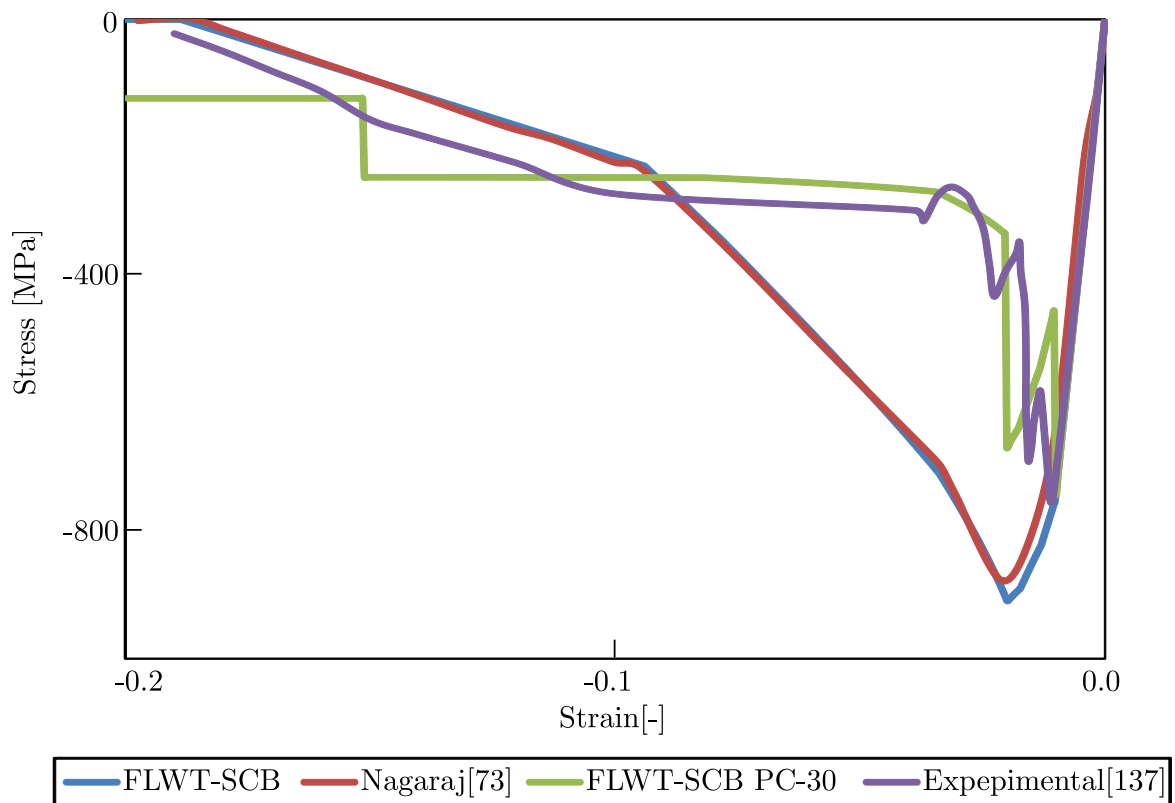


Figure 9.36: Compressive stress-strain behaviour of a 1 x 1 mm single element laminate with $[90^\circ/45^\circ/0^\circ/ - 45^\circ]_{2s}$ stacking sequence considered various methods

response under compressive loads. In contrast, utilizing a linear-brittle PC-30 model (green line in Figure 9.36) leads to a more precise prediction of the overall softening response caused by progressive damage.

9.4.2 Open-hole compression analysis

The next numerical example deals with PFA of the open-hole laminar composites under compression. Both the linear and linear-brittle softening curves were utilized as post-peak softening laws in the PFA. The analysis refers to experimental data provided by Wisnom et al. [6], using quasi-isotropic laminate with a stacking sequence of $[45^\circ/90^\circ/ - 45^\circ/0^\circ]_{4s}$. Additionally, reference numerical results have been also provided for comparison purposes [68, 74]. In the conducted compressive tests, one side of the laminate was clamped while a prescribed displacement u was applied to the opposite side for loading, as depicted in Figure 9.37. In order to decrease the number of DOFs, the model only considered half of the laminate through its thickness due to its symmetrical stacking sequence. Consequently, displacements in the thickness direction were constrained to zero within the symmetry plane. To investigate the size effect, three different scales of the open-hole tick laminate ($m = 4$) are studied, and their dimensions are given in Table 9.16.

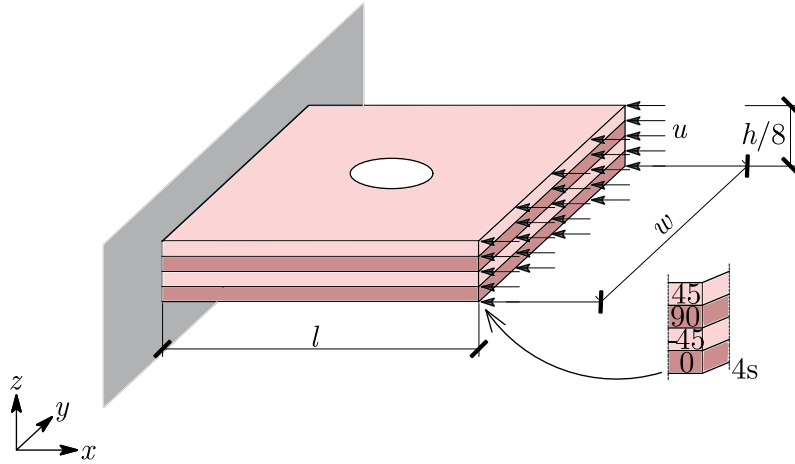


Figure 9.37: Geometry and boundary conditions of open-hole sublaminates scaled laminates loaded in compression

Table 9.16: List of employed scales for the open-hole tick laminate with a stacking sequence of $[45^\circ/90^\circ/-45^\circ/0^\circ]_{4s}$ loaded in compression along with their dimensions

Scale	Hole diameter d [mm]	Specimen Width w [mm]	Specimen Width l [mm]
1	6.35	32	32
2	12.7	64	64
4	25.4	128	128

Although the stacking sequence used in the current example differs slightly from the one used in a previous single element test, the resulting damage modes are still the same. This is due to the dispersed-ply nature of the laminate, which means that the plies are distributed throughout the material rather than being concentrated in certain areas. This dispersion helps to minimize the occurrence of delamination, which is a common type of damage that can occur in composite materials.

9.4.2.1 Fiber post-peak softening law impact

The initial part explores how the compressive failure strength of the scale-1 specimen (refer to Table 9.16) is affected by the fiber post-peak softening laws of both linear and linear-brittle nature. To quantify the mesh dependency, two different meshes were used: Mesh 1, which consists of 48 Q8 layered FEs, and Mesh 2, which consists of 407 Q8 layered FEs (see Figure 9.38a)).

Figure 9.39 illustrates the stress-strain response obtained from the FLWT-SCB prediction model (Mesh 1), incorporating multiple fiber softening laws. It is accompanied by the numerical response obtained by Su et al. [68], who utilized the CDM damage model with a zigzagging approximation of linear softening. These results were obtained through simulations performed in ABAQUS user subroutine UMAT, using the fully fine mesh of shell elements depicted in Figure 9.38b).

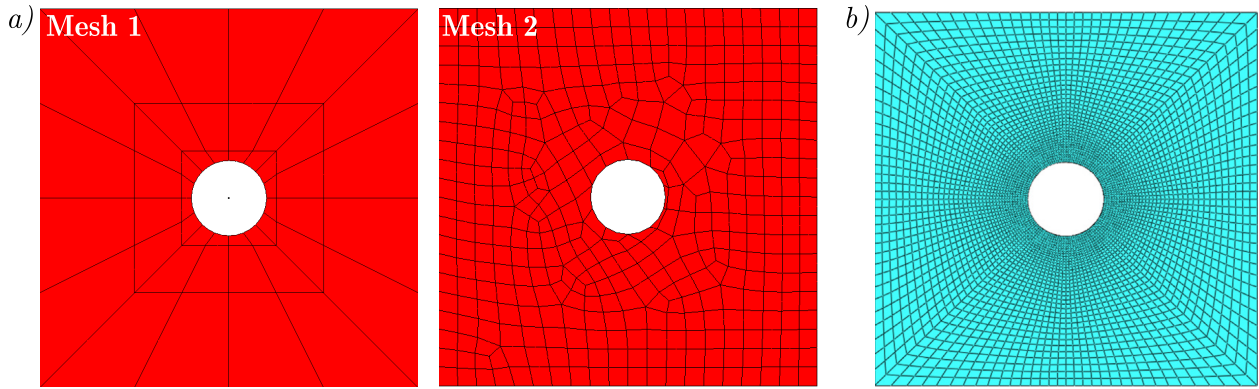


Figure 9.38: Generated meshes of an open-hole specimen (Scale-1): (a) Mesh 1 (48 elements) and Mesh 2 (407 elements) used in FLWT-SCB model; (b) Mesh used in reference numerical model [68]

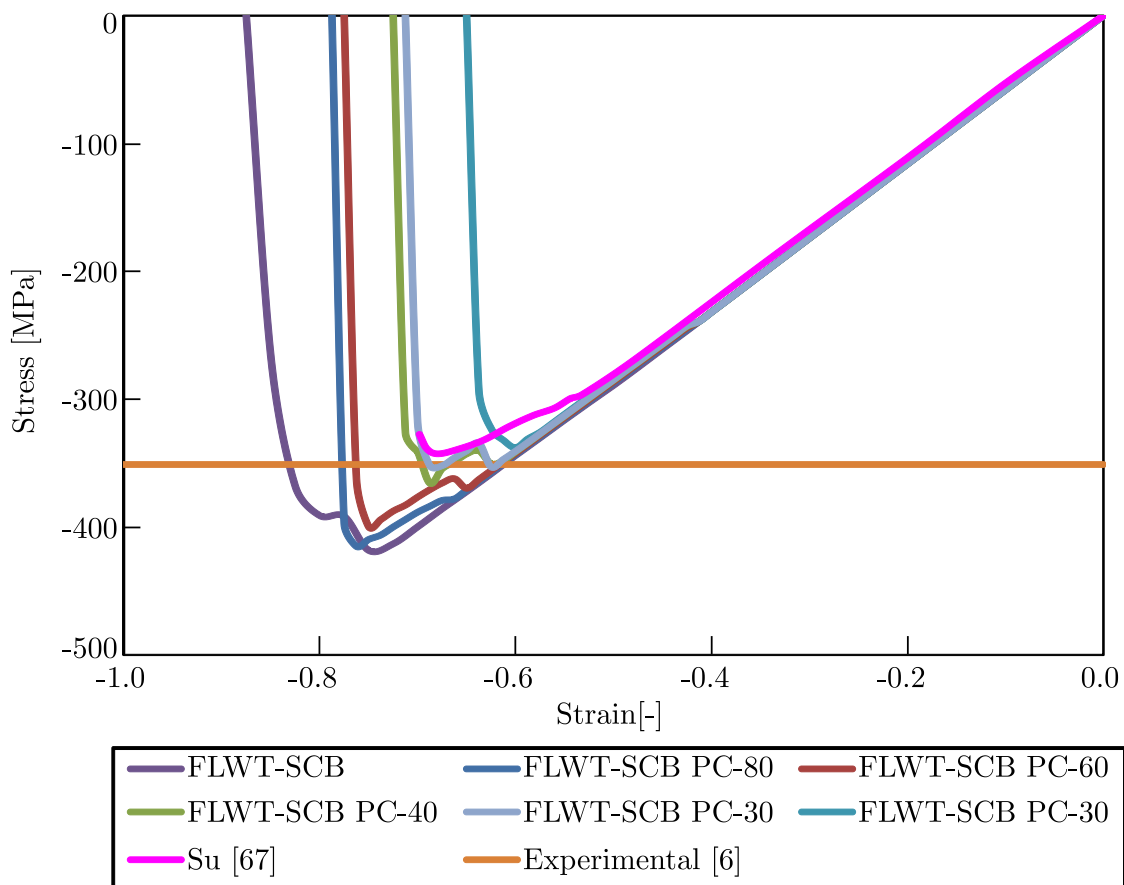


Figure 9.39: Compressive stress - strain responses of an open-hole laminar composite with $[045^\circ/90^\circ/ -45^\circ/0^\circ]_{4s}$ stacking sequence, considering various fiber softening laws and damage models

Compared to the experimental observations [6] (orange line in Figure 9.39), the FLWT-SCB framework with linear fiber softening (purple line in Figure 9.39) results in an overestimation of the predicted maximum stress by approximately 19%. On the other hand, the FLWT-SCB that incorporates linear-brittle fiber softening, provides a more precise estimate of the maximum stress and the overall softening behaviour due failure progression. Like in the previous example, the PC-30 FLWT-SCB model (represented by the red line in the Figure 9.39) once more predicts a peak stress with the lowest error (0.5%) and is therefore selected for further

analyses. Furthermore, the Figure 9.40 demonstrates that the predicted maximum stress remains consistent regardless of the mesh refinement, providing evidence for the independence of the obtained results from the element size.

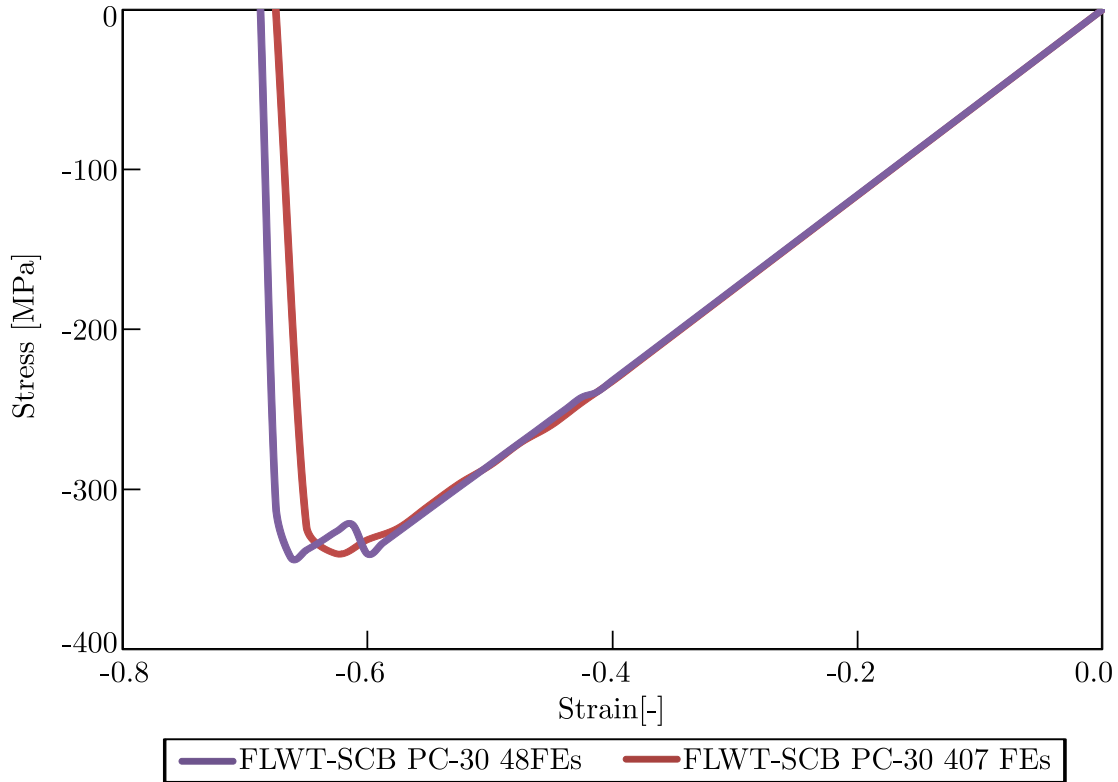


Figure 9.40: Compressive stress - strain responses of an open-hole laminar composite with $[045^\circ/90^\circ/-45^\circ/0^\circ]_{4s}$ stacking sequence, predicted by PC-30 FLWT-SCB model considering different generated meshes from Figure 9.38

Similar to the FLWT-SCB PC-30 model, the Su's damage model [68] performs well in predicting maximum stress and post-failure response (pink line in Figure 9.40), achieving a relative error of 2.4% when compared to experimental results. It should be noted that achieving this level of accuracy required a much finer mesh (see Figure 9.38b) than the one used in the proposed framework (48FEs), resulting in higher computational costs.

The open-hole specimen in compression exhibits a brittle failure mechanism straight across the laminate, as seen in Figure 9.41a from experimental observations [6]. The FLWT-SCB PC-30 model also predicts a brittle failure mechanism, as illustrated in Figure 9.41b (bottom) through spatial plots of both matrix and fiber damage variables at the failure load. Matrix failure initiates in the elements from the lower and upper edges of the hole, as shown in Figure 9.41b (top), indicating matrix cracks or splitting in the top 45° ply of Figure 9.41a (top). In contrast, fiber damage in the top 45° ply initiates at a distance from the hole edge and propagates towards the side edges in a slightly curved manner, similar to the experimental observation. As the load in the 45° plies surrounding the hole is unable to transfer across the hole, the fibers in these plies would not fail in the immediate vicinity of the hole. This, in turn, could lead to matrix damage or splitting along the fiber direction, which was discussed earlier.

It is worth mentioning that due to numerical instability caused by the complete failure of a significant number of elements, the simulation are unable to achieve the final rupture of the entire specimen. Nonetheless, the simulation have effectively captured the gradual damage

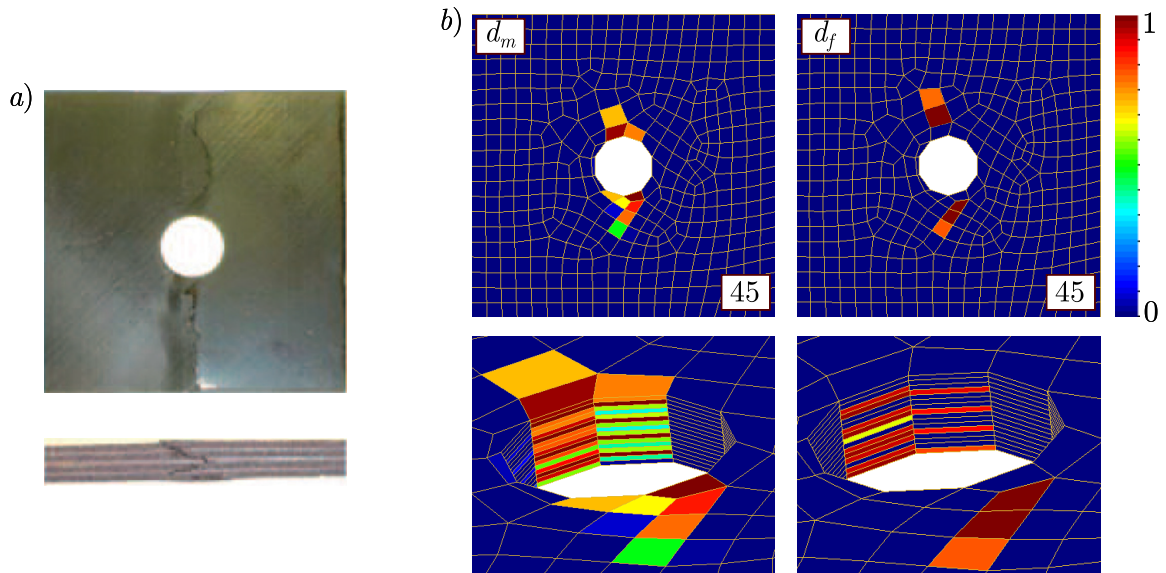


Figure 9.41: Failure pattern in top 45° ply (top) and damage distribution through the laminate thickness (bottom) of an open-hole $[45^\circ/90^\circ/ -45^\circ/0^\circ]_{4s}$ laminate in compression obtained by: (a) Experiment [6]; (b) FLWT-SCB PC-30

until their termination, and therefore, the comparison between the experiment and simulation remains unaffected.

In their study, Wisnom et al. [6] investigated intermediate failure pattern by conducting interrupted tests. Their findings revealed that the brittle failure was caused by local fiber micro-buckling around the upper hole edge, as depicted in Figure 9.42a. The same failure pattern was also observed in proposed framework, as illustrated in Figure 9.42b through a contour plot of the fiber compression damage variable (d_{fc}) at the time when d_{fc} first reaches 1. This coincided with the time when the peak stress value in the stress-strain curve is reached (see Figure 9.40), after which stress began to decrease. It should be noted that the asymmetry of the failure pattern observed in the experiment might be attributed to various uncertainties such as loading alignment errors and material imperfections.

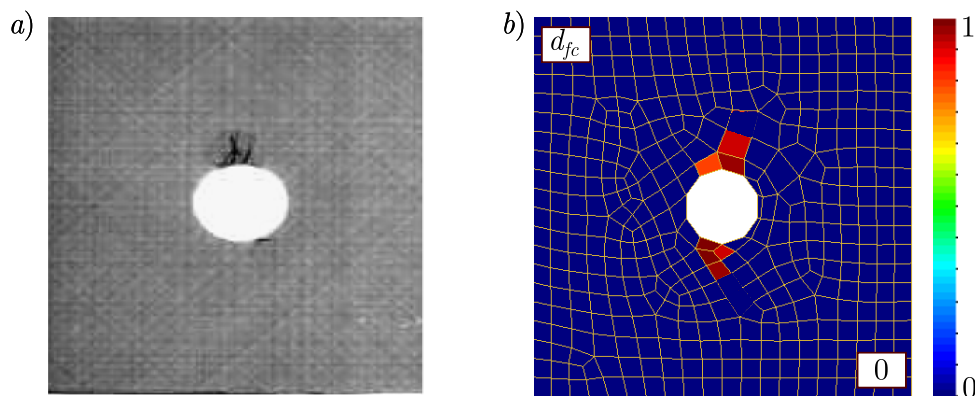


Figure 9.42: Failure pattern in 0° ply of an open-hole $[45^\circ/90^\circ/ -45^\circ/0^\circ]_{4s}$ laminate in compression obtained by: (a) Experiment [6]; (b) FLWT-SCB PC-30

9.4.2.2 Size effect

After model validation, the FLWT-SCB PC-30 model was used to study the size effect on the open-hole compression (OHC) strength of $[45^\circ/90^\circ/-45^\circ/0^\circ]_{4s}$ laminate. Specifically, two additional scales were analysed, each with larger in-plane dimensions, as shown in Table 9.16.

Table 9.17 presents the maximum stresses predicted by the proposed model, as well as the corresponding experimental [6] and reference numerical results. The reference numerical results were obtained from Nagaraj's model [74], which combined a CUF-based structural model with an SCB damage model.

Table 9.17: Comparison of maximum stress values for all OHC $[45^\circ/90^\circ/-45^\circ/0^\circ]_{4s}$ laminates from Table 9.16 using FLWT-SCB PC-30 framework, Nagaraj's model [74], and experimental data

Scale	FLWT-SCB PC-30	Nagaraj [74]	Experimental [6]	Δ^a [%]	Δ^b [%]
1	352.92	355.12	351	0.5	1.2
2	303.44	312.68	301	0.8	3.9
4	290.22	288.56	285	1.8	1.2

^a Percentage difference of proposed model compared to experimental data

^b Percentage difference of reference numerical [74] model compared to experimental data

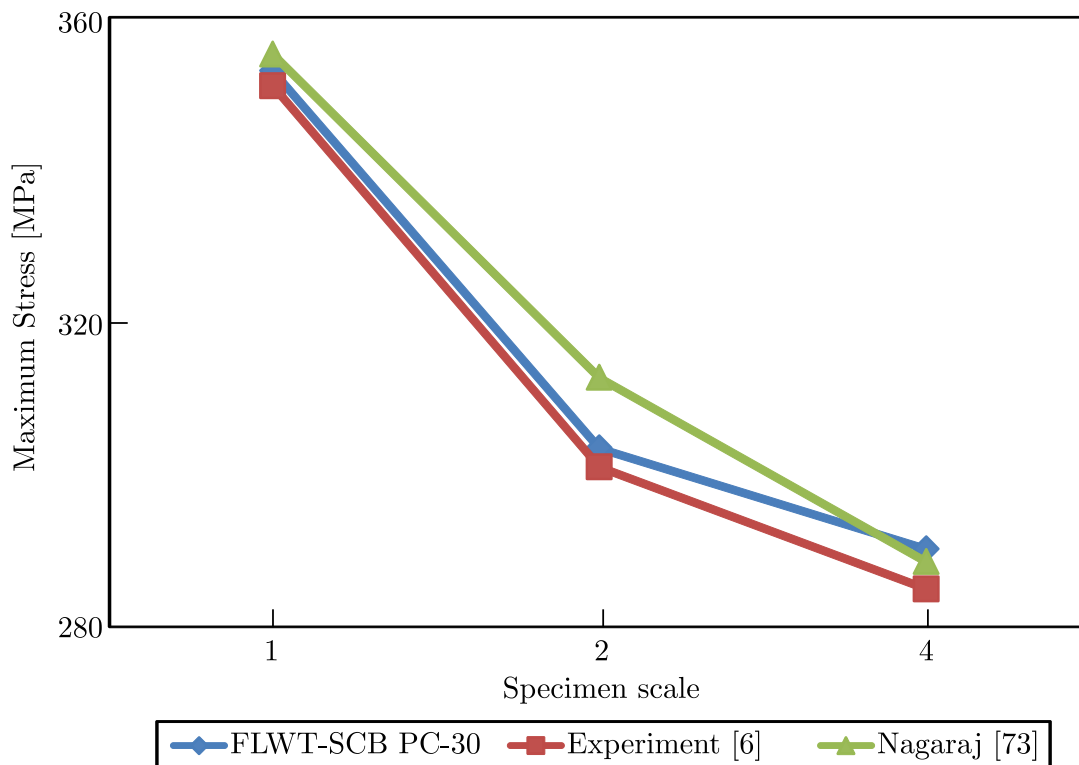


Figure 9.43: Predicted in-plane size effect of an open-hole $[45^\circ/90^\circ/-45^\circ/0^\circ]_{4s}$ laminates from Table 9.16 loaded in compression

Table 9.17 shows that the maximum stress predictions by the proposed model for all three scales exhibit excellent correlation with experimental results [6], with a maximum error below 2%.

Similarly, Nagaraj’s results also correlate well with experimental data, with a maximum error of 3.9% for Scale-2. The predicted in-plane size effect from the FLWT-SCB PC-30 model is illustrated in Figure 9.43. Figure 9.43 shows that the maximum stress of the open-hole laminate in compression decreases as the specimen’s in-plane size increases. This finding is consistent with both experimental and reference numerical observations.

Table 9.18 provides comprehensive details on both the proposed and reference numerical models [74], which includes their discretization, number of DOFs, and required computational time. As shown in Table 9.18, different meshes were employed in Nagaraj’s damage model, with 48, 128 and 256 elements being utilized for Scale-1, Scale-2 and Scale-4, respectively. Additionally, Nagaraj’s study modeled the whole laminate instead of using only half of the laminate through its thickness due to its symmetrical stacking sequence. Consequently, this resulted in a higher number of DOFs and a consequent increase in computational cost. On the other hand, the proposed FLWT-SCB PC-30 model adopted the same mesh, consisting of 48 elements, for all three scales, thereby reducing computational costs for larger scales. Therefore, this approach improved computational efficiency of PFA for OHC laminar composites without compromising the accuracy of the results. Note that, despite using the same number of finite elements in the FLWT-SCB PC-30 model for all three scales, the computation time varied. This discrepancy arose because, in certain steps of the incremental-iterative procedure, a greater number of iterations were required in different scales due to the occurrence of failure in a larger number of finite elements.

Table 9.18: Computational efficiency comparison of FLWT-SCB PC-30 and Nagaraj [74] models

Model	Scale	In-plane discretization	Number of DOFs	Computational time [s]
FLWT-SCB PC-30	1	48 Q8	9027	890
	2	48 Q8	9027	921
	4	48 Q8	9027	968
Nagaraj [74]	1	48 Q9	22176	1774
	2	128 Q9	57024	6543
	4	256 Q9	114048	11369

9.5 Progressive failure analysis of cross-laminated timber panels in bending

This section illustrates the capability of the FLWT-SCB model to predict the post-failure behaviour of CLT panels in bending. The model is extended to account for different failure behaviour of timber in tension and compression, and validation is done through the extensive experimental research, conducted by Dr. Ivan Glišović, Dr. Marija Todorović and Nađa Simović in the Laboratory of Structures at the Faculty of Civil Engineering, University of Belgrade. In this way, the computational framework has extended its applicability to the area of computational mechanics of bio-based (i.e. wood) composites that are applied in civil (structural) engineering and aligned with green building policies in Europe. The experimental program is conducted within the Substrate4CLT project [166].

9.5.1 Material properties

Preliminary experimental research was conducted on small clear timber samples in order to assess the quality of local timber used for the production of CLT. The strength class of timber was evaluated in accordance with EN 338 [155], based on bending strength, bending modulus of elasticity and density. It was concluded that timber used for the production of CLT panels meets the criteria for classification in the strength class C24 according to EN 338.

Four-point bending test was carried out in accordance with EN 408 [167]. A total of 20 prismatic samples with square cross-section 20 x 20 mm and length in the wood fiber direction of 400 mm were tested. Bending strength of structural timber was determined based on bending strength of small timber samples and correction factors which account for sample size, in accordance with EN 384 [168]. Bending strength of structural timber was determined as $f_{m,mean} = 43.8\text{N/mm}^2$, while mean value of timber modulus of elasticity parallel to wood fiber equalled to $E_{0,mean} = 11242\text{N/mm}^2$. Density of timber was determined in accordance with ISO 13061-2 [169]. A total of 40 samples with dimensions of 20 x 20 x 25 mm were tested. Mean value of timber density was determined as $\rho_{mean} = 424\text{kg/m}^3$.

In addition, shear test parallel to wood fiber was performed according to ASTM D143-09 standard [170]. In accordance with these standards, the test was carried out on samples in a form of a notched cuboid so that the pressure is applied in the shear plane of a sample. A total of 20 samples were tested, which were cut so that the shear occurs in the longitudinal layer, along the tangential surface. Based on the test results, mean value of timber shear strength was determined as $f_{v,mean} = 5.3\text{N/mm}^2$.

Material properties were adopted based on the performed tests on small clear timber samples (*) and values available in Gustafsson [142] (**). The timber tensile stress at failure in bending is greater than stress at failure in axial tension, which takes into account the material description. The values are listed in Table 9.19.

Table 9.19: Timber strength properties

Property [MPa]	Value
E_L^*	11242
f_t^*	43.8
f_c^*	36.3
f_v^*	5.3
$f_{t,90}^{**}$	3.0
$f_{c,90}^{**}$	6.0
$f_{v,TR}^{**}$	6.0

The general relationships proposed by Bodig and Jayne [171] were used to calculate the moduli of elasticity in the radial and tangential direction, as well as shear moduli in the shear planes:

$$\begin{aligned}
 E_L : E_T : E_R &\approx 20 : 1.6 : 1 \\
 G_{LT} : G_{LR} : G_{TR} &\approx 10 : 9.4 : 1 \\
 E_L : G_{LT} &\approx 14 : 1
 \end{aligned} \tag{9.3}$$

where E_L , E_T , E_R are the moduli of elasticity in the longitudinal, tangential and radial directions, respectively, while G_{LT} , G_{LR} , G_{TR} are the shear moduli in the shear orthotropic planes. The values of Poisson's ratios ν_{LT} , ν_{LR} , ν_{TR} were adopted based on values given in [171] for softwood. The values of moduli of elasticity, shear moduli and Poisson's ratios are given in Table 9.20.

Table 9.20: Timber elastic properties

Property [MPa]	Value
E_L	11242
E_T	899.36
E_R	562.1
G_{LT}	803
G_{LR}	754.82
G_{TR}	80.3
ν_{LT} (-)	0.37
ν_{LR} (-)	0.42
ν_{TR} (-)	0.47

The material elastic and strength properties in unique lamina coordinate system (123) are used in numerical simulation (see Section 7.2 for explanation). The moduli for the 2 and 3 directions are defined as the average values of the corresponding T and R values for solid timber (see Table 9.20), while the strength parameters are equal to those listed in Table 9.19. Table 9.21 provide the elastic and strength properties of the continuous lamina:

Table 9.21: Material properties of a continuous CLT lamina used in numerical simulations

Property [MPa]	Value
E_1	11242
$E_2 = E_3$	730.73
$G_{12} = G_{13}$	774.41
G_{23}	80.3
$\nu_{12} = \nu_{13}$ (-)	0.395
ν_{23} (-)	0.47
X_t	43.8
X_c	36.3
$Y_t = Z_t$	3
$Y_c = Z_c$	6
$S = T$	5.3
R	3

9.5.2 Experimental test set-up for CLT specimens

The experimental program included investigation of five CLT panels (specimens A1-5). Dimensions of tested CLT panels were: 48 cm width \times 400 cm length \times 15 cm thickness. The panels consisted of five 3 cm thick layers made of boards (laminations) with approximate width of 12 cm. Longitudinal laminations were formed by joining the boards using finger joints. Arrangement of finger joints within the laminations was completely arbitrary. Transverse laminations did not contain finger joints due to their short lengths. In order to prevent deformations due to drying, longitudinal grooves were cut into the laminations. Melamine-urea-formaldehyde adhesive was used for finger joints and layers. Adjacent laminations within the layers had no edge bonding.

All panels were tested in bending as simply supported beams with a span of 380 cm (approximately 25 times the panel thickness) symmetrically loaded with two concentrated forces at a distance of 90 cm (6 times the panel thickness), in accordance with EN 16351 [172]. With this arrangement of forces, a constant bending moment was obtained in the middle part of the panels, without shear force. A schematic illustration of the test layout is given in Figure 9.44.

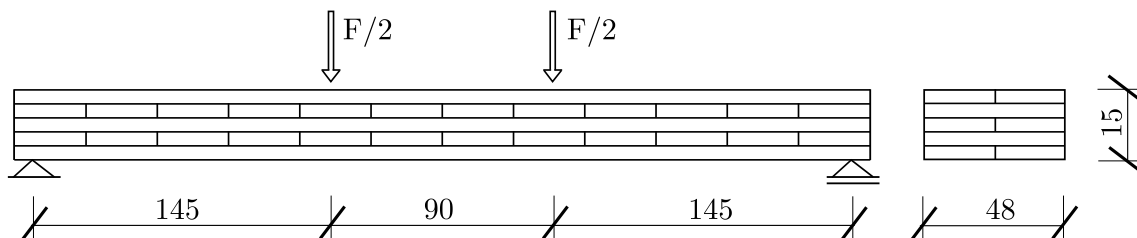


Figure 9.44: Panel testing layout

Testing of CLT panels was performed in a closed steel frame (Figure 9.45). The load was applied using a hydraulic jack. In the experimental procedure the load was transformed from one concentrated force to two forces distributed along the panels' width using a steel rectangular hollow section with welded steel sheets at the points of force input. Steel roller bearings were used at the supports. Also, roller bearings were used at the load application points to ensure that the load acts vertically. Steel plates were placed under the load application points and at the supports to minimize local indentations.

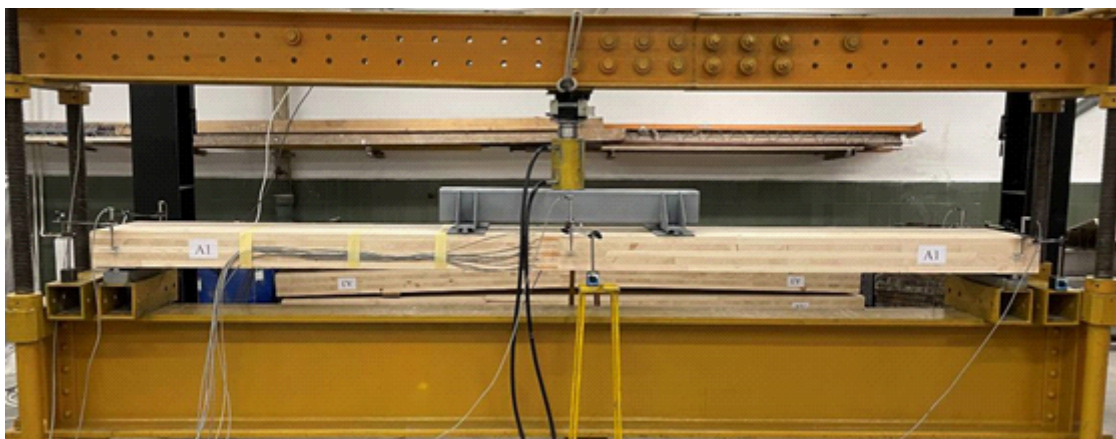


Figure 9.45: Test set-up for CLT specimens [source Substrate4CLT project [166]]

The load was applied at a controlled rate of in order to achieve panel failure in about 5 min. Load application was measured using a loading cell Deflection of the panels was measured using linear variable differential transducers (LVDTs). The mid-span deflection was measured on both sides using two LVDTs, positioned to allow reading near the neutral axis, while deflection at the supports was measured on both sides using four LVDTs. In addition to the measured deflections, in the mid-span, strains were measured around the cross-section using strain gauges. Strain data from strain gauges, deflection data from LVDTs and corresponding load data from the loading cell were collected using the acquisition system.

During the testing of all panels, humidity and air temperature were controlled next to the testing frame. Humidity was between 50 and 60% and temperature was about 25°C. Immediately after each test was completed, the moisture content of timber was measured using a digital hygrometer at various points on the panel. The recorded moisture content in all specimens ranged from 9.8 to 11.2%.

9.5.3 Model applicability verification, results and discussion

This subsection consists of a validation example, used to prove the applicability of the FLWT-SCB damage model to predict damage progression of CLT panels in out-of-plane bending. Validation is made against the experimental data obtained from tests elaborated in previous subsections. Geometry, boundary and loading conditions were adopted in accordance with the tested specimens. Due to symmetry in loading and boundary conditions, only a quarter of the laminate was modelled to reduce the number of DOFs. The removed parts were replaced with appropriate symmetry constraints: $V^I = 0$ for the XZ symmetry plane and $U^I = 0$ for the YZ one. The end support was modelled as a roller support, where the displacements in the thickness direction were constrained, while the displacements in longitudinal direction were allowed. The quasi-3D stress analysis was performed using 24×3 Q8 layered quadrilateral elements with reduced integration. Every lamination was divided in two sub-laminations, adopting the linear distribution of displacements along the sub-lamination thickness. In order to avoid stress concentrations, an external load was smeared on subarea of $160 \times 240 \text{ mm}^2$, according to the experimental setup.

Behaviour of the tested CLT panels is described through load-deflection curves, failure modes, load-carrying capacity and deformability, bending stiffness values, as well as strain distribution along the panels' height. Figure 9.46 illustrates the load-deflection curve predicted by the developed FLWT-SCB prediction model, along with those for the tested CLT panels. Figure 9.47 shows a magnified curve predicted using FLWT-SCB. In the experimental results, the displayed values of deflection at failure, for each specimen, represent the mean values of measurements of two LVDTs placed in the mid-span on both sides of the panel.

A brittle behaviour of all experimentally tested CLT panels is observed; with a linear elastic behaviour until the load peak value is reached, followed by abrupt loss of stiffness leading to failure (dashed lines in Figure 9.46). Progressive failure analysis (PFA) conducted for CLT panel also showed linear-elastic behaviour until failure, replicating experimental results very closely. It is barely seen (Figure 9.47) that insignificant stiffness reduction occurs shortly before the peak value of the load is reached, when a single fiber start to buckle in the top longitudinal lamination. Plastification of timber in the compression zone is actually difficult to observe experimentally, due to early appearance of cracks in the tension zone.

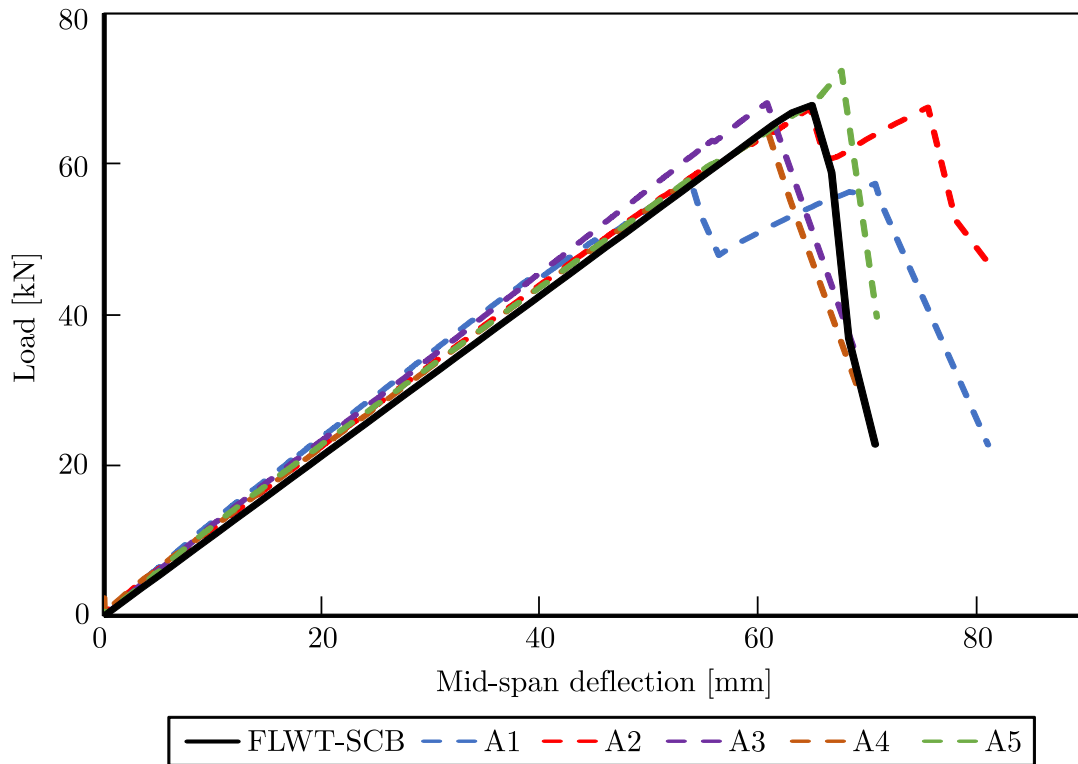


Figure 9.46: Load-deflection curve predicted by the FLWT-SCB prediction model along with the load-deflection curves for all tested CLT panels



Figure 9.47: Magnified load-displacement curve predicted using FLWT-SCB

Failure of all experimentally tested specimens occurred due to tensile failure of the outer longitudinal layer (FT failure), as shown in Figure 9.48. Failure in tension zone is accompanied by pronounced shear cracks that extend along the glued line between outer longitudinal layer and adjacent transverse layer and/or through transverse layer. In addition, a combination of fibre tearing and rolling shear failure was also observed. Tension failure was initiated at wood

defects (knots) or finger joints of longitudinal laminations in maximum bending moment area, between load application points. At the moment of failure, simultaneous fracturing of several boards of the bottom longitudinal layer was observed in all specimens.



Figure 9.48: Typical failure mode of Series A panels (specimen A1)

The overall damage pattern predicted using the FLWT-SCB is illustrated through a spatial plots of fiber damage variables (Figure 9.49) at the failure load, associated with the fiber tension ($d_{ft} = 1$). As can be seen from Figure 9.49, ultimate failure occurred due the FT failure of the bottom longitudinal lamination. This is quite similar to the observation from experiments (Figure 9.48). At the moment of failure, plasticization of timber in the compression zone (see top longitudinal layer in Figure 9.49) is barely noticeable. RS failure appears in transverse layer, after the load reaches the maximum value and starts dropping, as can be seen through spatial plots of transverse damage variables (Figure 9.50). This is also in accordance with experimental observation.

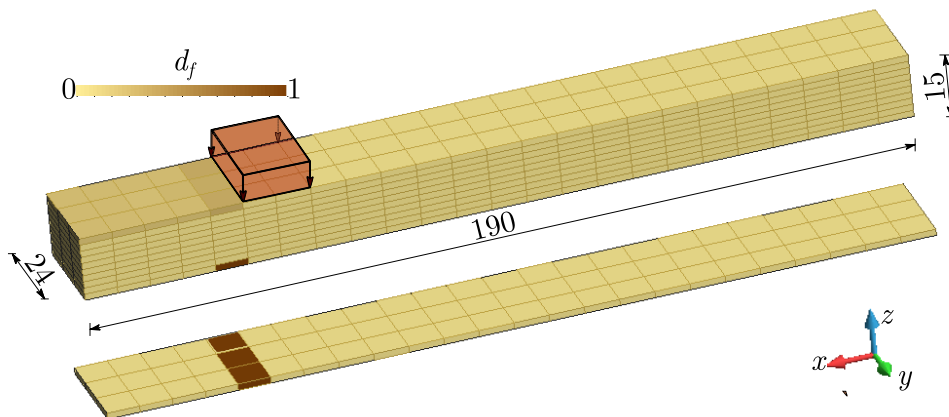


Figure 9.49: Fiber tension (FT) failure patterns of CLT panel, plotted using the FLWTFEM at the failure load ($d_{ft} = 1$). The bottom figure illustrates only the bottom lamination

Both numerical and experimental results in terms of maximum load and mid-span deflection at maximum load, mid-span deflection at ultimate failure and bending stiffness are given in Table 9.22. Corresponding values for loads and deflections were read from load-deflection curves (Figure 9.46).

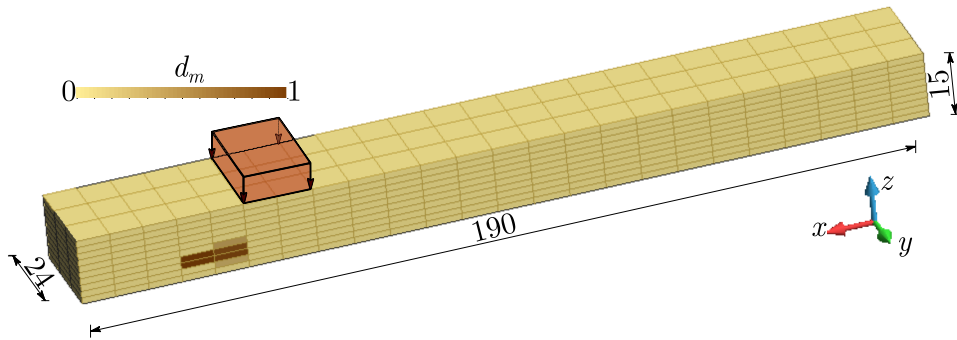


Figure 9.50: Rolling shear (RS) failure pattern of CLT panel plotted using the FLWTFEM after the load reaches the maximum value and starts dropping

Table 9.22: Experimental test and numerical results of CLT panels

Specimen	Maximum load F_{max} (kN)	Deflection at maximum load w_{odg} (mm)	Deflection at failure w_{max} (mm)	Bending stiffness EI_{global} (kN/mm ²)
A1	57.8	53.8	71.4	12.26 x 10 ⁸
A2	67.5	75.6	75.6	11.49 x 10 ⁸
A3	68.1	60.9	60.9	11.92 x 10 ⁸
A4	64.2	60.8	60.8	11.24 x 10 ⁸
A5	72.4	67.7	67.7	11.44 x 10 ⁸
Average	66 (cv, 8.3%)	63.8 (cv, 12.9%)	67.3 (cv, 9.7%)	11.67 x 10 ⁸ (cv, 3.5%)
FLWT-SCB	67.83	64.96	64.96	11.20 x 10 ⁸
ARD(%)	2.77	1.81	3.48	4.03

cv = coefficient of variation; ARD = average relative differences

Average relative difference for the maximum load obtained using FLWT-SCB against the experimental value is only 2.77%. When mid-span deflection at failure is concerned, numerical and experimental results were also compatible, with difference of 3.48%.

The out-of-plane bending stiffness of the panels was determined based on measurement of "global" deflection of the panels. "Global" deflection reflects a mechanism of both bending and shear deformation of CLT panels. Due to high span-to-depth ratio ($l/h \approx 25$) of tested panels which ensures the dominance of bending deformations, the influence of shear deformations on calculated bending stiffness can be neglected. Bending stiffness of tested panels was calculated based on the slope of load-deflection curves, for the linear-elastic region of behaviour between $0.1F_{max}$ and $0.4F_{max}$ (F_{max} - maximum load) according to the following expression:

$$EI_{global} = \frac{3al^2 - 4a^3}{48} \frac{w_2 - w_1}{F_2 - F_1} \quad (9.4)$$

where: EI_{global} - "global" bending stiffness; F_1 - load corresponding to 10% of the maximum load ($0.1F_{max}$); F_2 - load corresponding to 40% of the maximum load ($0.4F_{max}$); w_1 - mid-span

deflection corresponding to the load F_1 ; w_2 - mid-span deflection corresponding to the load F_2 ; l - spacing of specimen supports (span); a - distance of the applied force from the nearest support.

Numerical prediction of bending stiffness agreed well with experimental results, with a difference of 4.03%. These results confirm that timber can be effectively modelled as an orthotropic material. The variability of elasticity modulus measurements was the reason for deviation between numerical and experimental results.

To get insight the deformation pattern within CLT specimens, an example of typical strain distribution for tested CLT panels at different load levels is given in Figure 9.51, left. The profiles show compressive and tensile strains along x -axis as negative and positive values, respectively, and the position of strain gauges along the height on y -axis, measured from the lower edge of the cross-section. The given strain values represent the mean values of the corresponding measurements on both sides of the specimen.

To evaluate the strain behaviour predicted by using the FLWT-SCB, the longitudinal strain distribution through the thickness, at the mid-span of the CLT panel for different load levels, is illustrated in Figure 9.51, right. Since these are plate elements composed of longitudinal and transverse layers in which there is no edge bonding of adjacent laminations, a certain discrepancy in strain values measured on both sides of the panels was recorded. This is not the case for numerically obtained strain values due the fact that each timber lamination was observed as a continuous layer.

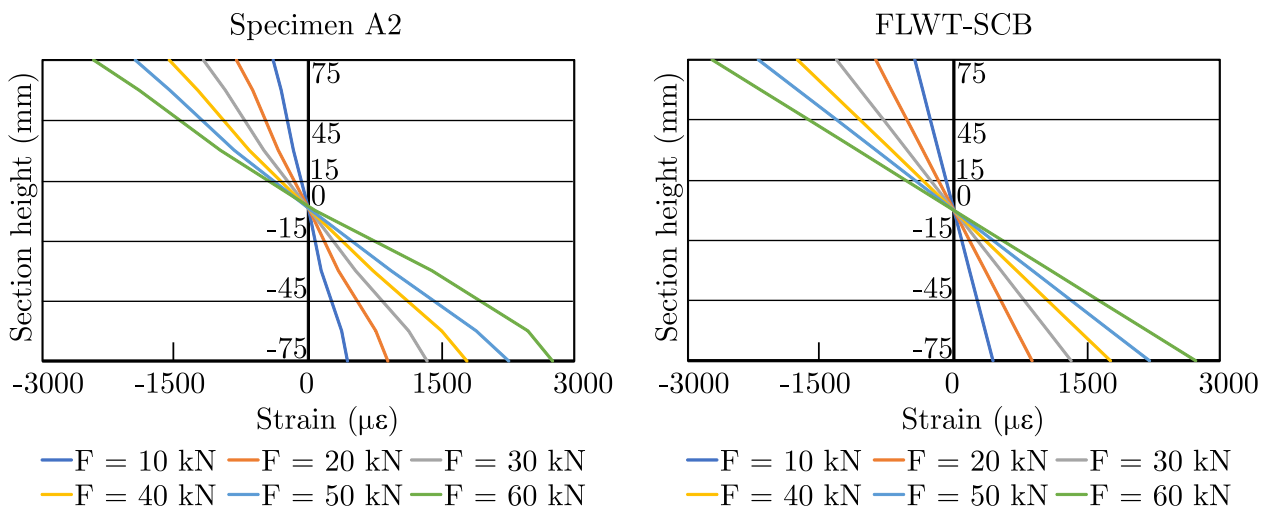


Figure 9.51: Longitudinal strain distribution through the thickness, at the mid-span of CLT panel obtained from: left) experimental tests (specimen A2); right) FLWT-SCB prediction model

Strain distribution in the cross-section is linear up to failure, thus confirming the assumption of bending theory that plane sections remain plane during deformation. Measured strains on longitudinal and transverse laminations of the CLT panels indicate that there is no sliding between the laminations. This is in line with the perfect bonding assumption between laminations, used in the FLWT.

It can be verified that the overall strain distribution predicted by FLWT-SCB is quite similar when compared against the experimental measured strains. Also, the strain values in tension and compression zones were approximately the same at all load levels. Small differences between numerical and experimental results can be justified due the fact that each lamination

was homogenized with the average modulus of elasticity, while in reality each lamination is inhomogeneous and the material properties of timber vary. With load increase, no displacement of neutral axis position was recorded, which confirms that wood plastification on the compressed side of the cross-section was limited due to early appearance of cracks in tension zone.

10 Conclusions and recommendations for future work

The tendency for optimal design with laminar composites is frequently governed by uncertainties in failure prediction and the significant computational costs associated with progressive failure analysis (PFA), especially for larger structures. To address these challenges, this thesis presents an innovative prediction model that integrates the smeared crack band (SCB) damage model and the full layerwise theory (FLWT). This novel approach aims to enhance the computational efficiency of PFA in laminar composites while preserving the accuracy of 3D finite element models.

The governing equations of motion of the FLWT are established using the principle of virtual displacements, assuming a piece-wise linear variation of all three displacement components across the plate thickness. Following the finite element analysis, the nodal displacements are determined, and the stresses are computed using the constitutive relations. However, as the interlaminar stresses obtained in this manner do not exhibit a continuous distribution through the laminate thickness, they are subsequently recalculated by assuming a quadratic distribution within each layer for every stress component.

Damage progression and post-failure behaviour are addressed through the implementation of the SCB damage model with strain-softening. Within the SCB approaches, the damage is distributed throughout the finite element domain, and the fracture mechanism is represented by the degradation of material stiffness. This degradation is controlled by damage variables, which are determined based on equivalent strains specifically defined for each failure mode. To minimize the mesh dependency issue, the fracture energy is scaled using a characteristic element length. The initiation of failure and the modes of failure are determined using the Hashin failure criterion. The response of damaged lamina, in both the fiber and matrix directions, is characterized by distinct strain-softening curves. These curves represent the progressive softening of the material, with the peak stress corresponding to the strength of the fibers and matrix, respectively. To accurately capture the post-failure behaviour of timber in tension and compression during the PFA of CLT panels, the proposed strain-softening curves are further modified. These modifications account for the specific post-failure behaviour exhibited by timber in different loading conditions, ensuring a more realistic representation of the material response during the analysis of CLT panels.

Application of layered quadrilateral elements for continuum damage modelling in laminar composites is a relatively unexplored topic in the literature, as the standard practice typically involves the use of linear solid elements. However, the adoption of a layered approach based on the FLWT in finite element modelling offers several advantages.

First, the FLWT-based model accurately captures the 3D stress distribution within the laminate and considers the continuous transverse (interlaminar) stresses between adjacent layers. These interlaminar stresses play a crucial role in damage modelling and provide essential inputs for accurate predictions. Also, this model includes the prediction of transverse normal stress σ_z , which plays a crucial role in capturing localized effects such as holes, cutouts, or stress-deformation states around point supports. Additionally, the layerwise plate theory offers improved robustness and stability in the analysis, exhibiting a weak dependency between the size of the structure and the mesh and allowing for more reliable predictions regardless of the structure's size.

The developed FLWT-SCB prediction model is incorporated into an original FLWTFEM framework. It offers a user-friendly experience by providing a comprehensive graphical environment, enabling the end user to easily visualize input data and calculation results. The effectiveness of the proposed model has been confirmed through extensive verification using various benchmark examples, encompassing both static and progressive failure analyses of laminar composites and CLT panels (bio-based laminar composites) with arbitrary geometries, loading and boundary conditions, and stacking sequences. The accuracy of the model has been demonstrated for both intact and damaged laminar composites. Based on numerous numerical analyses, the following conclusions can be drawn.

The most important conclusions drawn from the linear static analysis of laminar composites are as follows:

- The importance of applying the proposed model to accurately predict the stress distribution in thick CLT panels composed of 3 and 5 layers is demonstrated. The desired zig-zag displacement distribution, aligned with the exact solution, is successfully achieved using both linear and quadratic layered finite elements. The correct discontinuous shape of the in-plane stress components σ_x and σ_y , with considerably different slopes in soft and stiff layers, is exhibited when employing the FLWT. The obtained results for σ_x and σ_y show excellent agreement with the exact solution, even when using a coarse mesh and a relatively simple (Q4) element type. Additionally, Q8 FLWT-based model captured the characteristic continuous course of transverse shear stress distributions (τ_{xz} and τ_{yz}), although a minor overprediction is observed.
- The convergence of results for τ_{xz} and τ_{yz} to the exact solution for Q8 elements is achieved through mesh refinement. Convergence of the results is also attained through the sublaminar concept, wherein the physical lamina is divided into multiple numerical layers with identical elastic properties.
- The prediction of transverse shear stresses by linear (Q4) elements is unsuccessful due to the utilization of a relatively low number of integration points in the reduced integration of element stiffness matrices.
- Experimental data reveals that the proposed model yields a slightly stiffer response (in terms of deflection) for thin 3-layer CLT panels under concentrated loading. A better agreement of -4.9% is achieved for 4-point concentrated loading compared to centre loading, which exhibits -8.6% discrepancy. The obtained values are understandably lower compared to FSDT due to the more precise consideration of transverse shear deformation. Under concentrated loading, FLWT accurately predicted the normal stress σ_x . The accuracy of results depends on the density of the mesh and the selected element type.
- Outstanding agreement is achieved for the normal stress σ_x in both slender ($L/h=33.3$) and thick ($L/h=16.7$) CLT panels, across all considered L/B ratios, when compared with the results obtained from commonly used k - and γ -methods. In comparison to FLWT, the γ -method slightly overpredicts transverse shear stress, especially in thick plate situations.

- The proposed model offers an alternative to commercial software for calculating orthotropic plate-like structures. This is confirmed through computational analysis of complex-shaped CLT floors with 5 and 7 layers, commonly used as standard floor structures in residential-commercial buildings. The slabs were subjected to a realistic combination of permanent and variable loads according to Eurocode 1. The analysis confirmed the model's accuracy, with an average relative difference of only -0.31% for 5-layer plates and -0.16% for 7-layer plates in comparison to the solid-like model in Abaqus. Furthermore, even with approximately 30% fewer DOFs for the same mesh size, the FLWT-based model exhibited excellent agreement with the results from Abaqus.

The most important conclusions derived from the PFA of laminar composites are as follows:

- The FLWT-SCB model demonstrated a brittle behaviour of both open-hole and centre-notched tensile specimens, with a linear elastic increase of the load until reaching the peak value, followed by an abrupt loss of stiffness leading to failure.
- Unlike Reddy's GSM model used in various studies, the results obtained by using FLWT-SCB were mesh-independent. This mesh independency was achieved by adjusting the equivalent strain at the final failure state, preserving the fracture energy rather than keeping it constant.
- The results obtained by FLWT-SCB showed good agreement with experimental results, regardless of the stacking sequences, as confirmed by examining the load-displacement behaviour and comparing them to the experimental results. FLWT-SCB allows for coarser meshes compared to standard finite element models, leading to improved computational efficiency without compromising accuracy.
- The FLWT-SCB model successfully predicted both fiber tension and matrix tension failure patterns in open-hole laminar composites, with complete fracture induced by complete fiber failure concentrated around the circular hole across the width of the 0° ply.
- The benchmark numerical study demonstrated that the FLWT-SCB prediction model accurately predicted the effect of specimen size and laminate orthotropy on the tensile strength of open-hole laminar composites. Also, the FLWT-SCB prediction model showed consistent prediction of tensile strengths in centre-notched laminar composites, which closely align with experimental data, in contrast to the reference numerical results. The mesh discretization remained constant for all specimens without compromising accuracy or significantly affecting computational time.
- The accurate description of the lamina response in the fiber direction under compression in laminar composites involves the utilization of linear-brittle softening with a stress plateau, in contrast to the linear softening approach employed in the FLWT-SCB model for lamina response under tension.
- The stress-strain response of the single element laminate in compression, obtained by the FLWT-SCB prediction model aligns well with reference numerical results, while showing dissimilarities when compared to experimental measurements. This indicates the limited ability of FLWT-SCB damage model with linear softening to explain laminate response under compressive loads, highlighting the need for a linear-brittle model.
- The FLWT-SCB framework with linear fiber softening tends to overestimate the predicted maximum compression stress compared to experimental observations, whereas the FLWT-SCB model incorporating linear-brittle fiber softening provides a more precise estimation of the maximum stress and overall softening behaviour.
- The FLWT-SCB PC-30 model, which is a linear-brittle FLWT-SCB model with 30% residual stress, exhibits consistent predictions of the maximum stress regardless of mesh refinement, demonstrating the independence of the results from the element size.

- The open-hole specimen in compression exhibits a brittle failure mechanism straight across the laminate, with matrix failure initiating from the lower and upper edges of the hole and fiber damage initiating at a distance from the hole edge and propagating towards the side edges. Although the simulations may not achieve the final rupture of the entire specimen due to numerical instability caused by the complete failure of a significant number of elements, they effectively capture the gradual damage until termination, ensuring the validity of the comparison between experiments and simulations.
- The predicted in-plane size effect from the FLWT-SCB PC-30 model demonstrates a decrease in the maximum stress of the open-hole laminate in compression as the specimen's in-plane size increases, consistent with experimental and reference numerical observations.
- The applicability of the FLWT-SCB framework has been extended beyond conventional composites to include bio-based composites, such as wood. The model's accuracy and performance were confirmed through extensive experimental research conducted by Dr. Ivan Glišović, Dr. Marija Todorović and Nađa Simović, at the Laboratory of Structures, Faculty of Civil Engineering, University of Belgrade, which involved the comparison of load-deflection relationships, stiffness, and ultimate load carrying capacities of CLT specimens.
- Ultimate failure in the CLT specimens occurred primarily due to fiber tension failure in the bottom longitudinal lamination, while rolling shear failure appeared in the transverse layers after reaching the maximum load.
- The proposed FLWT-SCB model demonstrated good agreement with experimental results, with an average relative difference of only 2.77% for maximum load, 3.48% for mid-span deflection at failure, and 4.03% for bending stiffness. The predicted strain distribution closely matched the experimentally measured strains.
- Finally, the advantages of the FLWT-SCB damage models were highlighted, including savings in computational costs and the ability to provide accurate 3D stress fields necessary for predicting damage initiation and evolution in problems with highly localized stress peaks. The use of layered quadrilateral elements also relaxed element aspect-ratio and size constraints, improving computational efficiency in the PFA of large-scale composite structures.

Based on the assumptions and limitations underlying the presented FLWT-SCB model, as well as the key findings of this dissertation, the following recommendations are provided for future research:

- Implement cohesive elements to account for matrix-driven effects and delamination: Although the current work focuses on fiber-dominated progressive damage analysis, future studies should consider incorporating cohesive elements to capture nonlinear shear, through-thickness stresses, and delamination. The perfect-bonding assumption may be conservative in areas where delamination should occur, leading to excessive ply failure. Enriching the displacement field with new variables representing jump discontinuities and using Heaviside functions for interlaminar relative displacements can enhance the layerwise formulation, as given in [12, 110]
- Extend the FLWT-SCB framework to CLT floor structures and structural elements with arbitrary geometry and boundary conditions: CLT structures commonly experience tension perpendicular to wood fiber and shear, which are critical modes of loading. The framework's potential applicability to these scenarios should be explored, providing insights into predicting and addressing perpendicular to wood fiber fracture and cracking along wood fiber.

- Consider probabilistic predictions and Monte Carlo simulations: Recognize that almost no parameter in failure analysis is deterministic. Incorporate probability prediction of limit load by treating lamina elastic material properties and strength as random variables. Monte Carlo simulations can be employed to investigate the probabilistic behaviour, taking into account the challenges of obtaining material and property data, which are not always easy to obtain experimentally. This approach provides valuable insights into the uncertainty and variability associated with laminar composites.
- Considerations for long-term and climate effects: Take into account the influence of moisture and temperature on the behavior of wood. Variations in moisture content and moisture gradients can have a notable impact on the tensile stress perpendicular to the wood fiber, which is crucial for failure analysis. By incorporating these effects into the analysis, a better understanding of the long-term performance of laminar composites can be achieved.
- Incorporate mechanical and piezoelectric coupling for laminated structures with piezoelectric layers: Explore the use of piezoelectric materials in actively controlling the elastic deformations of civil engineering structures. Extend the proposed theory by incorporating the mechanical and piezoelectric coupling in the constitutive relations, enabling the analysis of laminated structures with piezoelectric layers.

Appendix

Codes generated within this doctoral dissertation are elaborated in this section. The codes are generated within GiD problemtype files, as well as within MATLAB FLWTFEM code. Red text indicates the author's contribution to the FLWTFEM framework.

1. GiD problemtype files

FLWTFEM.mat

BOOK: Orthotropic
MATERIAL: MAT1
TITLE: Moduli_of_Elasticity
QUESTION: Type:
VALUE: Orthotropic
STATE: DISABLED
QUESTION: E1:
VALUE: 0.0
HELP: Elasticity module in direction 1
QUESTION: E2:
VALUE: 0.0
HELP: Elasticity module in direction 2
QUESTION: E3:
VALUE: 0.0
HELP: Elasticity module in direction 3
TITLE: Poisson_Ratios
QUESTION: ni12:
VALUE: 0
HELP: Poisson ratio 12
QUESTION: ni13:
VALUE: 0
HELP: Poisson ratio 13
QUESTION: ni23:
VALUE: 0
HELP: Poisson ratio 23
TITLE: Shear_Moduli
QUESTION: G12:
VALUE: 0.0
HELP: Shear module 12
QUESTION: G13:

VALUE: 0.0
HELP: Shear module 13
QUESTION: G23:
VALUE: 0.0
HELP: Shear module 23
TITLE: Normal_Strengths
QUESTION: Xt:
VALUE: 0.0
HELP: Tensile normal strengths 1
QUESTION: Xc:
VALUE: 0.0
HELP: Compressive normal strengths 1
QUESTION: Yt:
VALUE: 0.0
HELP: Tensile normal strengths 2
QUESTION: Yc:
VALUE: 0.0
HELP: Compressive normal strengths 2
color
VALUE: 0.0
HELP: Tensile normal strengths 3
QUESTION: Zc:
VALUE: 0.0
HELP: Compressive normal strengths 3
TITLE: Shear_Strengths
QUESTION: R:
VALUE: 0.0
HELP: Shear strengths 23
QUESTION: S:
VALUE: 0.0
HELP: Shear strengths 13
QUESTION: T:
VALUE: 0.0
HELP: Shear strengths 12
TITLE: Other
QUESTION: Mass_Density:
VALUE: 0
HELP: Mass Density of the Material
END MATERIAL

BOOK: Lamina
MATERIAL: LAM1
QUESTION: Type:
VALUE: Lamina
STATE: DISABLED
QUESTION: Material:
VALUE:
QUESTION: Fiber_Angle:
VALUE: 0.0

QUESTION: Thickness:
 VALUE: 0.0
 END MATERIAL

FLWTFEM.prb

PROBLEM DATA
 TITLE: Analysis
 QUESTION:
 Analysis_Type:#CB#(Bending,FreeVibration,ProgressiveFailure)
 VALUE: Bending
 DEPENDENCIES:(Bending, RESTORE,SubLayers:,#CURRENT#,
 HIDE,Number_of_Modes:,#CURRENT#, HIDE,Criterion:,#CURRENT#)
 DEPENDENCIES:(FreeVibration, HIDE,SubLayers:,#CURRENT#,
 RESTORE,Number_of_Modes:,#CURRENT#, HIDE,Criterion:,#CURRENT#)
 DEPENDENCIES:(ProgressiveFailure, RESTORE,SubLayers:,#CURRENT#,
 HIDE,Number_of_Modes:,#CURRENT#, RESTORE,Criterion:,#CURRENT#)
 QUESTION: SubLayers:
 VALUE: 4
 QUESTION: Number_of_Modes:
 VALUE: 10
 QUESTION: Criterion:#CB#(Tsai-Wu,Hoffman,Tsai-Hill,Hashin)
 VALUE: Hashin
 END PROBLEM DATA

2. MATLAB files

LW_3D.m

```
classdef LW_3D < LW_L1
properties
MatrixKL;
VectorQ;
IndexDOF;
Displacements;
StressesXYZ;
Stresses123;
StressNodalXYZ;
StressNodal123;
StrainsXYZ;
Strains123;
StrainsNodalXYZ;
StrainsNodal123;
end

methods
% Class Constructor
function obj = LW_3D(id,type,integration,section,nodes,load)
obj = objLW_L1(id,type,integration,section,nodes,load);
if nargin~ =0
```

```

end
end

% Calculate Element Stiffness Matrix
function obj = calcMatrixKL(obj)
nnodes = length(obj.ElementNodes);
nodedoflayer = 3 * nnodes;
nlayers = length(obj.Section.Layers);
nq = length(obj.GaussCoefsK);
K = zeros ( 3 * nnodes * (nlayers+1) );
for gp = 1:nq
xi = obj.GaussPointsK(gp,1);
eta = obj.GaussPointsK(gp,2);
[shape, NatDev, ~] = Shape(obj.ElementType, xi, eta);
J11 = NatDev(:,1)' * obj.NodalCoordinates(:,1);
J12 = NatDev(:,1)' * obj.NodalCoordinates(:,2);
J21 = NatDev(:,2)' * obj.NodalCoordinates(:,1);
J22 = NatDev(:,2)' * obj.NodalCoordinates(:,2);
detJ = J11*J22 - J12*J21;
invJ = 1/detJ * [J22 -J21; -J12 J11];
XYDev = NatDev * invJ;
matrixB(1:3, :) = kron(XYDev(:,1)', [100; 000; 010]) + kron(XYDev(:,2)', [000; 010; 100]);
matrixB(4, :) = kron(shape, [001]);
matrixBbar(1:2, :) = kron(shape, [100; 010]);
matrixBbar(3:4, :) = kron(XYDev', [001]);
for I = 1:nlayers + 1
for J = 1:nlayers + 1
if abs(I-J) < 2
K ( (I-1)*nodedoflayer+1:I*nodedoflayer , (J-1)*nodedoflayer+1:J*nodedoflayer ) =
K ( (I-1)*nodedoflayer+1:I*nodedoflayer, (J-1)*nodedoflayer+1:J*nodedoflayer) +
(matrixB' * obj.Section.MatrixA1(:, :, I, J) * matrixB +
matrixBbar' * obj.Section.MatrixA2(:, :, I, J) * matrixBbar) * detJ * obj.GaussCoefsK(gp);
end
end
end
end
obj.MatrixKL = K;
end

```

```

% Calculate Element Force Vector
function obj = calcVectorQ(obj)
nnodes = length(obj.ElementNodes);
nlayers = length(obj.Section.Layers);
Q = zeros(nnodes * 3 * (nlayers + 1), 1);
for gp = 1:length(obj.GaussCoefsM)
xi = obj.GaussPointsM(gp,1);
eta = obj.GaussPointsM(gp,2);
[shape, NatDev, ~] = Shape(obj.ElementType, xi, eta);
J11 = NatDev(:,1)' * obj.NodalCoordinates(:,1);
J12 = NatDev(:,1)' * obj.NodalCoordinates(:,2);

```

```
J21 = NatDev(:,2)' * obj.NodalCoordinates(:,1);
J22 = NatDev(:,2)' * obj.NodalCoordinates(:,2);
detJ = J11*J22 - J12*J21;
PRODUCT1 = ( kron(shape, eye(3)) )' * obj.DistributedLoad(4:6)' * detJ;
PRODUCT2 = ( kron(shape, eye(3)) )' * obj.DistributedLoad(1:3)' * detJ;
Q(1 : 3*nnodes , 1) = Q(1:3*nnodes,1) + PRODUCT1 * obj.GaussCoefsM(gp);
Q(3*nnodes*nlayers + 1 : end , 1) = Q(3*nnodes*nlayers + 1:end,1) +
PRODUCT2 * obj.GaussCoefsM(gp);
end
obj.VectorQ = Q;
end

% Derive Element Code Numbers
function obj = deriveIndexDOF(obj)
nnodes = length(obj.ElementNodes);
nlayers = length(obj.Section.Layers);
ndof = 3 * (nlayers+1);
obj.IndexDOF = zeros( nnodes * ndof , 1 );
for layer = 1:nlayers + 1
for node = 1:nnodes
obj.IndexDOF((layer-1)*3*nnodes + 3*node - 2) =
(obj.ElementNodes(node).NodeID-1)*ndof + 3*layer - 2; obj.IndexDOF((layer-1)*3*nnodes +
3*node - 1) =
(obj.ElementNodes(node).NodeID-1)*ndof + 3*layer - 1; obj.IndexDOF((layer-1)*3*nnodes +
3*node ) =
(obj.ElementNodes(node).NodeID-1)*ndof + 3*layer;
end
end
end

% Calculate Element Stresses
function obj = CalcStresses(obj, sublayers)
ngaus = size(obj.GaussPointsStress,1);
nlayers = length(obj.Section.Layers);
nnodes = length(obj.ElementNodes);
NodalCoords = obj.NodalCoordinates(:,1:2);
PreliminaryStressMatrixGaussXYZ = zeros(6,2,nlayers,ngaus);
derStressMatrixGaussXYZ = zeros(3,2,nlayers,ngaus);
TauVectorGaussXYZ = zeros(3*nlayers,3,ngaus);
TauVectorGaussXYZ(1,1,:) = obj.DistributedLoad(4);
TauVectorGaussXYZ(2,1,:) = obj.DistributedLoad(1);
TauVectorGaussXYZ(1,2,:) = obj.DistributedLoad(5);
TauVectorGaussXYZ(2,2,:) = obj.DistributedLoad(2);
TauVectorGaussXYZ(1,3,:) = -obj.DistributedLoad(6);
TauVectorGaussXYZ(2,3,:) = obj.DistributedLoad(3);
VectorCGaussXYZ = zeros(3*nlayers, 3, ngaus);
StressMatrixGaussXYZ = zeros(6, 2, nlayers, ngaus);
obj.StressesXYZ = zeros(6, sublayers+1, nlayers, ngaus);
obj.Stresses123 = zeros(6, sublayers+1, nlayers, ngaus);
for layer = 1:nlayers
```

```
CBar = obj.Section.Layers(layer).MatrixCBar;
h = obj.Section.Layers(layer).Thickness;
Disp_Bottom = obj.Displacements((layer-1)*3*nnodes+1 : layer *3*nnodes);
Disp_Top = obj.Displacements(layer*3*nnodes+1 : (layer+1)*3*nnodes);
for gp = 1:ngaus
xi = obj.GaussPointsStress(gp,1);
eta = obj.GaussPointsStress(gp,2);
[shape,NatDev,SecDev] = Shape(obj.ElementType, xi, eta);
J11 = NatDev(:,1)' * obj.NodalCoordinates(:,1);
J12 = NatDev(:,1)' * obj.NodalCoordinates(:,2);
J21 = NatDev(:,2)' * obj.NodalCoordinates(:,1);
J22 = NatDev(:,2)' * obj.NodalCoordinates(:,2);
detJ = J11*J22 - J12*J21;
invJ = 1/detJ * [J22 - J21; -J12J11];
XYDev = NatDev * invJ;
J1 = [J11^2 J12^2 2*J11*J12; J21^2 J22^2 2*J21*J22; J11*J21 J12*J22 J21*J12 + J11*J22];
J2 = SecDev' * NodalCoords;
MatrixB1 = zeros(3, 3*nnodes);
MatrixB2 = kron(shape, [001]);
MatrixBbar1 = kron(shape, [100; 010]);
MatrixBbar2 = zeros(2, 3*nnodes);
MatrixH1 = zeros(3, 3*nnodes);
MatrixH2 = zeros(3, 3*nnodes);
MatrixG1 = zeros(1, 3*nnodes);
MatrixG2 = zeros(1, 3*nnodes);
MatrixM1 = zeros(2, 3*nnodes);
MatrixM2 = zeros(2, 3*nnodes);
MatrixN1 = zeros(1, 3*nnodes);
MatrixN2 = zeros(1, 3*nnodes);
for i = 1:nnodes
MatrixB1(:, 3*i-2:3*i) = [XYDev(i,1) 0 0; 0 XYDev(i,2) 0; XYDev(i,2) XYDev(i,1) 0]; Ma-
trixBbar2(:, 3*i-2:3*i) = [0 0 XYDev(i,1); 0 0 XYDev(i,2)];
dNd2 = J1 ( (SecDev(i,:))' - J2 * XYDev(i,:)' );
MatrixH1(:, 3*i-2:3*i) = [dNd2(1) 0 0; 0 dNd2(3) 0; dNd2(3) dNd2(1) 0];
MatrixH2(:, 3*i-2:3*i) = [dNd2(3) 0 0; 0 dNd2(2) 0; dNd2(2) dNd2(3) 0];
MatrixG1(:, 3*i-2:3*i) = [0 0 XYDev(i,1)];
MatrixG2(:, 3*i-2:3*i) = [0 0 XYDev(i,2)];
MatrixM1(:, 3*i-2:3*i) = [XYDev(i,1) 0 0; XYDev(i,2) XYDev(i,1) 0];
MatrixM2(:, 3*i-2:3*i) = [0 0 dNd2(1); 0 0 2*dNd2(3)];
MatrixN1(:, 3*i-2:3*i) = [0 XYDev(i,2) 0];
MatrixN2(:, 3*i-2:3*i) = [0 0 dNd2(2)];
end
PreliminaryStressMatrixGaussXYZ([1 2 6 3], 1, layer, gp) = CBar([1 2 6 3], [1 2 6]) * MatrixB1
* Disp_Bottom + CBar([1 2 6 3], 3) * MatrixB2 * (Disp_Top - Disp_Bottom) / h;
PreliminaryStressMatrixGaussXYZ([1 2 6 3], 2, layer, gp) = CBar([1 2 6 3], [1 2 6]) * MatrixB1
* Disp_Top + CBar([1 2 6 3], 3) * MatrixB2 * (Disp_Top - Disp_Bottom) / h;
PreliminaryStressMatrixGaussXYZ([5 4], 1, layer, gp) = CBar([5 4], [5 4]) * MatrixBbar2 *
Disp_Bottom + CBar([5 4], [5 4]) * MatrixBbar1 * (Disp_Top - Disp_Bottom) / h;
PreliminaryStressMatrixGaussXYZ([54], 2, layer, gp) = CBar([5 4], [5 4]) * MatrixBbar2 *
Disp_Top + CBar([5 4], [5 4]) * MatrixBbar1 * (Disp_Top - Disp_Bottom) / h;
```

```

derStressMatrixGaussXYZ([1 2], 1, layer, gp) = -CBar([1 6], [1 2 6]) * MatrixH1 * Disp_Bottom
- CBar([6 2], [1 2 6]) * MatrixH2 * Disp_Bottom - CBar([1 6], 3) * MatrixG1 * (Disp_Top -
Disp_Bottom) / h - CBar([6 2], 3) * MatrixG2 * (Disp_Top - Disp_Bottom) / h;
derStressMatrixGaussXYZ([1 2], 2, layer, gp) = -CBar([1 6], [1 2 6]) * MatrixH1 * Disp_Top
- CBar([6 2], [1 2 6]) * MatrixH2 * Disp_Top - CBar([1 6], 3) * MatrixG1 * (Disp_Top -
Disp_Bottom) / h - CBar([6 2], 3) * MatrixG2 * (Disp_Top - Disp_Bottom) / h;
derStressMatrixGaussXYZ(3, 1, layer, gp) = -CBar(5, [5 4]) * MatrixM2 * Disp_Bottom -
CBar(4, 4) * MatrixN2 * Disp_Bottom - CBar(5, [5 4]) * MatrixM1 * (Disp_Top - Disp_Bottom)
/ h - CBar(4, 4) * MatrixN1 * (Disp_Top - Disp_Bottom) / h;
derStressMatrixGaussXYZ(3, 2, layer, gp) = -CBar(5, [5 4]) * MatrixM2 * Disp_Top - CBar(4,
4) * MatrixN2 * Disp_Top - CBar(5, [5 4]) * MatrixM1 * (Disp_Top - Disp_Bottom) / h -
CBar(4, 4) * MatrixN1 * (Disp_Top - Disp_Bottom) / h;
TauVectorGaussXYZ(nlayers+layer+1, 1:3, gp) = (PreliminaryStressMatrixGaussXYZ([5 4 3],1,
layer, gp) + PreliminaryStressMatrixGaussXYZ([5 4 3],2, layer, gp))/2*h;
end
end
for layer = 2*nlayers+2 : 3*nlayers
J = layer - 2*nlayers - 1;
for gp = 1:ngaus
TauVectorGaussXYZ(layer, 1:3, gp) = derStressMatrixGaussXYZ(1:3, 2, J, gp) - derStressMa-
trixGaussXYZ(1:3, 1, J+1, gp);
end
end
for layer = 1:nlayers
h = obj.Section.Layers(layer).Thickness;
ds = obj.Section.Layers(layer).Material.ds;
for gp = 1:ngaus
StressMatrixGaussXYZ([1 2 6], [1 2], layer, gp) = PreliminaryStressMatrixGaussXYZ([1 2 6],
[1 2], layer, gp);
VectorCGaussXYZ(:, 1, gp) = obj.Section.MatrixL_TauVectorGaussXYZ(:, 1, gp);
VectorCGaussXYZ(:, 2, gp) = obj.Section.MatrixL_TauVectorGaussXYZ(:, 2, gp);
VectorCGaussXYZ(:, 3, gp) = obj.Section.MatrixL_TauVectorGaussXYZ(:, 3, gp);
StressMatrixGaussXYZ([5 4], 1, layer, gp) = VectorCGaussXYZ(3*layer, [1 2], gp)';
StressMatrixGaussXYZ([5 4], 2, layer, gp) = VectorCGaussXYZ(3*layer-2, [1 2], gp)' * h2 +
VectorCGaussXYZ(3*layer-1, [1 2], gp)' * h + VectorCGaussXYZ(3*layer, [1 2], gp)';
StressMatrixGaussXYZ(3, 1, layer, gp) = VectorCGaussXYZ(3*layer, 3, gp);
StressMatrixGaussXYZ(3, 2, layer, gp) = VectorCGaussXYZ(3*layer-2, 3, gp) * h2 +
VectorCGaussXYZ(3*layer-1, 3, gp) * h + VectorCGaussXYZ(3*layer, 3, gp);
CONSTANTS = zeros(3,nlayers,3);
for stress = 1:3
CONSTANTS(:, layer, stress) = VectorCGaussXYZ(3*layer-2:3*layer , stress, gp);
end
for micro = 1:sublayers+1
A = StressMatrixGaussXYZ([1 2 6], 1, layer, gp);
B = StressMatrixGaussXYZ([1 2 6], 2, layer, gp);
obj.StressesXYZ([1 2 6], micro, layer, gp) = A + (B-A)/sublayers*(micro-1);
SubThickness = (micro-1)*h/sublayers;
obj.StressesXYZ(5, micro, layer, gp) = (CONSTANTS(1,layer,1)*SubThickness2 + CON-
STANTS(2,layer,1)*SubThickness + CONSTANTS(3,layer,1));
obj.StressesXYZ(4, micro, layer, gp) = (CONSTANTS(1,layer,2)*SubThickness2 + CON-

```

```
STANTS(2,layer,2)*SubThickness + CONSTANTS(3,layer,2));
obj.StressesXYZ(3, micro, layer, gp) = (CONSTANTS(1,layer,3)*SubThickness2 + CON-
STANTS(2,layer,3)*SubThickness + CONSTANTS(3,layer,3));
obj.Stresses123(:, micro, layer, gp) = obj.Section.Layers(layer).MatrixR * obj.StressesXYZ(:,
micro, layer, gp);
for node = 1:nnodes
obj.StressNodal123 (:, micro, layer, node) =
obj.Section.Layers(layer).MatrixR * obj.StressNodalXYZ(:, micro, layer, node);
end
end
end
end
end
end
```

```
% Calculate Element Strains function obj = CalcStrains(obj, sublayers)
ngaus = size(obj.GaussPointsStress,1);
nlayers = length(obj.Section.Layers);
nnodes = length(obj.ElementNodes);
NodalCoords = obj.NodalCoordinates(:,1:2);
PreliminaryStrainsMatrixGaussXYZ = zeros(6,2,nlayers,ngaus);
StrainsMatrixGaussXYZ = zeros(6, 2, nlayers, ngaus);
obj.StrainsXYZ = zeros(6, sublayers+1, nlayers, ngaus);
obj.Strains123 = zeros(6, sublayers+1, nlayers, ngaus);
for layer = 1:nlayers
CBar = eye(6);
h = obj.Section.Layers(layer).Thickness;
Disp_Bottom = obj.Displacements( (layer-1)*3*nnodes+1 : layer *3*nnodes);
Disp_Top = obj.Displacements( layer *3*nnodes+1 : (layer+1)*3*nnodes);
for gp = 1:ngaus
xi = obj.GaussPointsStress(gp,1);
eta = obj.GaussPointsStress(gp,2);
[shape,NatDev,SecDev] = Shape(obj.ElementType, xi, eta);
J11 = NatDev(:,1)' * obj.NodalCoordinates(:,1);
J12 = NatDev(:,1)' * obj.NodalCoordinates(:,2);
J21 = NatDev(:,2)' * obj.NodalCoordinates(:,1);
J22 = NatDev(:,2)' * obj.NodalCoordinates(:,2);
detJ = J11*J22 - J12*J21;
invJ = 1/detJ * [J22 -J21; -J12 J11];
XYDev = NatDev * invJ;
J1 = [J112 J122 2*J11*J12; J212 J222 2*J21*J22; J11*J21 J12*J22 J21*J12 + J11*J22];
J2 = SecDev' * NodalCoords;
MatrixB1 = zeros(3, 3*nnodes);
MatrixB2 = kron(shape, [0 0 1]);
MatrixBbar1 = kron(shape, [1 0 0;0 1 0]);
MatrixBbar2 = zeros(2, 3*nnodes);
MatrixH1 = zeros(3, 3*nnodes);
MatrixH2 = zeros(3, 3*nnodes);
MatrixG1 = zeros(1, 3*nnodes);
MatrixG2 = zeros(1, 3*nnodes);
MatrixM1 = zeros(2, 3*nnodes);
```

```
MatrixM2 = zeros(2, 3*nnodes);
MatrixN1 = zeros(1, 3*nnodes);
MatrixN2 = zeros(1, 3*nnodes);
for i = 1:nnodes
MatrixB1 (:, 3*i-2:3*i) = [XYDev(i,1) 0 0; 0 XYDev(i,2) 0; XYDev(i,2) XYDev(i,1) 0];
MatrixBbar2(:, 3*i-2:3*i) = [0 0 XYDev(i,1); 0 0 XYDev(i,2)];
dNd2 = J1 ( (SecDev(i,:))' - J2 * XYDev(i,:) )';
MatrixH1(:, 3*i-2:3*i) = [dNd2(1) 0 0; 0 dNd2(3) 0; dNd2(3) dNd2(1) 0];
MatrixH2(:, 3*i-2:3*i) = [dNd2(3) 0 0; 0 dNd2(2) 0; dNd2(2) dNd2(3) 0];
MatrixG1(:, 3*i-2:3*i) = [0 0 XYDev(i,1)];
MatrixG2(:, 3*i-2:3*i) = [0 0 XYDev(i,2)];
MatrixM1(:, 3*i-2:3*i) = [XYDev(i,1) 0 0; XYDev(i,2) XYDev(i,1) 0];
MatrixM2(:, 3*i-2:3*i) = [0 0 dNd2(1); 0 0 2*dNd2(3)];
MatrixN1(:, 3*i-2:3*i) = [0 XYDev(i,2) 0];
MatrixN2(:, 3*i-2:3*i) = [0 0 dNd2(2)];
end
PreliminaryStrainsMatrixGaussXYZ([1 2 6 3], 1, layer, gp) = CBar([1 2 6 3], [1 2 6]) * MatrixB1
* Disp_Bottom + CBar([1 2 6 3], 3) * MatrixB2 * (Disp_Top - Disp_Bottom) / h;
PreliminaryStrainsMatrixGaussXYZ([1 2 6 3], 2, layer, gp) = CBar([1 2 6 3], [1 2 6]) * MatrixB1
* Disp_Top + CBar([1 2 6 3], 3) * MatrixB2 * (Disp_Top - Disp_Bottom) / h;
PreliminaryStrainsMatrixGaussXYZ([5 4], 1, layer, gp) = CBar([5 4], [5 4]) * MatrixBbar2 *
Disp_Bottom + CBar([5 4], [5 4]) * MatrixBbar1 * (Disp_Top - Disp_Bottom) / h;
PreliminaryStrainsMatrixGaussXYZ([5 4], 2, layer, gp) = CBar([5 4], [5 4]) * MatrixBbar2 *
Disp_Top + CBar([5 4], [5 4]) * MatrixBbar1 * (Disp_Top - Disp_Bottom) / h;
end
end
for layer = 1:nlayers
h = obj.Section.Layers(layer).Thickness;
for gp = 1:ngaus
StrainsMatrixGaussXYZ(:, [1 2], layer, gp) =
PreliminaryStrainsMatrixGaussXYZ(:, [1 2], layer, gp);
for micro = 1:sublayers+1
A = StrainsMatrixGaussXYZ(:, 1, layer, gp);
B = StrainsMatrixGaussXYZ(:, 2, layer, gp);
obj.StrainsXYZ(:, micro, layer, gp) = A + (B-A)/sublayers*(micro-1);
obj.Strains123(:, micro, layer, gp) = obj.Section.Layers(layer).MatrixR *
obj.StrainsXYZ(:, micro, layer, gp);
for stress = 1:6
obj.StrainsNodalXYZ(stress, micro, layer, :) =
obj.ExtrapolationMatrix * reshape(obj.StrainsXYZ(stress, micro, layer, :), nkaus, 1);
end
for node = 1:nnodes
obj.StrainsNodal123 (:, micro, layer, node) =
obj.Section.Layers(layer).MatrixR * obj.StrainsNodalXYZ(:, micro, layer, node);
end
end
end
end
end
end
```

FLWTFEM.m

```
% GENERATION OF FINITE ELEMENTS and CALCULATION of CHARACTERISTIC MATRICES
disp('GENERATION OF FINITE ELEMENTS...')
FEs = LW_3D.empty(NELEM,0);
for elem = 1:NELEM
FEs(elem) = LW_3D(elem, ELEMENTSDATA(elem,1), ELEMENTSDATAelem,2, ELEMENTS-
DATA(elem,3), NODES(ELEMENTSDATAelem,4), ELEMENTSDATA(elem,5));
FEs(elem) = FEs(elem).deriveGauss();
FEs(elem) = FEs(elem).calcMatrixKL();
FEs(elem) = FEs(elem).calcMatrixM();
FEs(elem) = FEs(elem).calcVectorQ();
FEs(elem) = FEs(elem).deriveIndexDOF();
end
clear elem node ELEMENTSDATA

% GENERATION OF GLOBAL COMPUTATIONAL MODEL
disp('GENERATION OF GLOBAL COMPUTATIONAL MODEL...')
MODEL = MODEL.calcSystemMatrices(FEs, SDOF);
MODEL = MODEL.calcSystemVectors(NODES, FEs, NDOF, SDOF);
Knn = MODEL.SystemMatrixKL(MODEL.UnknownDOFs, MODEL.UnknownDOFs);
Knp = MODEL.SystemMatrixKL(MODEL.UnknownDOFs, MODEL.ZeroDOFs);
Kpn = MODEL.SystemMatrixKL(MODEL.ZeroDOFs, MODEL.UnknownDOFs);
Kpp = MODEL.SystemMatrixKL(MODEL.ZeroDOFs, MODEL.ZeroDOFs);
PDOF = size(MODEL.ZeroDOFs,1);

% BENDING ANALYSIS
if strcmp(ANALYSISTYPE,'Bending') == 1
Sn = MODEL.SystemVectorQ(MODEL.UnknownDOFs, 1) +
MODEL.SystemVectorP(MODEL.UnknownDOFs, 1);
Disp_step = zeros(SDOF, 1);
Disp_step(MODEL.UnknownDOFs, 1) = Knn \ Sn;
for elem = 1:NELEM
FEs(elem).Displacements = Disp_step( FEs(elem).IndexDOF, 1);
FEs(elem) = FEs(elem).CalcStresses(SUBLAYERS);
FEs(elem) = FEs(elem).CalcStrains(SUBLAYERS);
end
end

% PROGRESSIVE FAILURE ANALYSIS
STEPS = 50;
ITERATIONS = 10;
if strcmp(ANALYSISTYPE,'ProgressiveFailure') == 1
NUMBEROFRECORDS = STEPS+1;
Disp_step = zeros(SDOF, NUMBEROFRECORDS+1);
RR_step = zeros(SDOF, NUMBEROFRECORDS);
FF_step = zeros(SDOF, NUMBEROFRECORDS);
Reactions = zeros(SDOF, NUMBEROFRECORDS);
DIVISION = 0:1/STEPS:1;
```

```
STRESS123 = zeros(6,2,NELEM,LAYERS,4,NUMBEROFRECORDS);
STRESS123_eff = zeros(6,2,NELEM,LAYERS,4,NUMBEROFRECORDS);
STRAINS123 = zeros(6,2,NELEM,LAYERS,4,NUMBEROFRECORDS);
Disp_eq = zeros(4,2,NELEM,LAYERS,4,NUMBEROFRECORDS);
Stress_eq = zeros(4,2,NELEM,LAYERS,4,NUMBEROFRECORDS);
DISP_EQ = zeros(4,NUMBEROFRECORDS,NELEM,LAYERS,4);
STRESS_EQ = zeros(2,NUMBEROFRECORDS,NELEM,LAYERS,4);
LAYERS = length(FEs(NELEM).Section.Layers);
BB= [];
TT = [];
Qp = zeros(SDOF,NUMBEROFRECORDS);
NEP = MODEL.UnknownDOFs;
POZ = MODEL.ZeroDOFs;
FailureF = zeros(1,4,NELEM,LAYERS,4,2);
FailureM = zeros(1,4,NELEM,LAYERS,4,2);
FAILUREF = zeros(1,4,NELEM,LAYERS,4,STEPS+1);
FAILUREM = zeros(1,4,NELEM,LAYERS,4,STEPS+1);
KnnL = MODEL.SystemMatrixKL(NEP, NEP);
KnpL = MODEL.SystemMatrixKL(NEP, POZ);
KpnL = MODEL.SystemMatrixKL(POZ, NEP);
KppL = MODEL.SystemMatrixKL(POZ, POZ);
Damage_matrix = zeros(LAYERS, 5, NELEM, NUMBEROFRECORDS);
dm = zeros(LAYERS,NUMBEROFRECORDS, NELEM,4);
df = zeros(LAYERS,NUMBEROFRECORDS, NELEM,4);
N = zeros(STEPS+1,ITERATIONS);
RR = zeros(SDOF, NUMBEROFRECORDS);
Br = 0.3;
Qp = MODEL.SystemVectorqp * DIVISION*3;
Disp_step(NEP, 2) = KnnL (-KnpL * Qp(POZ,2));
for step = 2:STEPS+1
Disp_step(POZ, step) = Qp(POZ,step);
Reactions(POZ,step) = Kpn * Disp_step(NEP, step) + Kpp * Disp_step(POZ, step);
delta_Disp_Current_Iter = zeros(SDOF, ITERATIONS);
Disp_Current_Iter = zeros(SDOF, ITERATIONS);
Disp_Current_Iter(:,1) = Disp_step(:, step);
FF = zeros(SDOF, ITERATIONS);
FF(NEP, 1) = Knn * Disp_step(NEP, step);
residual = zeros(length(NEP), 1);
n = 0;
for iter = 2:ITERATIONS
for elem = 1:NELEM
FEs(elem).Displacements = Disp_Current_Iter( FEs(elem).IndexDOF, iter-1);
FEs(elem) = FEs(elem).CalcStresses(SUBLAYERS);
FEs(elem) = FEs(elem).CalcStrains(SUBLAYERS);
maxFailureIndex = 0;
for layer = 1:length(FEs(elem).Section.Layers)
Xt = FEs(elem).Section.Layers(layer).Material.Xt;
Xc = FEs(elem).Section.Layers(layer).Material.Xc;
Yt = FEs(elem).Section.Layers(layer).Material.Yt;
Yc = FEs(elem).Section.Layers(layer).Material.Yc;
```

```

Zt = FEs(elem).Section.Layers(layer).Material.Zt;
Zc = FEs(elem).Section.Layers(layer).Material.Zc;
R = FEs(elem).Section.Layers(layer).Material.R;
S = FEs(elem).Section.Layers(layer).Material.S;
T = FEs(elem).Section.Layers(layer).Material.T;
for qp = 1:4
for micro = 1:2
STRESS123(:,micro,elem,layer,qp,step) = FEs(elem).Stresses123(:,micro,layer,qp);
STRAINS123(:,micro,elem,layer,qp,step) = FEs(elem).Strains123(:,micro,layer,qp);
STRESS123_eff(:,micro,elem,layer,qp,step) = FEs(elem).Section.Layers(layer).Material.MatrixM
* STRESS123(:,micro,elem,layer,qp,step);
Disp_eq(1,micro,elem,layer,qp,step) = (STRAINS123(1,micro,elem,layer,qp,step) *
(STRAINS123(1,micro,elem,layer,qp,step)>0));
Disp_eq(2,micro,elem,layer,qp,step) =
(-STRAINS123(1,micro,elem,layer,qp,step))*(STRAINS123(1,micro,elem,layer,qp,step)<0);
Disp_eq(3,micro,elem,layer,qp,step) =
sqrt((STRAINS123(2,micro,elem,layer,qp,step)*(STRAINS123(2,micro,elem,layer,qp,step)>0))2
+ (STRAINS123(6,micro,elem,layer,qp,step))2);
Disp_eq(4,micro,elem,layer,qp,step) =
sqrt((-STRAINS123(2,micro,elem,layer,qp,step)*(STRAINS123(2,micro,elem,layer,qp,step)<0))2
+ (STRAINS123(6,micro,elem,layer,qp,step))2);
Stress_eq(1,micro,elem,layer,qp,step) =
((STRESS123(1,micro,elem,layer,qp,step))*(STRESS123(1,micro,elem,layer,qp,step)>0)
* (STRAINS123(1,micro,elem,layer,qp,step))*(STRAINS123(1,micro,elem,layer,qp,step)>0)) /
Disp_eq(1,micro,elem,layer,qp,step);
Stress_eq(2,micro,elem,layer,qp,step) =
((-STRESS123(1,micro,elem,layer,qp,step))*(STRESS123(1,micro,elem,layer,qp,step)<0)
(-STRAINS123(1,micro,elem,layer,qp,step))*(STRAINS123(1,micro,elem,layer,qp,step)<0)) /
Disp_eq(2,micro,elem,layer,qp,step);
Stress_eq(3,micro,elem,layer,qp,step) =
((STRESS123(2,micro,elem,layer,qp,step))*(STRESS123(2,micro,elem,layer,qp,step)>0)
(STRAINS123(2,micro,elem,layer,qp,step))*(STRAINS123(2,micro,elem,layer,qp,step)>0)
+ STRESS123(6,micro,elem,layer,qp,step)* STRAINS123(6,micro,elem,layer,qp,step))
/ Disp_eq(3,micro,elem,layer,qp,step);
Stress_eq(4,micro,elem,layer,qp,step) =
((-STRESS123(2,micro,elem,layer,qp,step))*(STRESS123(2,micro,elem,layer,qp,step)<0)
(-STRAINS123(2,micro,elem,layer,qp,step))*(STRAINS123(2,micro,elem,layer,qp,step)<0)
+ STRESS123(6,micro,elem,layer,qp,step)* STRAINS123(6,micro,elem,layer,qp,step))
/ Disp_eq(4,micro,elem,layer,qp,step);
if strcmp(CRITERION,'Hashin') == 1
if STRESS123_eff(1,micro,elem,layer,qp,step) > 0
Mode1 = (STRESS123_eff(1,micro,elem,layer,qp,step)/Xt)2;
Disp_eq_f = Disp_eq(1,micro,elem,layer,qp,step);
Stress_eq_f = Stress_eq(1,micro,elem,layer,qp,step);
Mode1 = abs(STRESS123_eff(1,micro,elem,layer,qp,step)/Xc);
Disp_eq_f = Disp_eq(2,micro,elem,layer,qp,step);
Stress_eq_f = Stress_eq(2,micro,elem,layer,qp,step);
end
if STRESS123_eff(2,micro,elem,layer,qp,step) > 0
Mode2 = ((STRESS123_eff(2,micro,elem,layer,qp,step))/Yt)2 +

```

```
(STRESS123_eff(6,micro,elem,layer,qp,step)/T)^2;  
Disp_eq_m = Disp_eq(3,micro,elem,layer,qp,step);  
Stress_eq_m = Stress_eq(3,micro,elem,layer,qp,step);  
else  
Mode2 = (STRESS123_eff(2,micro,elem,layer,qp,step)/Yc)^2 +  
(STRESS123_eff(6,micro,elem,layer,qp,step)/T)^2;  
Disp_eq_m = Disp_eq(4,micro,elem,layer,qp,step);  
Stress_eq_m = Stress_eq(4,micro,elem,layer,qp,step);  
end  
FailureF(1, 1, elem, layer, qp,micro) = Mode1;  
FailureF(1, 2, elem, layer, qp,micro) = Disp_eq_f;  
FailureF(1, 3, elem, layer, qp,micro) = Stress_eq_f;  
FailureF(1, 4, elem, layer, qp,micro) = Gf;  
FailureM(1, 1, elem, layer, qp,micro) = Mode2;  
FailureM(1, 2, elem, layer, qp,micro) = Disp_eq_m;  
FailureM(1, 3, elem, layer, qp,micro) = Stress_eq_m;  
FailureM(1, 4, elem, layer, qp,micro) = Gm;  
end  
end  
end  
end  
end for elem = 1:NELEM  
Lc = sqrt(A);  
for layer = 1:length(FEs(elem).Section.Layers)  
for qp = 1:4  
if FAILUREF(1, 1, elem, layer,qp,step) > 1  
n=n+1;  
disp('DA')  
DISP_EQ(1, step, elem, layer,qp) =  
FAILUREF(1 , 2, elem, layer, qp,step) / sqrt(FAILUREF(1, 1, elem, layer, qp,step));  
STRESS_EQ(1, step, elem, layer,qp) =  
FAILUREF(1 , 3, elem, layer, qp,step) / sqrt(FAILUREF(1, 1, elem, layer, qp,step));  
DISP_EQ(3, step, elem, layer,qp) =  
(FAILUREF(1 , 4, elem, layer, qp,step)/Lc - STRESS_EQ(1, step, elem, layer,qp)*DISP_EQ(1,  
step, elem, layer,qp))/2 + Br*STRESS_EQ(1, step, elem, layer,qp)*DISP_EQ(1, step, elem,  
layer,qp)) / Br/STRESS_EQ(1, step, elem, layer,qp);  
if FAILUREF(1 , 2, elem, layer, qp,step) <= DISP_EQ(3, step, elem, layer,qp)  
df(layer, step, elem,qp) = (FAILUREF(1 , 2, elem, layer, qp,step)-Br*DISP_EQ(1, step, elem,  
layer, qp)) / FAILUREF(1 , 2, elem, layer, qp,step);  
else  
df(layer, step, elem,qp) = 1;  
end  
FEs(elem).Section.Layers(layer).Material.df = max(df(layer, step, elem,:));  
end  
if FAILUREM(1, 1, elem, layer,qp,step) > 1  
n=n+1;  
disp('DA')  
DISP_EQ(2, step, elem, layer,qp) =  
FAILUREM(1 , 2, elem, layer, qp,step) / sqrt(FAILUREM(1, 1, elem, layer,qp,step));  
STRESS_EQ(2, step, elem, layer,qp) =
```

```
FAILUREM(1 , 3, elem, layer, qp,step) / sqrt(FAILUREM(1, 1, elem, layer,qp,step));
DISP_EQ(4, step, elem, layer,qp) =
2*FAILUREM(1 , 4, elem, layer, qp,step) / STRESS_EQ(2, step, elem, layer,qp)/Lc;
dm(layer, step, elem,qp) = max(0, min(1, DISP_EQ(4, step, elem, layer,qp)*(FAILUREM(1
, 2, elem, layer, qp,step) - DISP_EQ(2, step, elem, layer,qp))/FAILUREM(1 , 2, elem, layer,
qp,step))/(DISP_EQ(4, step, elem, layer,qp) - DISP_EQ(2, step, elem, layer,qp)))));
FEs(elem).Section.Layers(layer).Material.dm = max(dm(layer, step, elem,:));
end
end
FEs(elem).Section.Layers(layer).Material.ds = 1-(1-FEs(elem).Section.Layers(layer).Material.df)
*(1-FEs(elem).Section.Layers(layer).Material.dm);
Damage_matrix(layer,1,elem,step) = FEs(elem).Section.Layers(layer).Material.df;
Damage_matrix(layer,2,elem,step) = FEs(elem).Section.Layers(layer).Material.dm;
Damage_matrix(layer,3,elem,step) = FEs(elem).Section.Layers(layer).Material.ds;
Damage_matrix(layer,4,elem,step) = FAILUREF(1, 1, elem, layer,3,step);
Damage_matrix(layer,5,elem,step) = FAILUREM(1, 1, elem, layer,3,step);
end
FEs(elem).Section = FEs(elem).Section.calcCoeffMatrices();
FEs(elem) = FEs(elem).calcMatrixKL();
end N(step,iter) = n;
MODEL = MODEL.calcSystemMatrices(FEs,SDOF);
NEP = MODEL.UnknownDOFs;
POZ = MODEL.ZeroDOFs;
Knn = MODEL.SystemMatrixKL(NEP, NEP);
Knp = MODEL.SystemMatrixKL(NEP, POZ);
Kpp = MODEL.SystemMatrixKL(POZ, POZ);
Kpn = MODEL.SystemMatrixKL(POZ, NEP);
RR(NEP, step) = -Knp * Disp_step(POZ, step);
residual(:,1) = RR(NEP, step) - FF(NEP, iter-1);
if N(step,iter)> N(step,iter-1)
delta_Displ_Current_Iter(NEP, iter) = Knn residual;
Displ_Current_Iter(:,iter) = Displ_Current_Iter(:,iter-1) + delta_Displ_Current_Iter(:, iter);
FF(NEP, iter) = Knn * Displ_Current_Iter(NEP, iter);
elseif iter == ITERATIONS
disp('No Convergence')
break
else
Displ_Current_Iter(NEP,iter) = Displ_Current_Iter(NEP,iter-1);
Displ_step(NEP, step+1) = Displ_Current_Iter(NEP,iter) + Knn (-Knp*(Qp(POZ,step)-
Qp(POZ,step-1)));
break
end
end
end
end
clear Knn Mnn Sn elem vector values number mode

% GENERATION OF POST PROCESS NODES
disp('GENERATION OF POST PROCESS NODES and ELEMENTS...')
zz = zeros(LAYERS*SUBLAYERS+1, 1);
```

```
hh = 0;
count = 1;
for layer = 1:LAYERS
for sublayer = 1:SUBLAYERS
hh = hh + FEs(1).Section.Layers(layer).Thickness / SUBLAYERS;
count = count + 1;
zz(count) = hh;
end
end
zz = zz - hh/2;
POSTNODES( NNODE * (LAYERS*SUBLAYERS + 1) ) = PostNode();
for layer = 1:LAYERS*SUBLAYERS + 1
for node = 1:NNODE
POSTNODES( (layer-1)*NNODE + node ) =
PostNode((layer-1)*NNODE + node, NODES(node).XCoord, NODES(node).YCoord, zz(layer));
end
end
clear zz hh sublayer count layer node
for node = 1:NNODE
CurrentNodeDisp = Disp_step( (node-1)*NDOF+1 : node*NDOF, :);
POSTNODES( node ).DispX = CurrentNodeDisp(1, :);
POSTNODES( node ).DispY = CurrentNodeDisp(2, :);
POSTNODES( node ).DispZ = CurrentNodeDisp(3, :);
count = 0;
for layer = 1:LAYERS
X_bottom = CurrentNodeDisp(3*layer-2, :);
X_top = CurrentNodeDisp(3*layer+1, :);
Y_bottom = CurrentNodeDisp(3*layer-1, :);
Y_top = CurrentNodeDisp(3*layer+2, :);
Z_bottom = CurrentNodeDisp(3*layer, :);
Z_top = CurrentNodeDisp(3*layer+3, :);
for sublayer = 1:SUBLAYERS
count = count + 1;
POSTNODES(count*NNODE + node).DispX =
X_bottom + (X_top-X_bottom) / SUBLAYERS * sublayer;
POSTNODES(count*NNODE + node).DispY =
Y_bottom + (Y_top-Y_bottom) / SUBLAYERS * sublayer;
POSTNODES(count*NNODE + node).DispZ =
Z_bottom + (Z_top-Z_bottom) / SUBLAYERS * sublayer;
end
end
end
clear node CurrentNodeDisp count layer sublayer
clear X_bottom Y_bottom Z_bottom X_top Y_top Z_top

% GENERATION OF POST PROCESS ELEMENTS
count = 0;
countlayer = 0;
POSTELEMENTS(NELEM*LAYERS*SUBLAYERS) = PostElement();
for layer = 1:LAYERS
```

```
for sublayer = 1:SUBLAYERS
countlayer = countlayer+1;
for elem = 1:NELEM
array = (countlayer-1)*NNODE + [FEs(elem).ElementNodes(1:3).NodeID];
if strcmp(FEs(elem).ElementType, 'Q4') == 1 ||
strcmp(FEs(elem).ElementType, 'Q8') == 1
array = (countlayer-1)*NNODE + [FEs(elem).ElementNodes(1:4).NodeID];
end
count = count + 1;
POSTELEMENTS(count) = PostElement(count, POSTNODES([array array+NNODE]));
if strcmp(ANALYSISTYPE,'Bending') == 1
ngaus = size(FEs(elem).StressesXYZ, 4);
POSTELEMENTS(count).StressesXYZ = zeros(6,2,ngaus);
POSTELEMENTS(count).Stresses123 = zeros(6,2,ngaus);
for gaus = 1:ngaus
POSTELEMENTS(count).StressesXYZ(:, :, gaus) =
FEs(elem).StressesXYZ(:, [sublayer sublayer+1], layer, gaus);
POSTELEMENTS(count).Stresses123(:, :, gaus) =
FEs(elem).Stresses123(:, [sublayer sublayer+1], layer, gaus);
end
end
if strcmp(ANALYSISTYPE,'ProgressiveFailure') == 1
ngaus = size(FEs(elem).StressesXYZ, 4);
POSTELEMENTS(count).StressesXYZ = zeros(6,2,ngaus,STEPS+1);
POSTELEMENTS(count).Stresses123 = zeros(6,2,ngaus,STEPS+1);
for step = 1:STEPS+1
for gaus = 1:ngaus
POSTELEMENTS(count).Stresses123(:, :, gaus, step) =
STRAINS123(:, [sublayer sublayer+1], elem, layer, step);
POSTELEMENTS(count).Index(1, step) = Damage_matrix(layer, 1, elem, step);
POSTELEMENTS(count).Index(2, step) = Damage_matrix(layer, 2, elem, step);
POSTELEMENTS(count).Index(3, step) = Damage_matrix(layer, 3, elem, step);
POSTELEMENTS(count).Index(4, step) = Damage_matrix(layer, 4, elem, step);
POSTELEMENTS(count).Index(5, step) = Damage_matrix(layer, 5, elem, step);
end
end
end
end
end
clear count countlayer layer sublayer elem array
clear gaus ngaus
```

Bibliography

- [1] E. J. Barbero. *Introduction to Composite Materials Design*. CRC Press, July 2010. ISBN: 9780429109478. DOI: 10.1201/9781439894132.
- [2] R. Brandner et al. “Cross laminated timber (CLT): overview and development”. In: *European Journal of Wood and Wood Products* 74 (3 May 2016), pp. 331–351. ISSN: 1436736X. DOI: 10.1007/s00107-015-0999-5.
- [3] R. Cvetkovic et al. “Innovative structural CLT system in projecting and building of student houses”. In: *Facta universitatis - series: Architecture and Civil Engineering* 13 (1 2015), pp. 57–64. ISSN: 0354-4605. DOI: 10.2298/FUACE1501057C.
- [4] O. O. Ochoa and J. N. Reddy. *Finite Element Analysis of Composite Laminates*. 1992. DOI: 10.1007/978-94-015-7995-7_3.
- [5] G. Hochreiner et al. *CLT Plates under Concentrated Loading – Experimental Identification of Crack Modes and Corresponding Failure Mechanisms*. 2014. DOI: 10.1007/978-94-007-7811-5_63.
- [6] M. R. Wisnom, S. R. Hallett, and C. Soutis. “Scaling effects in notched composites”. In: *Journal of Composite Materials* 44 (2 Jan. 2010), pp. 195–210. ISSN: 00219983. DOI: 10.1177/0021998309339865.
- [7] A. C. Orifici, I. Herszberg, and R. S. Thomson. “Review of methodologies for composite material modelling incorporating failure”. In: *Composite Structures* 86 (1-3 Nov. 2008), pp. 194–210. ISSN: 02638223. DOI: 10.1016/j.compstruct.2008.03.007.
- [8] D. W. Sleight. *Progressive Failure Analysis Methodology for Laminated Composite Structures*. 1999.
- [9] M. R. Garnich and V. M. Akula. *Review of degradation models for progressive failure analysis of fiber reinforced polymer composites*. Jan. 2009. DOI: 10.1115/1.3013822.
- [10] K. V. Williams, R. Vaziri, and A. Poursartip. “A physically based continuum damage mechanics model for thin laminated composite structures”. In: *International Journal of Solids and Structures* 40 (9 May 2003), pp. 2267–2300. ISSN: 00207683. DOI: 10.1016/S0020-7683(03)00016-7.
- [11] A. Forghani et al. “A structural modelling framework for prediction of damage development and failure of composite laminates”. In: *Journal of Composite Materials* 47 (20-21 Sept. 2013), pp. 2553–2573. ISSN: 00219983. DOI: 10.1177/0021998312474044.
- [12] J. N. Reddy. *Mechanics of Laminated Composite Plates and Shells*. CRC Press, Nov. 2003. ISBN: 9780429210693. DOI: 10.1201/b12409.
- [13] E. Jočić and M. Marjanović. “Progressive failure analysis of open-hole composite laminates using FLWT-SCB prediction model”. In: *International Journal of Mechanical Sciences* 227 (Aug. 2022). ISSN: 00207403. DOI: 10.1016/j.ijmecsci.2022.107407.

- [14] *GiD Customization Manual. CIMNE – International Center for Numerical Methods in Engineering, 2016.*
- [15] M. Marjanović, G. Meschke, and E. Damnjanović. “Object-oriented framework for 3D bending and free vibration analysis of multilayer plates: Application to cross-laminated timber and soft-core sandwich panels”. In: *Composite Structures* 255 (Jan. 2021). ISSN: 02638223. DOI: 10.1016/j.compstruct.2020.112859.
- [16] P. H. Petit and M. E. Waddoups. “A Method of Predicting the Nonlinear Behavior of Laminated Composites”. In: *Journal of Composite Materials* 3 (1 1969), pp. 2–19. ISSN: 1530793X. DOI: 10.1177/002199836900300101.
- [17] R. S. Sandhu. “Nonlinear behavior of unidirectional and angle ply laminates”. In: *Journal of Aircraft* 13 (2 1976), pp. 104–111. ISSN: 00218669. DOI: 10.2514/3.58638.
- [18] G. A. Abu-Farsakh and Y. A. Abdel-Jawad. “New failure criterion for nonlinear composite materials”. In: *Journal of Composites Technology and Research* 16 (2 1994), pp. 138–145. ISSN: 08846804. DOI: 10.1520/ctr10403j.
- [19] S. P. Engelstad, J. N. Reddy, and N. F. Knight. “Postbuckling response and failure prediction of graphite-epoxy plates loaded in compression”. In: *AIAA Journal* 30 (8 1992), pp. 2106–2113. ISSN: 00011452. DOI: 10.2514/3.11187.
- [20] S. W. Tsai and E. M. Wu. “A General Theory of Strength for Anisotropic Materials”. In: *Journal of Composite Materials* 5 (1 Jan. 1971), pp. 58–80. ISSN: 0021-9983. DOI: 10.1177/002199837100500106.
- [21] S. Singh and A. Kumar. “Postbuckling response and strength of laminates under combined in-plane loads”. In: *Composites Science and Technology* 59 (5 Apr. 1999), pp. 727–736. ISSN: 02663538. DOI: 10.1016/S0266-3538(98)00125-0.
- [22] R. Hill. “A theory of the yielding and plastic flow of anisotropic metals”. In: *Proceedings of the Royal Society of London. Series A. Mathematical and Physical Sciences* 193 (1033 May 1948), pp. 281–297. ISSN: 0080-4630. DOI: 10.1098/rspa.1948.0045.
- [23] O OCHOA and J ENGBLOM. “Analysis of progressive failure in composites”. In: *Composites Science and Technology* 28 (2 1987), pp. 87–102. ISSN: 02663538. DOI: 10.1016/0266-3538(87)90092-3.
- [24] Z. Hashin. “Fatigue Failure Criteria for Unidirectional Fiber Composites”. In: *Journal of Applied Mechanics* 48 (4 Dec. 1981), pp. 846–852. ISSN: 0021-8936. DOI: 10.1115/1.3157744.
- [25] J. D. Lee. “Three dimensional finite element analysis of damage accumulation in composite laminate”. In: *Computers Structures* 15 (3 Jan. 1982), pp. 335–350. ISSN: 00457949. DOI: 10.1016/0045-7949(82)90026-8.
- [26] W. Hwang and C. Sun. “Failure analysis of laminated composites by using iterative three-dimensional finite element method”. In: *Computers Structures* 33 (1 Jan. 1989), pp. 41–47. ISSN: 00457949. DOI: 10.1016/0045-7949(89)90127-2.
- [27] F.-K. Chang and G. S. Springer. “The Strengths of Fiber Reinforced Composite Bends”. In: *Journal of Composite Materials* 20 (1 Jan. 1986), pp. 30–45. ISSN: 0021-9983. DOI: 10.1177/002199838602000103.
- [28] S. Tolson and N. Zabararas. “Finite element analysis of progressive failure in laminated composite plates”. In: *Computers Structures* 38 (3 Jan. 1991), pp. 361–376. ISSN: 00457949. DOI: 10.1016/0045-7949(91)90113-Z.
- [29] O. Hoffman. “The Brittle Strength of Orthotropic Materials”. In: *Journal of Composite Materials* 1 (2 Apr. 1967), pp. 200–206. ISSN: 0021-9983. DOI: 10.1177/002199836700100210.

- [30] S. C. Tan and R. J. Nuismer. “A Theory for Progressive Matrix Cracking in Composite Laminates”. In: *Journal of Composite Materials* 23 (10 1989), pp. 1029–1047. ISSN: 1530793x. DOI: 10.1177/002199838902301006.
- [31] S. C. Tan. “A Progressive Failure Model for Composite Laminates Containing Openings”. In: *Journal of Composite Materials* 25 (5 1991), pp. 556–577. ISSN: 1530793X. DOI: 10.1177/002199839102500505.
- [32] S. C. Tan and J. Perez. “Progressive Failure of Laminated Composites with a Hole under Compressive Loading”. In: *Journal of Reinforced Plastics and Composites* 12 (10 1993), pp. 1043–1057. ISSN: 15307964. DOI: 10.1177/073168449301201002.
- [33] P. P. Camanho and F. L. Matthews. “A progressive damage model for mechanically fastened joints in composite laminates”. In: *Journal of Composite Materials* 33 (24 1999), pp. 2248–2280. ISSN: 00219983. DOI: 10.1177/002199839903302402.
- [34] *Simulia, Abaqus, User Manual. Version 6.13. Providence, RI, USA: DS SIMULIA Corp. 2013.*
- [35] F. K. Chang and K. Y. Chang. “A Progressive Damage Model for Laminated Composites Containing Stress Concentrations”. In: *Journal of Composite Materials* 21 (9 1987), pp. 834–855. ISSN: 1530793x. DOI: 10.1177/002199838702100904.
- [36] Y. Kim and C. Hong. “Progressive Failure Model for the Analysis of Laminated Composites Based on Finite Element Approach”. In: *Journal of Reinforced Plastics and Composites* 11 (10 Oct. 1992), pp. 1078–1092. ISSN: 0731-6844. DOI: 10.1177/073168449201101001.
- [37] W. P. Lin and H. T. Hu. “Nonlinear Analysis of Fiber-Reinforced Composite Laminates Subjected to Uniaxial Tensile Load”. In: (). DOI: 10.1106/002199802021463.
- [38] W. P. Lin. “Parametric Study on the Failure of Fiber-Reinforced Composite Laminates under Biaxial Tensile Load”. In: (). DOI: 10.1106/002199802023218.
- [39] H. T. Hahn and S. W. Tsai. “On the Behavior of Composite Laminates After Initial Failures”. In: *Journal of Composite Materials* 8 (3 1974), pp. 288–305. ISSN: 1530793X. DOI: 10.1177/002199837400800306.
- [40] Y. Reddy, C. Moorthy, and J. Reddy. “Non-linear progressive failure analysis of laminated composite plates”. In: *International Journal of Non-Linear Mechanics* 30 (5 Sept. 1995), pp. 629–649. ISSN: 00207462. DOI: 10.1016/0020-7462(94)00041-8.
- [41] E. J. Barbero et al. “Determination of material parameters for Abaqus progressive damage analysis of E-glass epoxy laminates”. In: *Composites Part B: Engineering* 46 (2013), pp. 211–220. ISSN: 13598368. DOI: 10.1016/j.compositesb.2012.09.069.
- [42] C. Mcgregor et al. “A Constitutive Model for Progressive Compressive Failure of Composites”. In: *Journal of Composite Materials* 42 (25 Dec. 2008), pp. 2687–2716. ISSN: 0021-9983. DOI: 10.1177/0021998308096330.
- [43] S. R. Hallett and M. R. Wisnom. *Experimental investigation of progressive damage and the effect of layup in notched tensile tests*. 2006. DOI: 10.1177/0021998305053504.
- [44] E. Abisset, F. Daghia, and P. Ladevèze. “On the validation of a damage mesomodel for laminated composites by means of open-hole tensile tests on quasi-isotropic laminates”. In: *Composites Part A: Applied Science and Manufacturing* 42 (10 Oct. 2011), pp. 1515–1524. ISSN: 1359835X. DOI: 10.1016/j.compositesa.2011.07.004.
- [45] Z. P. Bažant. “Instability, Ductility, and Size Effect in Strain-Softening Concrete”. In: *Journal of the Engineering Mechanics Division* 102 (2 Apr. 1976), pp. 331–344. ISSN: 0044-7951. DOI: 10.1061/JMCEA3.0002111.

- [46] P. P. Camanho, P. Maimí, and C. G. Dávila. “Prediction of size effects in notched laminates using continuum damage mechanics”. In: *Composites Science and Technology* 67 (13 2007), p. 2715. DOI: 10.1016/j.compscitech.2007.02.005.
- [47] E. H. Kim et al. “Composite damage model based on continuum damage mechanics and low velocity impact analysis of composite plates”. In: *Composite Structures* 95 (Jan. 2013), pp. 123–134. ISSN: 02638223. DOI: 10.1016/j.compstruct.2012.07.002.
- [48] L. Wang et al. “Continuum damage modeling and progressive failure analysis of carbon fiber/epoxy composite pressure vessel”. In: *Composite Structures* 134 (Dec. 2015), pp. 475–482. ISSN: 02638223. DOI: 10.1016/j.compstruct.2015.08.107.
- [49] S. R. Hallett et al. “Modelling the interaction between matrix cracks and delamination damage in scaled quasi-isotropic specimens”. In: *Composites Science and Technology* 68 (1 Jan. 2008), pp. 80–89. ISSN: 02663538. DOI: 10.1016/j.compscitech.2007.05.038.
- [50] C. Bouvet et al. “Low velocity impact modelling in laminate composite panels with discrete interface elements”. In: *International Journal of Solids and Structures* 46 (14-15 July 2009), pp. 2809–2821. ISSN: 00207683. DOI: 10.1016/j.ijsolstr.2009.03.010.
- [51] X. C. Sun, M. R. Wisnom, and S. R. Hallett. “Interaction of inter- and intralaminar damage in scaled quasi-static indentation tests: Part 2 - Numerical simulation”. In: *Composite Structures* 136 (Feb. 2016), pp. 727–742. ISSN: 02638223. DOI: 10.1016/j.compstruct.2015.09.062.
- [52] B. Karihaloo and Q. Xiao. “Modelling of stationary and growing cracks in FE framework without remeshing: a state-of-the-art review”. In: *Computers & Structures* 81 (3 Feb. 2003), pp. 119–129. ISSN: 00457949. DOI: 10.1016/S0045-7949(02)00431-5.
- [53] M. J. Swindeman et al. “Strength Prediction in Open Hole Composite Laminates by Using Discrete Damage Modeling”. In: *AIAA Journal* 51 (4 Apr. 2013), pp. 936–945. ISSN: 0001-1452. DOI: 10.2514/1.J051773.
- [54] H. W. Wang et al. “Application of extended finite element method in damage progress simulation of fiber reinforced composites”. In: *Materials and Design* 55 (2014), pp. 191–196. ISSN: 18734197. DOI: 10.1016/j.matdes.2013.09.071.
- [55] J.-H. Song, P. M. A. Areias, and T. Belytschko. “A method for dynamic crack and shear band propagation with phantom nodes”. In: *International Journal for Numerical Methods in Engineering* 67 (6 Aug. 2006), pp. 868–893. ISSN: 0029-5981. DOI: 10.1002/nme.1652.
- [56] F. P. Meer and L. J. Sluys. “A phantom node formulation with mixed mode cohesive law for splitting in laminates”. In: *International Journal of Fracture* 158 (2 Aug. 2009), pp. 107–124. ISSN: 0376-9429. DOI: 10.1007/s10704-009-9344-5.
- [57] J. Reiner et al. “A progressive analysis of matrix cracking-induced delamination in composite laminates using an advanced phantom node method”. In: *Journal of Composite Materials* 51 (20 Aug. 2017), pp. 2933–2947. ISSN: 0021-9983. DOI: 10.1177/0021998316684203.
- [58] X. J. Fang et al. “High-fidelity simulations of multiple fracture processes in a laminated composite in tension”. In: *Journal of the Mechanics and Physics of Solids* 59 (7 July 2011), pp. 1355–1373. ISSN: 00225096. DOI: 10.1016/j.jmps.2011.04.007.
- [59] X. J. Fang et al. “An augmented cohesive zone element for arbitrary crack coalescence and bifurcation in heterogeneous materials”. In: *International Journal for Numerical Methods in Engineering* 88 (9 Dec. 2011), pp. 841–861. ISSN: 00295981. DOI: 10.1002/nme.3200.
- [60] B. Y. Chen et al. “A floating node method for the modelling of discontinuities in composites”. In: *Engineering Fracture Mechanics* 127 (2014), pp. 104–134. ISSN: 00137944. DOI: 10.1016/j.engfracmech.2014.05.018.

- [61] B. Y. Chen et al. “Modelling the tensile failure of composites with the floating node method”. In: *Computer Methods in Applied Mechanics and Engineering* 308 (Aug. 2016), pp. 414–442. ISSN: 00457825. DOI: 10.1016/j.cma.2016.05.027.
- [62] X. Lu et al. “A separable cohesive element for modelling coupled failure in laminated composite materials”. In: *Composites Part A: Applied Science and Manufacturing* 107 (Apr. 2018), pp. 387–398. ISSN: 1359835X. DOI: 10.1016/j.compositesa.2018.01.014.
- [63] X. F. Hu, X. Lu, and T. E. Tay. “Modelling delamination migration using virtual embedded cohesive elements formed through floating nodes”. In: *Composite Structures* 204 (Nov. 2018), pp. 500–512. ISSN: 02638223. DOI: 10.1016/j.compstruct.2018.07.120.
- [64] S. T. Pinho, L. Iannucci, and P. Robinson. “Physically-based failure models and criteria for laminated fibre-reinforced composites with emphasis on fibre kinking: Part I: Development”. In: *Composites Part A: Applied Science and Manufacturing* 37 (1 Jan. 2006), pp. 63–73. ISSN: 1359835X. DOI: 10.1016/j.compositesa.2005.04.016.
- [65] S. T. Pinho, L. Iannucci, and P. Robinson. “Physically based failure models and criteria for laminated fibre-reinforced composites with emphasis on fibre kinking. Part II: FE implementation”. In: *Composites Part A: Applied Science and Manufacturing* 37 (5 May 2006), pp. 766–777. ISSN: 1359835X. DOI: 10.1016/j.compositesa.2005.06.008.
- [66] B. Y. Chen et al. “Numerical analysis of size effects on open-hole tensile composite laminates”. In: *Composites Part A: Applied Science and Manufacturing* 47 (1 2013), pp. 52–62. ISSN: 1359835X. DOI: 10.1016/j.compositesa.2012.12.001.
- [67] M. Ridha et al. “Modelling complex progressive failure in notched composite laminates with varying sizes and stacking sequences”. In: *Composites Part A: Applied Science and Manufacturing* 58 (Mar. 2014), pp. 16–23. ISSN: 1359835X. DOI: 10.1016/j.compositesa.2013.11.012.
- [68] Z. C. Su et al. “Progressive damage modeling of open-hole composite laminates under compression”. In: *Composite Structures* 122 (Apr. 2015), pp. 507–517. ISSN: 02638223. DOI: 10.1016/j.compstruct.2014.12.022.
- [69] P LADEVEZE and E LEDANTEC. “Damage modelling of the elementary ply for laminated composites”. In: *Composites Science and Technology* 43 (3 1992), pp. 257–267. ISSN: 02663538. DOI: 10.1016/0266-3538(92)90097-M.
- [70] J. Reiner et al. “Comparison of two progressive damage models for studying the notched behavior of composite laminates under tension”. In: *Composite Structures* 207 (Jan. 2019), pp. 385–396. ISSN: 02638223. DOI: 10.1016/j.compstruct.2018.09.033.
- [71] A. Forghani, A. Poursartip, and R. Vaziri. “An orthotropic non-local approach to modeling intra-laminar damage progression in laminated composites”. In: *International Journal of Solids and Structures* 180-181 (Dec. 2019), pp. 160–175. ISSN: 00207683. DOI: 10.1016/j.ijsolstr.2019.07.015.
- [72] D. Yoon et al. “Development and evaluation of crack band model implemented progressive failure analysis method for notched composite laminate”. In: *Applied Sciences (Switzerland)* 9 (24 Dec. 2019). ISSN: 20763417. DOI: 10.3390/app9245572.
- [73] M. H. Nagaraj et al. “Progressive damage analysis of composite structures using higher-order layer-wise elements”. In: *Composites Part B: Engineering* 190 (June 2020). ISSN: 13598368. DOI: 10.1016/j.compositesb.2020.107921.
- [74] M. H. Nagaraj et al. “Compressive damage modeling of fiber-reinforced composite laminates using 2D higher-order layer-wise models”. In: *Composites Part B: Engineering* 215 (June 2021). ISSN: 13598368. DOI: 10.1016/j.compositesb.2021.108753.

- [75] B. Dhas et al. “A Phase-Field Damage Model for Orthotropic Materials and Delamination in Composites”. In: *Journal of Applied Mechanics* 85 (1 Jan. 2018). ISSN: 0021-8936. DOI: 10.1115/1.4038506.
- [76] C. Miehe, F. Welschinger, and M. Hofacker. “Thermodynamically consistent phase-field models of fracture: Variational principles and multi-field FE implementations”. In: *International Journal for Numerical Methods in Engineering* 83 (10 Sept. 2010), pp. 1273–1311. ISSN: 00295981. DOI: 10.1002/nme.2861.
- [77] A. Mesgarnejad, B. Bourdin, and M. M. Khonsari. “Validation simulations for the variational approach to fracture”. In: *Computer Methods in Applied Mechanics and Engineering* 290 (June 2015), pp. 420–437. ISSN: 00457825. DOI: 10.1016/j.cma.2014.10.052.
- [78] M. Ambati, T. Gerasimov, and L. D. Lorenzis. “A review on phase-field models of brittle fracture and a new fast hybrid formulation”. In: *Computational Mechanics* 55 (2 Feb. 2015), pp. 383–405. ISSN: 0178-7675. DOI: 10.1007/s00466-014-1109-y.
- [79] M. A. Msekh et al. “Abaqus implementation of phase-field model for brittle fracture”. In: *Computational Materials Science* 96 (PB 2015), pp. 472–484. ISSN: 09270256. DOI: 10.1016/j.commatsci.2014.05.071.
- [80] R. U. Patil, B. K. Mishra, and I. V. Singh. “An adaptive multiscale phase field method for brittle fracture”. In: *Computer Methods in Applied Mechanics and Engineering* 329 (Feb. 2018), pp. 254–288. ISSN: 00457825. DOI: 10.1016/j.cma.2017.09.021.
- [81] P. Zhang et al. “Phase field modeling of fracture in fiber reinforced composite laminate”. In: *International Journal of Mechanical Sciences* 161-162 (Oct. 2019). ISSN: 00207403. DOI: 10.1016/j.ijmecsci.2019.07.007.
- [82] P. Zhang et al. “An explicit phase field model for progressive tensile failure of composites”. In: *Engineering Fracture Mechanics* 241 (Jan. 2021). ISSN: 00137944. DOI: 10.1016/j.engfracmech.2020.107371.
- [83] T. Q. Bui and X. Hu. “A review of phase-field models, fundamentals and their applications to composite laminates”. In: *Engineering Fracture Mechanics* 248 (May 2021). ISSN: 00137944. DOI: 10.1016/j.engfracmech.2021.107705.
- [84] X. Nie and B. Sc. *FAILURE MECHANISM OF ROLLING SHEAR FAILURE IN CROSS-LAMINATED TIMBER*. 2015. DOI: 10.14288/1.0215881.
- [85] Z. Wang et al. “Influence of technical characteristics on the rolling shear properties of cross laminated timber by modified planar shear tests”. In: *Maderas. Ciencia y tecnología* (ahead 2018), pp. 0–0. ISSN: 0718-221X. DOI: 10.4067/S0718-221X2018005031601.
- [86] P. Mestek and P. Dietsch. *Design concept for CLT-reinforced with self-tapping screws* *. 2011.
- [87] Q. Zhou et al. “Measurement of rolling shear modulus and strength of cross laminated timber fabricated with black spruce”. In: *Construction and Building Materials* 64 (Aug. 2014), pp. 379–386. ISSN: 09500618. DOI: 10.1016/j.conbuildmat.2014.04.039.
- [88] L. Franzoni et al. “Influence of orientation and number of layers on the elastic response and failure modes on CLT floors: modeling and parameter studies”. In: *European Journal of Wood and Wood Products* (2016), p. 10. DOI: 10.1007/s00107-016-1038-xř.
- [89] N. Pagano. “Exact Solutions for Rectangular Bidirectional Composites and Sandwich Plates”. In: *Journal of Composite Materials* 4 (1 Jan. 1970), pp. 20–34. ISSN: 0021-9983. DOI: 10.1177/002199837000400102.

- [90] T. A. van der Put. “A continuum failure criterion applicable to wood”. In: *Journal of Wood Science* 55 (5 Oct. 2009), pp. 315–322. ISSN: 1435-0211. DOI: 10.1007/s10086-009-1036-2.
- [91] J. A. Nairn. “Predicting failure of notched cross-laminated timber plates including the effect of environmental stresses”. In: *Wood Material Science and Engineering* 16 (5 2021), pp. 299–311. ISSN: 17480280. DOI: 10.1080/17480272.2020.1718205.
- [92] S. Navaratnam et al. “The use of digital image correlation for identifying failure characteristics of cross-laminated timber under transverse loading”. In: *Measurement: Journal of the International Measurement Confederation* 154 (Mar. 2020). ISSN: 02632241. DOI: 10.1016/j.measurement.2020.107502.
- [93] Z. Huang et al. “Modeling of Cross-Laminated Timber (CLT) panels loaded with combined out-of-plane bending and compression”. In: *Engineering Structures* 250 (Jan. 2022). ISSN: 18737323. DOI: 10.1016/j.engstruct.2021.113335.
- [94] H. Daneshvar et al. “Structural behaviour of deep CLT lintels subjected to concentric and eccentric loading”. In: *Journal of Building Engineering* 43 (Nov. 2021). ISSN: 23527102. DOI: 10.1016/j.jobe.2021.103101.
- [95] R. Cherry et al. *Out-of-grade sawn pine: A state-of-the-art review on challenges and new opportunities in cross laminated timber (CLT)*. June 2019. DOI: 10.1016/j.conbuildmat.2019.03.293.
- [96] *European Committee for Standardization, EN 1995: 2008-06 Eurocode 5: Design of timber structures-Part 1-1: General Common rules and rules for buildings*.
- [97] K. Franz. “Prof. Dr.-Ing. Karl Möhler 60 Jahre”. In: *Holz als Roh- und Werkstoff* 30 (6 June 1972), pp. 234–236. ISSN: 0018-3768. DOI: 10.1007/BF02617593.
- [98] L. P. Qiu, E. C. Zhu, and J. W. V. D. Kuilen. “Modeling crack propagation in wood by extended finite element method”. In: *European Journal of Wood and Wood Products* 72 (2 Mar. 2014), pp. 273–283. ISSN: 00183768. DOI: 10.1007/s00107-013-0773-5.
- [99] M. Lavrenčič and B. Brank. “Failure analysis of ribbed cross-laminated timber plates”. In: *Coupled Systems Mechanics* 7 (1 Feb. 2018), pp. 79–93. ISSN: 22342192. DOI: 10.12989/csm.2018.7.1.079.
- [100] Y. Ma et al. “Flexural and shear performance of CLT panels made from salvaged beetle-killed white spruce”. In: *Construction and Building Materials* 302 (Oct. 2021). ISSN: 09500618. DOI: 10.1016/j.conbuildmat.2021.124381.
- [101] G. Kirchhoff. “Über das Gleichgewicht und die Bewegung einer elastischen Scheibe.” In: *Journal für die reine und angewandte Mathematik (Crelles Journal)* 1850 (40 July 1850), pp. 51–88. ISSN: 0075-4102. DOI: 10.1515/crll.1850.40.51.
- [102] R. D. Mindlin. “Influence of Rotatory Inertia and Shear on Flexural Motions of Isotropic, Elastic Plates”. In: *Journal of Applied Mechanics* 18 (1 Mar. 1951), pp. 31–38. ISSN: 0021-8936. DOI: 10.1115/1.4010217.
- [103] J. N. Reddy. “A Simple Higher-Order Theory for Laminated Composite Plates”. In: *Journal of Applied Mechanics* 51 (4 Dec. 1984), pp. 745–752. ISSN: 0021-8936. DOI: 10.1115/1.3167719.
- [104] E. Carrera. “Theories and Finite Elements for Multilayered Plates and Shells: A Unified compact formulation with numerical assessment and benchmarking”. In: *Archives of Computational Methods in Engineering* 10 (3 Sept. 2003), pp. 215–296. ISSN: 1134-3060. DOI: 10.1007/BF02736224.

- [105] S. A. Lur'e and N. P. Shumova. "Kinematic models of refined theories concerning composite beams, plates, and shells". In: *Mechanics of Composite Materials* 32 (5 Sept. 1996), pp. 422–430. ISSN: 0191-5665. DOI: 10.1007/BF02313861.
- [106] J. N. Reddy and D. H. Robbins. "Theories and Computational Models for Composite Laminates". In: *Applied Mechanics Reviews* 47 (6 June 1994), pp. 147–169. ISSN: 0003-6900. DOI: 10.1115/1.3111076.
- [107] E. J. Barbero, J. N. Reddy, and J. Teply. "An accurate determination of stresses in thick laminates using a generalized plate theory". In: *International Journal for Numerical Methods in Engineering* 29 (1 Jan. 1990), pp. 1–14. ISSN: 0029-5981. DOI: 10.1002/nme.1620290103.
- [108] M. Četković and D. Vuksanović. "Bending, free vibrations and buckling of laminated composite and sandwich plates using a layerwise displacement model". In: *Composite Structures* 88 (2 Apr. 2009), pp. 219–227. ISSN: 02638223. DOI: 10.1016/j.compstruct.2008.03.039.
- [109] M. Marjanović and D. Vuksanović. "Layerwise solution of free vibrations and buckling of laminated composite and sandwich plates with embedded delaminations". In: *Composite Structures* 108 (1 2014), pp. 9–20. ISSN: 02638223. DOI: 10.1016/j.compstruct.2013.09.006.
- [110] M. Marjanović, G. Meschke, and D. Vuksanović. "A finite element model for propagating delamination in laminated composite plates based on the Virtual Crack Closure method". In: *Composite Structures* 150 (Aug. 2016), pp. 8–19. ISSN: 02638223. DOI: 10.1016/j.compstruct.2016.04.044.
- [111] M. Marjanović, D. Vuksanović, and G. Meschke. "Geometrically nonlinear transient analysis of delaminated composite and sandwich plates using a layerwise displacement model with contact conditions". In: *Composite Structures* 122 (Apr. 2015), pp. 67–81. ISSN: 02638223. DOI: 10.1016/j.compstruct.2014.11.028.
- [112] M. Marjanović et al. "Three-dimensional stress analysis and design of cross-laminated timber panels using full-layerwise-theory-based finite element method". In: *Thin-Walled Structures* 157 (Dec. 2020). ISSN: 02638231. DOI: 10.1016/j.tws.2020.107156.
- [113] A. K. Nayak, R. A. Shenoi, and S. S. Moy. "Dynamic response of composite sandwich plates subjected to initial stresses". In: *Composites Part A: Applied Science and Manufacturing* 37 (8 Aug. 2006), pp. 1189–1205. ISSN: 1359835X. DOI: 10.1016/j.compositesa.2005.05.034.
- [114] O. Zienkiewicz and R. Taylor. *The Finite Element Method: Solid mechanics*. Vol. 2. Butterworth-Heinemann, 2000.
- [115] M. Dudzinski, M. Rozgic, and M. Stiemer. "oFEM: An object oriented finite element package for Matlab". In: *Applied Mathematics and Computation* 334 (Oct. 2018), pp. 117–140. ISSN: 00963003. DOI: 10.1016/j.amc.2017.11.042.
- [116] T. Rahman and J. Valdman. "Fast MATLAB assembly of FEM matrices in 2D and 3D: Nodal elements". In: *Applied Mathematics and Computation* 219 (13 2013), pp. 7151–7158. ISSN: 00963003. DOI: 10.1016/j.amc.2011.08.043.
- [117] D. H. Roubins and J. N. Reddy. *MODELLING OF THICK COMPOSITES USING A LAYERWISE LAMINATE THEORY*, p. 993.
- [118] R. Talreja. "A continuum mechanics characterization of damage in composite materials". In: *Proceedings of the Royal Society of London. A. Mathematical and Physical Sciences* 399 (1817 June 1985), pp. 195–216. ISSN: 0080-4630. DOI: 10.1098/rspa.1985.0055.

- [119] D. C. Drucker. “A Definition of Stable Inelastic Material”. In: *Journal of Applied Mechanics* 26 (1 Mar. 1959), pp. 101–106. ISSN: 0021-8936. DOI: 10.1115/1.4011929.
- [120] D. Hull and T. W. Clyne. *An Introduction to Composite Materials*. Cambridge University Press, Aug. 1996. ISBN: 9780521381901. DOI: 10.1017/CB09781139170130.
- [121] S. W. Tsai and V. D. Azzi. “Strength of laminated composite materials”. In: *AIAA Journal* 4 (2 1966), pp. 296–301. ISSN: 00011452. DOI: 10.2514/3.3431.
- [122] R. Talreja. *Assessment of the fundamentals of failure theories for composite materials*. Dec. 2014. DOI: 10.1016/j.compscitech.2014.10.014.
- [123] S. W. Tsai. *A Survey of Macroscopic Failure Criteria for Composite Materials*. DOI: 10.1177/07316844840030010.
- [124] B. W. Rosen. *STRENGTH OF UNIAXIAL FIBROUS COMPOSITES*. 1970. DOI: 10.1016/B978-0-08-006421-5.50034-4.
- [125] J. F. Labuz and A. Zang. “Mohr–Coulomb Failure Criterion”. In: *Rock Mechanics and Rock Engineering* 45 (6 Nov. 2012), pp. 975–979. ISSN: 0723-2632. DOI: 10.1007/s00603-012-0281-7.
- [126] Y. S. N. Reddy and J. N. Reddy. *Linear and non-linear failure analysis of composite laminates with transverse shear*. 1992, pp. 227–255.
- [127] T. E. Tay et al. “Progressive failure analysis of composites”. In: *Journal of Composite Materials* 42 (18 Sept. 2008), pp. 1921–1966. ISSN: 00219983. DOI: 10.1177/0021998308093912.
- [128] M. Hinton, A. Kaddour, and P. Soden. “A comparison of the predictive capabilities of current failure theories for composite laminates, judged against experimental evidence”. In: *Composites Science and Technology* 62 (12-13 Sept. 2002), pp. 1725–1797. ISSN: 02663538. DOI: 10.1016/S0266-3538(02)00125-2.
- [129] Z. Xia. “A meso/micro-mechanical model for damage progression in glass-fiber/epoxy cross-ply laminates by finite-element analysis”. In: *Composites Science and Technology* 60 (8 June 2000), pp. 1171–1179. ISSN: 02663538. DOI: 10.1016/S0266-3538(00)00022-1.
- [130] Y. Zhang, Z. Xia, and F. Ellyin. “Viscoelastic and Damage Analyses of Fibrous Polymer Laminates by Micro/meso-mechanical Modeling”. In: *Journal of Composite Materials* 39 (22 Nov. 2005), pp. 2001–2022. ISSN: 0021-9983. DOI: 10.1177/0021998305052024.
- [131] P. Ladevèze et al. “A mesomodel for localisation and damage computation in laminates”. In: *Computer Methods in Applied Mechanics and Engineering* 183 (1-2 Mar. 2000), pp. 105–122. ISSN: 00457825. DOI: 10.1016/S0045-7825(99)00214-5.
- [132] P. Maimí et al. “A continuum damage model for composite laminates: Part II - Computational implementation and validation”. In: *Mechanics of Materials* 39 (10 Oct. 2007), pp. 909–919. ISSN: 01676636. DOI: 10.1016/j.mechmat.2007.03.006.
- [133] P. Ladevèze. “Multiscale modelling and computational strategies for composites”. In: *International Journal for Numerical Methods in Engineering* 60 (1 May 2004), pp. 233–253. ISSN: 00295981. DOI: 10.1002/nme.960.
- [134] R. Talreja. “Multi-scale modeling in damage mechanics of composite materials”. In: *Journal of Materials Science* 41 (20 Nov. 2006), pp. 6800–6812. ISSN: 0022-2461. DOI: 10.1007/s10853-006-0210-9.
- [135] Z. P. Bažant and T. B. Belytschko. “Wave Propagation in a Strain-Softening Bar: Exact Solution”. In: *Journal of Engineering Mechanics* 111 (3 Mar. 1985), pp. 381–389. ISSN: 0733-9399. DOI: 10.1061/(ASCE)0733-9399(1985)111:3(381).

- [136] T. Belytschko and D. Lasry. “A study of localization limiters for strain-softening in statics and dynamics”. In: *Computers Structures* 33 (3 1989), pp. 707–715. ISSN: 00457949. DOI: 10.1016/0045-7949(89)90244-7.
- [137] A Matzenmiller, J Lubliner, and R. L. Taylor. *A constitutive model for anisotropic damage in fiber-composites*. 1995, pp. 125–152.
- [138] N. Zobeiry, R. Vaziri, and A. Poursartip. “Characterization of strain-softening behavior and failure mechanisms of composites under tension and compression”. In: *Composites Part A: Applied Science and Manufacturing* 68 (2015), pp. 29–41. ISSN: 1359835X. DOI: 10.1016/j.compositesa.2014.09.009.
- [139] I. R. Glišović. “Teorijska i eksperimentalna analiza nosača od lepljenog lameliranog drveta ojačanih karbonskim trakama”. Univerzitet u Beogradu, Građevinski Fakultet, 2013.
- [140] P. J. Gustafsson and H. Danielsson. “Perpendicular to grain stiffness of timber cross sections as affected by growth ring pattern, size and shape”. In: *European Journal of Wood and Wood Products* 71 (1 Jan. 2013), pp. 111–119. ISSN: 0018-3768. DOI: 10.1007/s00107-012-0648-1.
- [141] B. K. Dahl. “Mechanical properties of clear wood from Norway spruce”. Norwegian University of Science and Technology, 2009.
- [142] P. J. Gustafsson. *Fracture perpendicular to grain - structural applications*. Ed. by S. Thelandersson and H. J. Larsen. 2003.
- [143] E. C. for Standardization (CEN). *Eurocode 5: Design of timber structures. Part 1-1: General - Common rules and rules for buildings*. EN 1995-1-1, 2004.
- [144] I. Glišović et al. “Numerical analysis of glulam beams reinforced with CFRP plates”. In: *Journal of Civil Engineering and Management* 23 (7 Oct. 2017), pp. 868–879. ISSN: 18223605. DOI: 10.3846/13923730.2017.1341953.
- [145] H. Danielsson. *Perpendicular to grain fracture analysis of wooden structural elements : models and applications*. Media-Tryck, 2013. ISBN: 9789174734751.
- [146] A Coll et al. *GiD v.13 user manual, CIMNE. Barcelona: International Centre for Numerical Methods in Engineering*. 2016.
- [147] J. sergio Rodrigues alves filho and P. R. B. Devloo. *Object oriented programming in scientific computations: The beginning of a new era*. Jan. 1991. DOI: 10.1108/eb023828.
- [148] G. Miller. “An object-oriented approach to structural analysis and design”. In: *Computers Structures* 40 (1 1991), pp. 75–82. ISSN: 00457949. DOI: 10.1016/0045-7949(91)90459-Y.
- [149] T. Zimmermann, Y. Dubois-Pèlerin, and P. Bomme. “Object-oriented finite element programming: I. Governing principles”. In: *Computer Methods in Applied Mechanics and Engineering* 98 (2 July 1992), pp. 291–303. ISSN: 00457825. DOI: 10.1016/0045-7825(92)90180-R.
- [150] G. Archer, G. Fenves, and C. Thewalt. “A new object-oriented finite element analysis program architecture”. In: *Computers Structures* 70 (1 Jan. 1999), pp. 63–75. ISSN: 00457949. DOI: 10.1016/S0045-7949(98)00194-1.
- [151] A. Cardona, I. Klapka, and M. Geradin. “Design of a new finite element programming environment”. In: *Engineering Computations* 11 (4 Apr. 1994), pp. 365–381. ISSN: 0264-4401. DOI: 10.1108/02644409410799344.
- [152] N. J. Pagano and R. Talreja. *Local Mechanics Concepts for Composite Material Systems*. 1992.

- [153] *DIN 1052:2004: Design of Timber Structures – General Rules and Rules for Buildings.*
- [154] R Hearmon. “Elasticity of Wood and Plywood”. In: *Nature* 162 (4125 Nov. 1948), pp. 826–826. ISSN: 0028-0836. DOI: 10.1038/162826a0.
- [155] *European Committee of Standardization (CEN), EN 338: Structural Timber – Strength Classes.* 2009.
- [156] H. Unterwieser and G. Schickhofer. *Characteristic Values and Test Configurations of CLT with Focus on Selected Properties.* 2013.
- [157] R. Stürzenbecher, K. Hofstetter, and J. Eberhardsteiner. “Cross Laminated Timber: A Multi-Layer, Shear Compliant Plate and its Mechanical Behavior”. In: CNR-IVALSA, 2010.
- [158] C. Czaderski et al. “Versuche und Berechnungen an allseitig gelagerten 3-schichtigen Brettsper Holzplatten”. In: *Holz als Roh- und Werkstoff* 65 (5 Oct. 2007), pp. 383–402. ISSN: 0018-3768. DOI: 10.1007/s00107-007-0184-6.
- [159] H Blass and P Fellmoser. “Design of solid wood panels with cross layers”. In: 2004.
- [160] *European Committee of Standardization (CEN), EN 1991-1-1: Eurocode 1: Actions on Structures - Part 1-1: General Actions Densities, Self-Weight, Imposed Loads for Buildings.* 2004.
- [161] M Walner-Novak, K Koppelhuber, and K Pock. *Cross-Laminated Timber Structural Design Basic design and engineering principles according to Eurocode.* 2014.
- [162] E. Carrera et al. *Finite Element Analysis of Structures Through Unified Formulation.* Wiley, Aug. 2014. ISBN: 9781119941217. DOI: 10.1002/9781118536643.
- [163] X. Xu et al. “A numerical investigation into size effects in centre-notched quasi-isotropic carbon/epoxy laminates”. In: *Composites Science and Technology* 111 (May 2015), pp. 32–39. ISSN: 02663538. DOI: 10.1016/j.compscitech.2015.03.001.
- [164] J. Reiner, N. Zobeiry, and R. Vaziri. “A stacked sublaminar-based damage-plasticity model for simulating progressive damage in composite laminates under impact loading”. In: *Thin-Walled Structures* 156 (Nov. 2020). ISSN: 02638231. DOI: 10.1016/j.tws.2020.107009.
- [165] X. Li et al. “Experimental study of damage propagation in Over-height Compact Tension tests”. In: *Composites Part A: Applied Science and Manufacturing* 40 (12 Dec. 2009), pp. 1891–1899. ISSN: 1359835X. DOI: 10.1016/j.compositesa.2009.08.017.
- [166] www.substrate4clt.com.
- [167] *European Committee for Standardization, EN 408:2010+A1: Timber structures - Structural timber and glued laminated timber - Determination of some physical and mechanical properties.* 2012.
- [168] *European Committee for Standardization, EN 384: Structural timber - Determination of characteristic values of mechanical properties and density.* 2016.
- [169] *International Organization for Standardization, ISO 13061-2: Physical and mechanical properties of wood - Test methods for small clear wood specimens - Part 2: Determination of density for physical and mechanical tests.* 2014.
- [170] *American Society for Testing and Materials, ASTM D143-09: Standard test methods for small clear specimens of timber.* 2009.
- [171] J. Bodig and B. Jayne. *Mechanics of Wood and Wood Composites.* 1982, p. 736.
- [172] *European Committee for Standardization, EN 16351: Timber structures - Cross laminated timber -Requirements.* 2015.

Biography

Emilija Jočić was born on March 4, 1991 in Smederevo, where she finished elementary school and Grammar school, natural sciences. She enrolled the BSc studies at the Faculty of Civil Engineering in Belgrade in 2010 and graduated in 2014 (Module Structures) with the average grade of 8.80/10. She defended her final paper “Transverse vibrations of circular plates using spectral element method” with the highest grade thus acquire the title Bachelor of Science. She enrolled the MSc studies at the Faculty of Civil Engineering in Belgrade in 2014 and graduated in 2015 (Module Structures) with the average grade of 9.43/10. She defended her MSc thesis “Free vibration analysis of stiffened plate assemblies using spectral element method” on the Chair of engineering mechanics and theory of structures with the highest grade thus acquire the title Master of Science. She enrolled the PhD studies at the Faculty of Civil Engineering in Belgrade in 2015. She has passed all the exams from the curriculum with the average grade of 10/10. In 2013/2014 the foundation “Prof. Milan Đurić” awarded her for achieved results in the theory of structures courses during the studies. In 2010 the Faculty of Civil Engineering in Belgrade awarded her for the accomplishments during the year. She was scholarship holder from Republic of Serbia for the period from 2011 until 2013. She participated in the project of the Republic Seismological Institute "Improvement of harmonization of seismic hazard maps of the Western Balkans", from March to September 2014. During MSc studies, she was hired as a student demonstrator in the subjects of Technical Physics.

She started working at the Faculty of Civil Engineering in July 2016, where she was employed as a trainee researcher at the Institute for Numerical Analysis and Design of Structures on the project "Towards Development of Sustainable Cities: Influence of Traffic Induced Vibrations on Buildings and Humans" (TR36046 lead by Prof. Dr Mira Petronijević). Since January 2018 she has been employed as a Teaching Assistant - PhD Student for the scientific filed Engineering mechanics and theory of structures. She has been teaching exercises in the subjects Structural Analysis, Matrix structural analysis and Computer aided numerical structural analysis and design. Emilija spent three months (March-June 2021) on a research stay at Ruhr University Bochum, Institute for Structural Mechanics, under supervision of Prof. Dr.techn. Günther Meschke. This research stay was part of her participation in the Erasmus+ KA103 student program. Currently, she is a participant in the Substrate4CLT project, funded by the Science Fund of the Republic of Serbia within the IDEA Program (project leader Assoc. Prof. Dr. Marija Nefovska-Danilović). Emilija is using MS Office, AutoCAD, programming language MATLAB, and civil engineering software packages Radimpex Tower, SAP2000, Abaqus. She is a member of Serbian Society of Mechanics. She speaks and writes English and Spanish. She is married. So far, Emilija has contributed as an author or co-author to the publication of the following papers: two papers (M21a), two papers (M21), one paper (M22), two papers (M24), eight papers (M33), one paper (M45), and one paper (M63). The list of papers published in relation to this dissertation is provided in the Contributions.

Contributions

International Journal Papers

1. **Jočić E**, Marjanović M (2022). Progressive failure analysis of open-hole composite laminates using FLWT-SCB prediction model. *Int. J. Mech.* (**M21a**), 227:107407.
2. Marjanović M, Marković N, **Damnjanović E**, Cvetković R (2020). Three-dimensional stress analysis and design of cross-laminated timber panels using full-layerwise-theory-based finite element method. *Thin. Wall. Struct.* (**M21a**), 157:107156.
3. Marjanović M, Meschke G, **Damnjanović E** (2020). Object-oriented framework for 3D bending and free vibration analysis of multilayer plates: Application to cross-laminated timber and soft-core sandwich panels. *Compos. Struct.* (**M21**); 255: 112859.

International Conferences M33

1. **Jočić E**, Marjanović M (09/2022). Progressive failure analysis of composite laminates loaded in compression. 16th Conference hosted by ASES. Arandelovac, Serbia, 148-157.
2. **Damnjanović E**, Milojević M, Marjanović M (05/2021). Probabilistic first-ply failure analysis of composite laminates. 16th Conference hosted by ASES. Arandelovac, Serbia, 55-62.
3. Obradović N, Todorović M, Marjanović M, **Damnjanović E** (2020). Diagrams for stress and deflection prediction in cross-laminated timber (CLT) panels with non-classical boundary conditions. International Conference on Contemporary Theory and Practice in Construction XIV. Banja Luka, Bosnia and Herzegovina, 55-62.
4. **Damnjanović E**, Marjanović M (06/2019). Three-Dimensional Stress Analysis of Laminated Composite Plates using FLWT-based Finite Elements. The 7th International Congress of Serbian Society of Mechanics. Sremski Karlovci, Serbia.

National monograph M45

1. Marjanović M, **Damnjanović E** (2019). Bending analysis of cross-laminated-timber (CLT) panels using layered finite elements. In: Prašćević Ž, Pejović R, Salatić R, Nefovska-Danilović M (Eds.): *Theory of Civil Engineering Structures - Monograph dedicated to the memory of Professor Miodrag Sekulović*”, Faculty of Civil Engineering, University of Belgrade, Faculty of Civil Engineering, University of Montenegro. Belgrade, 91-100.

Изјава о ауторству

Име и презиме аутора Емилија Јочић
Број индекса 905/15

Изјављујем

да је докторска дисертација под насловом

Progressive failure analysis of laminar composites under three-dimensional stress state using layered finite elements

(Анализа прогресивног лома композитних ламината у условима просторног стања напона применом слојевитих коначних елемената)

- резултат сопственог истраживачког рада;
- да дисертација у целини ни у деловима није била предложена за стицање друге дипломе према студијским програмима других високошколских установа;
- да су резултати коректно наведени и
- да нисам кршио/ла ауторска права и користио/ла интелектуалну својину других лица.

Потпис аутора

У Београду, јун 2023.



Изјава о истоветности штампане и електронске верзије докторског рада

Име и презиме аутора	Емилија Јочић
Број индекса	905/15
Студијски програм	Грађевинарство
Наслов рада	Progressive failure analysis of laminar composites under three-dimensional stress state using layered finite elements
Ментор	Доц. др Мирослав Марјановић

Изјављујем да је штампана верзија мог докторског рада истоветна електронској верзији коју сам предао/ла ради похрањена у **Дигиталном репозиторијуму Универзитета у Београду**.

Дозвољавам да се објаве моји лични подаци везани за добијање академског назива доктора наука, као што су име и презиме, година и место рођења и датум одбране рада.

Ови лични подаци могу се објавити на мрежним страницама дигиталне библиотеке, у електронском каталогу и у публикацијама Универзитета у Београду.

Потпис аутора

У Београду, јун 2023.



Изјава о коришћењу

Овлашћујем Универзитетску библиотеку „Светозар Марковић“ да у Дигитални репозиторијум Универзитета у Београду унесе моју докторску дисертацију под насловом:

Progressive failure analysis of laminar composites under three-dimensional stress state using layered finite elements

(Анализа прогресивног лома композитних ламината у условима просторног стања напона применом слојевитих коначних елемената)

која је моје ауторско дело.

Дисертацију са свим прилозима предао/ла сам у електронском формату погодном за трајно архивирање

Моју докторску дисертацију похрањену у Дигиталном репозиторијуму Универзитета у Београду и доступну у отвореном приступу могу да користе сви који поштују одредбе садржане у одабраном типу лиценце Креативне заједнице (Creative Commons) за коју сам се одлучио/ла.

1. Ауторство (CC BY)
2. Ауторство – некомерцијално (CC BY-NC)
3. Ауторство – некомерцијално – без прерада (CC BY-NC-ND)
4. Ауторство – некомерцијално – делити под истим условима (CC BY-NC-SA)
5. Ауторство – без прерада (CC BY-ND)
6. Ауторство – делити под истим условима (CC BY-SA)

(Молимо да заокружите само једну од шест понуђених лиценци.
Кратак опис лиценци је саставни део ове изјаве).

Потпис аутора

У Београду, јун 2023.



1. **Ауторство.** Дозвољаваате умножавање, дистрибуцију и јавно саопштавање дела, и прераде, ако се наведе име аутора на начин одређен од стране аутора или даваоца лиценце, чак и у комерцијалне сврхе. Ово је најслободнија од свих лиценци.

2. **Ауторство – некомерцијално.** Дозвољаваате умножавање, дистрибуцију и јавно саопштавање дела, и прераде, ако се наведе име аутора на начин одређен од стране аутора или даваоца лиценце. Ова лиценца не дозвољава комерцијалну употребу дела.

3. **Ауторство – некомерцијално – без прерада.** Дозвољаваате умножавање, дистрибуцију и јавно саопштавање дела, без промена, преобликовања или употребе дела у свом делу, ако се наведе име аутора на начин одређен од стране аутора или даваоца лиценце. Ова лиценца не дозвољава комерцијалну употребу дела. У односу на све остале лиценце, овом лиценцом се ограничава највећи обим права коришћења дела.

4. **Ауторство – некомерцијално – делити под истим условима.** Дозвољаваате умножавање, дистрибуцију и јавно саопштавање дела, и прераде, ако се наведе име аутора на начин одређен од стране аутора или даваоца лиценце и ако се прерада дистрибуира под истом или сличном лиценцом. Ова лиценца не дозвољава комерцијалну употребу дела и прерада.

5. **Ауторство – без прерада.** Дозвољаваате умножавање, дистрибуцију и јавно саопштавање дела, без промена, преобликовања или употребе дела у свом делу, ако се наведе име аутора на начин одређен од стране аутора или даваоца лиценце. Ова лиценца дозвољава комерцијалну употребу дела.

6. **Ауторство – делити под истим условима.** Дозвољаваате умножавање, дистрибуцију и јавно саопштавање дела, и прераде, ако се наведе име аутора на начин одређен од стране аутора или даваоца лиценце и ако се прерада дистрибуира под истом или сличном лиценцом. Ова лиценца дозвољава комерцијалну употребу дела и прерада. Слична је софтверским лиценцама, односно лиценцама отвореног кода.